Imperial College of Science, Technology and Medicine
Department of Mathematics

Lagrangian Transport in an Idealised Meandering Oceanic Jet

Josephine Park

Submitted in part fulfilment of the requirements for the degree of
Doctor of Philosophy in Mathematics of
the Diploma of Imperial College, September 17, 2020

Declaration of Originality

I declare that this work is my own and anything else is appropriately referenced.

Copyright Declaration

The copyright of this thesis rests with the author. Unless otherwise indicated, its contents are licensed under a Creative Commons Attribution-NonCommercial 4.0 International Licence (CC BY-NC).

Under this licence, you may copy and redistribute the material in any medium or format. You may also create and distribute modified versions of the work. This is on the condition that: you credit the author and do not use it, or any derivative works, for a commercial purpose.

When reusing or sharing this work, ensure you make the licence terms clear to others by naming the licence and linking to the licence text. Where a work has been adapted, you should indicate that the work has been changed and describe those changes.

Please seek permission from the copyright holder for uses of this work that are not included in this licence or permitted under UK Copyright Law.

Abstract

Ocean general circulation models (OGCMs) frequently operate at a grid scale larger than the size of oceanic eddies, therefore eddying effects must be parameterised. One such example is that of eddy-induced Lagrangian transport. The current method of parameterising eddy-induced transport assumes isotropic and diffusive behaviour. However several studies employing numerical models (Kamenkovich et al. 2015, 2009, Berloff et al. 2002), or using satellite altimetry derived velocity fields or by taking real float data (Rypina et al. 2012) have have demonstrated Lagrangian behaviour contradicting these assumptions.

We proceed by running a numerical model simulating two differing meandering oceanic jets. Two novel spatial interpolation methods motivated by the non-divergence property of the numerical model will be tested and incorporated into a Lagrangian transport model.

Eddying Lagrangian statistics for the two jet regimes will be compared and will verify that a new non-diffusive, anisotropic parameterisation method will need to be considered. A new flow based dispersion measure with the aim of capturing sharper diffusivity estimates at the jet core will be motivated and introduced.

We then run three Stochastic Markov models with the aim of reproducing the observed Lagrangian statistics and outline the applicability of some further Stochastic models. In the final chapter, we decompose the flow into Empirical Orthogonal Functions and establish that eddy-induced meridional transport is largely influenced by small-scale flow variability that cannot be realistically be captured kinematically. The eddy-induced zonal transport however can be explained by a Stokes' drift.

Acknowledgements

Firstly, pursuing this PhD was made possible through the funding of EPSRC and the Mathematics of Planet Earth CDT, and so I am thankful for being awarded this opportunity.

I would like to offer my sincere thanks to my supervisor, Pavel Berloff, for guiding me and supporting me through my PhD, through thick and thin. In particular, his patience and expertise were invaluable and I will be forever grateful.

In addition, I have benefited from guidance and direction in regards to my dissertation from several colleagues, including Igor Shevchenko, Colin Cotter, David Ham, Ali Mashayek and Peter Haynes.

I would also like acknowledge numerous academic friends, both from our Geophysical Fluid Dynamics research group and from the Mathematics of Planet Earth Doctoral Training Centre; most notably, Michael Haigh, for offering infinite amounts of both professional and personal advice and guidance, and for tolerating and forgiving my periods of stress. I would also like to thank Hemant Khatri, Tom Bendall, Thomas Gibson and Niraj Agarwal for all the intellectually stimulating discussion.

I would like to thank Stephen Pring at the Met Office for agreeing to take me on as a summer student and suggesting a thoroughly enjoyable project.

Finally, I would like to thank my parents for always reassuring me and supporting me.

Contents

List of Tables

List of Figures

List of Symbols and Abbreviations

D_i	Single-Particle Dispersion (SPD) components, $i = 1, 2$
t	Time
α_i	Single-Particle Dispersion exponent : $D_i \sim t^{\alpha_i}$
QG	Quasi-geostrophic
U	Velocity scale
L	Length scale
f	Coriolis parameter
β	Coriolis parameter variation in the beta-plane approximation
f_0	Coriolis parameter at $y = 0$
ρ	Density
ϵ	Rossby number
H_i	Layer Depths
g	Gravity
u	Zonal velocity
v	Meridional velocity
ψ	Stream Function
S_k	Stratification parameter in each layer, $k = 1, 2$
ν	Viscosity
γ	Bottom friction
U_0	Background zonal velocity
q	Potential vorticity (PV) anomaly
R_d	Rossby deformation radius
S_d	A stratification parameter such that $S_d = (L/R_d)^2$
g'	Reduced gravity

N_x	Number of grid points in x
N_y	Number of grid points in y
C	Courant Number
$\mathbf{x}_n(t)$	Location of particle n at time t
$\overline{\mathbf{u}}$	Time mean velocity
FFE	Full-following-eddy
EO	Eddy-Only
$\langle \cdot \rangle$	Ensemble average
K_i	Diffusivity components, $i = 1, 2$
c	Tracer concentration
R_i	Lagrangian Autocorrelation Function (LACF) components, $i = 1, 2$
σ^2_{ij}	Lagrangian velocity variance $i, j = 1, 2$
T^i_L	Lagrangian integral time-scale $i = 1, 2$
T	Locality time-scale
ζ	Full potential vorticity
$\overline{\zeta}$	Zonally- and time-averaged Potential Vorticity
D_{PV}	PV-Mapped dispersion
K_{PV}	PV-Mapped diffusivity
$W(r)$	Wiener Process
ξ	White noise
Ω	Lagrangian looping parameter
E_k	Eddy-Kinetic-Energy
EOF	Empirical Orthogonal Function
PC	Principal Component

Chapter 1

Introduction

1.1 The Importance of Oceanic Material Transport, Jets and Mesoscale Eddies

Being able to effectively understand and parameterise Lagrangian transport is essential in various applications of ocean modelling as lateral material transport influences various oceanic and atmospheric processes. It has been shown that mixing can affect large-scale ocean processes such as the Meridional Overturning Circulation (MOC) (Marshall et al. 2017) as heat is transported poleward, and so understanding the rate of transport and the nature of transport pathways is of primordial importance (Thomas et al. 2015, Van Roekel et al. 2009). In turn, lateral transport affects the accuracy of global climate models (Fox-Kemper et al. 2011) as a result of the estimation of the rate of ocean uptake of atmospheric tracers, most notably of heat (Treguier et al. 2017), of Carbon Dioxide (Fox-Kemper et al. 2011, Marshall et al. 2017), and of the distribution of salinity (Weijer & van Sebille 2014), which also evidentially has an impact on global ocean circulation. Modelling of oceanic transport is also of interest in other fields of research outside of global earth system modelling, such as modelling nuclear or oil spills (Drouin et al. 2019), the distribution of rubbish (Hardesty et al. 2017), or marine life (Everett et al. 2017).

Jet structures are ubiquitous in the ocean and can be found in every major ocean basin in

the world. Key examples are the Gulf Stream in the North Atlantic, the Kuroshio extension in the Pacific and the Antarctic Circumpolar Current (ACC) in the Southern Ocean. Each of these play a key role in transporting and distributing tracers. Jets are largely driven by mesoscale eddy interaction (Khatri & Berloff 2018, Vallis 2006), and so we cannot fully separate jet-driven transport from eddy-driven transport. There is two-way non-linear interaction between large-scale dynamics and mesoscale eddies (Khatri & Berloff 2018, Booth & Kamenkovich 2008).

Kamenkovich et al. (2009) highlights the interaction between the eddying field and the time-mean field, stating that eddies have two effects on Lagrangian transport that must be taken into account: the effect that eddies have on the time-mean flow and hence its indirect effect on Lagrangian transport; and also the transport directly induced by the eddying flow itself.

Booth & Kamenkovich (2008) establishes a link between mesoscale eddies and the distribution of chlorofluorocarbon in a model of the North Atlantic, and verifies that understanding the role of mesoscale eddies is essential in understanding the transfer of atmospheric gases. Brach et al. (2018) found that eddies tend to cause microplastics to concentrate in patches in the North Atlantic subtropical gyre. In an effort to parameterise eddies in the mixed layer, Fox-Kemper et al. (2011) found that small-scale oceanic features play an important role in global ocean climate simulations.

Therefore, in order to understand oceanic Lagrangian transport and its effects on other ocean processes, it is important to understand how it is driven by small-scale structures, which are often poorly represented in coarse-grained general circulation models (GCMs).

1.1.1 The Gulf Stream

The subject of the Gulf Stream and its role in assisting or hindering Lagrangian transport has long been a subject of great interest. The North Atlantic climate is greatly influenced by the rate at which the Gulf Stream transports tracers eastward and northward (Liu et al. 2018, Thomas & Zhai 2013, Treguier et al. 2017). Bower et al. (1985) studied the Gulf Stream as a prelude to Lagrangian studies, establishing that sharp potential vorticity and temperature gradients

coincided with the jet core, though tracers appear more uniformly mixed in deep waters. This is in general agreement with later studies that verify, as the potential vorticity gradient weakens in deeper water, mixing across the jet increases (Bower & Lozier 1994). The role of meander induced transport has been studied in the context of the Gulf Stream in numerous pieces of literature, most notably Bower (1991). Closed orbits in between jet meanders are observed where fluid is trapped and hence dispersion is suppressed. By introducing a perturbation to the flow, particles are allowed to mix more freely.

Examples of the importance of eddies in tracer distribution is also illustrated by the Gulf Stream in the North Atlantic. Eddies are diagnosed by regions of significant particle mixing, and act as partial barriers to transport across their boundaries (Bower & Lozier 1994, Bower & Rossby 1989). Thomas & Zhai (2013) ran an eddy-permitting model of the North Atlantic to study the effect of eddies on the variability of the Atlantic Meridional Overturning Circulation and demonstrate that the eddy contribution is significant. The largest variability is seen at latitudes at which the Gulf Stream lies.

O'Dwyer et al. (2000) argues that the distribution of potential vorticity plays a significant role in float dispersion in the North Atlantic, in particular, near the Gulf Stream where the potential vorticity is nearly uniform, the dispersion is strongly isotropic. It appears that floats spread preferentially along PV contours.

Liu et al. (2018) demonstrates that Lagrangian Coherent Structures (LCS), such as vortices, persist in the Gulf Stream and are strongly associated with surface transport and mixing. They can transport fluid over long spatial and temporal periods, before they are reabsorbed by the Gulf Stream. They also demonstrate that the inhomogeneity associated with Gulf Stream Lagrangian transport is linked to entrainment and detrainment of fluid due to jet meanders, as was strongly suggested by the kinematic model written by Bower (1991), and also due to the pinching of said jet meanders and the vortices shed as a result. The nature of the meandering Gulf Stream jet varies as we travel downstream. Near the Gulf Stream separation point at Cape Hatteras, there is very little cross stream mixing. Downstream, however, the Gulf Stream develops strong meanders and the potential vorticity gradient associated with the jet core breaks, to form rings (Waterman & Hoskins 2013, Liu et al. 2018). Fig. 1.1 illustrates

this meander pinching and vortex shedding. These are phenomena that will be studied in this thesis.

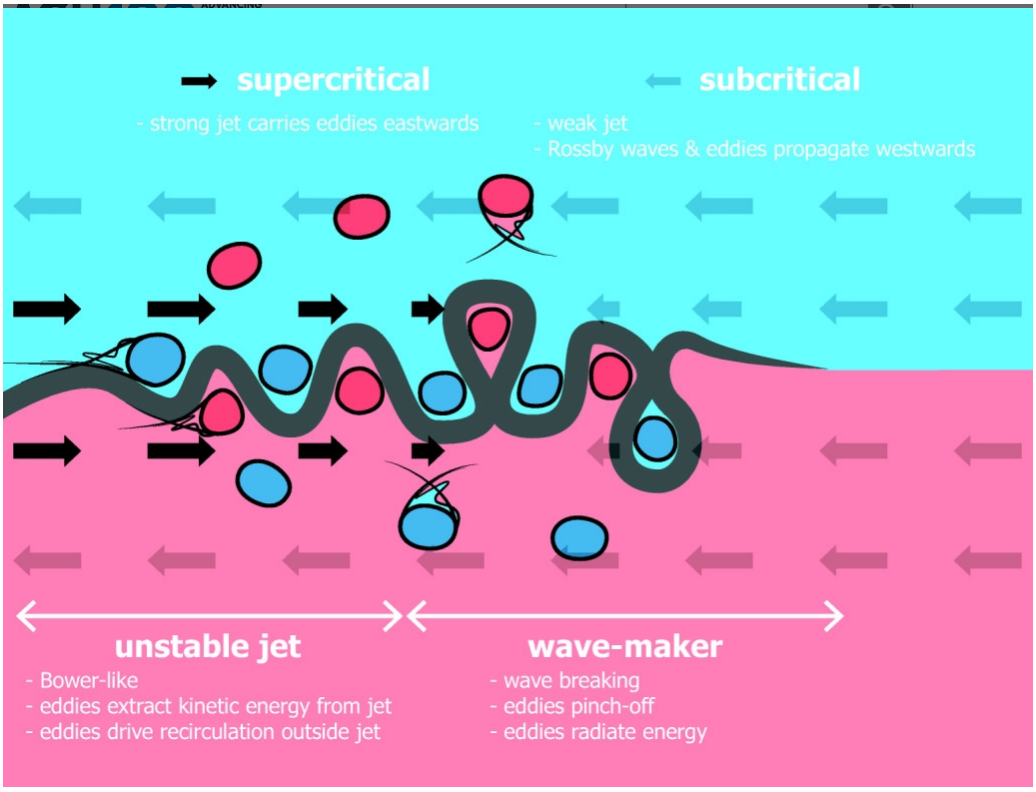

Figure 1.1: A schematic illustrating the two different jet regimes seen in the Gulf Stream as described by Liu et al. (2018) and Waterman & Hoskins (2013). Courtesy of Liu et al. (2018)

1.1.2 The Southern Ocean and the ACC

The Southern Ocean is unique as it is the only continuous ocean basin, i.e. it has no boundaries. It also connects other ocean basins, so is an important source of global tracer transport and is dominated by the ACC, which is a largely zonal jet circumnavigating the Antarctic continent. Hence, the ACC is the only continuous jet-like structure in the ocean. It has been shown that jets split, merge and move. Jet properties, such as strength, meander or width, may vary. This variability is largely driven by varying topography and mesoscale eddies.

Similarly to the Gulf Stream, it is of interest to understand whether the ACC acts as a barrier or blender to transport, and to understand where eddy mixing is enhanced; near the jet core or on its flanks. Ferrari & Nikurashin (2010) and Naveira Garabato et al. (2011) demonstrate that the ACC acts to suppress meridional eddy-induced mixing across the jet core,

except in regions of significant topography, and hypothesise that enhanced eddy mixing north of the ACC is a result of reduced mixing across the jet core. The suppression of eddy-induced cross-jet mixing, they suggest, is driven due to their finding that eddies propagate at a speed proportional to, but slower than, the mean flow.

By using a Lagrangian framework, Spence et al. (2014) was able to identify transient mesoscale eddies as having a role in transporting fluid away from the Southern Ocean. This clearly will have an effect on the ocean storage of heat or salt, and may affect global climate change, due to heating polar waters.

1.2 Diffusivity Estimates

Lagrangian diffusivity estimates broadly fall into three categories: particle, effective and tracer diffusivity. This thesis will primarily concern single particle statistics, but it is worth verifying the agreement between the different measures. We will briefly describe the three estimates here, before reviewing literature that reconcile the different estimates. Further details of diffusivity definitions are given in chapter 4.

Effective diffusivity, otherwise known as Nakamura diffusivity (Nakamura 1996), concerns the distortion of tracer contour lines via chaotic advection. It has typically been applied to the Southern Ocean. This is because it only provides contour averaged measures, as opposed to a two-dimensional tensor. The ACC is almost purely zonal with monotonic meridional gradients, hence their effective diffusivity can be interpreted as the meridional diffusivity or cross-jet diffusivity, though Abernathey & Marshall (2013) did estimate the effective diffusivity in a simplified version of the Eastern Pacific by using a zonally averaged-mean velocity and converting the domain into a zonally-periodic channel.

The tracer eddy diffusivity K is defined as follows:

$$\overline{v'C'} = -K\frac{\partial \overline{C}}{\partial y}, \tag{1.1}$$

where $\overline{v'C'}$ is the cross-current tracer flux and $\frac{\partial \overline{C}}{\partial y}$ is the mean cross-current tracer gradient.

The tracer diffusivity can be estimated either from Lagrangian or Eulerian estimates. Single particle diffusivity estimates are calculated from Lagrangian particle tracking experiments.

There has historically been disagreement between diffusivity estimates. Lagrangian estimates are often found to be several orders larger than the tracer-based estimates. Marshall et al. (2006) calculated Nakamura effective diffusivities in the southern ocean and they were found to be much smaller than those found using Lagrangian methods in Sallee et al. (2008).

Riha & Eden (2011) compares Lagrangian and Eulerian diffusivity estimates, and Klocker, Ferrari, Lacasce & Merrifield (2012) expands on this work by performing a quantitative comparison of tracer-based, particle-based and effective diffusivities calculated from particles and tracers numerically advected by a velocity field estimated in the South Pacific. They verify that there is agreement between the three estimates, as long as they are calculated over the appropriate time scale. Klocker, Ferrari, Lacasce & Merrifield (2012) also include two-particle dispersion derived diffusivity estimates in their analysis. The effective diffusivity is proportional to the two-particle dispersion at early times. However, at later times, the eddy driven mixing breaks down area conservation between tracer isolines. Though at latter times, the effective diffusivity agrees with the single particle diffusivity.

Both studies, (Riha & Eden 2011, Klocker, Ferrari, Lacasce & Merrifield 2012) conclude that Lagrangian diffusivities have often been over-estimated in the literature because Lagrangian particles in meandering chaotic jets, exhibit a negative lobe in the Lagrangian velocity autocorrelation function. This negative lobe is often associated with trapping of particles by coherent jets. Lagrangian studies based on surface drifter data often don't have long enough time series (see (Lumpkin et al. 2002, Lumpkin & Pazos 2007) and references therein), and therefore the Lagrangian statistics estimated beyond this negative lobe are considered to be noisy.

Furthermore, there are two methods of calculating the single particle diffusivity, one from the Lagrangian velocity variance, and the other from the dispersion. Riha & Eden (2011) compares the diffusivity of these two estimates, and finds that the dispersion derived diffusivity better captures the meridional cross jet diffusivity suppression, though stops short of explaining why. This will be discussed in greater detail in Chapter 4, where we also conclude that the dispersion derived estimate will be the diffusivity of choice.

1.3 Suppression of Cross-Jet Diffusivity

Several studies have demonstrated that eddying, meandering jets cause suppression of across-jet eddy diffusivity. As already mentioned, the ACC exhibits such suppression that cannot be explained by eddy kinetic energy alone, as the diffusivity is smaller around the jet core, where the eddy velocity is at its greatest, than on it's flanks.

Strong PV gradients have long been associated with mixing barriers (Haynes et al. 2007, Greenslade & Haynes 2008). Haynes et al. (2007) expands on the work done by Pierrehumbert (1991), by considering both a perturbed kinematic model of a meandering jet, and a similar dynamical model with a topographic forcing to which a perturbation is applied. Consistent with Pierrehumbert (1991), as the perturbation is increased, the transport barrier coinciding with the jet breaks. However, Haynes et al. (2007) also finds that this increased perturbation also results in an increased homogenisation of PV. Furthermore, the perturbation threshold at which the transport barrier breaks is higher in the dynamical model in which PV is conserved, than for the kinematic model, implying that strong PV gradients directly increase the strength of transport barriers.

More recently, the relationship between the mean flow and eddy propagation speed and cross jet mixing suppression was explicitly defined. Ferrari & Nikurashin (2010) demonstrated just this using an analytical approach in which the cross jet tracer derived diffusivity was analysed. By deriving an analytic expression for the diffusivity for a surface QG model, that was forced by a uniform zonal flow and a stochastically forced eddy field that can be seen as propagating waves, it was found that meridional mixing experienced greater suppression at the surface due to a closer agreement between the zonal flow speed and the eddy propagation speed. It is also found that when the zonal flow speed and eddy propagation speed are the same, the diffusivity is proportional to the eddy kinetic energy times the eddy decorrelation time-scale, which is consistent with the mixing length argument (Klocker & Abernathey 2014, Prandtl 1925).

The results presented in Ferrari & Nikurashin (2010) have been further verified by successive studies. Klocker, Ferrari & LaCasce (2012) also confirm the results hold by performing a similar

analytic study but for the single-particle derived diffusivity. This result is confirmed using the same velocity field as in Klocker, Ferrari, Lacasce & Merrifield (2012), and was apparent by the exhibited negative lobe in the Lagrangian autocorrelation function. They also further argued that care must be taken when calculating the Lagrangian particle derived diffusivity. By integrating the the first zero crossing in the Lagrangian velocity autocorrelation function, this would be equivalent to taking the maximum diffusivity. Simulations were run with the mean flow and with the mean flow removed. It was found that the diffusivity with the mean flow removed was maximized in the ACC jet core region, consistent with the mixing length argument. Suppression of mixing around the ACC jet core has further been confirmed by Abernathey & Marshall (2013).

Riha & Eden (2011) demonstrates that by removing the zonal mean flow from the velocity field, in an attempt to estimate a converged zonal diffusivity, there is no longer an increase in diffusivity in the vertical direction. They say this implies that removing it results in further break down of the meridional barrier to transport.

While the above studies are mostly focussed on the Southern Ocean and the ACC, Klocker & Abernathey (2014) verifies the results presented in Ferrari & Nikurashin (2010) but more generally. They also state, that in the absence of suppression effects caused by the mean flow, the diffusivity can be expressed as:

$$K = \Gamma\sqrt{2E}L_{mix}. \tag{1.2}$$

where L_{mix} is the mixing length, E is the eddy kinetic energy and Γ is the mixing efficiency, in agreement with the classic mixing length arguments. The two arguments: mixing length theory and cross-jet mixing suppression can then be combined to produce a more realistic diffusivity.

However, is cross-jet diffusivity suppressed when jets are not purely zonal? As mentioned previously, studies examining the relationship between eddy propagation speed, zonal mean flow speed and cross-jet diffusivity have largely focused on the ACC due to its' almost purely zonal orientation. However, many eddying jets, notably the Gulf Stream, are often not zonal.

Boland et al. (2012) compares transport in non-zonal jets. By introducing sloped topography to a two-layer QG model, non-zonal tilted jets are allowed to form and cross over PV gradients. Therefore, the PV gradients typically associated with strong mixing barriers are no longer aligned with the jets. By estimating transport using effective diffusivity, it was found that non-zonal jets are weaker barriers to transport due to this crossing of PV gradients. Smith (2007) considers the extreme case with a completely meridional mean flow and also finds that across-jet mixing is increased due to the dispersion of non-zonal shear.

In section 2 of Nakamura (2008), the relationship between the transport barrier geometry, defined as a minimum in the effective diffusivity, and the distribution of tracers is studied. For a non-forced 1D diffusion-reaction equation (which would just resemble the 1D diffusion equation), the effective diffusivity is found to be inversely proportional to the tracer gradient. That is, where the tracer gradient is large, the effective diffusivity is small. If we consider the tracer to be PV, then this is in agreement with the theory that sharp PV gradients correspond with diffusivity suppression. For a bounded and forced diffusion-reaction equation, weaker tracer gradients were found surrounding the barrier region, which is again consistent with the results found in Ferrari & Nikurashin (2010), Haynes et al. (2007).

From the studied literature, there is agreement that jets act as a transport barrier across its core, and that the extent to which this is the case is driven by the sharpness of PV gradients and the relative speed of eddy propagation to the zonal mean velocity. These are two phenomena that will be further discussed in this thesis.

1.4 Current Parameterisation Approach

Currently, most ocean general circulation models (OGCMs) don't operate at a sufficiently fine grid resolution to be able to model eddy effects. Since eddies play a significant role in tracer transport, arguably over the time-mean circulation in regions where eddies are highly energetic (Kamenkovich et al. 2015), these OGCMs will incorrectly approximate material transport; therefore eddy-induced transport processes must be parametrised. Current transport parametrisations are based on down-gradient diffusion as described in Taylor (1922). This as-

sumes that Lagrangian particles behave according to a random walk model and so material transport is assumed to be

1. homogeneous,
2. isotropic,
3. and diffusive.

However, evidence provided both from direct physical observations from subsurface floats, buoys and satellite altimetry and from numerical experiments suggest that this is not in fact the case.

1.5 Studies that Challenge this Approach

We have already discussed papers that find suppressed cross-jet mixing in oceanic jets, such as in the ACC (Ferrari & Nikurashin 2010, Naveira Garabato et al. 2011) and in the Gulf Stream (Bower & Lozier 1994). This implies that there is anisotropy between cross-jet and along-jet Lagrangian transport.

Rypina et al. (2012) analysed results from two different data sets of passive tracer trajectories in the North Atlantic: one was from data obtained from neutrally buoyant subsurface floats, and the second was obtained from near surface currents estimated from satellite altimetry data. Single-particle dispersion was used to quantify particle spreading and transport, and hence construct 'spreading ellipses' as displayed in fig. 1.2. It was found that dispersion is significantly inhomogeneous and anisotropic. Considerable anisotropy was demonstrated in the vicinity of the jet core of the Gulf Stream. Furthermore, anisotropy was found to be greater in the subtropical than subpolar gyre.

However, relying only on physical observations in order to analyse transport presents numerous problems. Firstly, data is spatially sparse and resources are limited, so limited data can be retrieved. In particular, certain parts of the ocean may be infrequently explored by floats or drifters. Furthermore, data in time is also sparse, particularly in the case of many subsurface

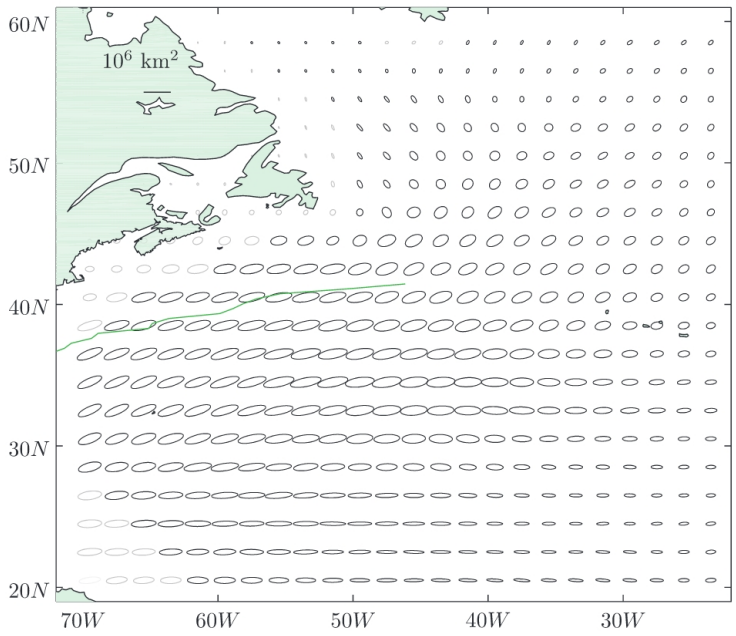

Figure 1.2: Spreading ellipses in the North Atlantic due to the eddy-only velocity field approximated using satellite altimery. They are calculated from diagonalising the single particle dispersion tensor. The green line indicates the core of the Gulf Stream. Taken from Rypina et al. (2012)

floats (e.g. ALICE), since they have to rise to the surface periodically in time for their location to then be determined by a satellite (LaCasce 2008).

As the time lag tends to infinity, the diffusivity coefficient will tend to a constant, however the asymptotic limit may be so large that particles leave the region of interest (Davis 1987, Ying et al. 2019). This is an issue which will be addressed in this paper. As a result, obtaining datasets big enough to calculate accurate statistics is an expensive and perhaps impossible task. Therefore we must use numerical models in order to obtain a larger and more complete data set of trajectories.

Chen & Waterman (2017) followed the methodology of Rypina et al. (2012). They verified the data-driven results found in Rypina et al. (2012) in a numerical setting by advecting particles in a barotropic QG model of an idealised Western Boundary Current (WBC). Similar such ellipses were plotted, verifying anisotropic spreading with zonally elongated ellipses observed upstream due to cross-stream mixing suppression.

Kamenkovich et al. (2015) used a double-gyre oceanic model to study the origins of anisotropic transport in the North Atlantic and found that it isn't the anisotropy in the velocity tensor that

causes anisotropic behaviour, but the difference in correlation time-scales. Kamenkovich et al. (2009) further verifies eddy-induced anisotropic transport and suggests that the anisotropy could be due to the zonally-elongated and hence anisotropic eddy shapes. Such eddies are expected to result in predominantly zonal Lagrangian velocities.

In an attempt to derive models more suited to the non-diffusive behaviour of eddy-induced transport, a selection of papers, Berloff et al. (2002), Berloff & McWilliams (2002) and Berloff & McWilliams (2003), examined the consequences of using higher order Markov models as transport models. They relate the issue of the poor parametrisation of eddy-induced transport with the assumption that Lagrangian trajectories exhibit immediate memory loss. It is assumed that the Lagrangian velocity de-correlates immediately. Berloff et al. (2002) generated numerical simulations of material transport by deploying floats in the model and studying certain transport properties. They found, using the power law fit for the single-particle dispersion tensor D to time t:

$$D \sim t^{\alpha}, \tag{1.3}$$

that generally transport was non-diffusive and there exist regions of sub-diffusivity and super-diffusivity. The zonal and meridional contributions to α also demonstrated significant anisotropy. A diffusive model, that is a Markov-0, model was found to be insufficient at capturing the Lagrangian behaviour. They found that at least a Markov-3 model is needed in order to capture super-diffusive behaviour. This will be further elaborated in chapter 6.

1.6 Layout of Thesis

In chapter 2 we will describe the dynamical model used to generate a realistic but simple oceanic meandering jet. Different parameter regimes will be described in order to simulate jets motivated by those illustrated in fig. 1.1. Chapter 3 outlines the transport model used to advect particles using the dynamical model velocity field. It will also test and verify the accuracy of two novel spatial interpolation methods. Chapter 4 outlines the resulting Lagrangian statistics

that can diagnose transport and will be used in chapter 6. It will also explore a new flow based dispersion measure motivated by O'Dwyer et al. (2000). This chapter will be used to verify non-diffusive and anisotropic transport. Chapter 5 will decompose the flow field into empirical orthogonal functions as a motivation behind building a kinematic model that captures eddy-induced advection. Finally, Lagrangian statistical parameters will then be used to explore the validity of different stochastic models in chapter 6.

Chapter 2

Dynamical Model

2.1 Quasi-Geostrophic Model

The dynamical model is a two layer quasi-geostrophic (QG) model on a β-plane in a doubly-periodic domain (Vallis 2006, Berloff et al. 2011). Fig. 2.1 displays a schematic of the model.

The following assumptions are made:

1. The Rossby number is assumed to be small. That is, $\epsilon = \frac{U}{fL} \ll 1$, where U is the horizontal velocity scale, L is the horizontal scale and f is the Coriolis parameter.

2. The Boussinesq approximation is assumed, that is density variations between isopycnals are assumed to be small. Referring to figure 2.1, $\Delta\rho = \rho_2 - \rho_1 \ll \rho_1, \rho_2$

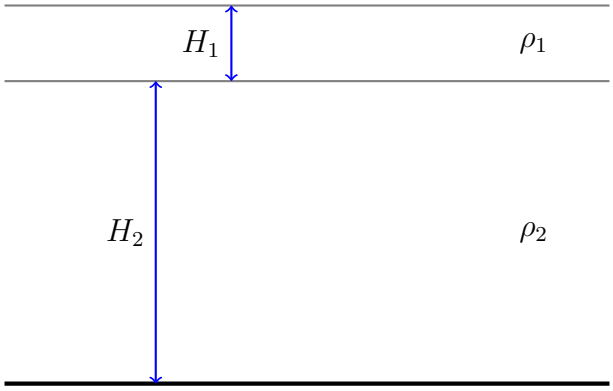

Figure 2.1: Schematic of the two layer quasi-geostrophic model where $\rho_k, k = 1, 2$ are the layer densities and H_k are the resting layer depths.

3. Hydrostatic balance is assumed : $\frac{\partial \rho}{\partial z} = -\rho_0 g$.

4. β-plane approximation, that is $f = f_0 + \beta y$ and variations in the Coriolis parameter are taken to be small, so $[\beta y] \sim \epsilon f_0$.

5. Time scales advectively, $T \sim L/U = 1/\epsilon f$.

6. No variations in layer thickness, i.e. rigid lid assumption.

7. The advective derivative is taken to be $D/Dt = \partial/\partial t + u_g \partial/\partial x + v_g \partial/\partial y$.

The governing equations are:

$$\frac{D_1}{Dt}\left(\nabla^2\psi_1 - S_1(\psi_1 - \psi_2)\right) + \beta v_1 = \nu\nabla^4\psi_1, \tag{2.1}$$

$$\frac{D_2}{Dt}\left(\nabla^2\psi_2 - S_2(\psi_2 - \psi_1)\right) + \beta v_2 = \nu\nabla^4\psi_2 - \gamma\nabla^2\psi_2, \tag{2.2}$$

where the subscript 1 denotes the top layer, and 2 the bottom, S_k are the stratification parameters: $S_k = f_0^2/g'H_k$ and $g' = \Delta\rho/\rho_1$ is the reduced gravity, ψ_k are the velocity stream functions, v_k are the meridional velocities, ν is the viscosity and γ is the bottom friction. The flow is forced by a uniform zonal velocity U_0 in the top layer.

The potential vorticity anomalies can be expressed in terms of the stream function by elliptic equations:

$$q_1 = \nabla^2\psi_1 - S_1(\psi_1 - \psi_2), \quad q_2 = \nabla^2\psi_2 - S_2(\psi_2 - \psi_1). \tag{2.3}$$

As the velocity is non-divergent, the velocity components are expressed as follows:

$$u_i = -\frac{\partial \psi_i}{\partial y}, \quad v_i = \frac{\partial \psi_i}{\partial x}. \tag{2.4}$$

The elliptic inversion problem (2.3) can be solved given the mass constraint condition as described in McWilliams (1977):

$$\frac{\partial}{\partial t}\int\int(\psi_1 - \psi_2)\mathrm{d}x\mathrm{d}y = 0. \tag{2.5}$$

In order to solve the PV inversion problem, we decouple the potential vorticity anomalies, expressing the stream function in terms of barotropic and baroclinic modes:

$$\phi_1 = \frac{H_1\psi_1 + H_2\psi_2}{H_2 + H_1}, \quad \phi_2 = \psi_1 - \psi_2, \tag{2.6}$$

where ϕ_1 is the barotropic mode and ϕ_2 is the baroclinic mode. Furthermore, let

$$\tilde{q_1} = \frac{H_1 q_1 + H_2 q_2}{H_1 + H_2}, \quad \tilde{q_2} = q_1 - q_2. \tag{2.7}$$

By calculating $q_1 - q_2$ and $(H_1 q_1 + H_2 q_2)/(H_1 + H_2)$, we obtain decoupled Helmholtz and Poisson equations:

$$\tilde{q_2} = \nabla^2\phi_2 - S_d\phi_2, \tag{2.8}$$

$$\tilde{q_1} = \nabla^2\phi_1, \tag{2.9}$$

where $S_d = (L/R_d)^2$ and $R_d = \sqrt{g'H_1H_2}/(f_0\sqrt{H_1 + H_2})$ is the Rossby deformation radius.

Equations 2.8 and 2.9 can be solved using fast Fourier transforms. As the domain is doubly-periodic, and so by construction all variables must be periodic, ϕ_k can be expressed in terms of their discrete Fourier transforms $\hat{\phi}_k$:

$$(\phi_k)_{i,j} = \frac{1}{N_x N_y} \sum_{n=1}^{N_x} \sum_{m=1}^{N_y} (\hat{\phi}_k)_{i,j} e^{-ik_n x} e^{-ik_m y}, \tag{2.10}$$

where N_x, N_y are the number of grid points in x and y respectively and

$$k_n = \frac{2\pi(n-1)}{N_x - 1}, \quad k_m = \frac{2\pi(m-1)}{N_y - 1}. \tag{2.11}$$

We can take the Laplacian term by term to find that,

$$\nabla^2(\phi_k)_{i,j} = \frac{1}{N_x N_y} \sum_{n=1}^{N_x} \sum_{m=1}^{N_y} -\left(k_m^2 + k_n^2\right) (\hat{\phi}_k)_{i,j} e^{-ik_n x} e^{-ik_m y}. \tag{2.12}$$

$\tilde{q}_k$ can also be expressed in terms of their Fourier transforms $\hat{\tilde{q}}_k$:

$$(\tilde{q}_k)_{i,j} = \frac{1}{N_x N_y} \sum_{n=1}^{N_x} \sum_{m=1}^{N_y} (\hat{\tilde{q}}_k)_{i,j} e^{-ik_n x} e^{-ik_m y}, \tag{2.13}$$

hence

$$(\hat{\phi}_1)_{i,j} = -\frac{(\hat{\tilde{q}}_1)_{i,j}}{k_m^2 + k_n^2}, \tag{2.14}$$

$$(\hat{\phi}_2)_{i,j} = -\frac{(\hat{\tilde{q}}_2)_{i,j}}{S_d + k_m^2 + k_n^2}. \tag{2.15}$$

Fast Fourier transforms are used to calculate Fourier transforms, $\hat{\tilde{q}}_k, \hat{\phi}_k$, and inverse Fourier transforms, $\tilde{q}_k = \mathcal{F}^{-1}(\hat{\tilde{q}}_k), \phi_k = \mathcal{F}^{-1}(\hat{\phi}_k)$, numerically. Hence, given the potential vorticity anomalies q_k, the stream functions ψ_k can be calculated.

2.2 The Numerical Method: CABARET

CABARET is a second order, non-dissipative, low-dispersive conservative advection scheme as described in Karabasov et al. (2009). It consists of three steps: a predictor step, an extrapolation step and a corrector step. Firstly let's demonstrate the idea using a one-dimensional conservation law:

$$\frac{\partial q}{\partial t} + \frac{\partial f(q)}{\partial x} = 0, \tag{2.16}$$

on a finite difference grid as shown in fig. 2.2 where discretisation in space is $x_{i+1} - x_i = h_i$ and in time is $t^{n+1} - t^n = \Delta t^n$. The discretisation does not need to be uniform, though in our case it will be. Suppose we know q at time t^n. The conserved variable q is located at the points with fractional i indices and the flux variable $f(q)$ is located at points with whole i indices.

Consider the top right hand square in fig. 2.2. The **predictor step** takes two half time steps from grid point E to grid point A first using a forward-time centred-in-space approximation, and then a backward-time centred-in-space approximation:

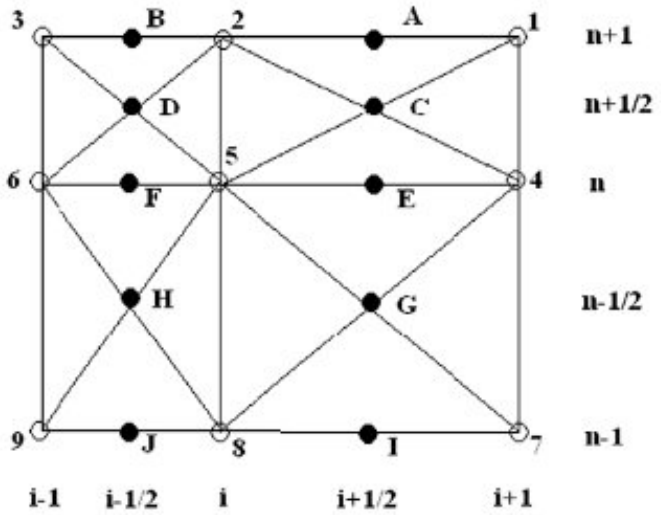

Figure 2.2: Finite difference grid on which the CABARET advection scheme is applied. (Taken from Karabasov et al. (2009))

$$\frac{q_C - q_E}{\frac{1}{2}\Delta t^n} + \frac{f_4 - f_5}{h_i} = 0, \tag{2.17}$$

$$\frac{q_A - q_C}{\frac{1}{2}\Delta t^n} + \frac{f_1 - f_2}{h_i} = 0. \tag{2.18}$$

We evaluate f_1 and f_2 ($= f(q_1), f(q_2)$ respectively) by **extrapolating** along the line connecting points 5, C and 1 using the midpoint rule:

$$q_C = \frac{q_1 + q_5}{2}. \tag{2.19}$$

This ensures that the scheme is second-order accurate and non-dissipative.

The final step is the **corrector** step, which removes spurious backscatter ensuring that the solution is non-oscillatory. The following flux limiter, is used

$$q_1 = 2q_C - q_5, \tag{2.20}$$

$$\text{if } (q_1 > \max(q_4, q_E, q_5)), \quad q_1 = \max(q_4, q_E, q_5), \tag{2.21}$$

$$\text{if } (q_1 < \min(q_4, q_E, q_5)), \quad q_1 = \min(q_4, q_E, q_5). \tag{2.22}$$

The CABARET scheme is stable for a courant number $0 < C < 1/d$ where d is the number of spatial dimensions.

Now let's apply this to the two-dimensional 2 layer QG model. Let's express equation 2.1 in the same format as 2.16:

$$\frac{\partial q_k}{\partial t} + \frac{\partial u_k q_k}{\partial x} + \frac{\partial v_k q_k}{\partial y} = F_k, \tag{2.23}$$

where $k = 1, 2$ denotes the layer. F_k is the forcing term representing the β, bottom friction and viscosity terms:

$$F_1 = \nu\nabla^4\psi_1 - \beta v_1, \tag{2.24}$$

$$F_2 = \nu\nabla^4\psi_2 + \gamma\nabla^2\psi_2 - \beta v_2. \tag{2.25}$$

Let's assume that the grid is uniformly spatially discretised with a discretisation of h. As before, the time step is $t^{n+1} - t^n = \Delta t^n$ and we assume we know all variables at time t^n.

The conserved variables q_k are located at the cell centres, with fractional i and j indices. The flux variables, $u_k q_k$, have either fractional i or j indices, and so are located on cell face centres.

The Courant-Friedrichs-Lewy condition requires that

$$C = \frac{u\Delta t}{\Delta x}, \tag{2.26}$$

therefore the time step is

$$\Delta t^n = \min_{i,j}\left(\frac{Ch}{\max\left(|\,(u_q)^n_{i,j+\frac{1}{2}}\,|, |\,(v_q)^n_{i+\frac{1}{2},j}\,|\right)}\right), \tag{2.27}$$

and for the CABARET scheme to be stable, $0 < C < 1/2$. First, the **predictor** step takes a half-step forward-in-time and centred-in-space approximation:

$$\frac{(q_k)^{n+\frac{1}{2}}_{i+\frac{1}{2},j+\frac{1}{2}} - (q_k)^n_{i+\frac{1}{2},j+\frac{1}{2}}}{\frac{1}{2}\Delta t^n}$$

$$+\frac{(u_k)^n_{i+\frac{1}{2},j}\,(q_k)^n_{i+\frac{1}{2},j}-(u_k)^n_{i-\frac{1}{2},j}\,(q_k)^n_{i-\frac{1}{2},j}}{h}+\frac{(u_k)^n_{i,j+\frac{1}{2}}\,(q_k)^n_{i,j+\frac{1}{2}}-(u_k)^n_{i,j-\frac{1}{2}}\,(q_k)^n_{i,j-\frac{1}{2}}}{h}$$
$$=(F_k)^{n+1/2}_{i+\frac{1}{2},j+\frac{1}{2}}\,. \quad (2.28)$$

How do we approximate $(F_k)^{n+\frac{1}{2}}_{i+\frac{1}{2},j+\frac{1}{2}}$? Let's separate the source term into its different components:

$$(F_k)^{n+\frac{1}{2}}_{i+\frac{1}{2},j+\frac{1}{2}}=\left(F^{\beta}_k\right)^{n+\frac{1}{2}}_{i+\frac{1}{2},j+\frac{1}{2}}+\left(F^{\text{visc}}_k\right)^{n+\frac{1}{2}}_{i+\frac{1}{2},j+\frac{1}{2}}+\left(F^{\text{bot}}_k\right)^{n+\frac{1}{2}}_{i+\frac{1}{2},j+\frac{1}{2}}\,. \quad (2.29)$$

In Karabasov et al. (2009) the β component of the source term is approximated using a second order predictor-corrector scheme. The bottom friction and viscous source terms are approximated by using second-order approximations of the stream function and its Laplacian. It is necessary to approximate the source terms using second-order methods in order to preserve the second-order accuracy of CABARET.

As we know all values at time t^n in eq. (2.28), we can find the PV anomaly at the half time step: $(q_k)^{n+\frac{1}{2}}$. Therefore, the stream function at the half time step at cell faces denoted by $\left(i\pm\frac{1}{2},j\pm\frac{1}{2}\right)$ indices can be found by solving the elliptic inversion problem eq. (2.3).

The cell centre stream functions are used to approximate the velocity components at the cell faces at the half time step using a centred-in-space finite difference approximation:

$$(\psi_k)^{n+\frac{1}{2}}_{i,j}=\frac{1}{4}\left((\psi_k)^{n+\frac{1}{2}}_{i+\frac{1}{2},j+\frac{1}{2}}+(\psi_k)^{n+\frac{1}{2}}_{i-\frac{1}{2},j+\frac{1}{2}}+(\psi_k)^{n+\frac{1}{2}}_{i+\frac{1}{2},j-\frac{1}{2}}+(\psi_k)^{n+\frac{1}{2}}_{i-\frac{1}{2},j-\frac{1}{2}}\right), \quad (2.30)$$

$$(u_k)^{n+\frac{1}{2}}_{i,j+\frac{1}{2}}=-\frac{(\psi_k)^{n+\frac{1}{2}}_{i,j+1}-(\psi_k)^{n+\frac{1}{2}}_{i,j}}{h}, \quad (2.31)$$

$$(v_k)^{n+\frac{1}{2}}_{i+\frac{1}{2},j}=\frac{(\psi_k)^{n+\frac{1}{2}}_{i+1,j}-(\psi_k)^{n+\frac{1}{2}}_{i,j}}{h}. \quad (2.32)$$

Next we proceed to the **extrapolator** step. The velocity at the next time step t^{n+1} is then extrapolated to the second-order using linear extrapolation. As an example, suppose we wish to approximate $y(\tilde{x})$ where $x_{k-1}<x_k<\tilde{x}$, then

$$y(\tilde{x})=y_{k-1}+\frac{\tilde{x}-x_{k-1}}{x_k-x_{k-1}}\,(y_k-y_{k-1})\,. \quad (2.33)$$

Now apply this to approximate the velocity at the next time level, that is: $(u_q)^{n+1}_{i,j+\frac{1}{2}}$ where

$t^{n-\frac{1}{2}} < t^{n+\frac{1}{2}} < t^{n+1}$. Hence

$$(u_k)^{n+1}_{i,j+\frac{1}{2}} = (u_k)^{n-\frac{1}{2}}_{i,j+\frac{1}{2}} + \frac{t^{n+1} - t^{n-\frac{1}{2}}}{t^{n+\frac{1}{2}} - t^{n-\frac{1}{2}}} \left((u_k)^{n+\frac{1}{2}}_{i,j+\frac{1}{2}} - (u_k)^{n-\frac{1}{2}}_{i,j+\frac{1}{2}} \right). \tag{2.34}$$

$$\frac{t^{n+1} - t^{n-\frac{1}{2}}}{t^{n+\frac{1}{2}} - t^{n-\frac{1}{2}}} = \frac{2\Delta t^n - \Delta t^{n-1}}{\Delta t^n - \Delta t^{n-1}}, \tag{2.35}$$

giving

$$(u_k)^{n+1}_{i,j+\frac{1}{2}} = (1+\delta)\,(u_k)^{n+\frac{1}{2}}_{i,j+\frac{1}{2}} - \delta\,(u_k)^{n-\frac{1}{2}}_{i,j+\frac{1}{2}}, \tag{2.36}$$

where

$$\delta = \frac{\Delta t^n}{\Delta t^n - \Delta t^{n-1}}. \tag{2.37}$$

The same is done to find the meridional component of the velocity. Now we have the updated velocities, we proceed to the **corrector** step and use these to apply the flux limiter, eq. (2.20), to find the values of the PV anomaly at the cell faces, that is, the flux variables.

Now we have all the flux variables at the time step t^{n+1} and the conserved variables at $t^{n+\frac{1}{2}}$, a backward-in-time and centred-in-space approximation can be taken to find $(q_k)^{n+1}_{i+\frac{1}{2},j+\frac{1}{2}}$.

2.3 Parameter Regimes

The dynamical model is initially perturbed by an alternating stream function and then spun up for a period of about 15,000 days until the field has reached equilibrium and the total energy has stabilised.

By choosing appropriate parameters, the dynamical model produces a meandering jet surrounded by eddying structures. We set:

- the basinscale = 520 km,
- Rossby deformation radius Rd = 25km,
- grid size of 512×512,

- layer depths $H_1 = 1\text{km}, H_2 = 3\text{km}$,
- viscosity $\nu = 1\text{m}^2\text{s}^{-1}$,
- $\beta = 2 \times 10^{-11}\text{m}^{-1}\text{s}^{-1}$,
- and a background eastward zonal velocity in the top layer of $U_0 = 6\text{cm s}^{-1}$.

As the Rossby deformation radius is much larger than the grid size of approximately 1km, the model is able to simulate eddies.

The bottom friction parameter, γ, is varied to produce different jets. The following values for γ are chosen:

1. $1 \times 10^{-8}\text{s}^{-1}$, giving a coherent jet and
2. $2.5 \times 10^{-8}\text{s}^{-1}$, giving a latent jet.

Fig. 2.3 shows snapshots of the PV anomaly after an initial spin-up period for the different parameter regimes.

In the appendix of Rypina et al. (2012), a jet was simulated using the same numerical model and parameters (with the exception of bottom friction which was set to 0 in Rypina et al. (2012)) in order to verify that the FFE technique did in fact capture the suppression of cross-stream material transport. The lack of bottom friction resulted in a jet with a much greater and more coherent meander than the one in our coherent jet. It more closely resembled the kinematic model studied in Bower (1991).

Berloff et al. (2011) chose bottom friction values of $\gamma = 10^{-8}, 10^{-7}, 10^{-6}$ s^{-1} to study multiple alternating zonal jets of varying latency using the CABARET numerical model. The same values for β, Rossby deformation radius, layer thickness and background zonal velocity were used. It was stated that a small γ is associated with jets that are strong relative to the background flow, and that the jet core acts as a transport barrier. At large values of bottom friction, the zonal jets become invisible in the instantaneous case. In fact, they argue that bottom friction is the dominant parameter in determining the degree of latency, which is

defined as the square root of the ratio of the jet PV variance to the eddy PV variance. It stated that in the small γ regimes, a demonstrable asymmetry was observed between eastward and westward jets, where the eastward jets were diagnosed by transport barriers, and the eastward jets corresponded to zones in which there was more PV mixing. For the purposes of studying the properties of material transport, we are not so interested in the case where there is a complete instantaneous break down of the zonal jet, as we are still interested in the degree to which the jet is a barrier to transport. Furthermore, the study focuses on multiple alternative zonal jets, which do appear latent in the ocean. However, as our focus is only on a single jet (which can be more coherent in the ocean, particularly when considering WBCs and their eastward jet extension), we are more interested in smaller bottom friction regimes. Similar parameter values were also used in Khatri & Berloff (2018), notably with a bottom friction parameter of 2×10^{-8} s^{-1}. So while the 'latent' jet in this study is not fully latent, we simply mean it is the more latent of the two. Simulations were run with larger bottom friction values, but we established that they didn't demonstrate enough jet coherence, though the studies carried out in this thesis could be extended to more latent jets.

Studying the effect jet strength and coherence has on Lagrangian transport is important in any attempt at parameterisation, as a wide variety of jet behaviours are observed in the ocean. The two jet regimes are inspired by Liu et al. (2018), Waterman & Hoskins (2013) and fig. 1.1. Furthermore, it has been found that topography, particularly in the Southern Ocean can affect jet structure (Chapman & Morrow 2014, Thompson & Salle 2012). Furthermore, the zonally symmetric structure is particularly relevant to the ACC as it is circumnavigates the whole Southern Ocean and is also predominantly zonal.

As we simulate the flow forward in time, we see that the meanders in the coherent jet are more regular and stable, in that the sharp potential vorticity gradient remains intact and in fact there is little disturbance to the meanders so that sometimes they appear to be propagating with a constant wave length. This is also consistent with Berloff et al. (2011).

The latent jet however is frequently distorted due to the sharp potential vorticity gradient being broken. This results in shedding of vortices. We expect that this break will result in a leaky barrier to transport. However it is important to note that the potential vorticity gradient

across the latent jet is greater than that in the coherent jet. This is in agreement with Dritschel & Scott (2011). In this paper, it was shown that vortices aide in PV mixing and hence the sharpening of the jet, or potential vorticity gradient. We can see that the return flows in the top layer are much more apparent in fig. 2.4. The jet core also appears wider and more smeared in the time-averaged sense.

There is however a very marked difference between the two regimes when we focus on the eddying flow in fig. 2.5. In agreement with Berloff et al. (2011), the greater the bottom friction, the greater the ratio of the eddying flow to the time-averaged flow, as the magnitude of the eddying velocity in the latent jet is greater than that in the coherent jet. The jet core is in fact more visible from the eddy zonal velocity in the latent regime, even in the bottom layer, than in the coherent regime.

The transition from a sharper jet in the top layer to a broader and weaker bottom layer yet is consistent with what was found in Greenslade & Haynes (2008). Instead of a two-layer model, a 20 layer QG model was ran in which effective diffusivities were calculated. The layers could generally be split into two types: upper layers in which there is are narrower mixing regions, referred to as surf zones, separated by a mixing barrier; and lower layers which consist of a single wide mixing region.

Particles will be advected by the transport model detailed in chapter 3 using the velocity fields outputted by these two parameter regimes, and Lagrangian particle statistics of the two will be compared.

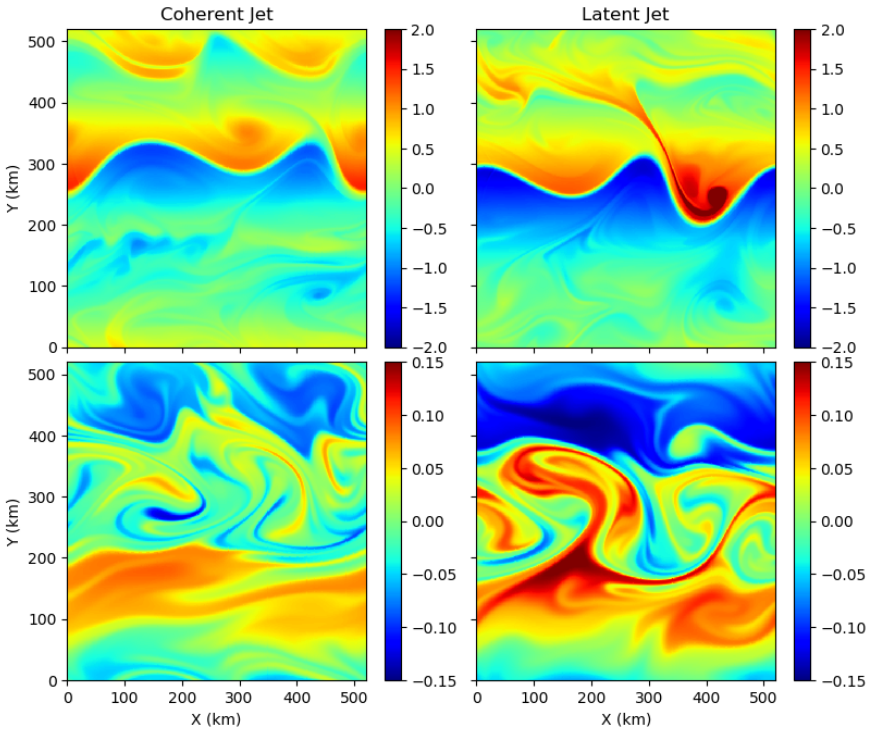

Figure 2.3: Snapshots of the non-dimensional potential vorticity anomaly after an initial spin-up period comparing different parameter regimes. The top row represents the top layer and the bottom row, the bottom layer.

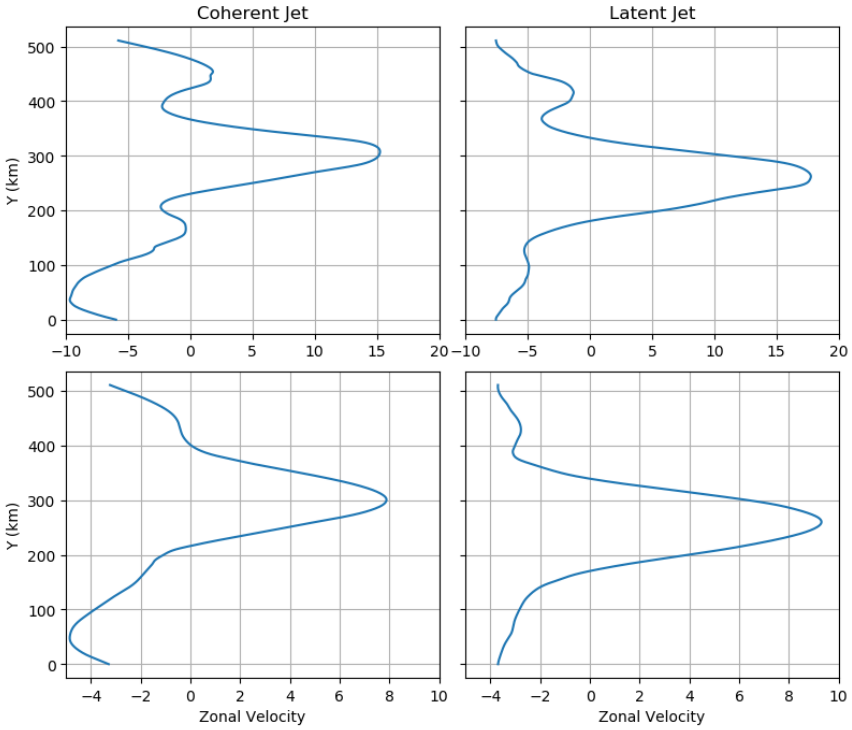

Figure 2.4: Zonally-averaed and time-averaged zonal velocity (cm s^{-1}) after an initial spin-up period comparing different parameter regimes. The top row represents the top layer and the bottom row, the bottom layer.

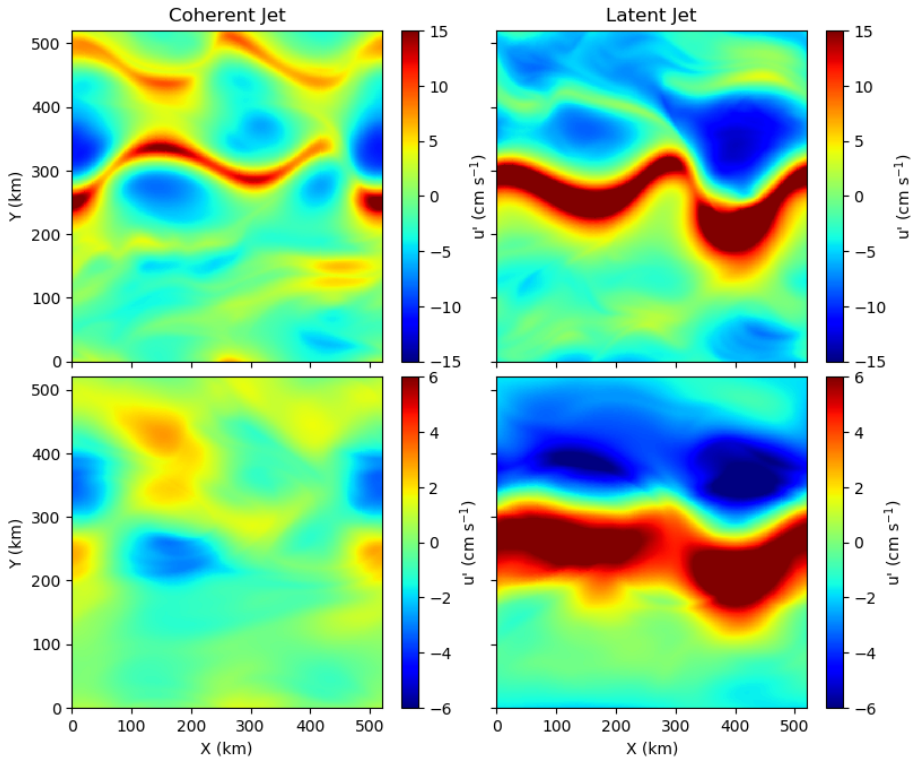

(a) Zonal velocity

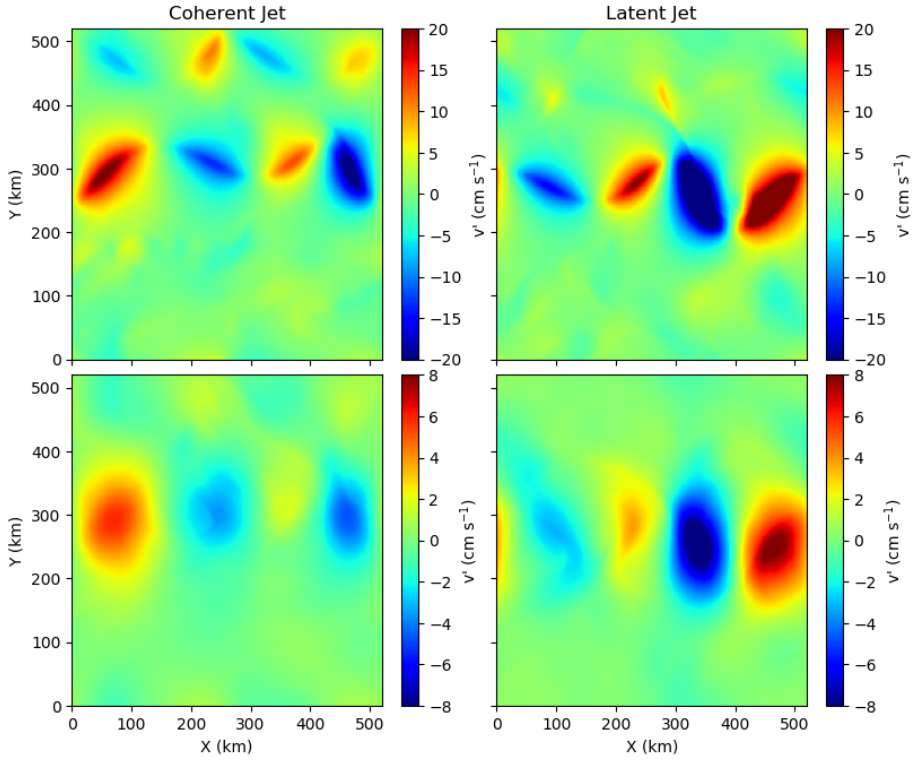

(b) Meridional velocity

Figure 2.5: Instantaneous velocity components (cm s^{-1}) after an initial spin-up period comparing different parameter regimes. The top row of each Figure represents the top layer and the bottom row, the bottom layer.

Chapter 3

Transport Model

Particles are advected according to the equation:

$$\frac{d\mathbf{x}_n(t)}{dt} = \mathbf{u}(t, \mathbf{x}_n), \tag{3.1}$$

where $\mathbf{x}_n(t)$ is the location of particle n at time t, and $\mathbf{u}(t, \mathbf{x}_n) = (u(t, \mathbf{x}_n), v(t, \mathbf{x}_n))$ is the velocity at the particle location. This is a continuous equation whereas the velocity field is only known at discrete grid points. Therefore the velocity field must be spatially interpolated, and then numerically integrated in time.

Initially, it makes sense to find the velocity by differentiating the stream function using finite differences e.g.:

$$u_{i,j} = -\frac{\psi_{i,j+1} - \psi_{i,j-1}}{2\Delta y}, \quad v_{i,j} = \frac{\psi_{i+1,j} - \psi_{i-1,j}}{2\Delta x}, \tag{3.2}$$

where i, j donate the grid point index and $\Delta x, \Delta y$ are the spatial grid spacings. However, an assumption made by the QG approximation is that the flow is non-divergent, but the resulting approximated velocities do not necessarily obey this assumption. As a result, after a period of time, particles that are initially released uniformly across the whole domain converge and diverge, forming clusters. It is important to prevent this in our particular study, as after a long enough period of time, the diffusive approximation should be reached. In order to overcome this problem, an accurate spatial interpolation method must be devised which performs spatial

polynomial interpolation on the stream function first, before differentiating it analytically to find the velocity.

The polynomial must be unique and sufficiently smooth to allow differentiation. Hence, a cubic polynomial approach will be considered. Two different methods will be described and tested.

Furthermore, the accuracy of the Runge-Kutta time-integration scheme will be tested, and an optimal time step will be selected.

3.1 Spatial Interpolation

3.1.1 2D-Cubic Interpolation

The idea behind this method is to perform one-dimensional cubic interpolation in each dimension. Suppose the interpolation point is located at (x, y). Cubic interpolation requires a 4×4 grid of points as shown in fig. 3.1.

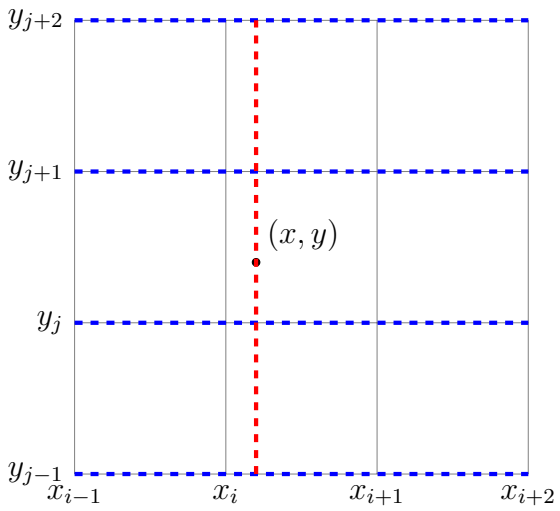

Figure 3.1: Schematic of two-dimensional cubic interpolation. The blue dashed lines indicate the location of four 1-D cubic polynomial approximations calculated at each of the four y grid points in terms of x. The red dashed line represents the location of the final cubic polynomial which is expressed in terms of the four blue 1-D cubic polynomials.

Firstly, construct four one-dimensional cubic polynomials in the y direction, that approximate the stream function on the blue dashed lines in fig. 3.1. Then we wish to construct a

one-dimensional polynomial along the red dashed line that will be expressed in terms of the above four cubic polynomials. Now we have a polynomial approximation for ψ and can analytically differentiate it to find u and v at (x, y). The four 1-D cubic polynomials in the y direction are found for each y coordinate once for each time step. The final cubic polynomial on the red line however must be found for each particle. Details of the derivation are included in appendix A and the code is given in appendix B.

3.1.2 Bicubic Interpolation

Alternatively to the previous scheme, we construct two-dimensional polynomials of the form

$$\psi(x, y) = \sum_{n,m=0}^{3} a_{nm} x^n y^m. \tag{3.3}$$

This gives us 16 unknown coefficients a_{nm}, therefore we can construct a solvable matrix equation with a unique solution for the 4×4 grid as in fig. 3.1. This matrix of coefficients a_{nm} is calculated for each time step for each grid point, however nothing further needs to be done for each particle except matrix multiplication, which is relatively cheap. As before, we can now analytically differentiate these polynomials to find the velocity components. Details of the derivation of bicubic interpolation are given in appendix C and code is provided in appendix D.

3.1.3 Comparison of Spatial Interpolation Methods

The above two spatial interpolation methods were applied to particles advected using three different flow fields:

- two equal and opposite plane waves;
- Stommel flow;
- and a stationary jet generated by the dynamical model.

The first two of these fields have closed streamlines and the third case is defined in a doubly-periodic domain, therefore, for a perfectly accurate transport model, a particle should return exactly to its starting position after one full loop. Hence the accuracy can be calculated as the particles deviation from its initial location after an integer number of loops:

$$\text{err} = \left\langle \frac{|\mathbf{x_i}(0) - \mathbf{x_i}(T_i)|}{|\mathbf{x_i}(0)|} \right\rangle, \tag{3.4}$$

where $\mathbf{x}_i(t)$ is the coordinate of the ith particle at time t, $\langle\cdot\rangle$ denotes an ensemble average, and T_i is the time at which the particle has concluded its integer number of loops.

The time integration scheme used is the Euler method, where $x(t_1) = x(t_0)+\Delta t u(t_0), y(t_1) = x(t_0) + \Delta t v(t_0)$.

Even though these fields are time-independent, so we would only need to work out the polynomial coefficients for one snapshot of data, we will force the code to calculate the coefficients at each time step to give us an accurate running time.

Two Plane Waves

Two equal and perpendicularly propagating plane waves will produce a grid of eddies. Such a stream function can be written as:

$$\psi = A_0 \left(\cos\left(\frac{2\pi k x}{N_x} + \frac{2\pi l y}{N_y} \right) + \cos\left(\frac{2\pi k x}{N_x} - \frac{2\pi l y}{N_y} \right) \right), \tag{3.5}$$

where k is the wave number in the x direction, l is the wave number in the y direction, N_x is the number of grid points in x, N_y is the number of grid points in y and A_0 is the wave amplitude. We wish to generate a field with similar dimensions to the jet produced by the dynamical model, and also with the same sized grid. This leads us to pick the values $A_0 = 200$ cm^2 s^{-1}, $N_x = N_y = 512, k = -2, l = 2$. The basinscale is 520km, the same as that of the QG model. The time is non-dimensionalised according to $U \sim L/T$ where U is the velocity scale, L is the basinscale and T is the time scale. The resulting stream function and velocity fields are plotted in fig. 3.2.

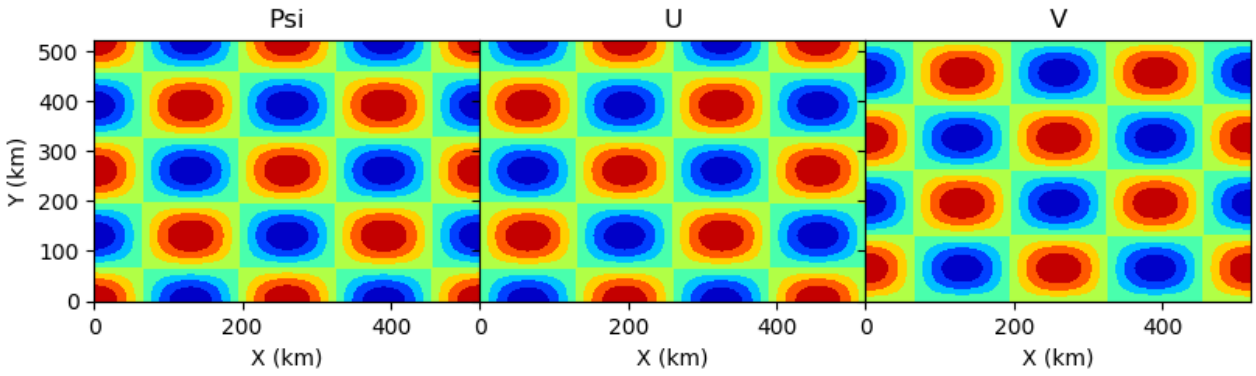

Figure 3.2: Stream function and velocity components of two equal and opposite plane waves on a 512×512 grid.

Spatial Interpolation Method	Time Step (seconds)			
	8640	4320	2160	1080
Bicubic Interpolation	0.4115	0.2756	0.2292	0.1519
2D cubic Interpolation	0.3921	0.3069	0.2144	0.1217
No Interpolation	0.3921	0.3069	0.2144	0.1217

Table 3.1: Accuracy of the interpolation methods for a single particle advected for 1,000 days by the two plane waves in fig. 3.2 using the Euler time integration method.

A single particle is advected for 1,000 days starting from $(x, y) = (100, 120)$ km. The resulting trajectories are plotted in fig. 3.3. The accuracy of the interpolation methods for varying time steps are shown in table 3.1 and the running time for varying particle ensemble sizes are shown in table 3.2.

Stommel Flow

The Stommel flow consists of a single wind-driven gyre in a square ocean domain with a β-effect. It also exhibits closed streamlines, meaning particles should transcribe a loop. The derivation

Spatial Interpolation Method	Numbers of particles		
	1	40,000	250,000
Bicubic Interpolation	847.632	927.196	1170.908
2D cubic Interpolation	27.672	57.512	201.664
No Interpolation	0.008	7.252	47.204

Table 3.2: Run time (seconds) of the interpolation methods for particles advected for 100 days by two plane waves with a time step of 8640s using the Euler method.

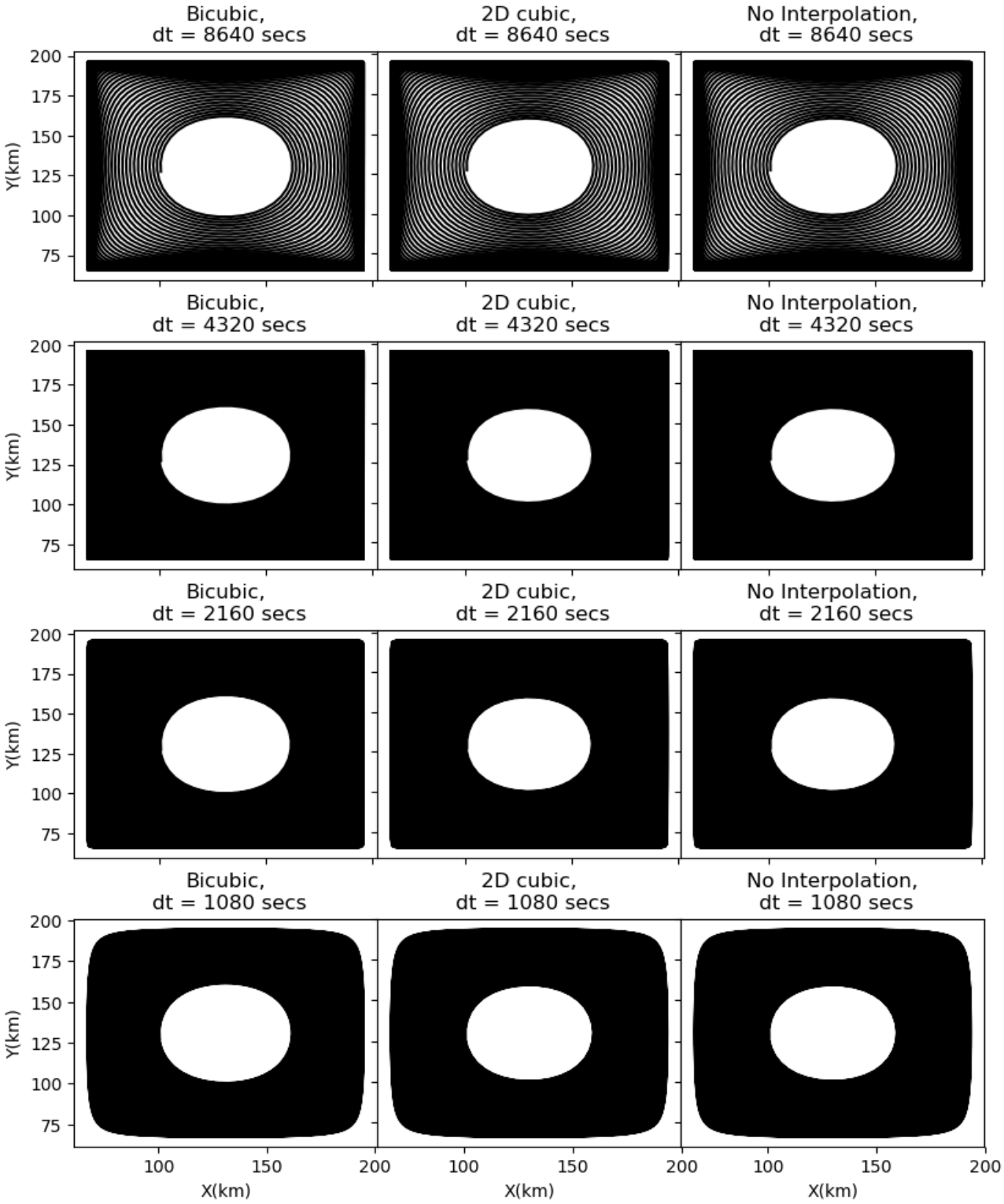

Figure 3.3: Trajectories of a particle starting at $(x, y) = (100, 120)$ km advected for 1,000 days by the two plane waves in fig. 3.2 using the Euler time-integration method. Four different time steps are compared, and Bicubic, 2D-cubic and analytical spatial interpolation solutions are compared.

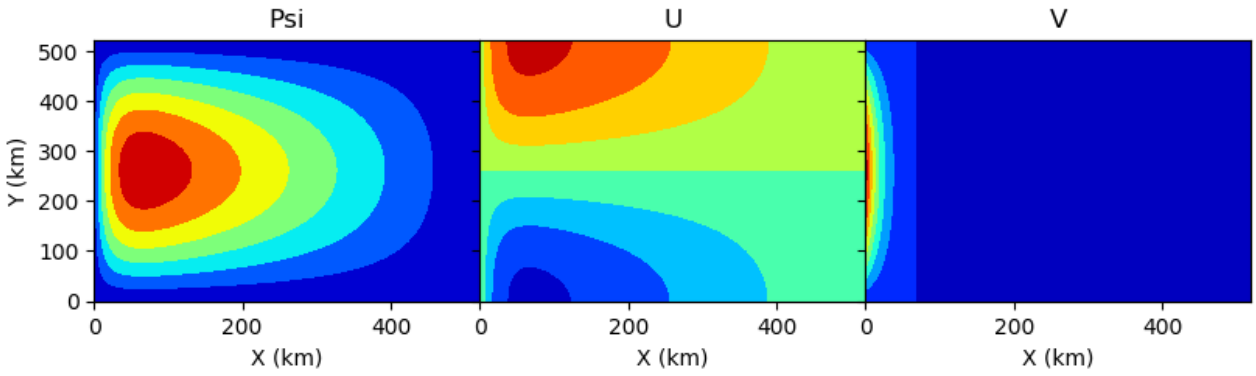

Figure 3.4: Stream function and velocity components for the Stommel Flow as described in eq. (3.6).

of the Stommel model is described in Vallis (2006).

$$\psi = \pi \left(1 - x - e^{-x/\epsilon}\right) \sin(\pi y), \tag{3.6}$$

is the non-dimensional stream function and $x \in [0, 1], y \in [0, 1]; \epsilon = r/(a\beta) \ll 1$, where r is friction coefficient, β is the Rossby parameter and a is the size of the domain in x. ϵ controls the size of the boundary layer. We set $\epsilon = 0.04$. Furthermore, we set the domain size $a = 520$km. As the 2D-cubic interpolation method requires unity grid spacing, eq. (3.6) must be re-scaled accordingly so that $x \in [0, N_x], y \in [0, N_y]$. Fig. 3.4 displays the resulting stream function and its velocity components.

A single particle is released near the centre of the gyre at $(x, y) = (150, 250)$ km to allow for maximum running time before the particle reaches the boundaries due to interpolation and time integration errors. Time steps of $\Delta t = 8640, 4320, 2160, 1080$ seconds are used and the particle is advected for 10,000 days. The resulting trajectories are plotted in fig. 3.5. The accuracy of the methods for the different time steps are shown in table 3.3 and running times are shown in table 3.4.

Stationary Jet

A snapshot of the meandering jet produced by the dynamical model is used to advect particles, as plotted in fig. 3.6. As the domain is doubly-periodic, in a perfect model, the particle should

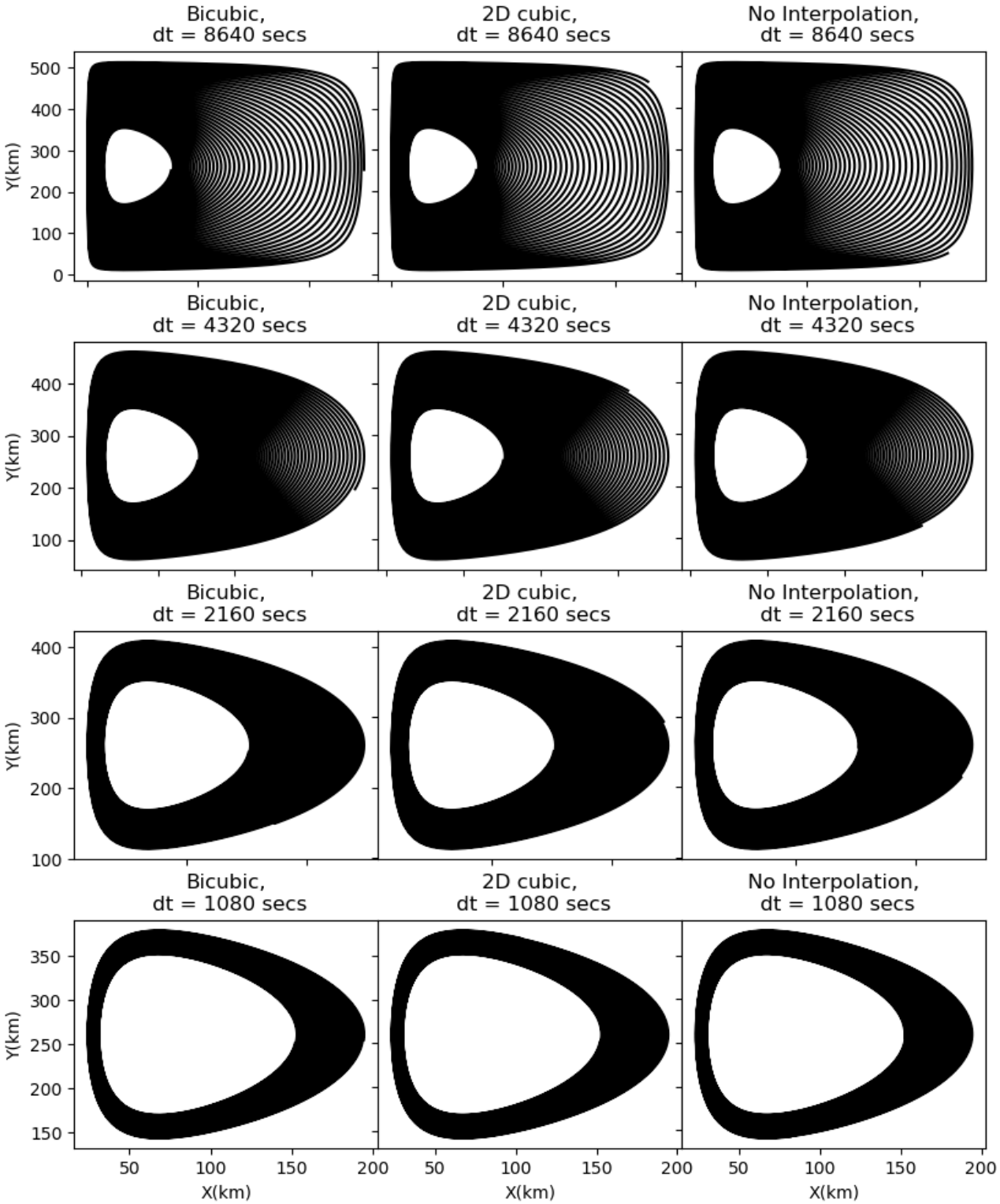

Figure 3.5: Trajectories of a particle starting at $(x, y) = (150, 250)$ km advected for 10,000 days by the Stommel flow in fig. 3.4 using the Euler method. Figure has the same layout as fig. 3.3.

Spatial Interpolation Method	Time Step (seconds)			
	8640	4320	2160	1080
Bicubic Interpolation	0.7848	0.6088	0.3821	0.2495
2D cubic Interpolation	0.7887	0.6146	0.3875	0.2503
No Interpolation	0.5610	0.5727	0.4473	0.2858

Table 3.3: Accuracy of the interpolation methods for a single particle advected for 10,000 days by the Stommel flow using the Euler method.

Spatial Interpolation Method	Numbers of particles		
	1	40,000	250,000
Bicubic Interpolation	908.028	969.096	947.464
2D cubic Interpolation	30.200	28.220	83.164
No Interpolation	0.004	4.248	25.940

Table 3.4: Run time (seconds) of the interpolation methods for particles advected for 100 days by the Stommel flow in fig. 3.4 using the Euler method.

return to its initial location. We choose to release a particle near the most energetic part of the jet as this is the area where the velocity is largest and so represents the region where interpolation would perform the worst across the domain. Fig. 3.7 shows the trajectories of the two different regimes for different time steps. Table 3.5 shows the accuracy of these trajectories.

Spatial Interpolation Method	Time Step (seconds)			
	8640	4320	2160	1080
Bicubic Interpolation	0.0737	0.0620	0.0591	0.0662
2D cubic Interpolation	0.0489	0.0564	0.0468	0.0333

Table 3.5: Accuracy of the interpolation methods for a single particle advected for 10,000 days by the stationary meandering jet in fig. 3.6 using the Euler method.

Conclusion

Both methods produce results with reasonable accuracy. However it is important to note that 2D-cubic performs markedly better in the stationary jet case. This is because 2D-cubic has inherent bias in the y-direction due to the asymmetry of the construction of the four initial 1D polynomials. Therefore, for fields in which there is larger variation in y, 2D-cubic is expected to perform better. It remains to test the performance of the 2D-cubic method on a meridional as opposed to a zonal jet.

For a single particle, 2D-cubic is much faster, whereas for a larger ensemble of particles

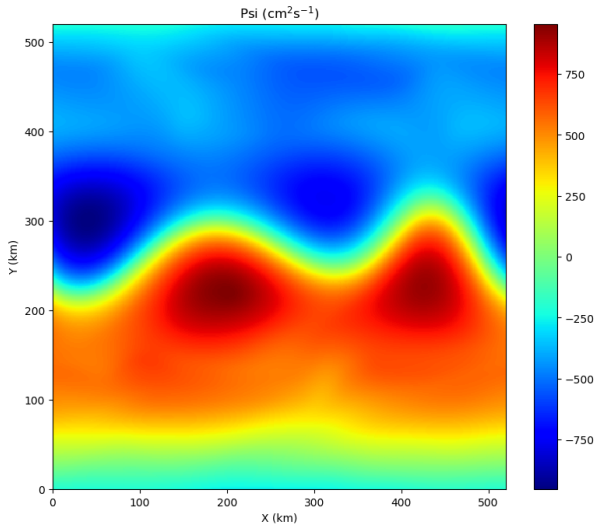

Figure 3.6: Snapshot of the stream function of the coherent meandering jet as in fig. 2.3.

Spatial Interpolation Method	Numbers of particles		
	1	40,000	250,000
Bicubic Interpolation	840.644	957.788	1021.028
2D cubic Interpolation	25.172	27.816	71.560

Table 3.6: Run time (seconds) of the interpolation methods for particles advected for 100 days by the stationary meandering jet in fig. 3.6 using the Euler method.

the difference is markedly less. For each time step, the coefficients for the four Lagrange cubic polynomials in the 2D-cubic interpolation case are cheap to calculate. However, calculating the cubic polynomial coefficients for the bicubic method requires matrix inversion, which is much more expensive. Though, for each particle in the 2D-cubic case, a further four more coefficients must be calculated, whereas nothing more is required in the bicubic case. Nevertheless, even with 250,000 particles, 2D-cubic is faster.

For the size of experiments being carried out, 2D-cubic is the favourable method due to both its computational cost and improved accuracy in the stationary jet case.

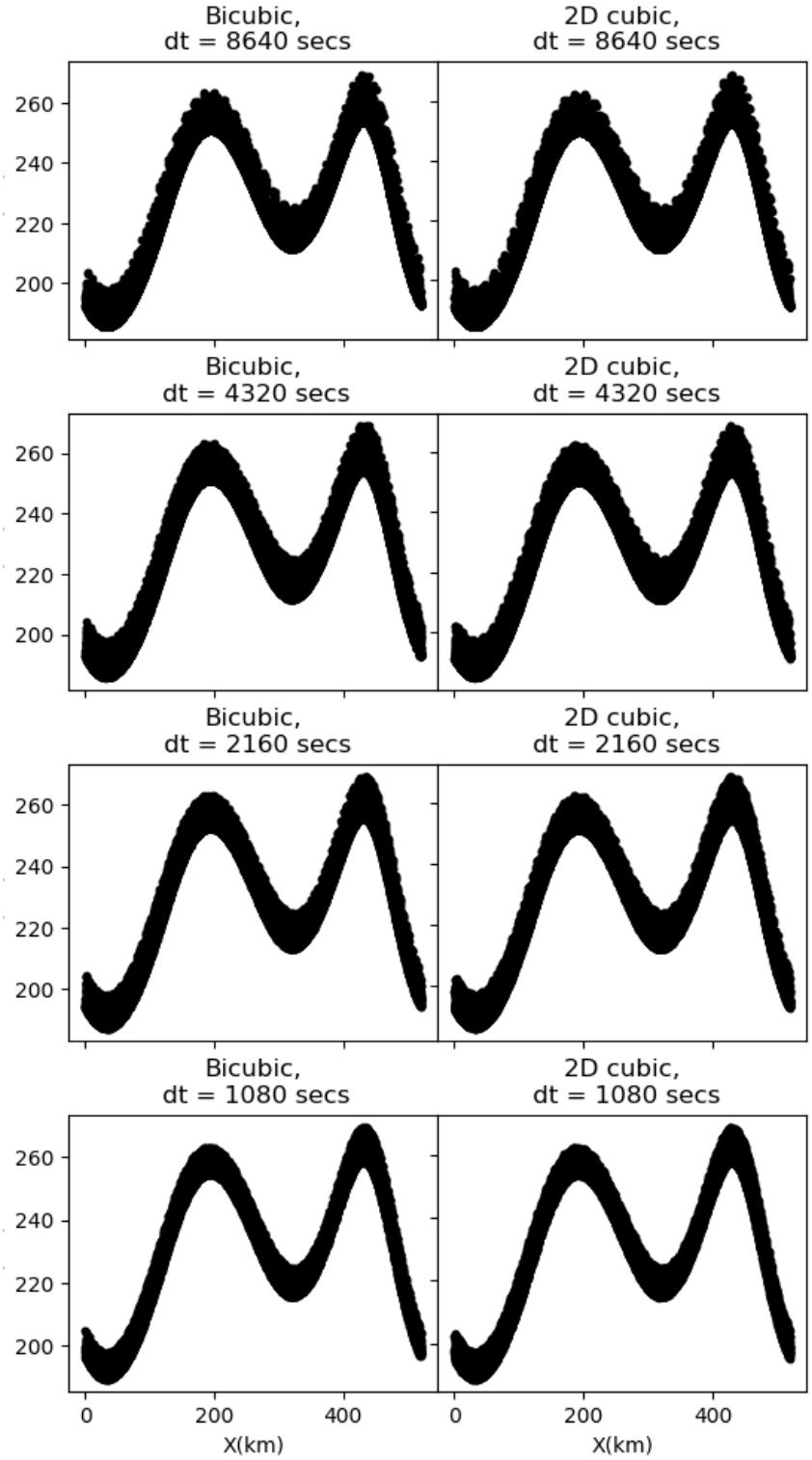

Figure 3.7: Scatter plot of a particle trajectory starting at $(x, y) = (100, 220)$ km advected for 10,000 days by the stationary jet in fig. 3.6 using the Euler method. Trajectories using four different time steps are used, and bicubic and 2D-cubic interpolation schemes are compared.

3.2 Time Integration

3.2.1 Runge-Kutta Fourth-Order Method

The time integration method used in the transport model is the Runge-Kutta fourth-order method (RK4). It's a used to solve equations of the form:

$$\frac{dx}{dt} = u(x,t), \quad x(t_0) = x_0,$$

where x is the unknown we would like to approximate. In our case it is the x-component of the particle location. u, t_0 and x_0 are all given. u would be the x-component of the velocity. Suppose the step-size is Δt, then

$$\begin{aligned} x_{n+1} &= x_n + \frac{\Delta t}{6}\left(k_1 + 2k_2 + 2k_3 + k_4\right), \\ t_{n+1} &= t_n + \Delta t, \end{aligned}$$

where

$$\begin{aligned} k_1 &= u\left(t_n, x_n\right), \\ k_2 &= u\left(t_n + \frac{\Delta t}{2}, x_n + \frac{\Delta t}{2}k_1\right), \\ k_3 &= u\left(t_n + \frac{\Delta t}{2}, x_n + \frac{\Delta t}{2}k_2\right), \\ k_4 &= u\left(t_n + \Delta t, x_n + \Delta t k_3\right). \end{aligned}$$

Hence temporal interpolation is required to approximate u at the half time step: $t_n + \frac{\Delta t}{2}$. Cubic Lagrange polynomial interpolation will be used, that is, the 1D version of 2D-cubic interpolation as described in appendix A.

3.2.2 Performance of RK4

We will test RK4 on the exactly the same test cases as before, with exactly the same parameters, but replacing the Euler method with RK4. We will also force the code to calculate the polynomial coefficients twice, for the current velocity field and at the half time step to give accurate running times. Figs. 3.8 to 3.10 show trajectories of a single particle advected by two plane waves, the Stommel flow and a stationary jet respectively. Tables 3.7, 3.9 and 3.9, give the accuracy of the trajectories and tables 3.8, 3.10 and 3.12, show the running times for increasing numbers of particles.

Spatial Interpolation Method	Time Step (seconds)			
	8640	4320	2160	1080
Bicubic Interpolation	0.2463	0.1723	0.1053	0.0650
2D cubic Interpolation	0.0403	0.0403	0.0403	0.0403
No Interpolation	0.0403	0.0403	0.0403	0.0403

Table 3.7: Accuracy of the interpolation methods for a single particle advected for 1,000 days by the two plane waves in fig. 3.2 using the RK4 method.

Spatial Interpolation Method	Numbers of particles		
	1	40,000	250,000
Bicubic Interpolation	1699.220	1894.40796	2264.292
2D cubic Interpolation	58.564	118.704	399.264
No Interpolation	0.008	29.132	179.916

Table 3.8: Run time (seconds) of the interpolation methods for particles advected for 100 days by the two plane waves in fig. 3.2 using the RK4 method.

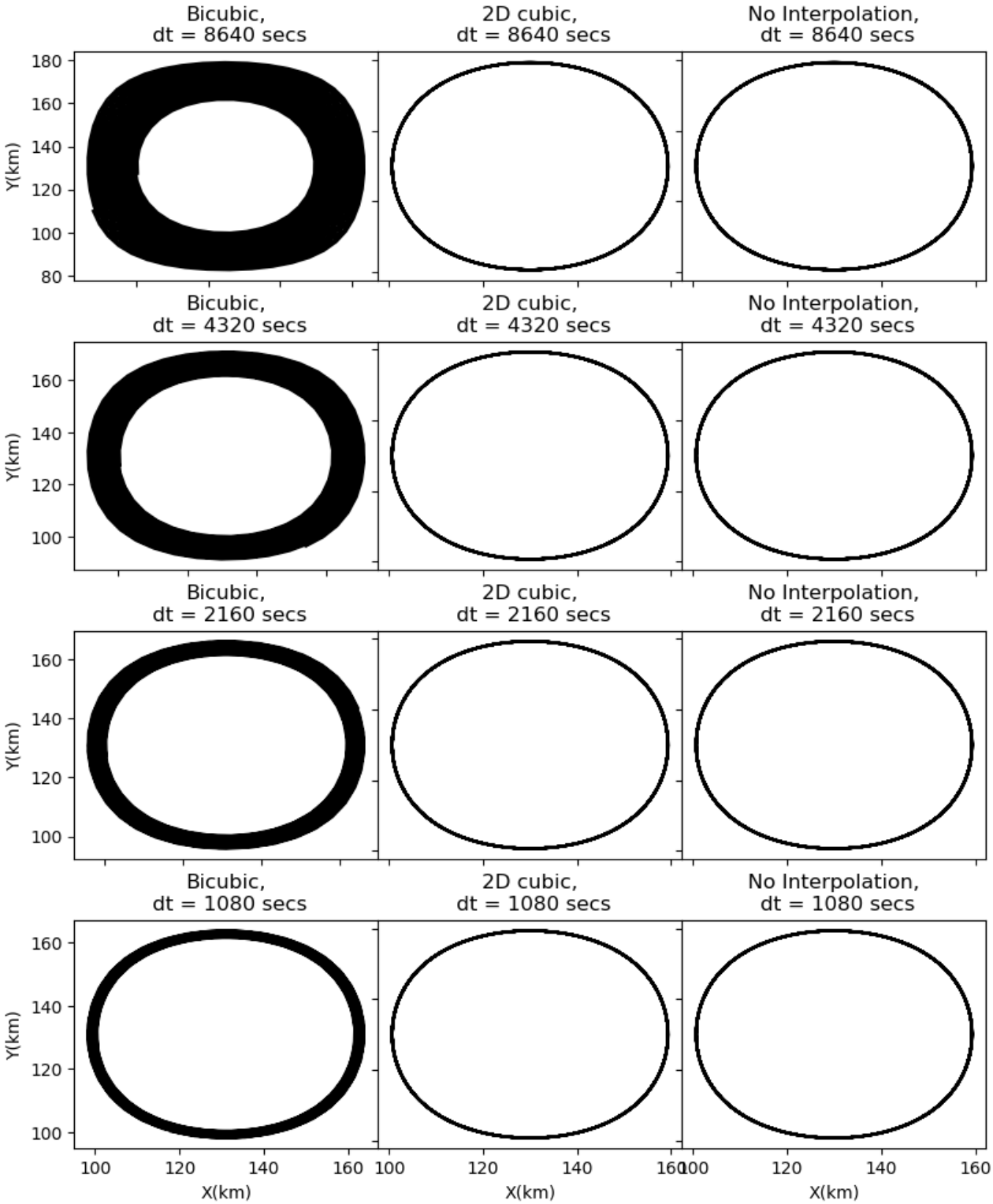

Figure 3.8: Trajectories of a particle starting at $(x, y) = (100, 120)$km advected for 1,000 days by the two plane waves in fig. 3.2 using the RK4 method. Figure has same layout as fig. 3.3.

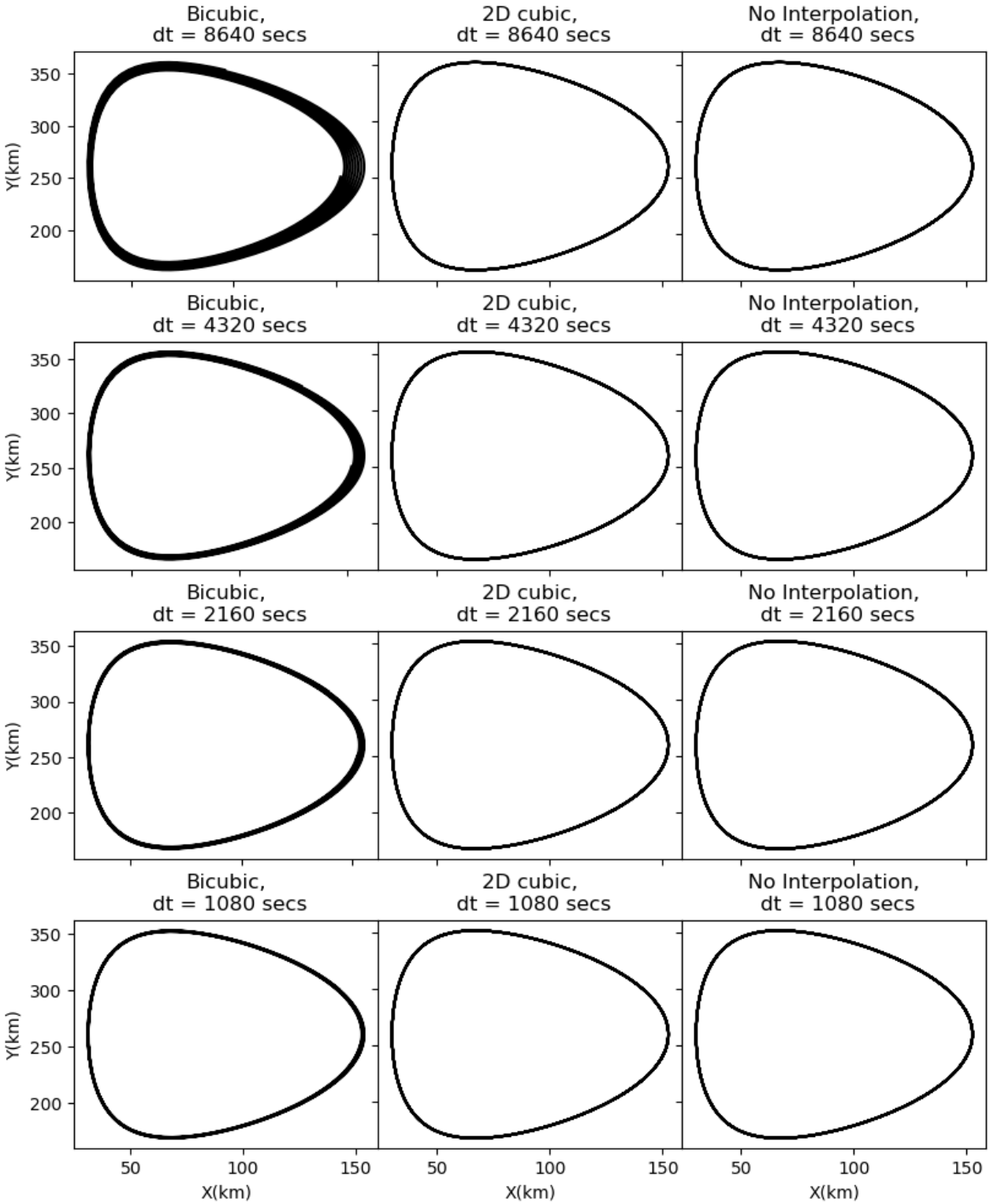

Figure 3.9: Trajectories of a particle starting at $(x, y) = (150, 250)$km advected for 10,000 days by the Stommel flow using the RK4 method. Figure has same layout as fig. 3.3.

Spatial Interpolation Method	Time Step (seconds)			
	8640	4320	2160	1080
Bicubic Interpolation	0.0901	0.0595	0.0315	0.0278
2D cubic Interpolation	0.0050	0.0050	0.0050	0.0050
No Interpolation	0.0052	0.0052	0.0052	0.0052

Table 3.9: Accuracy of the interpolation methods for a single particle advected for 10,000 days by the Stommel flow using the RK4 method.

Spatial Interpolation Method	Numbers of particles		
	1	40,000	250,000
Bicubic Interpolation	1690.640	1752.884	1974.720
2D cubic Interpolation	78.776	109.484	263.016
No Interpolation	0.008	23.936	151.840

Table 3.10: Run time (seconds) of the interpolation methods for particles advected for 100 days by the Stommel flow using the RK4 method.

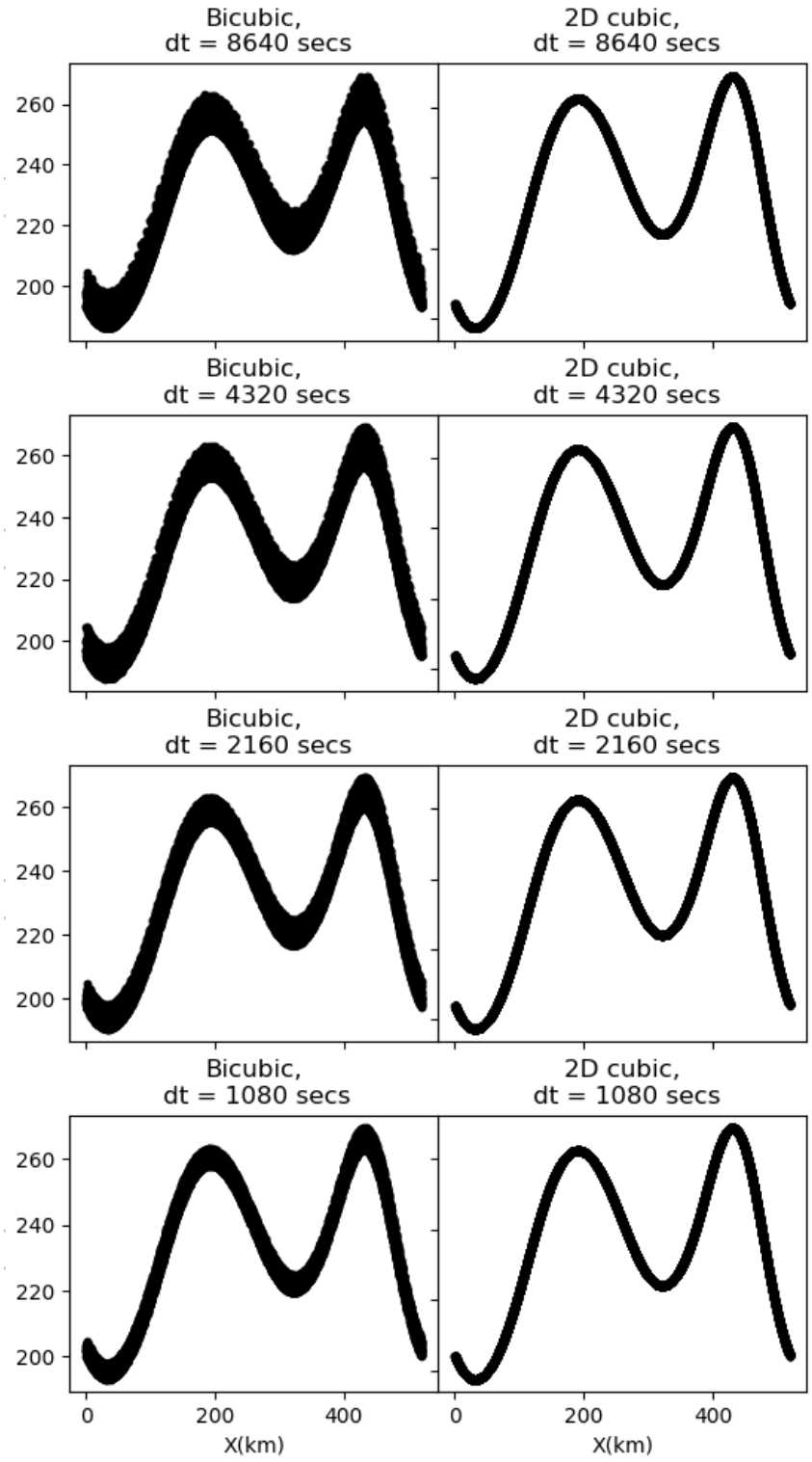

Figure 3.10: Scatter plot of a particle trajectory starting at $(x, y) = (100, 220)$km advected for 10,000 days by a stationary jet using the RK4 method. Compares trajectories for particles advected using four different time steps and compare bicubic and 2D-cubic interpolation.

Spatial Interpolation Method	Time Step (seconds)			
	8640	4320	2160	1080
Bicubic Interpolation	0.0769	0.0706	0.0509	0.0235
2D cubic Interpolation	0.0015	0.00053	0.000391	0.000353

Table 3.11: Accuracy of the interpolation methods for a single particle advected for 10,000 days by a stationary meandering jet using the RK4 method.

Spatial Interpolation Method	Numbers of particles		
	1	40,000	250,000
Bicubic Interpolation	1846.956	1964.612	2085.800
2D cubic Interpolation	48.156	81.212	255.496

Table 3.12: Run time (seconds) of the interpolation methods for particles advected for 100 days by a stationary meandering jet using the RK4 method.

Conclusion

The accuracy gain from using RK4 instead of Euler, is considerable. The accuracy of RK4 is demonstrated best when comparing the cases where no interpolation is used. For a time step of 8640 seconds, the accuracy for two plane waves increased from 0.3921 to 0.0403 and for the Stommel flow, from 0.5610 to 0.0052. That is, the accuracy improved by about an order of three. 2D-cubic interpolation is accurate to at least order four when comparing with the exact case when using RK4. We have demonstrated that using 2D-cubic spatial interpolation and RK4 for time integration produces sufficiently accurate results for use in our transport model.

3.2.3 Choice of Offline Time Step

A sufficiently small time step must be used so that the particle is advected by a distance smaller than the grid size, and that accuracy is insensitive to a further decrease in time step. The domain size is 520 km $\times$ 520 km, and the grid resolution is 512 $\times$ 512, therefore the grid size is approximately 1km. In the faster jet, the maximum velocity is about 20 cm/s. Hence

the maximum time step needed is approximately $\frac{1000}{0.2} = 5000$s. This is supported by the results in table 3.11. For a halved time step from 8640 seconds to 4320 seconds, the accuracy improves by three times, whereas if the time step is halved again to give 2160 seconds, the accuracy doesn't even double, and the improvement is even less for 1080 seconds, demonstrating that the transport model is increasingly insensitive to a further decrease in time step. This would suggest that the optimal time step should be between 4320 and 2160 seconds. A time step of 3600 seconds (an hour) is chosen for convenience.

Chapter 4

Analysis of Transport in a QG model

4.1 Background

The first question we must consider is how do we isolate the eddying component of Lagrangian transport? There are two such ways to do this:

- eddy-only (EO) trajectories, where the particles are advected by the eddy velocity only: $\mathbf{u}'(t) = \mathbf{u}(t) - \overline{\mathbf{u}} - \mathbf{U_0}$ where $\mathbf{U_0}$ is the background velocity and $\overline{\mathbf{u}}$ is the time-mean velocity;

- full-following-eddy (FFE) trajectories, which takes into account the mean flows ability to advect particles between eddies. Particles are advected by the full field, the mean displacement is calculated following the full trajectory and the resulting difference is cumulatively added. That is, say the particle starts at $\mathbf{x}_0$. The particle is advected for one time step using the full velocity and the resulting displacement $\mathrm{d}\mathbf{x}$ is calculated: $\mathbf{u}\mathrm{d}t = \mathrm{d}\mathbf{x}$. The contribution from the time-mean and background flow to this displacement is calculated: $(\bar{\mathbf{u}} + \mathbf{U_0})\mathrm{d}t = \mathrm{d}\bar{\mathbf{x}}$. Then the new particle location in the FFE trajectory is $\tilde{\mathbf{x}}_1 = \mathbf{x}_0 + \mathrm{d}\mathbf{x} - \mathrm{d}\bar{\mathbf{x}}$. This process is then repeated following the full trajectory, i.e from the location $\mathbf{x}_1 = \mathbf{x_0} + \mathrm{d}\mathbf{x}$, and the resulting displacement is added to $\tilde{\mathbf{x}}_1$.

Rypina et al. (2012) suggested the FFE method (referred to as eddy-following full-trajectory, or EFFT). The idea behind the FFE trajectories is that, in reality particles are advected by

the full flow, not the eddying flow, but we wish to calculate the contribution from the eddying flow to the full trajectory. The mean flow causes tracers to be advected faster through certain eddying regions. In the appendix of Rypina et al. (2012), the relevance of the FFE method was verified by testing it on a similar QG meandering jet and found that the EO diffusivities failed to account for the suppression of mixing across the jet core, which was clearly demonstrated by Lyaponov exponent maxima on the jet core.

By calculating appropriate Lagrangian statistics across the domain, we can diagnose and quantify anisotropic and non-diffusive material transport. Here, relevant statistics will be introduced. Further details can be found in LaCasce (2008), van Sebille et al. (2018) and Berloff et al. (2002).

4.1.1 Lagrangian Statistics

The first such statistic that will be discussed is single-particle dispersion (SPD):

$$D_x(t) = \frac{1}{N}\sum_{n=1}^{N}[x_n(t) - x_n(0)]^2, \quad D_y(t) = \frac{1}{N}\sum_{n=1}^{N}[y_n(t) - y_n(0)]^2, \tag{4.1}$$

where N is the number of particles and $(x_n(t), y_n(t))$ is the location of the nth particle at time t. It measures the ensemble mean spread of particles. Fitting the SPD to time using a power law, $D_i \sim t^{\alpha_i}$, one can diagnose its diffusive-ness (Berloff et al. 2002):

- if $0.8 < \alpha_i < 1.2$, transport is said to be roughly diffusive,
- if $\alpha_i < 0.8$, transport is said to be sub-diffusive,
- if $\alpha_i > 1.2$, transport is said to be super-diffusive.

α is found as the gradient of a log-log plot of SPD against time.

The absolute diffusivity, or eddy diffusivity tensor is found as half the time-derivative of single-particle dispersion:

$$K_i = \frac{1}{2}\frac{dD_i(t)}{dt}. \tag{4.2}$$

The diffusivity is used to calculate tracer distributions:

$$\frac{\partial c}{\partial t} + \mathbf{u} \cdot \nabla c = \nabla \cdot \mathbf{K} \nabla c. \tag{4.3}$$

When estimating the diffusivity, it is important to obtain local estimates, which, when using this method, can prove problematic, as particles will evidently not remain in the same geographic region. An alternative method of estimating the eddy-diffusivity was suggested by Nakamura (1996). It uses area as a coordinate and diffusivity is represented loosely as mass distributed across tracer contours. The variable that quantifies mixing is the equivalent length, L_e, of tracer contours. Chaotic advection acts to stretch L_e. This method provides instantaneous estimates of diffusivity, and it also does not require any averaging, and hence would result in less smearing of results. However, L_e is a scalar, not a tensor, and so is not appropriate for cases in which we observe anisotropic transport.

Another issue with estimating the diffusivity, which will be discussed in further detail throughout this thesis, is the assumption that it is constant. We need to run the transport model for a significant period of time in order to appropriately calculate K, but sampling error also increases with time when considering real data. This makes calculating K from float data troublesome as it is difficult to obtain long enough records (Griffa et al. 1995).

Another measure of interest is the Lagrangian autocorrelation function (LACF), which is defined as follows:

$$R_i(\tau) = \frac{\langle u_i(t) u_i(t+\tau) \rangle}{\langle u_i^2 \rangle}, \tag{4.4}$$

where u_i is the Lagrangian velocity as calculated from the Lagrangian trajectories, and $< \cdot >$ denotes an ensemble average. We can find the Lagrangian integral time-scale as follows:

$$T_L^i = \int_0^\infty R_i(\tau) \mathrm{d}\tau. \tag{4.5}$$

The Lagrangian autocorrelation function represents the memory of a particle, hence for a diffusive regime we see an immediate decay in R, where R would be a δ-function. Difficulties

in estimating T_L arise in real-world ocean datasets. Data is often too spatially and temporally sparse. T_L could be smaller than the sampling rate. Furthermore, R can oscillate or decay so slowly it doesn't reach zero in the observed time range.

The eddy-diffusivity coefficient can also be calculated from the Lagrangian integral time-scale:

$$K_i = \sigma_{ii}^2 T_L^i, \tag{4.6}$$

where σ_{ij}^2 is the velocity variance:

$$\sigma_{ij}^2 = \left\langle u_i' u_j' \right\rangle. \tag{4.7}$$

We obtain the following alternative relationship for the SPD from Taylor (1922):

$$D_i(t) = 2\sigma_{ii}^2 \int_0^t \int_0^{t'} R_i(\tau) d\tau dt', \tag{4.8}$$

which leads us to a short-time and large-time limit:

$$D_i(t) = \sigma_{ii}^2 t^2 \quad t << T_L^i, \tag{4.9}$$

$$D_i(t) = 2\sigma_{ii}^2 t T_L^i \quad t >> T_L^i. \tag{4.10}$$

Therefore there is a separation of time-scales exhibited by Lagrangian trajectories. At short times, we refer to this as the ballistic regime, and at long times, if the integral of the LACF converges, particles will spread diffusively. Hence, we are interested in what happens at intermediate time-scales.

4.2 Lagrangian Statistics Derived From a Simple Kinematic Model

A key result demonstrating the relationship between the background mean flow and eddy propagation speed was presented in Ferrari & Nikurashin (2010). It was found, analytically, that meridional cross jet eddy mixing is enhanced when the background mean velocity and eddy propagation speed was the same. The result was derived for tracer diffusivity, but was consolidated by Klocker, Ferrari & LaCasce (2012) for the particle derived diffusivity. It does however remain to be seen what the effect is on the along-jet diffusivity.

4.2.1 The Model

We take a similar approach to Ferrari & Nikurashin (2010), in that we consider a propagating plane wave with x and y dependence on top of a non-time varying background flow, but for the purposed of this study, we shall not consider stochasticity as it is not essential in demonstrating the cross-jet mixing suppression. The eddying stream-function is defined as follows:

$$\psi'(x, y, t) = A\cos(kx + ly - 2\pi ct), \tag{4.11}$$

where k and l are the zonal and meridional wavenumbers, A is the wave amplitude and c is the wave propagation speed. We will consider two types of background flows. The first is the same as that considered in Ferrari & Nikurashin (2010), where

$$\bar{u}(x, y) = U \tag{4.12}$$

We will also consider a Gaussian jet,

$$\bar{u}(x, y) = U\exp\left(\frac{-(y-r)^2}{2\sigma^2}\right), \tag{4.13}$$

where r is the centre of the jet, U is its amplitude, or maximum velocity, and σ is the

standard-deviation of the jet, or spread. The zonal profile of the time-mean zonal velocity produced by the dynamical QG model much more closely resembles a Gaussian jet, and so a Gaussian background jet will be more applicable.

We will also only consider the Full and FFE trajectories. EO trajectories do not account for the influence of the mean flow at all.

4.2.2 The Results

Uniform Background Flow

Firstly, we consider the case where $k = l = 2$ so we can appropriately examine the relationship between the zonal and meridional dispersion. We keep U constant and vary c relative to U, where $U = 6\text{cm s}^{-1}$. The basinscale is 520 km, the same as for the dynamical model. We plot the SPD for the full, EO and FFE trajectories in fig. 4.1.

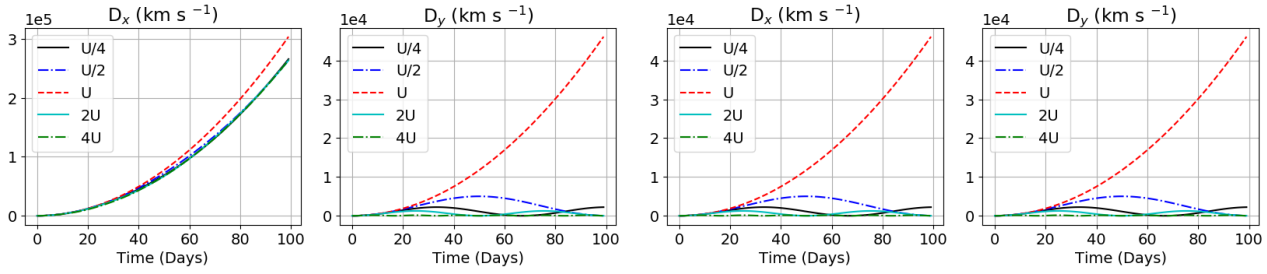

(a) Full SPD

(b) FFE SPD

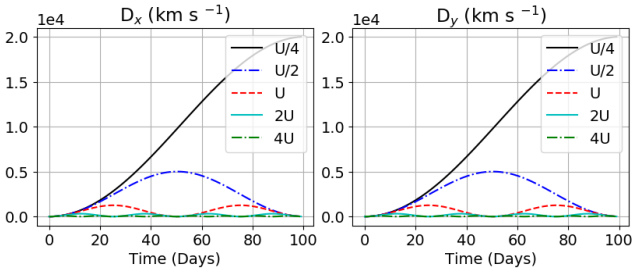

(c) EO SPD

Figure 4.1: Single Particle Dispersion for a propagating plane wave on a uniform background flow, where $k = l = 2$ and c is varied. The legend indicates how c relates to U.

As expected, when $c = U$, the meridional dispersion is quicker, as indicated by the red line, implying an enhancement of cross-jet diffusivity. Interestingly, the same behaviour is seen in the zonal FFE SPD, despite the mean flow being only zonal, and the rate of spread is also the

same as in the meridional direction (as the eddying stream-function is symmetric in x and y). This increase in FFE diffusivity is seen in fig. 4.1a in a slightly enhanced full zonal dispersion. The EO dispersion plot is included just for reference, and as expected, the dispersion is driven by the eddy propagation speed. The dispersion will scale with c^{-2}, due to integration of the velocity which is roughly of the form $\sin(\cdots - 2\pi ct)$. In fact, the mean flows acts to slow transport where $U \neq c$.

Furthermore, the SPD curve clearly shows super-diffusive behaviour when $U = c$, while when $c \neq U$, the dispersion is almost completely suppressed. We would expect that with some stochasticity, particles could be nudged, and so some spread would be seen. But without that stochasticity, particles just oscillate between plane waves.

The same experiment was run with $l = 2k$ to check the same behaviour occurs. We do not include the results as they are largely trivial. While the FFE zonal dispersion is slightly faster than the meridional dispersion, the qualitative behaviour is the same.

Gaussian Background Flow

Now we do the same but with a background Gaussian jet. We define r to be in the centre of domain, and c is again varied, while U is kept constant. This time, we split the domain into 5 bins in order to capture the jet core, the flanks, and the surf zone.

Firstly, let's compare the different values of c for the different bins, as plotted in fig. 4.2. As before, we set $k = l = 2$, and choose $\sigma \approx 51$ km. This value was chosen so the non-dimensional σ was 50 and the hence the Gaussian jet was sufficiently sharp. Bins 4 and 5 are not included as the field is symmetric in y and so exhibit the same statistics as bins 2 and 1 respectively. Dispersion is consistently largest when $c = U/4$. This is because, the background zonal velocity $\bar{u}$ decreases away from the jet core, and so will match the wave propagation speed. Where in the domain this occurs, depends on σ. And hence, in the surf region where there is a negligble bacgkround flow, the full zonal dispersion for $c = U/4$ is the most enhanced, as c is closer to $\bar{u}$ in this region.

We compare this to the case where σ is increased by a factor of 4, producing a much wider

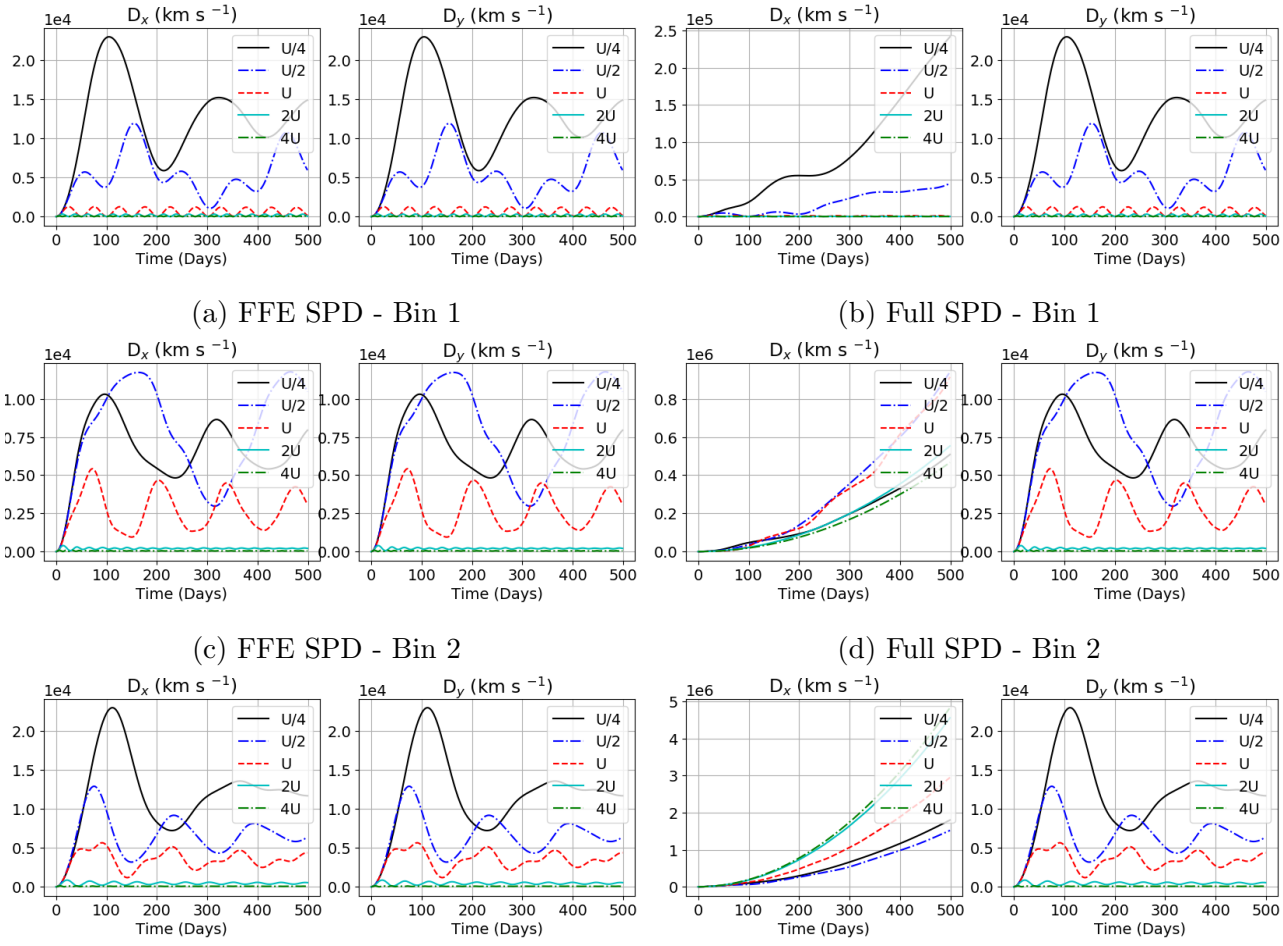

(a) FFE SPD - Bin 1

(b) Full SPD - Bin 1

(c) FFE SPD - Bin 2

(d) Full SPD - Bin 2

(e) FFE SPD - Bin 3

(f) Full SPD - Bin 3

Figure 4.2: Single Particle Dispersion for a propagating plane wave on a Gaussian background flow, where $k = l = 2$ and c is varied. The non-dimensional $\sigma = 50$. The legend indicates how c relates to U.

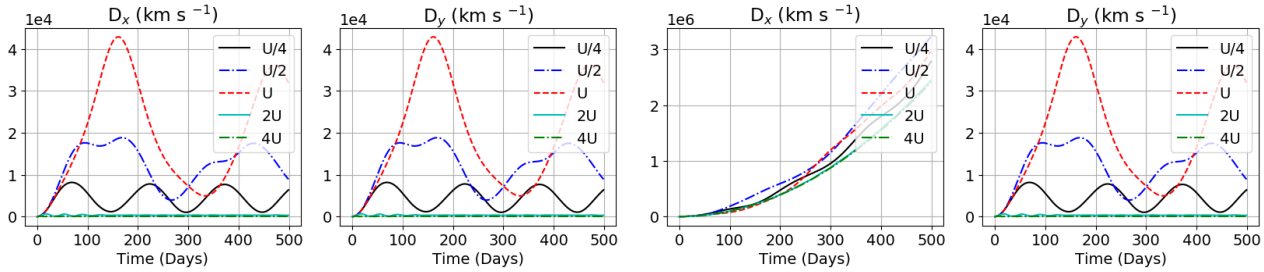

(a) FFE SPD - Bin 1

(b) Full SPD - Bin 1

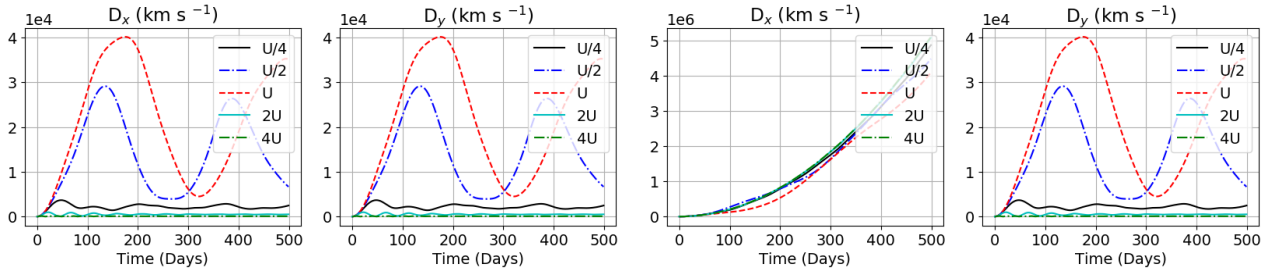

(c) FFE SPD - Bin 2

(d) Full SPD - Bin 2

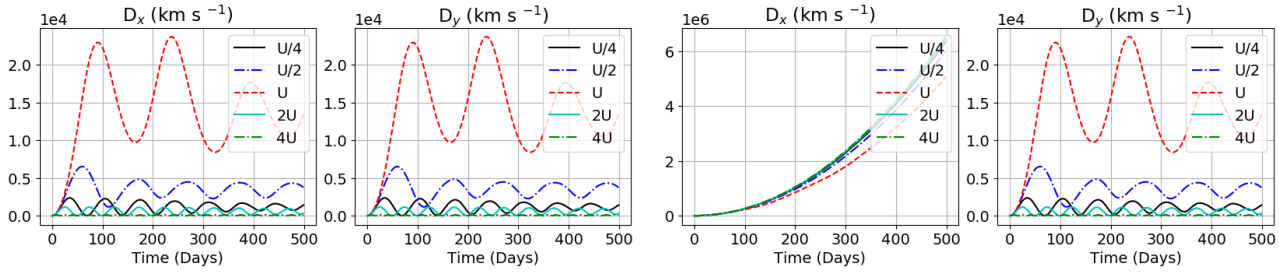

(e) FFE SPD - Bin 3

(f) Full SPD - Bin 3

Figure 4.3: Single Particle Dispersion for a propagating plane wave on a Gaussian background flow, where $k = l = 2$ and c is varied. The non-dimensional $\sigma = 200$. The legend indicates how c relates to U.

more smeared Gaussian jet. The SPD is plotted in fig. 4.3. In contrast to fig. 4.2, dispersion is enhanced most when $c = U$. This implies that for zonal jets with a velocity profile resembling a Gaussian jet, it is not just the eddy propagation speed that drives across and along-jet eddy transport, but the jet width that also plays a role.

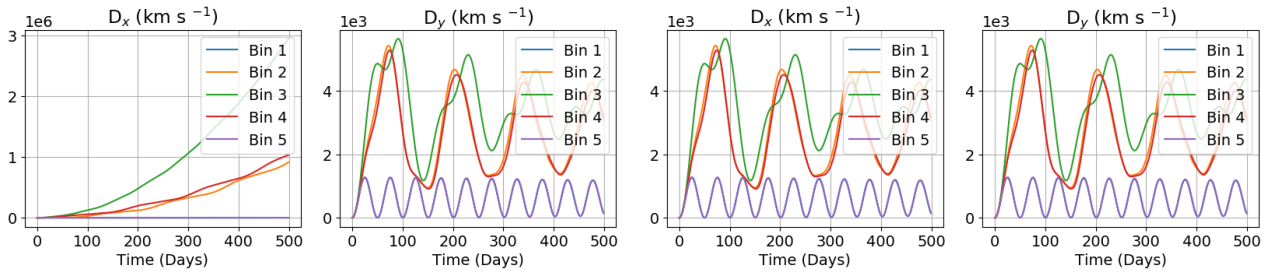

(a) Full SPD

(b) FFE SPD

Figure 4.4: Single Particle Dispersion for a propagating plane wave on a Gaussian background flow, where $k = l = 2$ and $c = U$. The SPD in the different bins is compared.

But how does the SPD vary across the jet? To answer this question, we examine the case where $U = c$ and $\sigma = 200$. The SPD is plotted in fig. 4.4. As expected, the dispersion is fastest in the central bins, and is suppressed elsewhere. This supports the theory presented by Ferrari & Nikurashin (2010), that mixing is suppressed on the flanks of the ACC. However, it is important to note that this behaviour clearly depends on how eddy-propagation speed and the Gaussian profile relate to eachother.

Relationship between eddy propagation speed and average background zonal flow

Can we establish a relationship between the single particle dispersion and the meridionally averaged background zonal velocity? Integrating the non-dimensional eq. (4.13) and normalising by the interval width between $y = ii = N$, and $y = 0$, with $r = N/2$ gives

$$\langle \overline{u}(y) \rangle = \frac{U}{N}\sqrt{\frac{\pi}{2}}(-\sigma)\left[\mathrm{erf}\left(-\frac{N}{2\sqrt{2}\sigma}\right) - \mathrm{erf}\left(\frac{N}{2\sqrt{2}\sigma}\right)\right], \tag{4.14}$$

$$= \frac{2U\sigma}{N}\sqrt{\frac{\pi}{2}}\mathrm{erf}\left(\frac{N}{2\sqrt{2}\sigma}\right). \tag{4.15}$$

We plot the variation in the average zonal velocity in fig. 4.5. As expected, as σ increases,

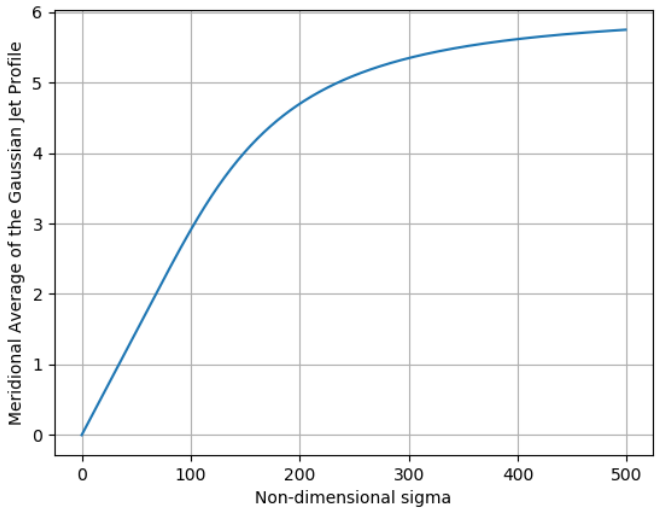

Figure 4.5: Change in the average of the background Gaussian zonal velocity profile against the non-dimensional σ or standard deviation. $U = 6, r = N/2$ where N in the non-dimensional domain width.

the jet becomes broader and hence exhibits less variation across the domain, so the average tends to U. However, the important thing to note, is to examine the size of σ for an average zonal velocity of $U/4$. It appears to be quite close to 50. Fig. 4.2 demosntrates that for a non-dimensional σ of 50, when the eddy propagation speed is $U/4$, dispersion is maximised. Therefore, dispersion is maximised when $c = \bar{u}$.

4.3 Analysis of Standard Lagrangian Statistics

In this section, we calculate and examine single-particle statistics as described at the beginning of this chapter. 5000 particles are released uniformly in 10 uniform zonal bins in 9 separate releases separated by 200 days and are advected for 1000 days. Statistics are averaged over particle ensembles and over the different releases. This is so the statistics hold no dependence on the time at which particles are released, and

Firstly, let us qualitatively examine Lagrangian transport by observing scatter plots of particles advected by the two regimes. Fig. 4.6 illustrates how particles spread when released from the jet core. This bin demonstrates the most noticeable differences between the two regimes. Notice in the upper right hand plot of fig. 4.6b, that we see a dense patch of particles

splitting away from the jet. Compare this with the PV anomaly in fig. 4.8b at the same time. We can identify a vortex responsible for trapping this cloud of particles and advecting them away from the jet. We hypothesise that, because of this vortex shedding, the latent jet is a leaky barrier to Lagrangian transport. After 150 days, we can see that the particles have mixed much more in the latent jet than the the coherent jet, where we can still see some of the jet structure retained in the scatter plot.

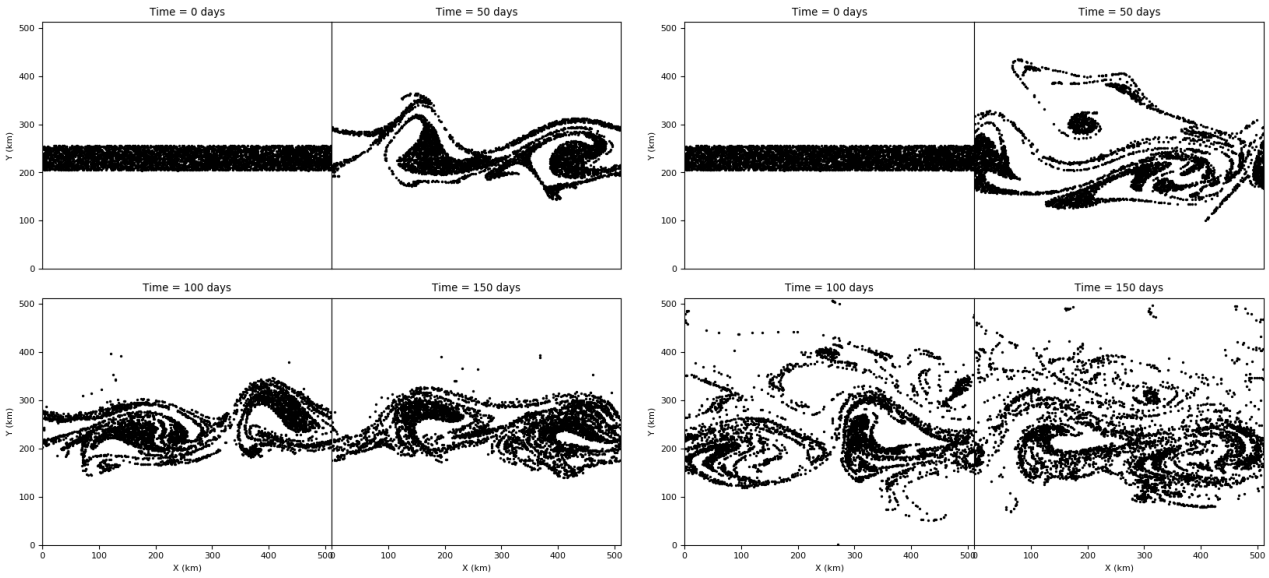

(a) Coherent Jet (b) Latent Jet

Figure 4.6: Snapshot scatter plots of particles released from time = 0 days in the top layer for the two regimes at 0, 50, 100 and 150 days for bin 5, roughly on the jet core.

4.3.1 Single-Particle Dispersion

The single-particle dispersion for the coherent jet for the three different trajectories in all 10 bins is plotted in fig. E.1 and in fig. E.2 for the latent jet.

Zonal SPD

Bins 5 and 6 are deemed to be the bins closest to the jet core. As expected, the full zonal dispersion is greatest around the jet core. This is due to an enhanced time-averaged stream function which is almost purely zonal. There is little change in the eddy-only zonal dispersion in the coherent jet, however we do see an enhancement of zonal dispersion near the jet core for

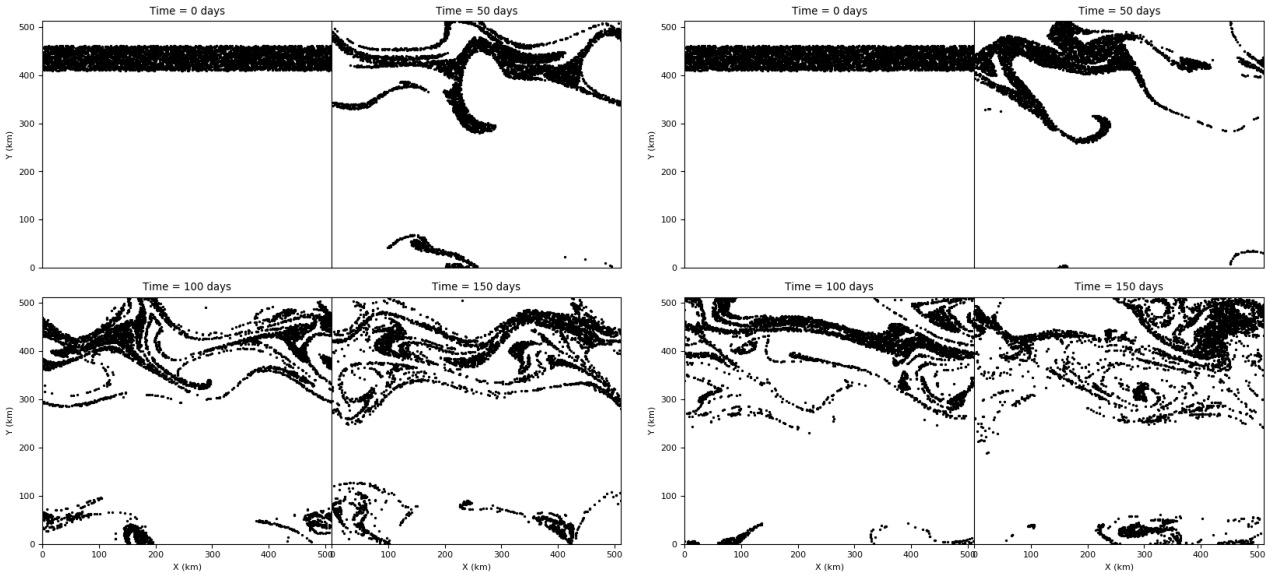

(a) Coherent Jet (b) Latent Jet

Figure 4.7: Same as fig. 4.6 but for particles released in bin 9, in the mixing return flow region.

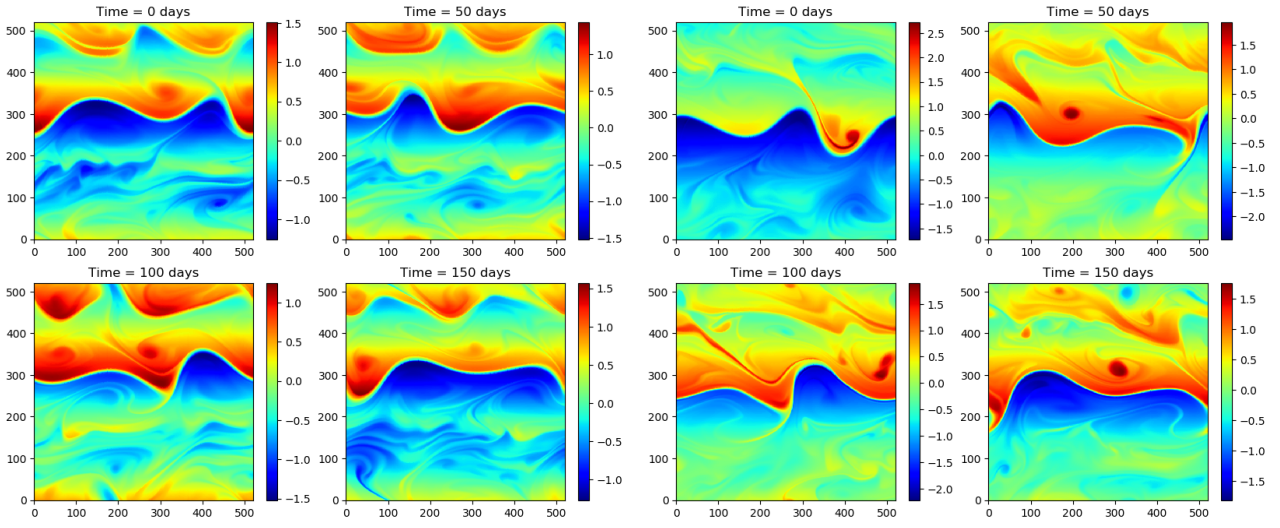

(a) Coherent Jet (b) Latent Jet

Figure 4.8: Snapshot PV anomaly (s^{-1}) in the top layer for the two regimes at times corresponding to the scatter plots in figs. 4.6 and 4.7.

the latent jet. If we refer to fig. 2.5a, we can qualitatively see that the coherent eddying stream function has no zonal structure, as opposed to the latent jet, in which a zonal jet structure can still be observed, which will result in the zonal transport of Lagrangian particles. The FFE trajectories do exhibit a slightly enhanced zonal dispersion for both regimes in the top layer near the jet core. We can conclude, that there is a non-linear interaction between the mean flow and eddying flow when advecting trajectories, and that there is an effect of shear as a result of the mean flow, on Lagrangian trajectories.

Meridional SPD

In regards to the meridional dispersion, it is important to note the initial gradient. For bins 5, 6 and 7 in the top layer we see a steeper initial dispersion, which then levels out. Other bins display a more linear behaviour. This suggests that particles are quickly leaving the bins near the jet core, and then exhibiting a dispersion similar to the surrounding bins. Therefore it is imperative that we consider the appropriate time-scale.

This initial growth of SPD also demonstrates the ballistic nature of material transport at early times. It is easier to verify this by looking at the log-log plot of the SPD against time. In figs. E.3 and E.4 we have also included the ballistic and diffusive log-log plots for comparison.

Both regimes and all the different trajectories exhibit early ballistic behaviour as expected. However at different times, the gradient of the log-log plot changes. Zonally, the full and FFE trajectories consistently exhibit gradients larger than diffusive, and meridionally, less than diffusive. EO trajectories spread faster than the diffusive regime zonally, however meridionally, the spreading rate appears much closer to diffusive. We quantify this rate of spreading with α which is further discussed in section 4.3.4.

The transitional time-scale between ballistic, and non-ballistic regimes, defined in eq. (4.5), will be discussed in section 4.3.3.

Furthermore, we note that the EO meridional dispersion in the top layer in both jet regimes increases at a significantly greater rate than for the FFE or full trajectories. This agrees with what was observed in Rypina et al. (2012), and was alluded to at the beginning of this chapter.

That is, EO trajectories do not capture the meridional transport barrier properly.

4.3.2 The Lagrangian Autocorrelation Function (LACF)

We calculate the Lagrangian autocorrelation function according to eq. (4.4). Figs. E.5 and E.6 plot the autocorrelation function, R, for the coherent jet. R_x in both the top and bottom layers rarely reaches zero, which makes calculating an Lagrangian integral time-scale difficult. Even in the eddying cases, we see a very slow decay to zero. We do however see a faster decay to zero for the eddying trajectory closer to the jet core.

Near the jet core, R_y is wildly oscillating and exhibits quite a small Lagrangian integral time-scale. This is in general agreement with Berloff et al. (2002). In fact we often observe a large first negative lobe. This is typically associated with sub-diffusivity. This behaviour will be confirmed in section 4.3.4. Super-diffusivity is however associated with a dominant positive second lobe, and a smaller first negative lobe. Away from the jet, R_x decays so slowly that we do not observe this behaviour. However, if we focus particularly on the bottom layer closer to the jet, this behaviour is clearly observed in the coherent jet. There is less oscillation of R_x around the jet core for the latent jet, implying a larger decorrelation time-scale.

4.3.3 Time Scale

There are two time-scales that we need to consider, the first of which concerns enforcing locality of the statistics, which we refer to as T, and the second is the Lagrangian integral time-scale T_L defined in eq. (4.5). Chen & Waterman (2017) also perform similar analysis in order to construct 'non-locality ellipses'. They carefully construct time integration limits that depend on the time it takes for the diffusivity to converge. It differs from our method slightly in that they consider the full diffusivity tensor. Let us first consider the locality time-scale, T.

Estimating the locality time-scale, T

After a certain period of time, Lagrangian trajectories will leave the bin from which they were released. Therefore, there will be a trade off between the locality of statistics and choosing a

sufficiently long time-scale in order to capture intermediate behaviour. Furthermore, we would expect different geographical regions to have significantly different time-scales.

For each bin, we choose the cut off time as the time at which $\sqrt{D_y(t)}$ becomes greater than the width of the bin. This enforces the retention of some locality of statistics.

Fig. 4.9 plots the time-scale across the domain. If the time-scale is plotted as 1000 days, the true time-scale must be at least 1000 days as this is the total time the particles are advected for.

Firstly, let's focus our attention on the coherent jet. In both the top layer and bottom layer we can see that there is a minimum in the time-scale at the jet core. This would imply that this region is chaotic with a rapid separation of particle trajectories as a small time-scale indicates that particles leave the bin quickly.

However, in the top layer for the coherent jet, it is interesting to observe multiple maxima in the time-scale suggesting an existence of multiple jets. Uniquely, the top layer for the coherent jet does exhibit zonal velocity maxima on the flanks of the jet core, which supports the idea of multiple jets, and meridional transport enhancement in the jet core. However, the eddy-only time-scale does not demonstrate this same behaviour. The emergence of multiple jets will be examined further in chapter 5. We do not see the same pattern however in the bottom layer, and the EO time-scale exhibits qualitatively the same behaviour as the FFE and full time-scales. This would again support the theory that EO statistics fail to capture the transport barrier and is consistent with the work of Ferrari & Nikurashin (2010) and Rypina et al. (2012).

Interestingly, this is less evident in the latent jet. We appear to have slight maxima in the mixing regions surrounding the jet, but they aren't as evident as for the coherent jet. T is also consistently smaller, implying there is significant Lagrangian mixing in the latent jet. The top and bottom layer are also qualitatively and quantitatively similar. This can be explained by studying the zonal velocity profiles. Unlike in the top layer of the coherent jet, there are not well pronounced velocity maxima on the flanks. Furthermore, the jets are much broader. If we refer to the work of Ferrari & Nikurashin (2010), we can hypothesise that there is a slower change in the difference between the zonal velocity and eddy propagation speed, and hence

mixing efficiency changes less drastically against y.

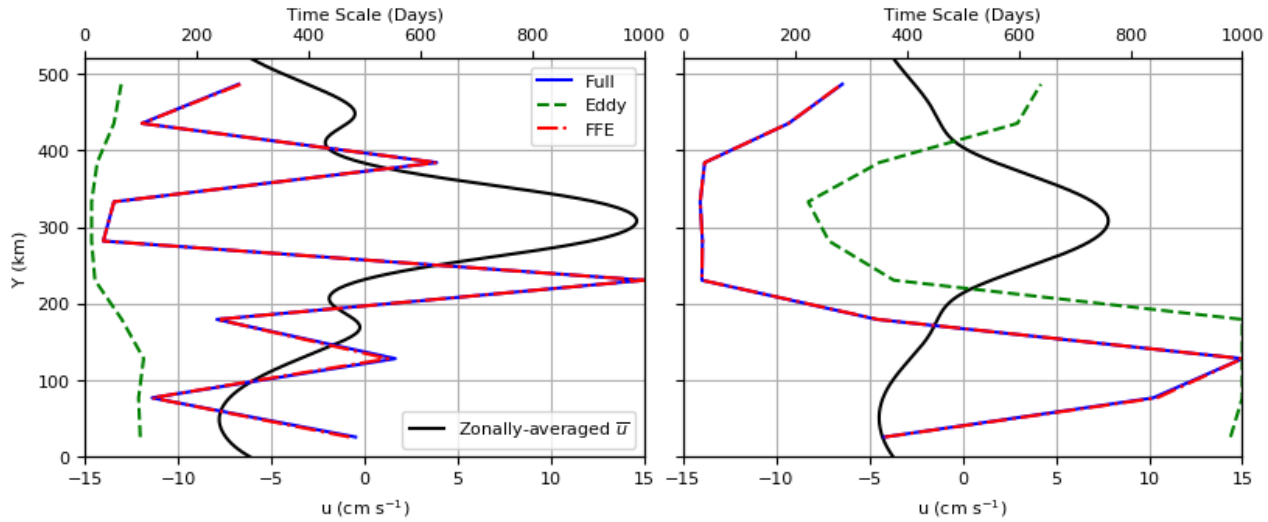

(a) Coherent Jet.

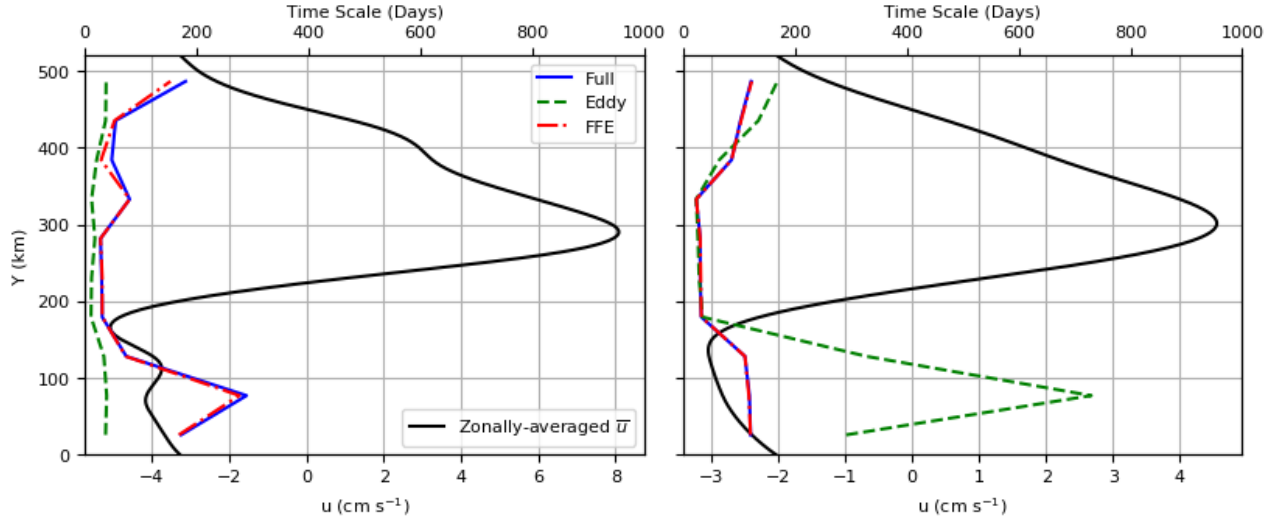

(b) Latent Jet

Figure 4.9: Time-Scale (days) estimated as the time at which the square root of meridional dispersion exceeds the bin width. The solid black line is the zonally-averaged time-averaged zonal velocity. The left column is the top layer and the right column is the bottom.

Estimating T_L

The Lagrangian integral time-scale defines the separation of the ballistic and diffusive regimes as described in expressions eqs. (4.9) and (4.10). However, difficulties arise in estimating this in highly non-diffusive, especially super-diffusive, regimes, as $R(\tau)$ can be highly oscillatory or may never decay to zero.

A work around for this problem would be to fit R to an exponential curve, i.e. $R \sim e^{-at}$. We take T_L to be a^{-1}. This was the method used in Berloff & McWilliams (2002). The reasoning behind this, as we shall see in section 6.3 is that for a 1st-order Markov model, which is able to capture the ballistic time-scale, the resulting LACF is $R = e^{-t/T_L}$. However, in the meridional direction, the LACF is oscillatory, hence T_L will be underestimated in the meridional direction. This prompts us to consider an alternative function to which to fit R.

Dosio et al. (2005) calculates autocorrelation functions in the atmospheric convective boundary layer and found qualitatively similar autocorrelation functions. In the horizontal, the autocorrelation was found to decay exponentially, and in the vertical, the autocorrelation function was found to be oscillatory. It was suggested to fit the oscillatory behaviour to

$$e^{-a\tau}\left[\cos(b\tau) - \frac{a}{b}\cos(b\tau)\right]. \tag{4.16}$$

The Lagrangian integral time-scale was then calculated to be the time at which $R(\tau)$ reaches to $0.37 = e^{-1}$, which therefore assumes an exponential shape prior to the integral time-scale. However, in order to enforce that $R(0) = 1$, R is fitted to

$$e^{-a\tau}\left[\cos(b\tau)\right]. \tag{4.17}$$

Similarly, we fit the meridional FFE LACF to the above function and plot the two curves in figs. E.7 and E.8 respectively. The corresponding T_L is also shown.

In order to verify that we are capturing the separation of the ballistic and intermediate regimes, we display T_L against the log-log plots of SPD against time in figs. E.3 and E.4.

As expected, we consistently obtain a much larger zonal T_L than meridional. This is in agreement with Kamenkovich et al. (2009) who stated that anisotropy in eddy-induced transport was driven by an anisotropic correlation time-scale tensor, as opposed to an anisotropic velocity variance.

4.3.4 Power Law Exponent

We calculate the power law exponent, α_i, from T_L up to T. T will have an enforced minimum so that we calculate α for a sufficient period of time beyond the ballistic time-scale, though this will result in some smearing of statistics. α_i is plotted in fig. 4.10. α_x consistently demonstrates super-diffusivity in the zonal direction. The zonal FFE dispersion is more noticeably super-diffusive than the EO dispersion. The Ferrari inspired kinematic model, studying the relationship between the background flow and the eddy propagation speed also demonstrates zonal super-diffusivity. While in the latent jet, a minima in α_x is seen in the jet core, the opposite is true for the coherent jet. Judging from the kinematic model, it suggests that in the latent jet, the maximum mean zonal velocity more closely matches the eddy propagation speed, while in the latent jet, the eddies are propagating slower relative to the maximal zonal mean velocity, hence maxima are seen on the jet flanks.

All trajectories are consistently sub-diffusive meridionally in the top layer, but not in the bottom layer. Despite estimating these values over a longer time-scale, non-diffusive behaviour is still observed. Evidently, due to the clear non-diffusive trajectory behaviour, approximating a diffusivity coefficient, which relies on the assumption that diffusivity is constant, is difficult. α_y is also qualitatively similar for both the FFE and EO trajectories, but with EO being larger in the top layer. This behaviour cannot just be explained using the model described in section 4.2 alone, though FFE seems to exhibit an extra two minima in the coherent jet corresponding the the return flows. This may be because FFE trajectories are more sensitive to background velocity changes, as suggested in section 4.2.

4.3.5 Eddy-Diffusivity Coefficients

We calculate the diffusivity according to eq. (4.2), and it is plotted in fig. 4.11 for the three different Lagrangian trajectories. There are limitations behind estimating the diffusivity as was alluded to early. Fig. 4.10 clearly demonstrates non-diffusive behaviour, therefore the diffusivity is not constant in time. The diffusivity is however a best guess estimated between the ballistic time-scale, T_L, and the locality time-scale, T. We do however enforce a minimum to the locality

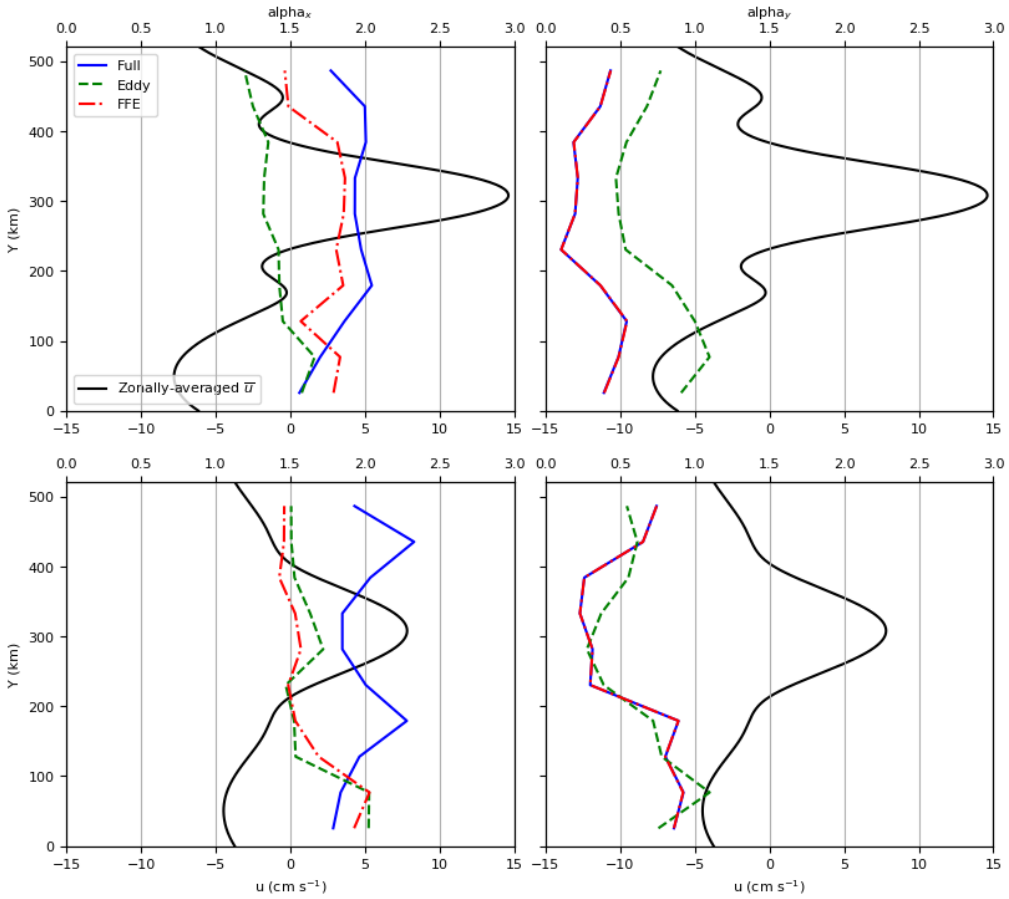

(a) Coherent Jet

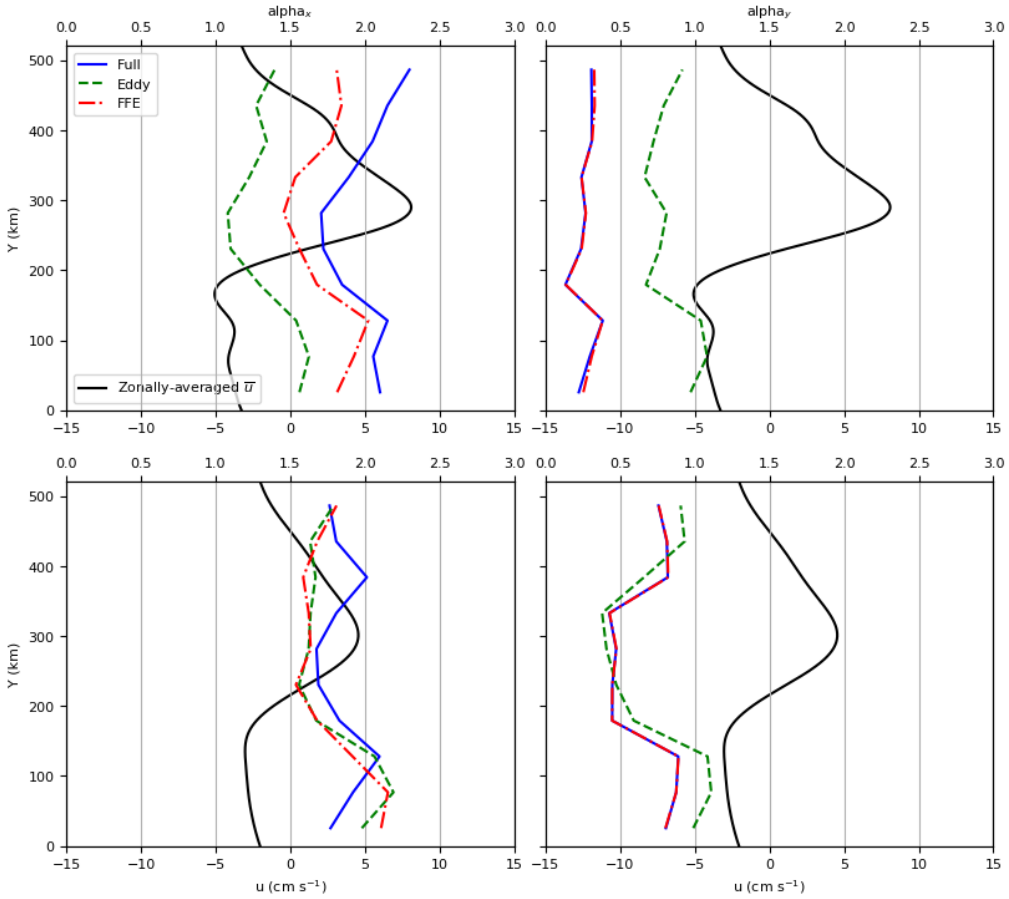

(b) Latent Jet

Figure 4.10: α_i for each bin fitted up to the locality time scale. The solid black line is the zonally-averaged time-averaged zonal velocity. The left row is the zonal direction, and the right row is the meridional direction. The top figure of each panel is the top layer and the bottom is the bottom layer.

time-scale T when it is not much larger than T_L, so that we estimate the diffusivity over a long enough time period.

Firstly, let us focus on the zonal diffusivity. In the top layer, the full diffusivity unsurprisingly captures the jet core with a maxima, this is due to the zonal time-averaged stream function. The EO diffusivity does not capture it well in the coherent jet, though FFE does show a slight maximum around the jet. This implies that the mean flow acts to advect particles from eddy to eddy, accelerating transport. 4.10 shows FFE trajectories are more super-diffusive than EO trajectories, which would agree with the behaviour seen for zonal diffusivities. The diffusivity profiles also show qualitatively similar behaviours in the top layer as for the power-law exponent, mirroring this potential relationship between the maximal mean zonal velocity and eddy propagation speed. FFE meridional diffusivity is consistently less than the EO diffusivity, supporting the theory that the mean flow acts to suppress mixing, particularly when there is a mismatch between the eddy propagation speed and zonal background flow, and that this in fact results in sub-diffusive spreading.

The EO K_y also captures the jet core to some degree, with a slight minimum around the jet core, and hence is capturing the transport barrier. This minimum is more pronounced in the latent jet, however it is important to note that K_y is about three times greater than that in the coherent jet. It is difficult to conclude whether there are diffusivity minima captured by the FFE estimates, as the diffusivity is mildly oscillatory. It looks as if there may be multiple jets. It could also be due to smearing of statistics, an issue which will be addressed later.

It is important to emphasise here that due to the need to calculate the diffusivity over a long time range after the ballistic time-scale, these results will not be entirely local.

Comparing different diffusivity measures

There are two different measures from which we can measure the diffusivity, either from the single-particle dispersion, or from the velocity variance and Lagrangian integral time-scale.

$$K_i = \frac{1}{2}\frac{\partial D_i}{\partial t}, \tag{4.18}$$

$$= \sigma_{ii}^2 T_L^{(i)}. \tag{4.19}$$

We plot the resulting diffusivities for the FFE trajectory in fig. 4.12. As the FFE transport is not technically diffusive, we would not necessarily see an agreement between the two measures. This is something that we will have to take into account when using the diffusivity as a parameter in further models.

The difference between the two diffusivities is particularly noticeable for K_y in the top layer. If we refer to fig. 4.10, Lagrangian transport is significantly sub-diffusive, and hence, as the dispersion is growing slower than time, when taking the time derivative, it ought to be underestimated, which agrees with what we see.

4.4 A Flow Based Dispersion Measure

As our flow field is made up of a strongly meandering jet, we expect to see significant meridional dispersion, just due to the fact that there is significant meridional jet meandering. However, a particle could remain on the jet core and hence exhibit marked meridional transport, even though the particle is not moving relative to the flow. This is why we introduce a flow based dispersion measure. By doing so, we hope to more effectively capture the meridional transport barrier.

Firstly, we must establish an appropriate diagnostic of the flow that allows us to map the particle location to its 'flow relative coordinate'. PV is well known to be a pretty good diagnostic of transport barriers (Dritschel & McIntyre 2008, Juckes & McIntyre 1987). Dritschel & McIntyre (2008) argue that multiple zonal jets act as eddy-transport barriers. These zonal jets form a 'PV staircase'. As our domain is doubly-periodic, we can think of our domain as having infinitely many zonal jets and hence forming a 'PV staircase'.

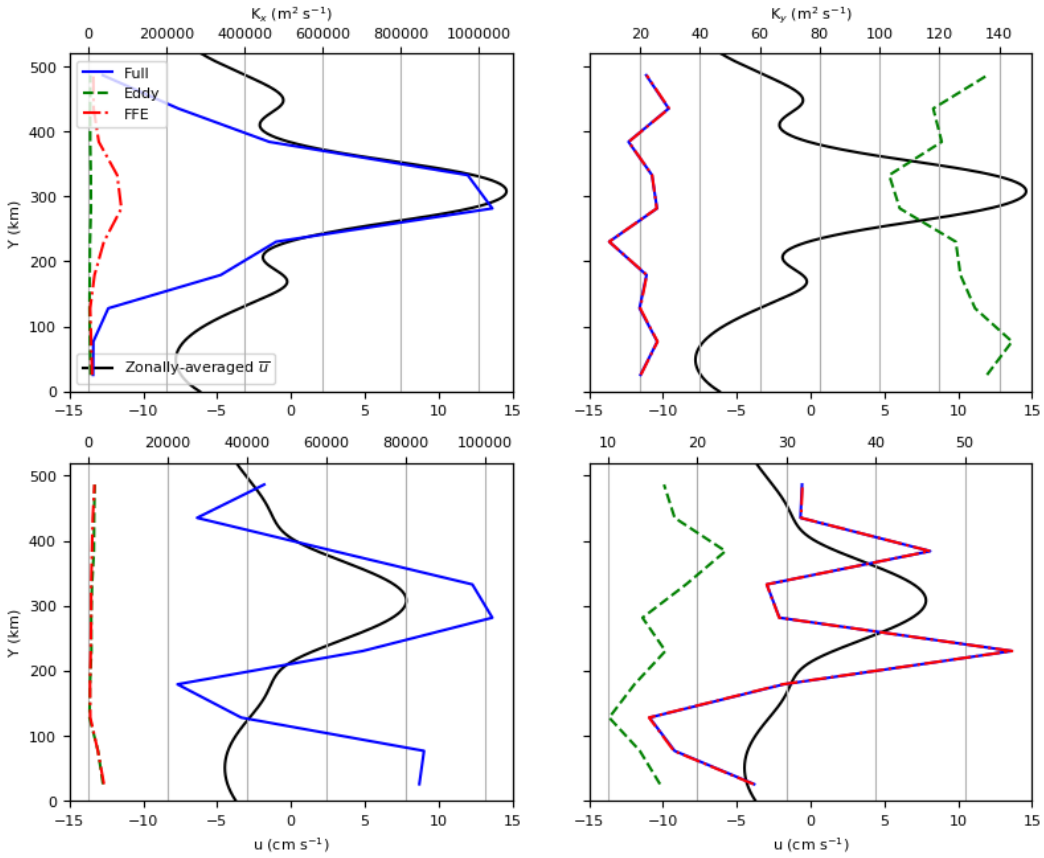

(a) Coherent Jet.

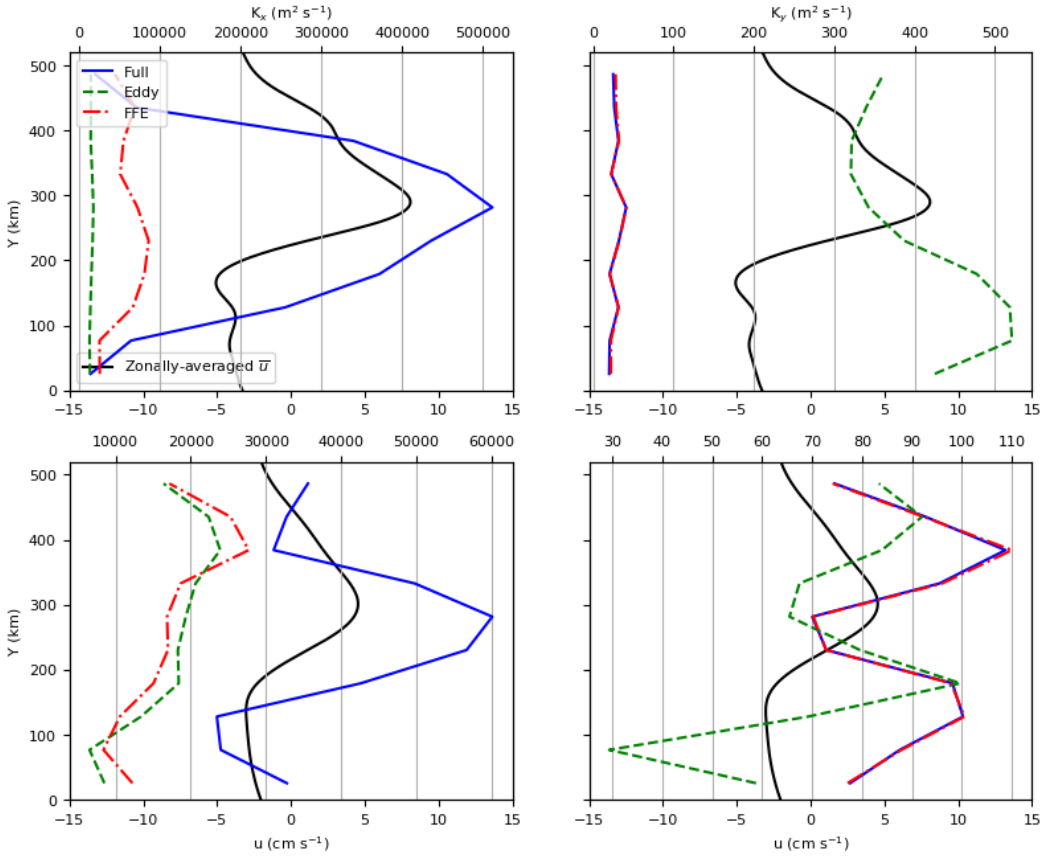

(b) Latent Jet.

Figure 4.11: The diffusivity (m^2 s^{-1}) calculated using the single-particle dispersion. The solid black line is the zonally-averaged time-averaged zonal velocity. The diffusivity is calculated over the time period prior to the Lagrangian time scale. The figure layout is the same as fig. 4.10.

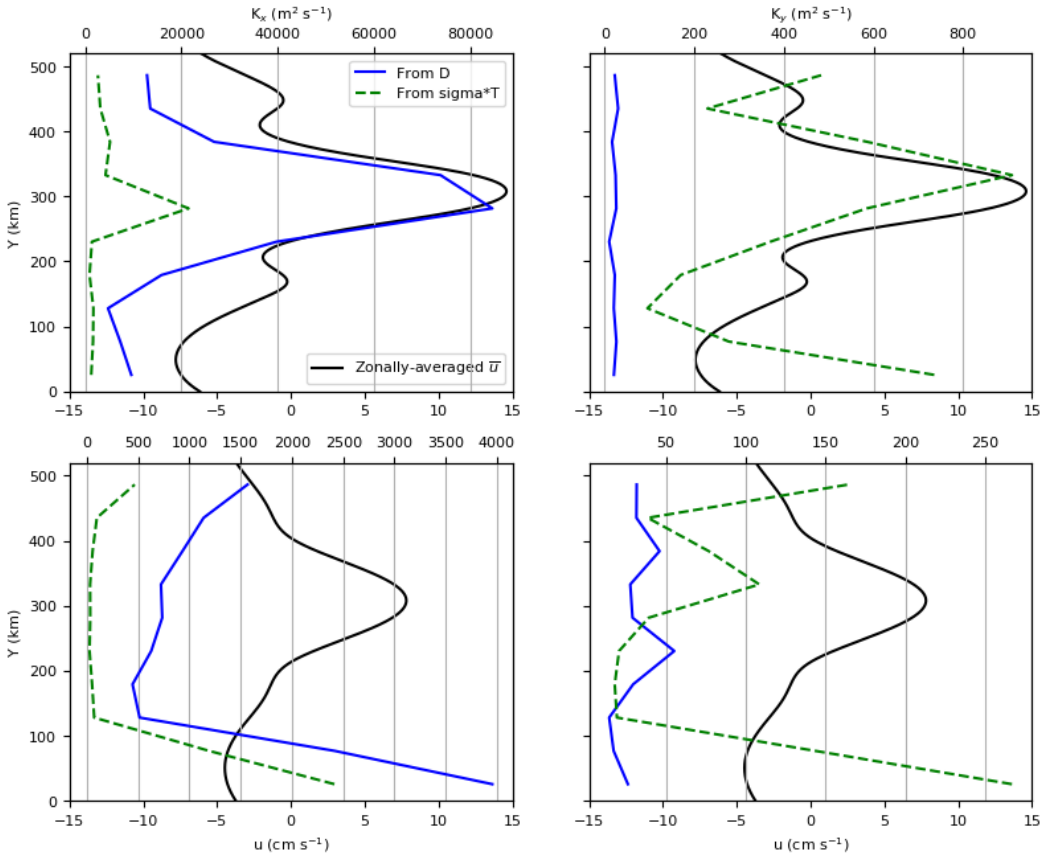

(a) Coherent Jet

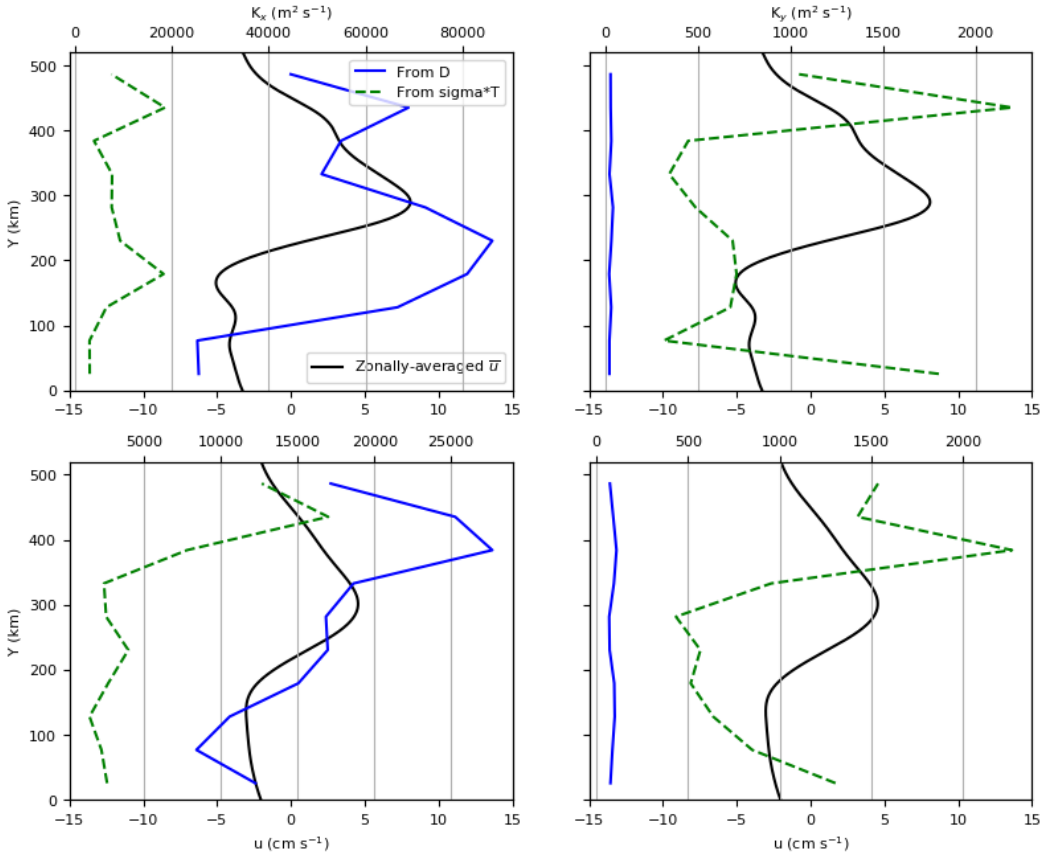

(b) Latent Jet

Figure 4.12: Comparing the diffusivity (m^2 s^{-1}) for the FFE trajectories from both SPD and as $\sigma_{ii}^2 T_L^i$. The solid black line is the zonally-averaged time-averaged zonal velocity. The diffusivity is calculated up to the time scale. The figure layout is the same as fig. 4.10.

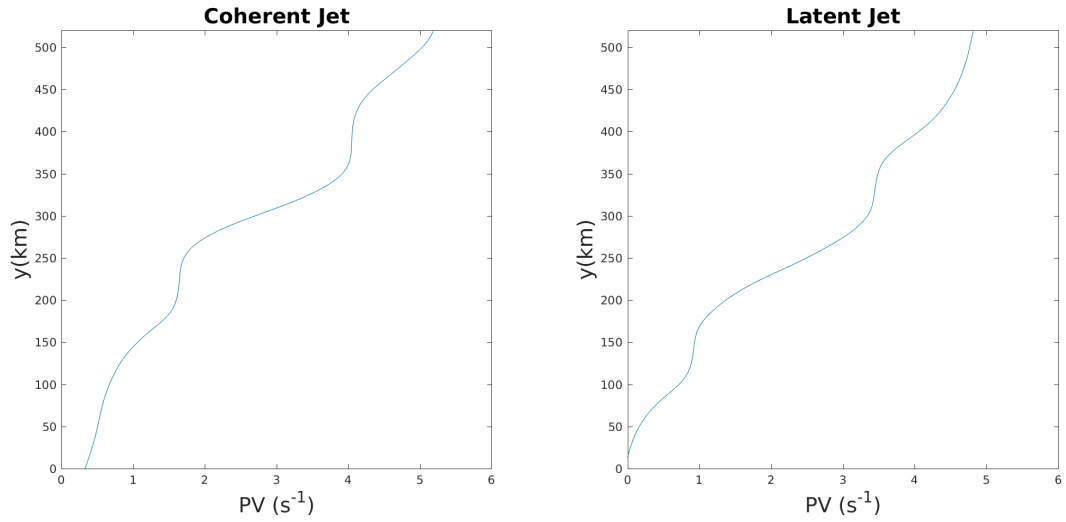

Figure 4.13: The zonally-averaged time-mean PV in the top layer for the first two regimes.

The zonally-averaged full PV is monotonically increasing in y, as shown in fig. 4.13, illustrating a perturbed PV staircase. This allows us to construct a one-to-one mapping between the meridional coordinate of particle location, y, and PV. Let's say the full PV at time t and (x, y) is $\zeta(x, y, t) = q(x, y, t) + \beta y$ and the zonally-averaged time-mean PV at Y is $\overline{\zeta}(Y)$. Initially a particle is located at (x_0, y_0) ,where the PV is $\zeta(x_0, y_0, 0)$. $\zeta(x_0, y_0, 0) = \overline{\zeta}(Y_0)$ for some Y_0. As the map $\overline{\zeta} \to Y$ is one-to-one, a unique Y_0 can be found, and so the PV-mapped meridional location of the particle at time $t = 0$ is Y_0. The same process is carried out at time $t = T$, giving a PV-mapped meridional location of Y_T. Hence, the PV-mapped dispersion is $D_{PV} = \langle (Y_T - Y_0)^2 \rangle$.

Notably, we require the flow diagnostic to be meridionally monotonic to ensure a one-to-one mapping, for this reason we cannot apply this method to the bottom layer.

As opposed to binning the domain uniformly in space, we bin the domain uniformly in the zonally-averaged time-mean PV. As a result, regions with high PV gradients have small bin widths. By doing this, we hope to capture the jet core and boundaries with more accuracy due to sharper bins that follow the jet structure. We see this in fig. 4.14, where the bins are clearly much narrower where the jet core is. The bin width is calculated by uniformly seeding particles and evaluating the proportion of which are allocated to each bin.

Figs. 4.15 and 4.16 compare scatter plots for bin 5 (a narrow bin) and bin 9 (a wide bin). We are picking up the sharpness of the jet core much more efficiently in fig. 4.15 than for the

uniform bins. We are clearly seeing a break up of the transport barrier, particularly for the latent jet. It is also important to note, that as we are binning according to the zonally- and time-averaged PV, the PV snapshot will not necessarily be meridionally monotonic across the domain. Just because a particle is in a certain PV bin, this does not imply it will match up to same spatial bin. To illustrate this, observe the initial scatter plot for the latent jet in bin 9 (fig. 4.16b). We can see a vortex which extends down from the main mixing region. As there is greater PV mixing in the latent jet, these PV filaments may play an important role in PV-mapped dispersion.

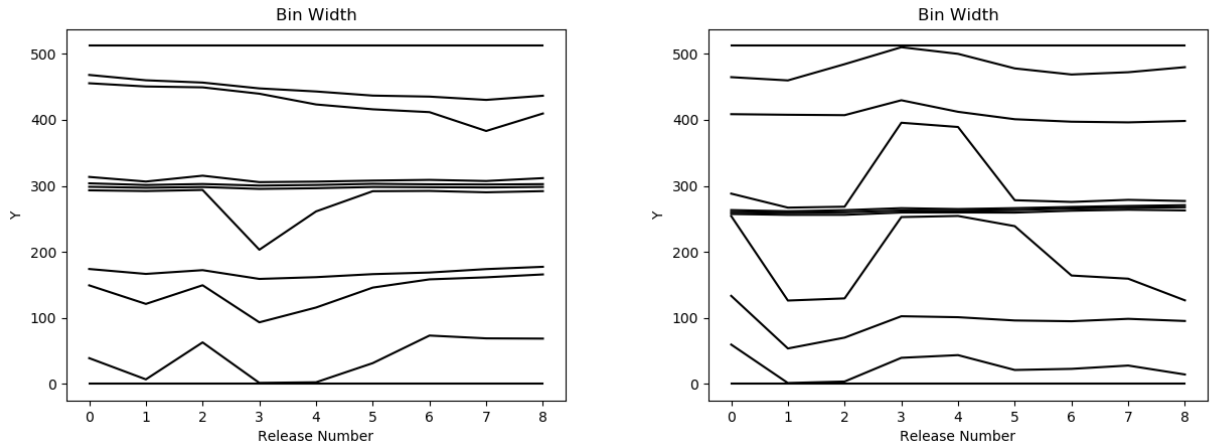

(a) Coherent Jet (b) Latent Jet

Figure 4.14: Bin width (km) plotted against the release number for the two parameter regimes. The bin width is calculated by uniformly releasing particles and calculating the proportion that are binned into the PV bin.

4.4.1 PV-Mapped Dispersion

In 9 releases, with time intervals of 200 days, 5000 particles are released uniformly in each bin and are advected for 1000 days. The resulting single-particle dispersion for the full trajectories and PV-mapped dispersion are calculated. Fig. E.9a compares the two dispersion measures for the coherent jet and fig. E.9b for the latent jet.

There are considerable differences observed between the two regimes. Firstly, let us consider the coherent jet. Bins 5-7 demonstrate a marked oscillatory behaviour, which is a key symptom of a meandering jet. These bins are also the narrowest, i.e exhibit the greatest PV gradient. We

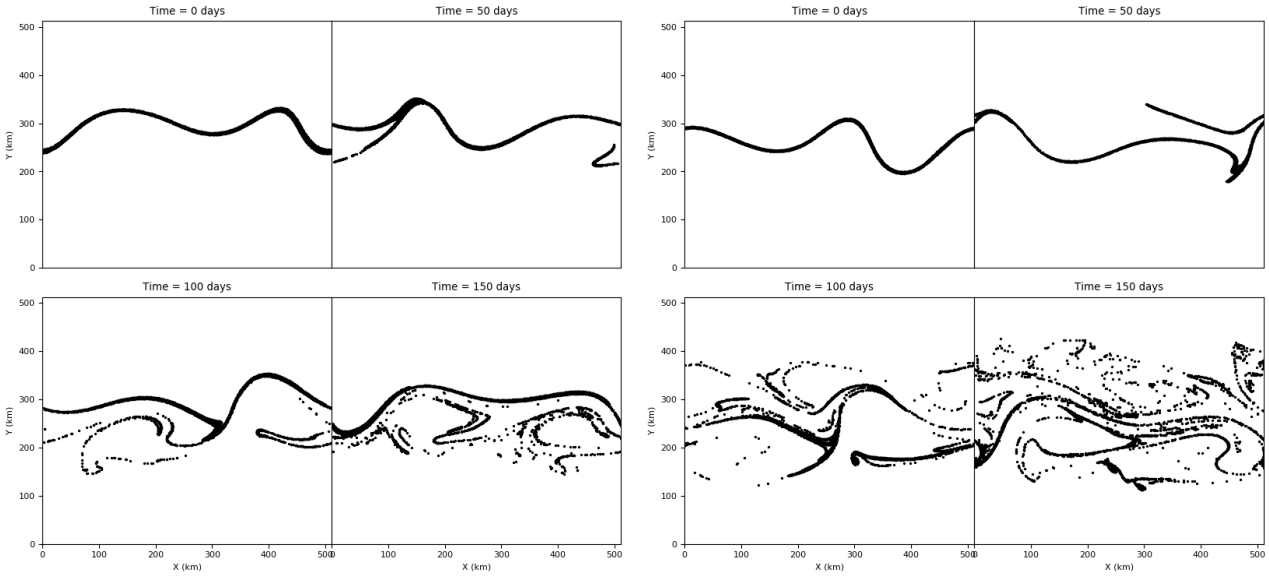

(a) Coherent Jet (b) Latent Jet

Figure 4.15: Snapshot scatter plots in the top layer for the two regimes at 0, 50, 100 and 150 days for particles released in PV bin 5, that is on the jet core.

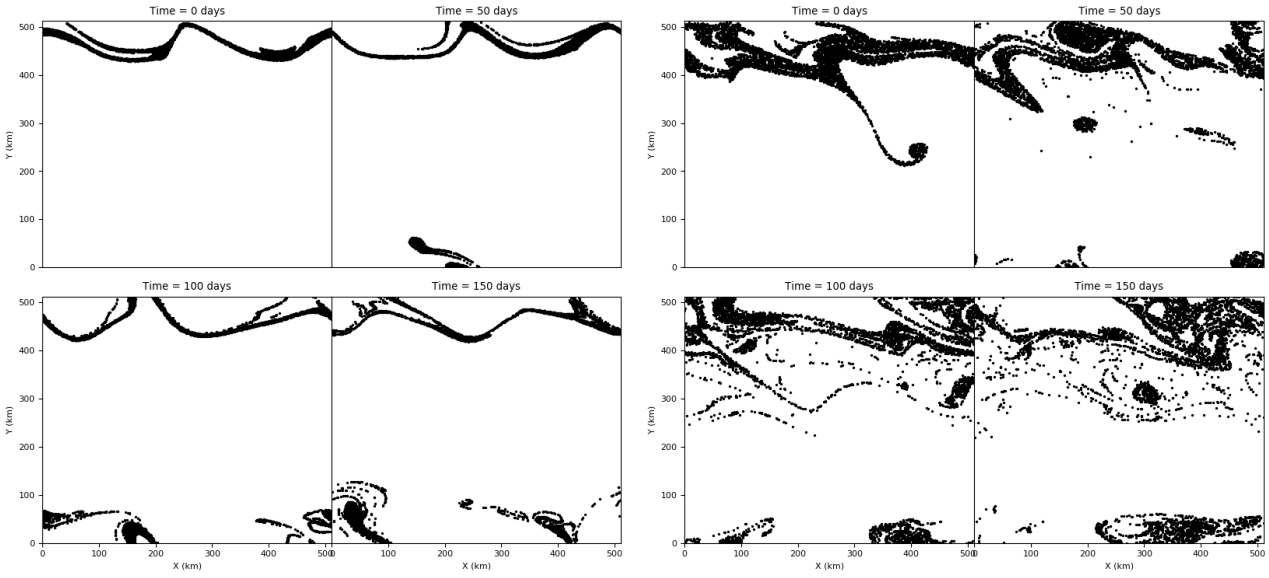

(a) Coherent Jet (b) Latent Jet

Figure 4.16: The same as fig. 4.15 but for particles released in PV bin 9, in the mixing return flow region.

do see a slightly slower initial PV-mapped dispersion growth, which indicates that the particles are not deviating as much from their PV isolines as much as the SPD suggests. That is, they aren't spreading away from the jet core as quickly. Qualitatively, we see a similar behaviour between the two measures, of a rapid increase in dispersion before levelling out, suggesting that particles do quickly deviate from their initial location, both in relation to the flow field and in space. These particles will then enter the surrounding bins 4 and 8. These are the widest bins. Here, we see a noticeably slower growth for PV-mapped dispersion. This implies less mixing in this region and may also shed light on why the dispersion levels out in bins 5-7.

We however see quantitatively and qualitatively different behaviour for the latent jet. Restricting our attention again to the jet core, D_{PV} is comparable to D_y, illustrating that particles are deviating from the PV isoline. We also do not see this initial oscillatory behaviour. This is in contrast to the mixing region where D_{PV} exhibits much slower growth than D_y.

4.4.2 PV-Mapped Lagrangian Autocorrelation Function

Following the same methodology as for the standard dispersion, we calculate the Lagrangian Autocorrelation Function, which is plotted in fig. E.10. The PV-mapped R in both regimes, but particularly in the latent jet, exhibit a rapid decay. They much more closely resemble a δ-function. Significant oscillatory behaviour is seen in the coherent jet, but hardly any is seen in the latent jet. We will discuss the implications this has for the time-scale in section 4.4.3.

4.4.3 PV-Mapped Time Scale

Much like with the standard dispersion, we have two time-scales of interest: the locality time-scale T and the Lagrangian integral time-scale T_L. We fit $R(\tau) \sim e^{-a\tau}$ where $a^{-1} = T_L$ as we see quite a rapid decay in the PV-mapped LACF. The resulting curve and integral time-scale is plotted and displayed with R in fig. E.10. Evidently we see a much smaller ballistic time-scale.

It is worth asking what the actual physical meaning of a PV-mapped LACF actually is, seeing as the PV-mapped Lagrangian velocity will not be a physical velocity.

The second time-scale is the locality time-scale T, plotted in fig. 4.17. This is calculated as a function of the bin width, to account for the varying bin width sizes for the PV-mapped dispersion. As expected, we obtain much sharper minima and maxima for the time-scale, this is particularly exaggerated for the latent jet. We are seeing very rapid exit from the bin around the jet core where the bin is narrow, whereas for the wider bins, the particles may not even leave the bin during the run time of 1000 days. This further illustrates the sharp barrier to transport that the jet core provides, where particles quickly diverge. Furthermore, unlike for the latent jet where there are multiple clear minima and maxima that largely correspond to zonal velocity maxima and minima respectively, the same behaviour is not seen in the latent jet. The PV time-scale further illustrates this. The broad time-scale maximum correspond to a broader jet without return flows.

The PV gradient for the latent jet is marginally larger, and therefore the uniform bins are most likely further smearing the statistics. The time-scale maxima in the mixing region also demonstrate how particles are sticking closer to their PV isolines than the SPD suggests. This can be explained by enhanced PV mixing in the mixing region of the latent jet.

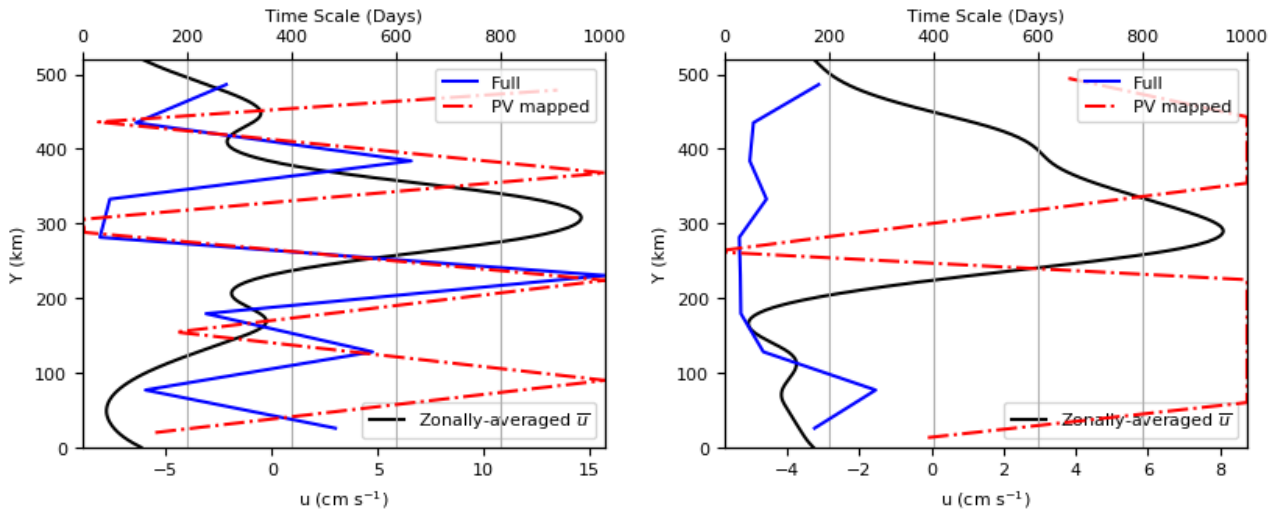

(a) Coherent Jet

(b) Latent Jet

Figure 4.17: PV locality time scale (days) calculated for each PV bin compared with the full meridional top layer time scale for each uniform bin. Calculated the same way as for fig. 4.9. The solid black line is the zonally-averaged time-averaged zonal velocity.

4.4.4 PV-Mapped Power Law Exponent

Fig. 4.18 plots the exponent for PV-mapped dispersion for the two regimes and compares it to the full SPD. We do not see a significant qualitative or quantitative difference between α_y for the two measures, suggesting we still see sub-diffusive spreading. Therefore, the measure that should explain the difference between observed dispersions is the diffusivity. However there are a couple of differences to note. Firstly, a small peak in α_y is seen in the latent jet for the PV Mapped trajectories that more or less lines up with the zonal background velocity maximum. Furthermore, the mixing regions appear to be much more meridionally super-diffusive according the PV Mapped statistics.

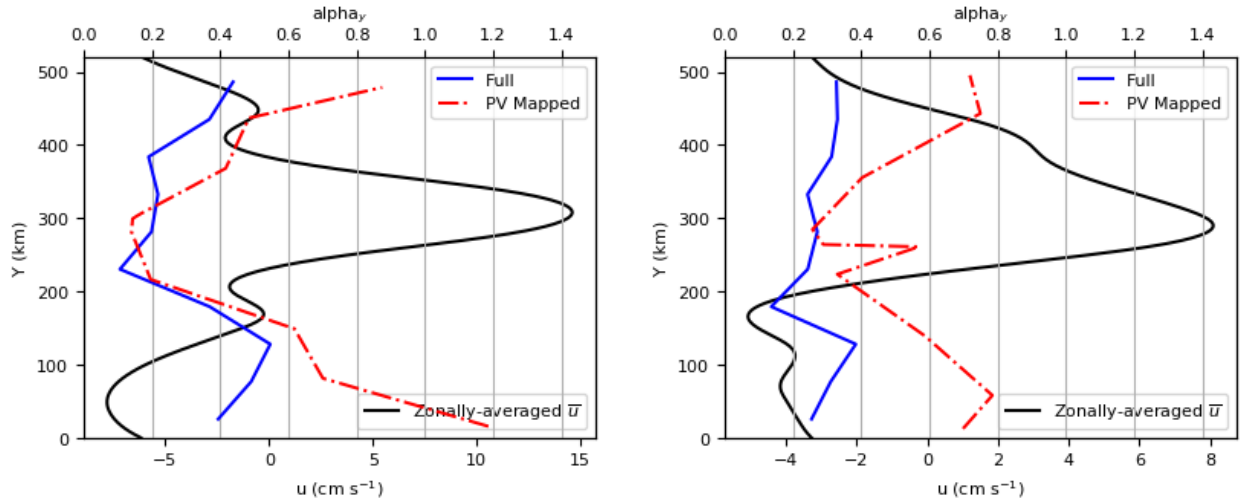

(a) Coherent Jet. (b) Latent Jet.

Figure 4.18: The meridional exponent α_y calculated using the single-particle dispersion for each uniform bin compared with the corresponding PV-mapped α_{PV} for each PV bin. The solid black line is the zonally-averaged time-averaged zonal velocity. α_y is calculated up to the locality time scale.

4.4.5 PV-Mapped Diffusivity Coefficients

We calculate the PV-mapped Diffusivity as

$$K_{PV} = \frac{1}{2}\frac{dD_{PV}}{dt}. \tag{4.20}$$

The results are plotted in fig. 4.19.

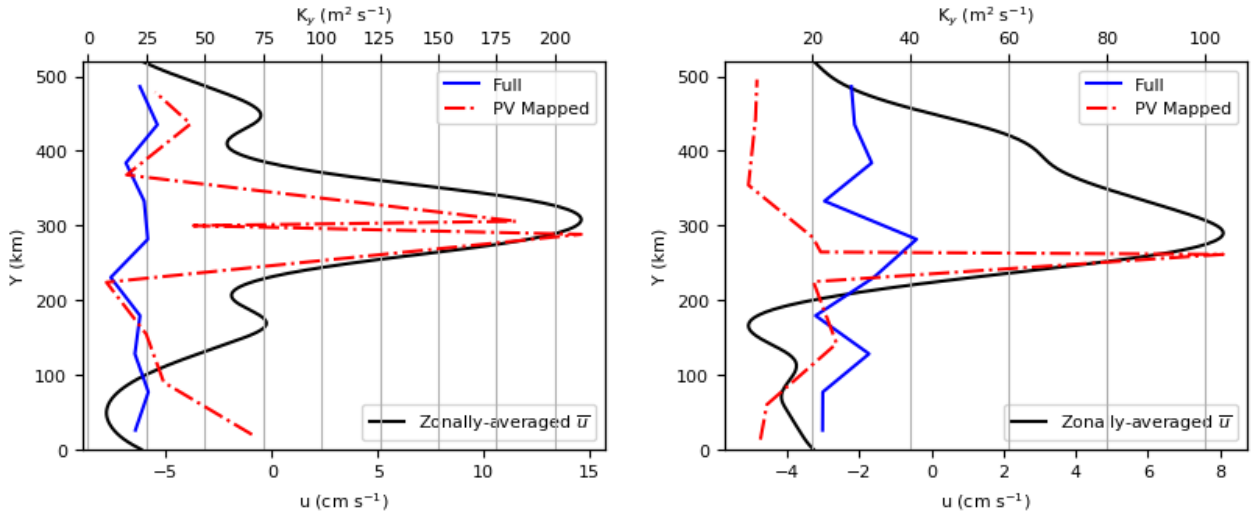

(a) Coherent Jet (b) Latent Jet

Figure 4.19: Comparison of PV-mapped calculated in PV bins and regular full diffusivity calculated in uniform bins (m^2 s^{-1}) for each jet regime.

The PV-mapped diffusivity shows a smaller diffusivity in the mixing regions surrounding the jet, but it does capture the diffusivity of the jet core particularly sharply. It appears that the standard diffusivity measure hardly picks up the jet core at all, as the statistics are smeared. The diffusivity values in the mixing region are much more comparable for the two jet regimes.

We should also note that K_{PV} for the coherent jet is about twice that of the latent jet around the jet core, as indicated from the top x axis. This is quite surprising as the FFE K_y values for the two regimes are more comparable. It suggests that the coherent jet is actually dispersing particles away from their PV isolines more effectively.

4.5 Summary and Conclusion

4.5.1 Standard Lagrangian Statistics

EO vs FFE

Firstly let us compare EO to FFE statistics. FFE trajectories deduct the advection due to mean flow following the full trajectory, whereas EO trajectories are produced by advecting particles by the velocity fluctuation only. It is a more relevant method of calculating Lagrangian statistics

for implementation in a coarse grained OGCM as it considers eddying effects on the full flow, and FFE trajectories explore the same range of the domain as the full trajectory.

Meridional Statistics

We consistently find that meridional EO dispersion and hence diffusivity is larger in the top layer and smaller in the bottom layer than the FFE statistics. This is in agreement with the findings of Kamenkovich et al. (2009), where meridional spreading was found to be greater in the eddy-only simulations in the upper ocean relative to the full Lagrangian simulations. Rypina et al. (2012) suggested that the eddying flow acts to disperse particles away from eddies whereas the mean-flow acts to keep particles in eddies. There is however no coherent jet in the bottom layer and the magnitude of the mean flow is closer to that of the eddying flow. In fact, referring to fig. 2.5b, in the latent jet, the eddying flow is greater than the mean flow. The bottom layer latent diffusivity for EO is quite comparable to the FFE diffusivity, as the mean flow will have less of an impact due to its smaller magnitude.

In the coherent jet however, there is a larger difference between the EO and FFE meridional diffusivities in the bottom layer. The meridional eddy velocity is smaller than that in the bottom layer of the latent jet. Ferrari & Nikurashin (2010) argues that, in the context of the Southern Ocean, the presence of a strong mean flow acts to suppress eddy-diffusivity across the jet. They state that, despite the eddying velocity being greater in the ACC, across-stream diffusivity is smaller. Section 4.2 implies that when the background flow matches the eddy propagation speed, super-diffusion occurs. This is only relevant for FFE trajectories, as EO trajectories do not capture this interplay between the mean flow and the eddy field.

Zonal Statistics

The difference between the zonal EO and FFE statistics is less pronounced. In the top layer, the FFE diffusivity is picking up a slight maximum around the jet core. This implies that the interaction between the eddying field and the mean-flow results in enhanced zonal transport, in agreement with section 4.2.

We also see, as was suggested by previous literature, significant anisotropy and non-diffusivity in our FFE statistics. Zonal dispersion is super-diffusive and meridional dispersion is

sub-diffusive, in both layers and both regimes, as illustrated by fig. 4.10. This is also in agreement with Rypina et al. (2012), where it was found that around the Gulf stream extension, anisotropy was more pronounced for the FFE trajectories. Clearly the diffusive approximation is not appropriate to use to synthetically reproduce our Lagrangian statistics.

Comparison between jet regimes

Another key issue to consider is the difference in Lagrangian transport between the two jet regimes. Fig. 4.9, that plots the locality time-scale for the two regimes, clearly demonstrates the difference. Maxima and minima are much more pronounced in the coherent jet than the latent jet. Particles in the jet core boundary leave the bin incredibly quickly, but remain in the mixing regions for a long period of time. The time-scale in the latent jet is consistently small and there is little variation across the domain. This suggests that particles are mixed much quicker and the jet is not as strong a barrier to transport. If we follow the hypothesis presented by Ferrari & Nikurashin (2010) and in section 4.2, that the interaction between the zonal mean flow and the eddy propagation speed is paramount in controlling transport, we can also conclude that the wider latent jet, lacking pronounced return flows, can also result in more homogeneous Lagrangian statistic profiles.

However, there are some limitations behind linking the results presented in section 4.2 and the Lagrangian statistics of the fully dynamical model. Firstly, the dynamical model clearly has very different zonal and meridional eddy field structures, unlike the kinematic model, where, apart from any variation in wave number, the structure was symmetric, and zonal and meridional velocity profiles were the same. Fig. 2.5b suggests that the meridional velocity can be represented as a row (or more) of propagating eddies that lie on the jet core (or on return flows or secondary jets), where as the zonal velocity still more closely resembles the meandering jet. Meridional EO diffusivity is greater than meridional FFE diffusivity, whereas zonal EO diffusivity is smaller. Furthermore, the FFE zonal transport is super-diffusive, whereas the meridional transport is sub-diffusive, implying there is an asymmetric explanation other than eddy-propagation speeds influencing transport. That is, we cannot rely on the studies presented in Ferrari & Nikurashin (2010) alone. Potentially, it is the presence of large, mostly zonal PV

gradients that also play a pivotal role. The relationship between PV gradients, eddy propagation speed an mean flow is something that could be studied in later work. That being said, FFE diffusivity does still capture the diffusivity suppression on the jet flanks more clearly than EO. It does however still remain to be seen what the explanation behind the difference between the magnitude of EO and FFE diffusivities is. We know that eddy propagation speed and the amplitude of the eddy field will be driving components of EO transport, but what effect do these have on FFE transport?

4.5.2 PV-Mapped Statistics

Though it is worth noting that these conclusions should be taken with a pinch of salt as the jet meander may cross several bins, and a single bin can encompass both mixing regions and barrier regions. We attempt to address statistical smearing by introducing a flow-relative dispersion method, which we refer to as PV-mapped dispersion. It is important to acknowledge certain limitations with the PV-mapped dispersion method.

Firstly, the main limitation is that it relies on finding a one-to-one mapping between the y-coordinate and a flow dependent variable. This is so coordinates can be mapped in both directions with each providing a unique solution. As a result, it is only really appropriate for β-plane models, or similar such models where the Coriolis parameter increases with y. If using a PV coordinate, it can only be used for flows where the PV forms a PV staircase. That is, the PV gradient is sufficiently sharp near the jet and there are mixing regions around it. As a result, we can't introduce a different map for the bottom layer. If we were to employ the PV-mapped technique to the bottom layer, we would have to use the map obtained in the top layer. This could still be a relevant thing to do as we can examine dispersion relative to the jet core which is defined by the PV gradient in the top layer.

Secondly, this method only applies in the meridional direction. Alternatively, if the flow is tilted, the coordinates would need to be diagonalised, but the method could still only be used in one direction. Essentially, this method is applicable for any jet dominated flow where the flow can be diagonalised around the direction of the jet (or jets if the flow consists of alternating

jets e.g. Berloff et al. (2011)).

The two most illustrative statistics of interest in comparing these two methods are the PV-mapped diffusivity and the locality time-scale. The PV-mapped and full locality time-scale are qualitatively similar. There is however marked difference between the two in the latent jet. Where the full locality time-scale didn't really capture much variation across the domain, the PV-mapped time scale indicates very sharp minima at the jet core, and very pronounced maxima on the flanks. This indicates that particles leave the jet core region in the latent jet particularly quickly and are then trapped in the flanks for a significant period of time. It also doesn't appear to exhibit any evidence of multiple jets.

The PV-mapped diffusivity (fig. 4.19) demonstrates a much sharper diffusivity maximum around the jet core for both jet regimes. We do however capture a slight minimum in the jet core surrounded by mixing region maximums in the coherent jet. This suggests that we do see a barrier in the coherent jet. We however do not capture this behaviour for the latent jet, instead we see a narrower maximum. K_{PV} in the latent jet is underestimated relative to K_y away from the jet core. However, we must remember that these bins are not strictly spatial bins, but PV bins. Therefore, the bin allocation of particles relies on the PV at their initial location as opposed to their y coordinate. This is demonstrated by fig. 4.16b. Keeping this in mind, we can infer that away from large PV gradients, particles remain relatively close to their PV isolines. The meridional dispersion that we observe is due to meridionally moving vortices. Particles however are not inclined to stick to the PV isoline at the latent jet core and instead diverge away from it. We cannot, however, conclude whether particles are crossing the jet or are being entrained away from the jet. By calculating two-particle statistics or by counting the number of particles that cross the maximum PV gradient similarly to the method used in Berloff et al. (2002), could provide further insight.

Furthermore, K_{PV} is consistently greater for the coherent jet than the latent jet, despite there being little difference between their FFE K_y values. This implies that particles are leaving their PV isolines more effectively in the coherent jet. Could this be due to the lack of coherent structures away from the jet, so particles are not trapped in regions of more uniform PV?

Chapter 5

Kinematic Models

5.1 Background

Kinematic models have frequently been used in ocean modelling to further understand oceanic processes. Particularly, analytic Rossby waves and jet fields have been used to advect particles. Subsequent cross-jet transport and mixing was analysed. These approaches were not taken with the aim of improving ocean modelling, nor have they been derived directly from ocean data, but they have been used as simple mechanisms for understanding transport processes, such as cross-jet transport.

Samelson & Wiggins (2006) documented several kinematic models used in Lagrangian ocean studies, such as those concerning meandering jets, travelling waves and cellular flows. Western boundary currents, such as the Gulf stream and Kuroshio extension, have been represented in kinematic models as meandering jets surrounded by eddies. Bower (1991) re-constructed a jet in this way. They were able to re-write the stream function in the moving frame allowing them to calculate trajectories relative to the flow field, similar to our PV-mapped dispersion methodology. It was found that cross-stream transport was enhanced with increasing depth, increasing meander amplitude and increasing wave speed. This was a key early kinematic model, meant to represent the Gulf Stream, establishing that the jet core acts a barrier to transport where little cross-stream mixing is seen, whereas enhanced mixing is observed on the jet flanks.

Samelson (1992) furthered this work and found that efficiency of fluid exchange is dependent on the jet meander frequency. They also found that trying to stimulate across jet mixing was quite difficult, as opposed to mixing around the jet in the 'surf regions'.

There have been some attempts to link data-driven kinematic models to Lagrangian transport in an atmospheric setting. Pierrehumbert (1991) introduced kinematic Rossby waves to help identify atmospheric transport barriers and verified the existence of potential vorticity barriers. It was also established that tracers released in a chaotic region in a two-dimensional flow will eventually become uniformly distributed. Kinematic models have also been applied to the stratospheric polar vortex by García-Garrido et al. (2017). Their aim was to capture the break up of the polar vortex, associated with stratospheric sudden warming. The flow field was decomposed into Fourier components, which were then reproduced analytically. The resulting kinematic model consisted of planetary waves superimposed on a background mean flow, which we will see is rather similar to our kinematic flow field.

Kinematic models have already been explored for use as parameterisations in ocean models. For example, Lacorata et al. (2014) constructed an analytic stream function as a lattice of cells in order to generate chaotic Lagrangian trajectories, and capture pair dispersion. This was used as a parameterisation method for sub-grid scale Lagrangian transport in the Mediterranean sea.

The link however has not been made between a data-driven kinematic model and oceanic Lagrangian transport. This is what we attempt to do in this chapter. We will take a similar approach to García-Garrido et al. (2017), in that we will decompose the flow into a series of dominant patterns which can then be synthetically reproduced. Though instead of Fourier analysis, we will de-construct the flow field into its dominant empirical orthogonal functions (EOFs) using principal component analysis and examine the contribution these EOFs make in driving Lagrangian transport.

5.2 Empirical Orthogonal Functions

Empirical orthogonal function (EOF) analysis is a statistical tool commonly used in oceanography and meteorology as a way of decomposing a time series into orthogonal variations. It

essentially decomposes a flow into independent spatial patterns, which can be ranked according to how much each pattern contributes to the flow variation. This allows us to reduce the complexity of the field. It has often been applied to sea surface temperature anomalies to identify modes or signatures such as El Niño (Roundy 2015). However, they have not yet been used to derive kinematic models or study Lagrangian transport.

The stream function anomaly, $\psi(\mathbf{x}, t)$ is stored at $N_x \times N_y = N$ spatial grid points at N_t times. Expressing ψ as a decomposition of orthogonal spatial modes gives:

$$\psi(\mathbf{x}_i, t_j) = \sum_{m=1}^{M} \alpha_m(t_j) e_m(\mathbf{x}_i), i = 1, \cdots, N, j = 1, \cdots, N_t,$$

where M is the number of modes, $e_m(\mathbf{x_i})$ are the orthogonal EOFs and $\alpha_m(t_j)$ represent the scalar contribution of the corresponding EOF. The spatial covariance matrix is defined as

$$C_{ij} = \frac{1}{N_t} \sum_{n=1}^{N_t} \psi(\mathbf{x}_i, t_n)\psi(\mathbf{x}_j, t_n), \tag{5.1}$$

where C is an $N \times N$ matrix. However, as $N = N_x \times N_y = 512 \times 512$, this would result in a covariance matrix too large to be stored and calculated. Therefore, we reduce the grid size to 128×128. Once the EOFs are calculated, they are then spatially interpolated to return the approximate EOFs on the 512×512 grid.

EOFs are the eigenvalues of the covariance matrix. We retain the principal components $\alpha_m(t_j)$, which indicate the amplitude of the EOF contribution at each time step, as follows:

$$\alpha_m(t_n) = \sum_{i=1}^{N} \psi(\mathbf{x}_i, t_n) e_m(\mathbf{x_i}). \tag{5.2}$$

The resulting EOFs are plotted in fig. 5.1 for the coherent jet and fig. 5.2 for the latent. The corresponding principal components are plotted in fig. 5.3.

The EOFs can be categorised as several distinct patterns:

- zonal bands (modes 5 and 6 for the coherent jet, or 1 and 4 for the latent jet), these will be referred to as 'zonal',

- alternating zonal jets, (modes 9 and 10 for both regimes), these will be referred to as 'altZonal',
- Rossby waves, (modes 1 and 2, 3 and 4 for the coherent jet, and 2 and 3, 7 and 8 for the latent jet). Rossby waves come in two patterns, those consisting of a wavelength the width of the domain, and those with a wavelength of half the domain. We will refer to these respectively as rossby and rossbyHalf.
- and oscillations (modes 7 and 8 for the coherent jet, and 5 and 6 for the latent jet). These will be referred to simply as oscillations.

Rossby waves come in pairs of EOF modes which represent a single row of alternating eddies. They can have different spatial and temporal periods associated with them. Similarly, oscillations are multiple rows of alternating eddies forming a lattice.

Fig. 5.4 plots the contribution of the first 20 EOFs to the total flow variance. We can see that the first 10 EOFs contribute over 90% of the flow variance in both parameter regimes. However, we must ask whether they contribute as much to Lagrangian statistics.

The first 10 EOFs for each regime are qualitatively similar, in that they both feature the above patterns, but appear in different orders of significance. One of note is the zonal jet, it appears that the zonal jet is much more dominant in the latent jet. We will examine if this has any influence on zonal dispersion.

The latent jet EOFs also demonstrate some variability away from the jet. That is, the full length Rossby wave EOFs exhibit some flow variability in the mixing region, and they are not quite aligned with the jet core, or with the half Rossby waves. Conversely, in the coherent jet, the Rossby waves and half Rossby waves are aligned with each other and are both aligned with the jet core. Oscillations also account for a greater proportion of the flow variability in the latent jet. Does the misalignment of Rossby waves result in the break of the meandering jet? We should also note modes 9 and 10, which appear to be alternating zonal jets. Do they explain the multiple minima and maxima observed in chapter 4, in particular, in the locality time-scale?

What can the principal components (PCs), plotted in fig. 5.3, tell us about the time variability of the EOFs? The rossbyHalf waves are clearly associated with high frequency variability. The full Rossby waves have a lower frequency. These can largely be thought of a small-scale variabilities present in oceanic mesoscale eddies. The average variation in amplitude varies relatively little. Therefore, as we average the statistics in time over multiple releases, the effect of the average temporal variability of EOFs won't be present. The oscillatory and largely zonal EOFs however have lower frequencies and temporal variability.

The structure and order of importance of EOFs in explaining flow variability already raise some important questions. However, first, we must examine the relationship between EOFs and Lagrangian transport.

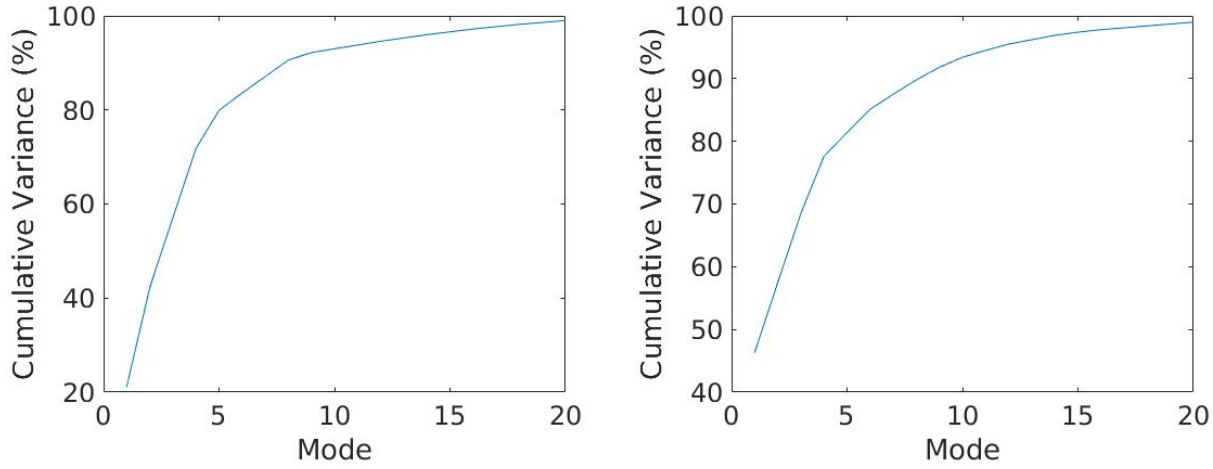

(a) Coherent Jet.

(b) Latent Jet.

Figure 5.4: Contribution of the first 20 EOFs to the stream function variance. The first 10 Modes account for about 90% of the flow variance.

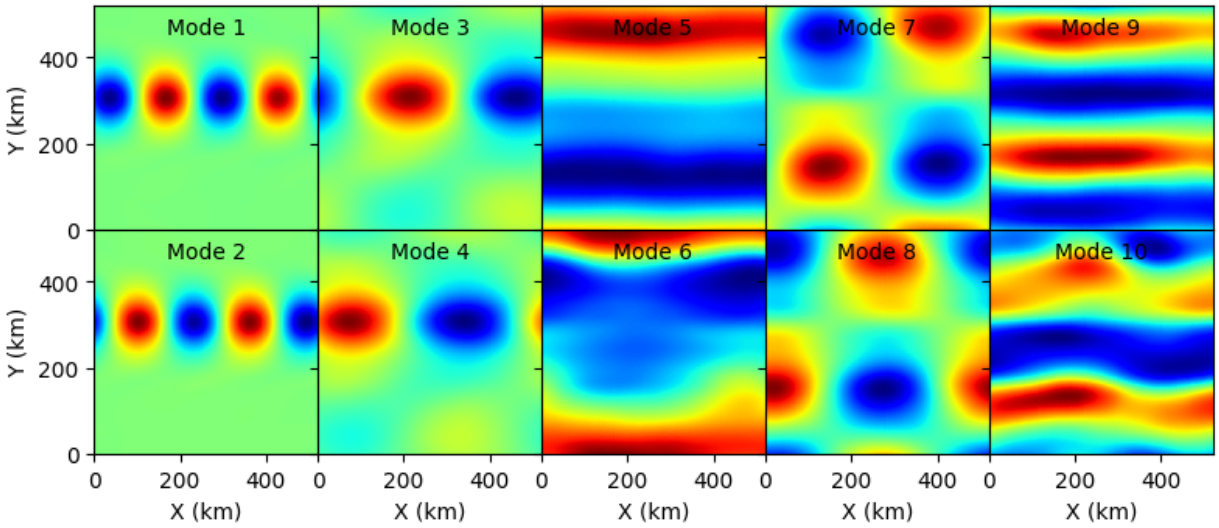

(a) Top Layer

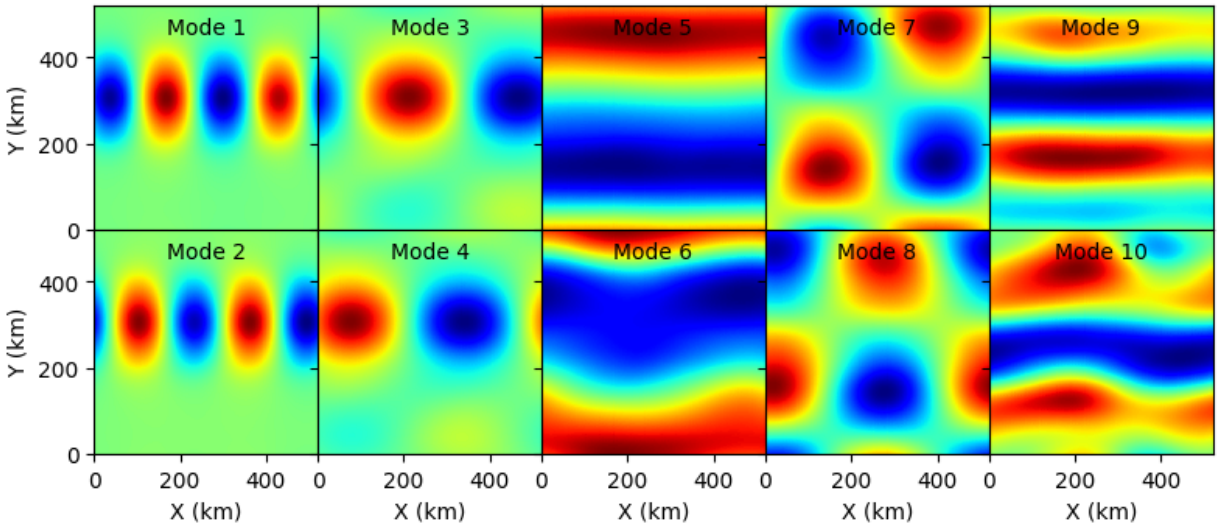

(b) Bottom Layer

Figure 5.1: The first 10 joint EOFs and their PCs for the coherent jet. Modes 1 and 2 makes up a Rossby wave with a wavelength half that of the domain, and modes 3 and 4 make up a Rossby wave with a wavelength the whole width of the domain. Modes 5 and 6 are zonal flows, modes 7 and 8 and oscillations and modes 9 and 10 are alternating zonal jets.

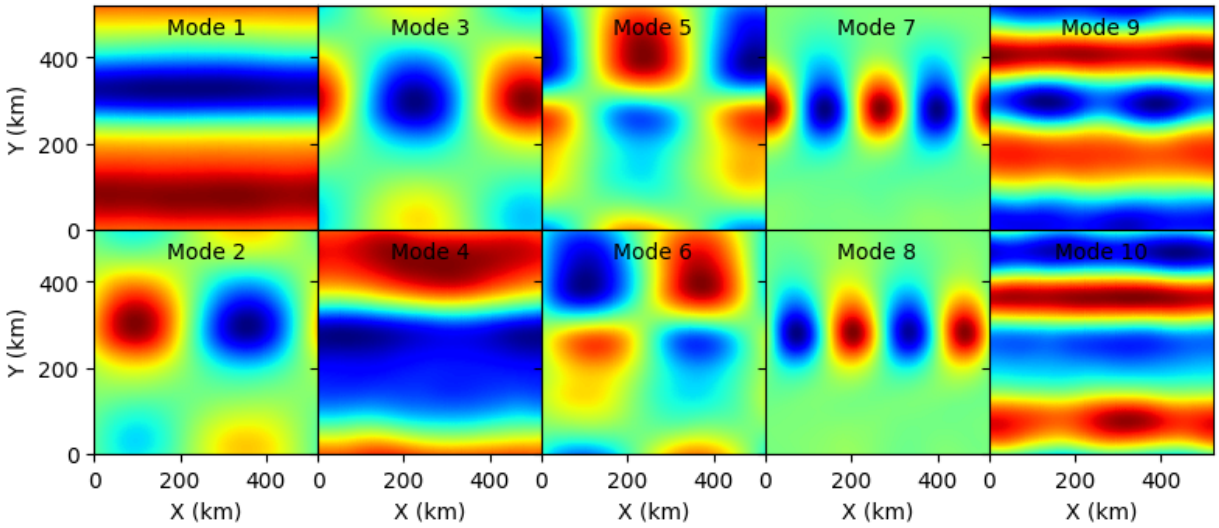

(a) Top Layer

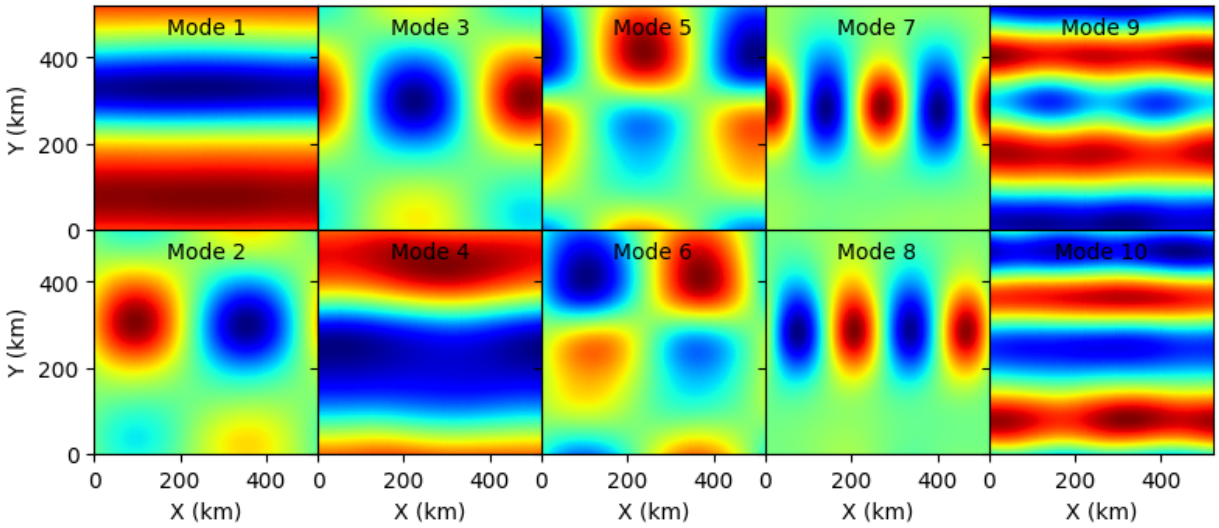

(b) Bottom Layer

Figure 5.2: The first 10 joint EOFs and their PCs for the latent jet. Can categorise patterns similarly to the coherent jet. Modes 7 and 8 are half length Rossby waves, modes 2 and 3 are full length Rossby waves, Modes 1 and 4 are zonal, modes 5 and 6 are oscillations, modes 9 and 10 are alternating zonal jets.

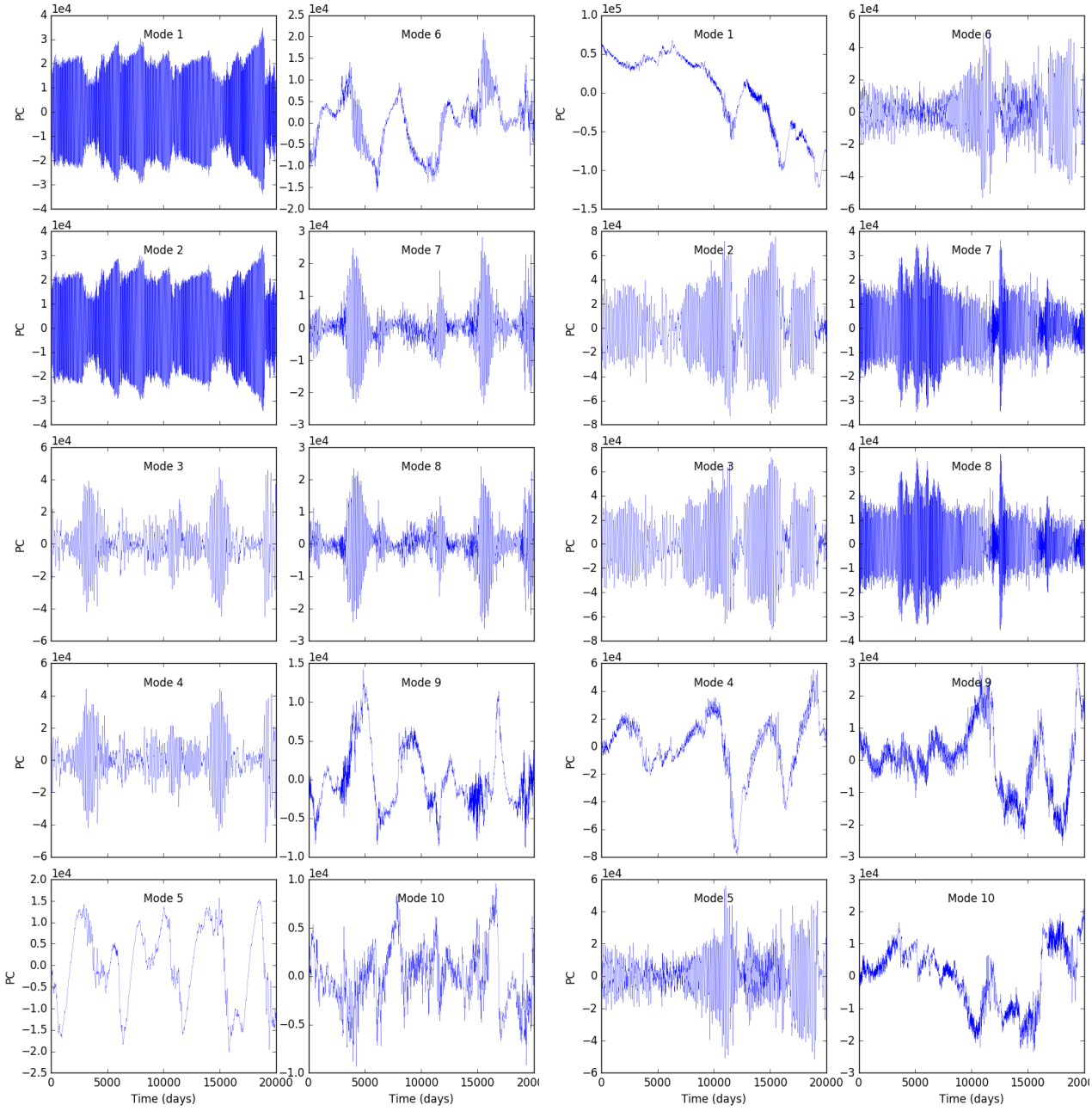

(a) Coherent Jet (b) Latent Jet

Figure 5.3: Joint layer Principal Components for the two jet regimes corresponding to the EOFs in figs. 5.1 and 5.2.

5.2.1 How Many EOFs do we Need to Capture Lagrangian Dispersion?

As Lagrangian transport is highly non-linear, just because the first 20 EOFs account for almost all of the flow variance, it does not mean that they will account for almost all of the Lagrangian transport, so we need to establish whether it is possible to capture the important Lagrangian dispersion behaviour using a finite number of EOF. Fig. 5.5 compares the EO SPD with the SPD of particles advected by the first 10 EOF modes and the first 20 EOF modes for the coherent and latent jets for bins 2 and 5. Figures for all 10 bins are included in appendix F. We compare the EOF trajectories with the EO trajectories as the EOFs represent the eddying field as they are constructed from the stream function anomaly.

Across the domain, particularly in the bottom layer, zonal spreading is captured very well by the first 10 EOFs and we gain very little by increasing the number of EOFs to 20. We also see similar patterns in both the coherent and latent jets. In particular, fig. 5.6 demonstrates that EOFs 1-10 underestimate zonal spreading around the zonal jet and the return flows, and overestimate zonal spreading elsewhere. By adding an additional 10 EOFs, we don't see a much more accurate zonal dispersion in the latent jet, though there is a slight improvement seen in the coherent jet.

The story is very different for the meridional direction. Increasing the number of EOFs from 10 to 20 does demonstrate a marked difference in the meridional spreading. Meridional dispersion is almost always underestimated. This implies that small-scale variabilities play an important role in enhancing meridional spreading, but less so for zonal spreading. This leads us to treat the two directions separately. But firstly, let's try to establish the role of different EOF patterns in Lagrangian spreading.

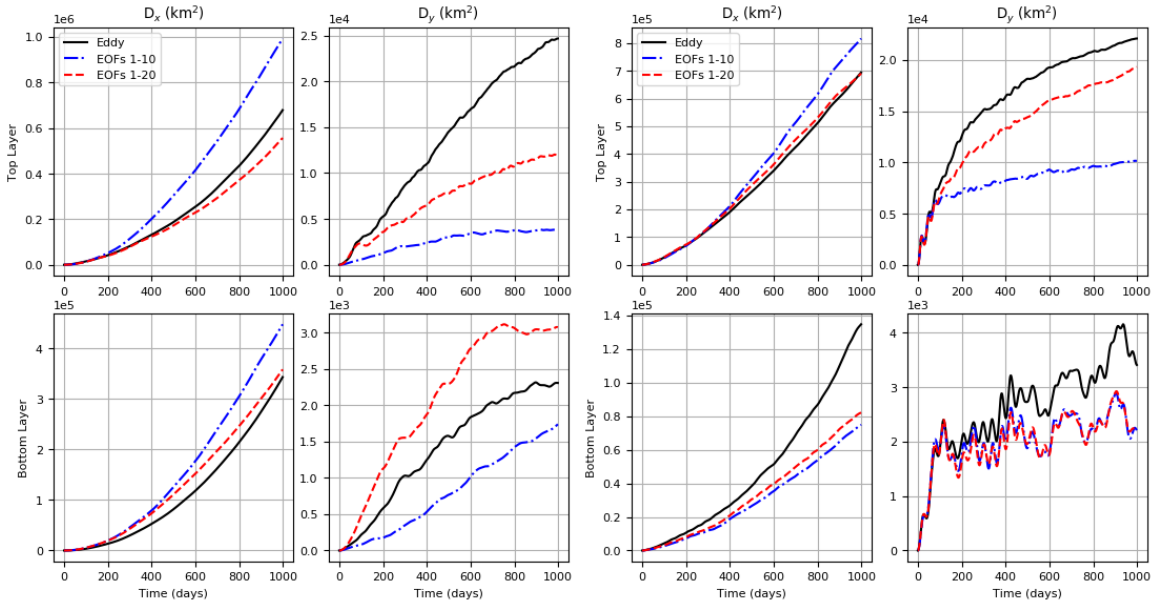

(a) Bin 2 - Coherent Jet

(b) Bin 5 - Coherent Jet

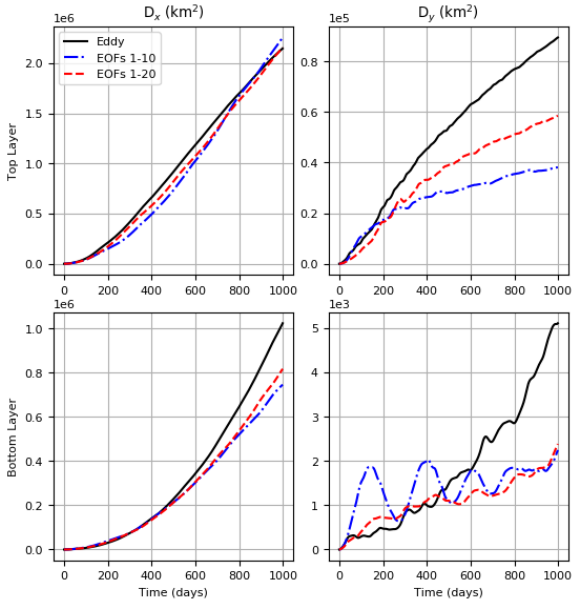

(c) Bin 2 - Latent Jet

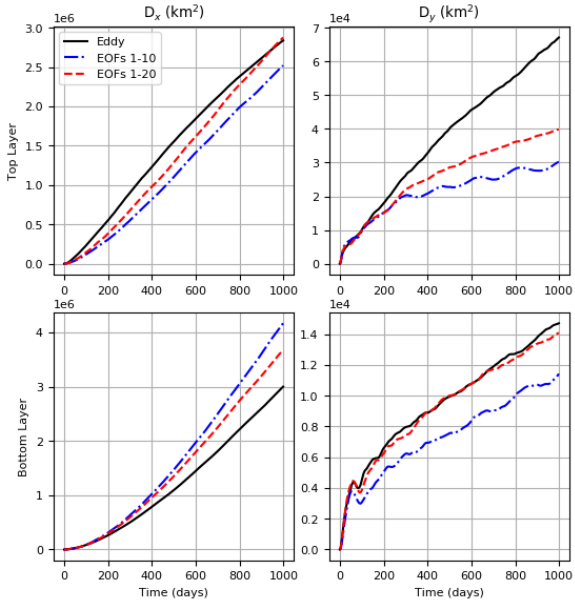

(d) Bin 5 - Latent Jet

Figure 5.5: Single-Particle Dispersion (km^2) against time (days) for each bin for different numbers of EOFs for the two jets.

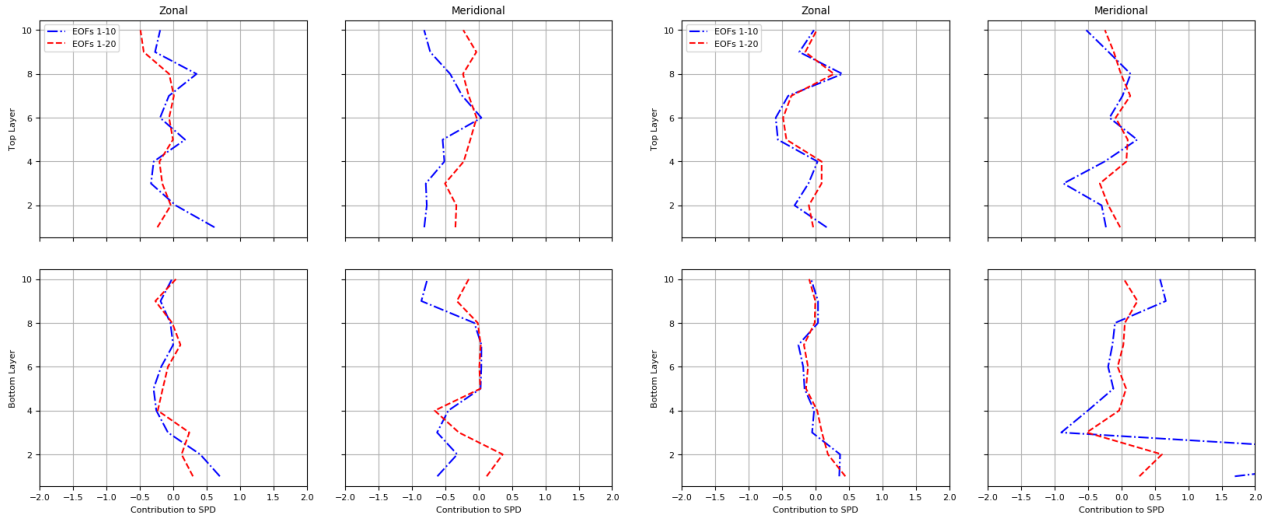

(a) Coherent Jet (b) Latent Jet

Figure 5.6: Compares fractional difference of the SPD of different EOF fields to the EO SPD at the time-scale. Meridional transport is more poorly captured in the mixing regions. Zonal transport is under estimated in the jet core and over estimated in the mixing regions.

5.2.2 Deducing the Role of EOF Patterns in Lagrangian Dispersion.

Pairs of EOF modes, as described previously, are deducted from the full stream function to construct a new field. Particles are then advected using the FFE methodology. Fig. 5.7 plots the resulting SPD for the different constructed fields for bins 2 and 5. Figures for all bins can be found in appendix F.

The pair of EOF modes 1-2 for the coherent jet, which resemble a Rossby wave with a wavelength of half the domain, seem to account for a significant portion of the zonal and meridional dispersion. By deducting these EOFs, we see a reduction in zonal dispersion, implying that these EOFs act to enhance zonal dispersion. In this section we investigate the reasons behind this.

However, it is important to note that the corresponding EOF pair for the latent jet, EOF modes 7 and 8, not only are much less dominant modes accounting for less of the flow field variance, but also account for little of the particle dispersion. For the latent jet, EOF modes 1 and 4, the zonal structures, are much more important. Furthermore, EOF modes 7 and 8 for the latent jet appear much more smeared than EOF modes 1 and 2 for the coherent jet.

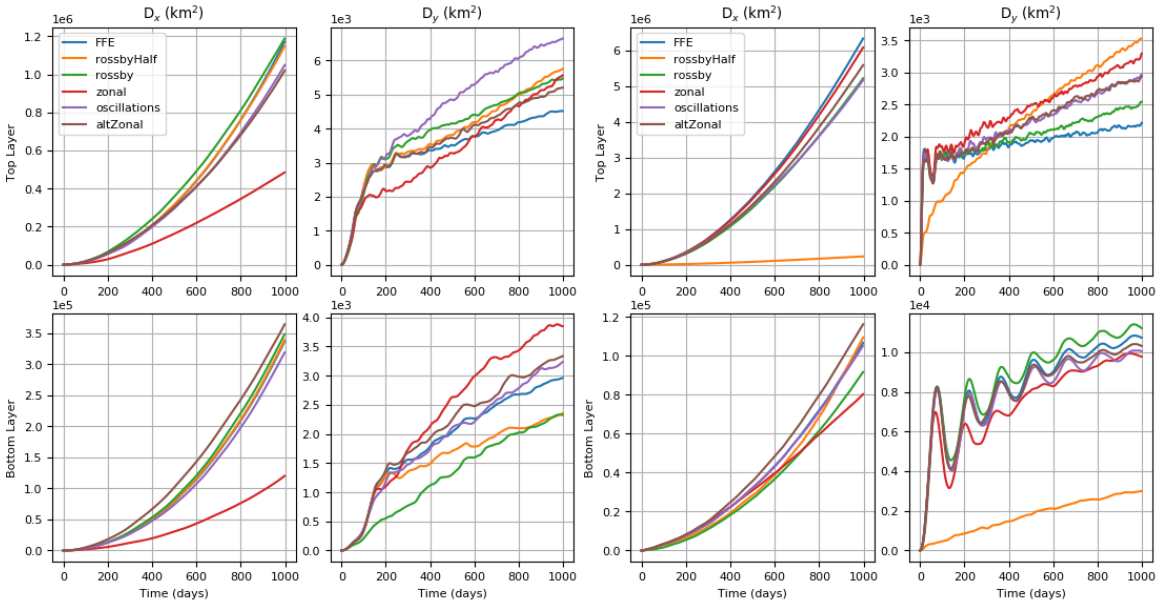

(a) Bin 2 - Coherent Jet

(b) Bin 5 - Coherent Jet

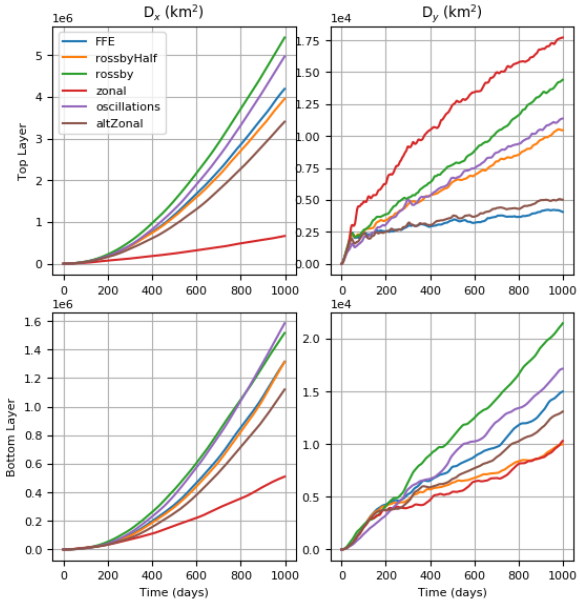

(c) Bin 2 - Latent Jet

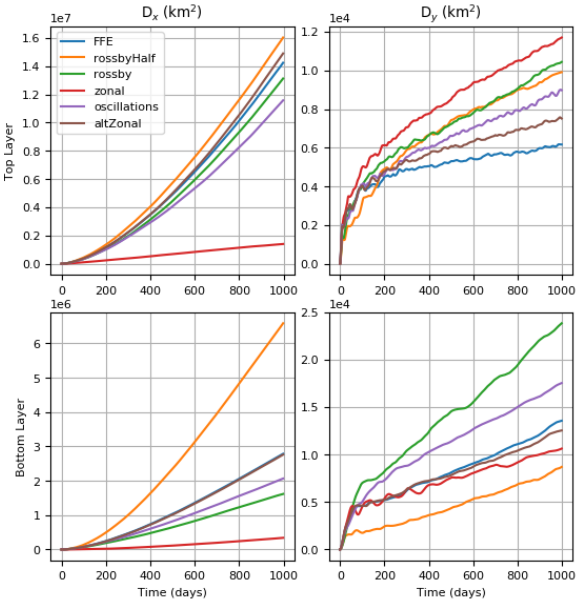

(d) Bin 5 - Latent Jet

Figure 5.7: Single-Particle Dispersion (km^2) against time (days) for each bin where different EOF pairs are deducted from the full field in the two jets.

5.2.3 Investigating the Role of Half-Wavelength Rossby Waves

It has been suggested that enhanced zonal dispersion is driven by the interaction between zonal transient eddies and the zonal time-mean flow (Ferrari & Nikurashin 2010, Naveira Garabato et al. 2011).

The pair of RossbyHalf EOFs have a period of 48 days in the coherent jet and 44 in the

latent jet; that is, the time it takes to travel a full wavelength of 260km. So in the coherent jet we have a propagation speed of roughly 6.3cms^{-1}, and in the latent jet, of 6.8cms^{-1}. How can we relate this to the arguments posed in Ferrari & Nikurashin (2010)? We include the averaged zonal velocities for each bin, layer and regime in figs. 5.8 and 5.9 for easier reference.

Firstly, whereas deducting the rossbyHalf EOFs in the coherent jet results in sub-diffusive dispersion, and results in a slower dispersion, this is not the case in the latent jet. In fact, in bins 4, 5, 6, 7 and 8 removing rossbyHalf waves act to reduce the zonal dispersion in the top layer for the coherent jet, in the latent jet there is a much smaller reduction in dispersion. The maximum background zonal velocity is much closer to the eddy propagation speed, and hence the average zonal velocity will be much smaller, and smaller than the eddy propagation speed, particular across the region which the EOFs occupy. This smaller difference in dispersion can be explained using the arguments posed in chapter 4 which say that zonal dispersion is maximised when the average back-ground zonal velocity agrees with the eddy propagation speed.

In the bottom layer however, where the propagation speed is greater than the background zonal velocity, the zonal dispersion is enhanced when deducting the rossbyHalf waves, particularly bins 7 and 8 in the latent jet. In bins 7 and 8, the rossbyHalf waves still have a significant amplitude and hence contribution to the flow field, but if we refer to fig. 5.9, the background zonal velocity is much smaller than the eddy propagation speed. In chapter 4, when the eddy propagation speed and background zonal velocity don't agree, we see sub-diffusive behaviour, and so in this case, it would make sense that removing the rossbyHalf waves would increase dispersion instead, as this sub-diffusive effect would be removed. The converse it true when the velocities match.

It is, however difficult to draw the same conclusions for the meridional dispersion. For the coherent jet, it is true that meridional dispersion appears reduced in both top and bottom layers by deducting the rossbyHalf waves, and that this behaviour is less apparent in the latent jet, in both layers. However, even though the background zonal velocity in the bottom layer is much smaller than in the top layer for the coherent jet, the reduction in dispersion is far greater, despite it being of a similar magnitude to the background zonal velocity in the top layer of the latent jet, where this reduction is meridional dispersion is not seen.

Bin	Average zonal velocity (cms^{-1})	
	Top Layer	**Bottom Layer**
1	-7.28	-4.22
2	-7.06	-4.19
3	-3.30	-2.75
4	-0.93	-1.26
5	1.03	2.00
6	12.07	6.88
7	10.60	6.37
8	-0.24	1.37
9	-1.04	-1.33
10	-3.80	-2.85

Figure 5.8: Average zonal velocity for each bin in the coherent jet.

Bin	Average zonal velocity (cms^{-1})	
	Top Layer	**Bottom Layer**
1	-3.66	-1.37
2	-4.04	-2.82
3	-4.15	-3.00
4	-4.39	-2.05
5	1.74	1.37
6	7.60	4.21
7	5.62	3.78
8	3.16	2.02
9	0.64	0.28
10	-2.50	-1.43

Figure 5.9: Average zonal velocity for each bin in the latent jet.

We therefore hypothesise that the relationship between background zonal velocity and eddy propagation cannot be the only phenomena controlling Lagrangian transport.

5.2.4 Investigating the role of full-wavelength Rossby waves

Using the same method as for the half-wavelength Rossby waves, we calculate the periods of the full-wavelength Rossby waves to be 166 days for the coherent jet, and 165 days for the latent jet. With a wavelength of 520 km (the size of the domain), this gives a propagation speed of 3.63 cm s^{-1} and 3.65 cm s^{-1} for the coherent and latent jets respectively. Therefore, this EOF pair are propagating at approximately half the speed of the half-wavelength Rossby waves.

This EOF pair have very little impact on dispersion in the coherent jet. In the top layer of the latent jet, there isn't a significant amount of difference between the effects of the RossbyHalf

and Rossby EOF pairs. We do see a small amount of zonal dispersion reduction in the bottom layer of the latent jet when removing the Rossby wave EOFs, similar to the effect of the rossbyHalf EOFs, but to a smaller degree. We found in chapter 4, reducing the wavenumber results in similar behaviours, but a smaller dispersion rate. Meridionally, however, we see enhancement of dispersion. And so, yet again, the arguments given in Ferrari & Nikurashin (2010) are not enough to explain the observed behaviours.

5.3 An EOF inspired kinematic model

5.3.1 Re-constructing the half-wavelength Rossby waves

We can now construct an analytic kinematic stream function that is derived from our EOFs that can aptly represent the corresponding parameter regimes. Following the methodology of Rypina et al. (2007), we can analytically represent a propagating Rossby wave as follows:

$$\psi(x, y, t) = \mathrm{A}\mathrm{sech}^2\left(\frac{y - y_c}{L}\right)\cos\left[k(x - ct)\right], \tag{5.3}$$

where A is the amplitude, L is some length scale that captures the width of the Rossby wave, y_c is the centre of the Rossby wave, k is the wavenumber and c is the propagation speed. We find different values for the above parameters for the top and bottom layers. We do not include the variation of the principal components in this kinematic model, as we expect the effect of the EOF variation over longer time scales to be negligible once we average particle statistics over several time releases.

We then compare the single-particle dispersion for the resulting kinematic model with the FFE dispersion in 5.10 for bins 2 and 5. The single particle dispersion for all 10 bins can be found in appendix F.

As expected, away from the jet core, the Rossby Half waves don't contribute to the SPD as the flow field is negligible. For the coherent jet, the Rossby Half wave accounts for most of the zonal spreading in both the top and bottom layers. Adding the zonal EOF has little

effect. This is in contrast to the latent jet, where, adding the zonal background flow does have a significant effect. In fact, in bins 4-8, we get very close to retrieving the FFE SPD with our kinematic model, which includes the zonal EOF along with the RossbyHalf wave.

In the top layer, the RossbyHalf wave also manages to capture the initial ballistic dispersion around the jet core before the dispersion curve levels out. As the wave only covers a small area of the domain, if particles leave this area, they will not be advected at all; if they remain in the jet core region, the particles will oscillate meridionally due to the wave structure.

This result isn't too surprising as the zonal EOF accounts for the greatest proportion of flow variability in the latent jet and the Rossby half waves are actually only the 7th and 8th most dominant modes, as opposed to the coherent jet where the Rossby half wave were the most dominant modes. So this suggests there is some relation between the dominance of EOFs in accounting for flow variability and for Lagrangian spreading.

Now we ask, what is the mechanism that drives this enhanced zonal spreading?

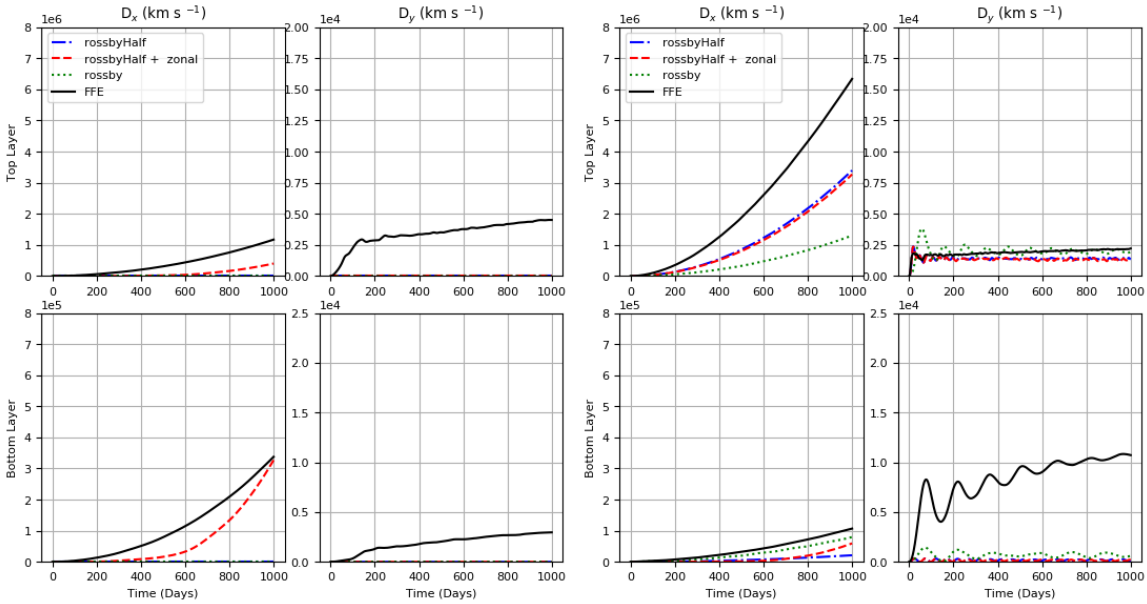

(a) Bin 2 - Coherent Jet

(b) Bin 5 - Coherent Jet

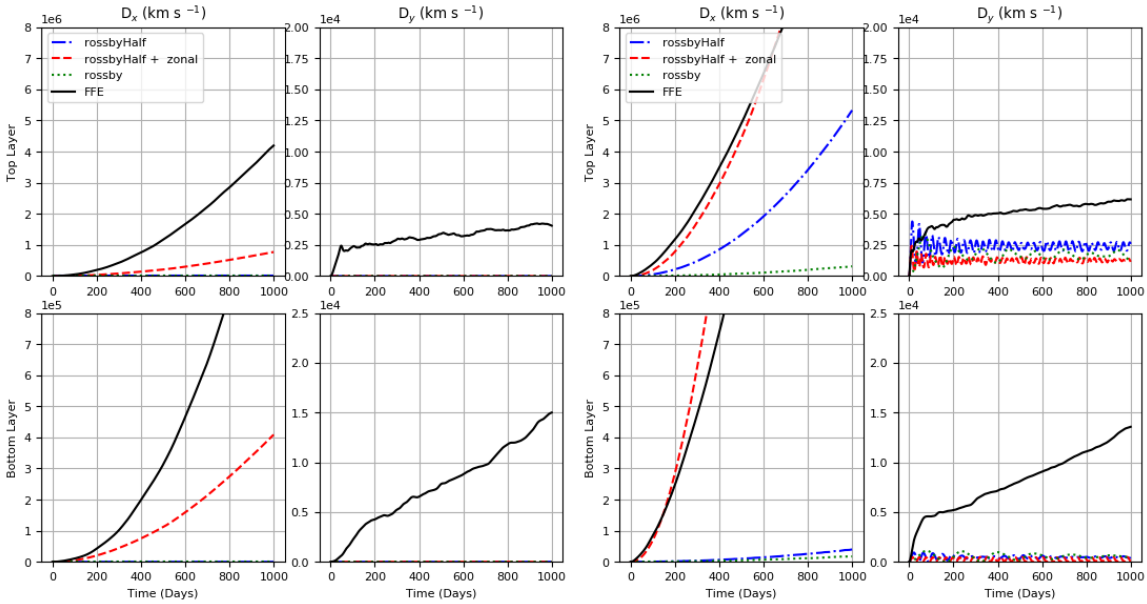

(c) Bin 2 - Latent Jet

(d) Bin 5 - Latent Jet

Figure 5.10: Comparing the single-particle dispersion (km^2) against time (days) for each bin for the kinematic field with and without the background flow for the two jets.

5.3.2 Investigating the role of the propagation speed of the kinematic model

Now we have an analytic expression for the Rossby half length waves, we can study the impact of the relationship between propagation speed and dispersion. We use a similar approach to

that carried out in chapter 4, but instead of the background flow being Gaussian or uniform, we consider the FFE trajectories of the kinematic model defined in eq. (5.3) with a time-mean flow of the dynamical model and the background zonal velocity of 6 cms $^{-1}$. The SPD in bin 6 for the two regimes is plotted in fig. 5.11. We show bin 6 as it is the bin with the maximal time mean zonal velocity, and hence is considered to be the location of the jet core. We also include the FFE SPD for the kinematic model of the Rossby half waves for the top layer coherent jet without the time-mean flow for comparison in fig. 5.12.

Fig. 5.12 and fig. 5.11a are exactly the same, demonstrating that the time mean does not have an impact on the zonal or meridional phase speed, and so we cannot rely alone on the arguments presented in Ferrari & Nikurashin (2010). We don't include the SPD figures for the other bins for clarity, but the SPD for experiments with and without the time-mean jet are exactly the same as each other for the other bins as well.

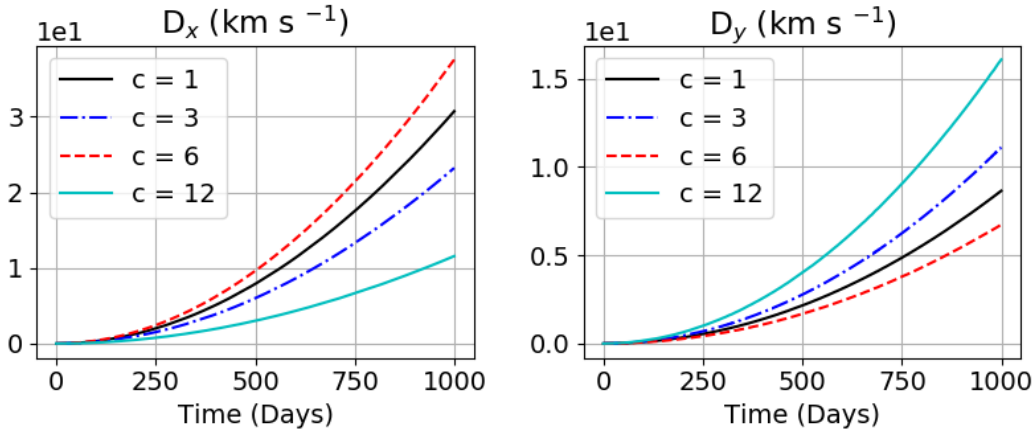

(a) Coherent Jet

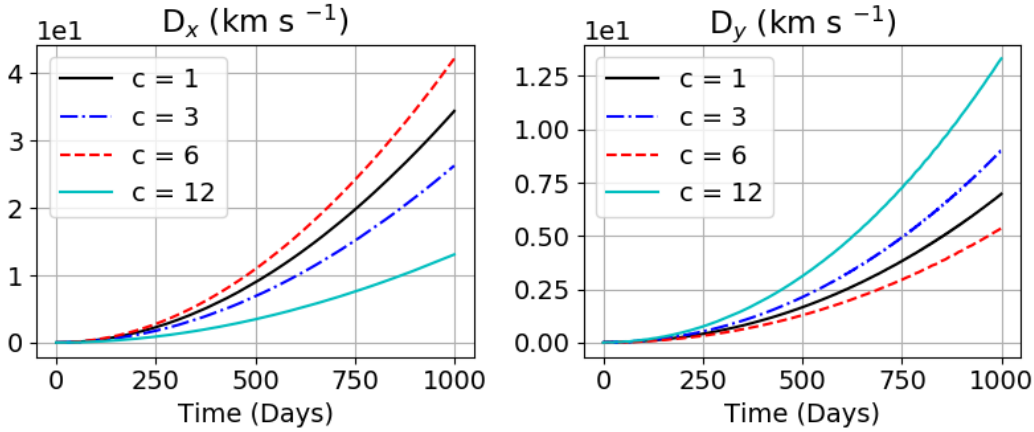

(b) Latent Jet

Figure 5.11: FFE SPD (km s^{-1}) for the analytic Rossby half waves and the time-mean dynamical streamfunction in bin 6 in the top layer for the two parameter regimes. The eddy propagation speeds c are in cms^{-1}

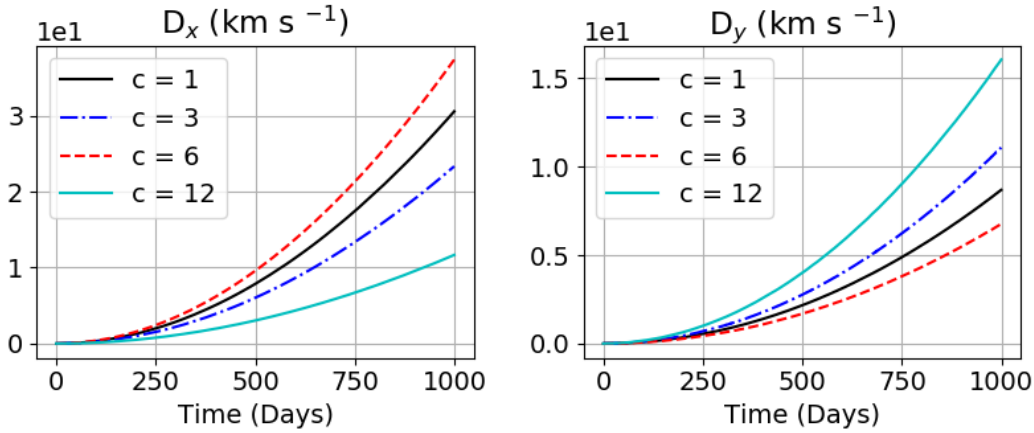

Figure 5.12: FFE SPD (km s^{-1}) for the analytic Rossby half wave and time-mean stream function (without the background zonal velocity) in bin 6 in the top layer for the coherent jet.

As the relationship between dispersion and eddy propagation speed is not monotonic, it

implies there may be a critical eddy propagation speed for which dispersion is maximised or minimised. We investigate for an eddy propagation speed of 4.5cms^{-1}. We choose this value as zonal dispersion for $c = 1.5$cms^{-1} is greater than that for $c = 3$cms^{-1}, and zonal dispersion for $c = 6$cms^{-1} is greater than that for $c = 12$cms^{-1}, implying that a critical point lies between $c = 3$ and $c = 6$cms^{-1}. We plot the FFE SPD dispersion for the field consisting of the coherent regime Rossby half waves, background zonal velocity and time-mean field in fig. 5.13, and we see that zonal dispersion is enhanced and meridional dispersion is minimised for $c = 4.5$cms^{-1}.

This does not follow the theory of Ferrari & Nikurashin (2010), as there is a critical value that suppresses cross-jet mixing as opposed to enhancing it. Where c is the same as the uniform background flow field, cross-jet diffusivity is enhanced. In fact, sub-diffusive behaviour is observed, much like when c does not equate the background flow, as observed in chapter 4. Zonal dispersion however is maximised, displaying the opposite behaviour.

The two differences between the EOF derived kinematic model derived in this chapter and the Ferrari inspired kinematic model of chapter 4 are the lack of a meridional wave number and that the background flow is the actual time-mean of the jet. Therefore, as long as there is a zonal (or meridional) wavenumber, we will see zonal (or meridional) dispersion enhancement. However, the question that remains to be answered, is what is the relationship between the critical eddy propagation speed of roughly $c = 4.5$cms^{-1} and the other model parameters?

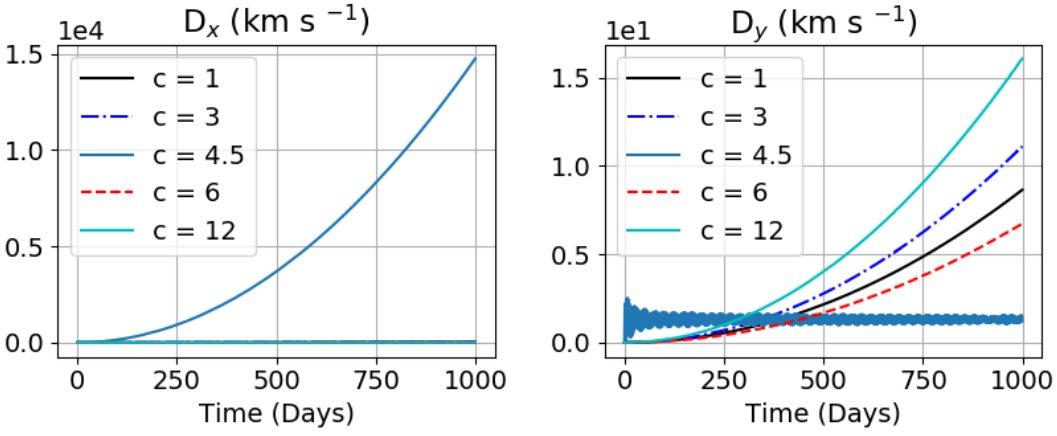

Figure 5.13: FFE SPD (km s^{-1}) for the analytic Rossby half waves, the time-mean dynamical streamfunction and background zonal velocity in bin 6 in the top layer. The eddy propagation speeds c are in cms^{-1}. Illustrates how $c = 4.5$cms^{-1} represents a critical speed.

5.3.3 Investigating the role of eddy amplitude of the kinematic model

We compare the zonal FFE SPD for different eddy amplitudes and propagation speeds in fig. 5.14 for a selection of bins. We do not include the critical eddy propagation speed found in the previous sections so we can more clearly examine the effect of the eddy amplitude without the figures being dominated by the critical value of c. However. we find that $c = 4.5\text{cms}^{-1}$ is a critical eddy propagation speed for the amplitudes investigated in this section. We do not include the meridional dispersion as the qualitative behaviour is the same for all amplitudes. $A = 526\text{s}^{-1}$ is the amplitude used for the top layer coherent jet. Increasing the eddy amplitude appears to effectively broaden the jet, with the FFE SPD dispersion for bin 3 for amplitudes of 526 and 1000 for closely resembling that for bin 5 for amplitudes of 50 and 100. It however does not change the qualitative relationship of the propagation speed. However, the relationship between eddy propagation speed and dispersion is reversed either side of the jet, in the so called surf regions. Furthermore, it does appear that the on the jet flanks, dispersion is either suppressed on enhanced relative to the jet core, dependent on the eddy propagation speed.

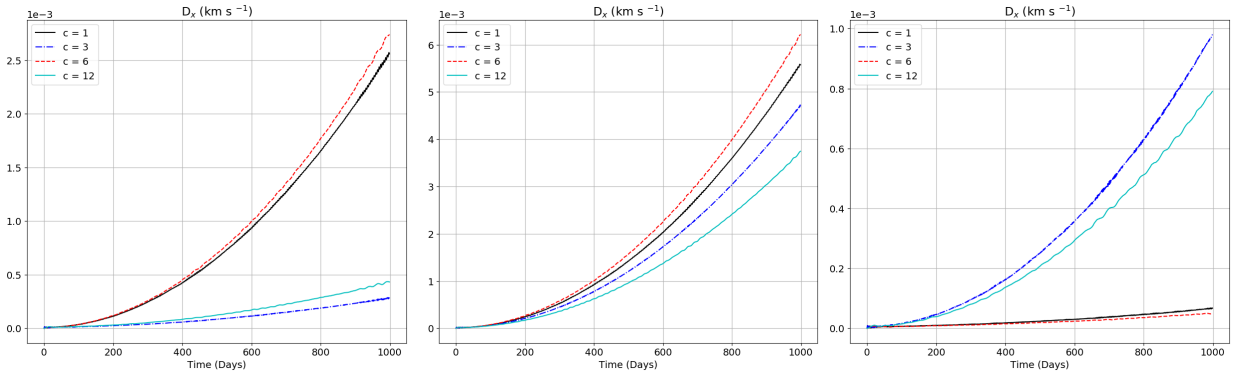

(a) $A = 50\text{s}^{-1}$, bin 5 (b) $A = 50\text{s}^{-1}$, bin 6 (c) $A = 50\text{s}^{-1}$, bin 8

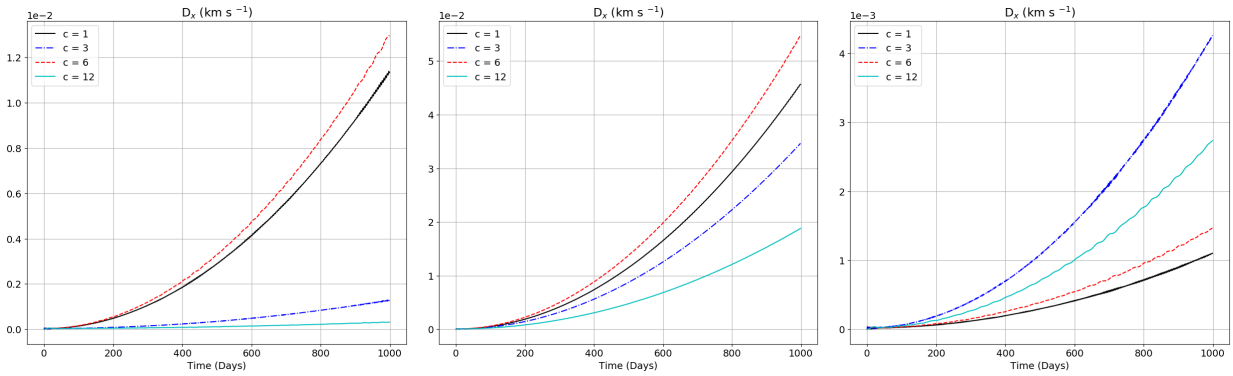

(d) $A = 100\text{s}^{-1}$, bin 5 (e) $A = 100\text{s}^{-1}$, bin 6 (f) $A = 100\text{s}^{-1}$, bin 8

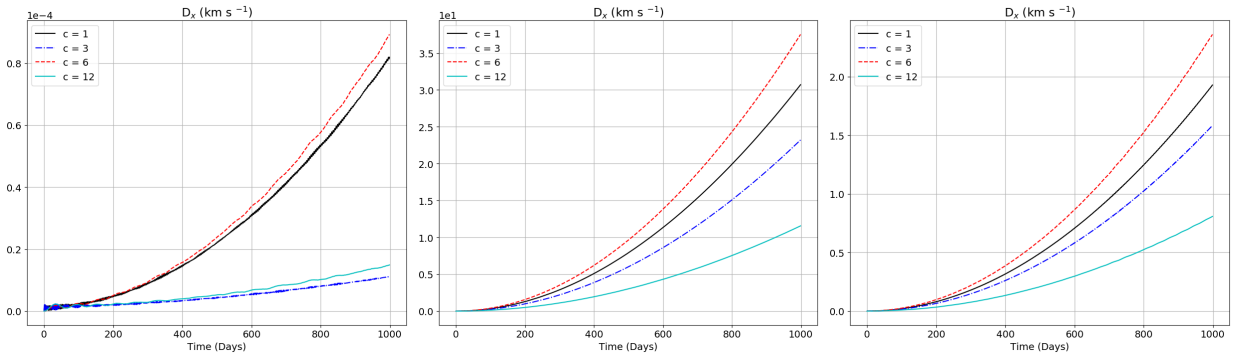

(g) $A = 526\text{s}^{-1}$, bin 3 (h) $A = 526\text{s}^{-1}$, bin 6 (i) $A = 526\text{s}^{-1}$, bin 8

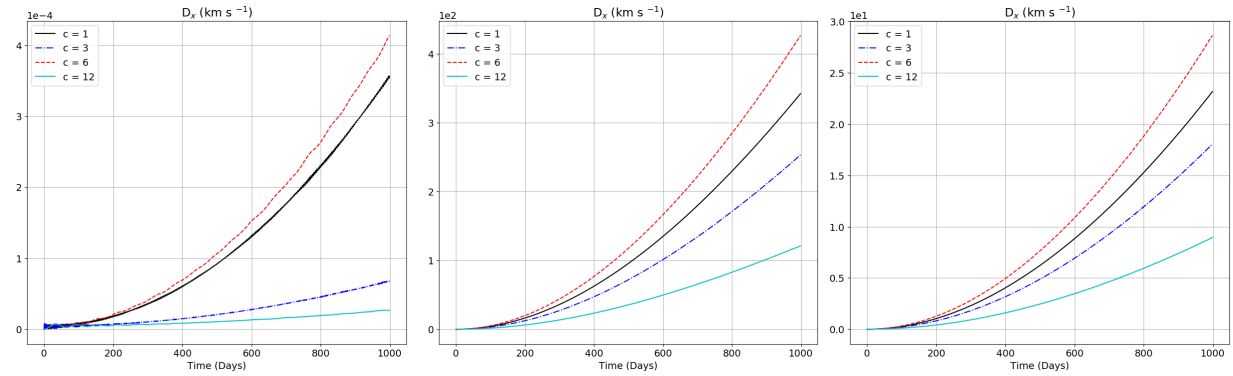

(j) $A = 1000\text{s}^{-1}$, bin 3 (k) $A = 1000\text{s}^{-1}$, bin 6 (l) $A = 1000\text{s}^{-1}$, bin 8

Figure 5.14: FFE SPD (km s^{-1}) for the analytic Rossby half waves and the time-mean dynamical streamfunction in bin 6 in the top layer for the coherent jet regime, but for different Rossby wave amplitudes.

5.3.4 Stokes' Drift

Introduction

Stokes' drift is defined as the difference between the average Lagrangian velocity and the average Eulerian velocity. To the leading order, Stokes' drift induced motion is periodic, however, surface gravity waves also induce a net drift (van den Bremer & Breivik 2018*b*). From an Eulerian point of view, the drift may appear to be zero, however the periodic circular orbits of particle trajectories are not closed, and so induce a net Lagrangian drift. The role of Stokes' drift velocities have frequently been studied in relation to the transport of surface drifters or tracers. For example, Stokes' Drift is often described as a major determinant in transport of plastic debris (Onink et al. 2019). The phenomenon of Stoke's Drift can also be linked to Rossby waves. Marshall et al. (2013) studied to effect of westward propagating Rossby waves and eddies that transport fluid westward via a Stokes Drift.

While the studies above are mostly concerned with waves in which there is a vertical oscillation of particles, some early studies did consider waves in the (x, y)-plane and their contribution to Stokes Drift. Thompson & Kawase (1993), Li et al. (1996) study the effect of equatorially trapped waves on Lagrangian particle trajectories and the subsequent effect of Stokes Drift. Thompson & Kawase (1993) finds that a Lagrangian drift, opposing the Eulerian mean, is found in much of the gyre interior in a one and a half layer model of a western boundary current and is explained using the Stokes' drift formulation. Particles will exhibit a drifting circular motion and move west along the equator before reaching the western boundary. It is concluded that the wave propagation, as opposed to the Eulerian mean flow, play an important role in determining the mean drift of particles. Li et al. (1996) further expand on this by focusing on the question of stirring processes, where it is concluded that a single-frequency travelling wave alone cannot produce chaotic stirring in the interior equatorial ocean. Given that when we remove the Rossby wave EOFs from the velocity field, that it doesn't result in a profound effect on the meridional dispersion, our studies support this theory. Li et al. (1996) in fact indicates that it is the combination of low frequency and high frequency waves that determine stirring properties. It is the interaction of different waves that result in chaotic mixing. However, our

primary concern is the effect of Rossby waves on zonal transport. We do not expect Stokes' drift due to the single Rossby wave alone to simulate meridional transport. Furthermore, as the time-mean zonal velocity has been found to have no impact on the qualitative behaviour of the FFE trajectories produced by particles advected by the kinematic model of the Rossby half waves, we will not consider the effect of the background flow in this section.

Contribution of Stokes' Drift to Lagrangian transport

Kamenkovich et al. (2009) argues that enhanced zonal dispersion can be explained by a Stokes' Drift. We derive the Stokes' drift for half Rossby waves, as expressed in eq. (5.3), in appendix G, obtaining the following results for the zonal stokes' drift $\overline{u_S}$ and the meridional stokes' drift $\overline{v_S}$:

$$\overline{u_S} = \frac{k}{4\omega}\frac{\partial^2}{\partial y^2}f^2, \tag{5.4}$$

$$\overline{v_S} = \frac{k}{4\omega}\frac{\partial^2}{\partial y \partial x}f^2. \tag{5.5}$$

For our half Rossby waves,

$$f(x,y) = A\text{sech}^2\left(\frac{y-y_c}{L}\right), \tag{5.6}$$

and therefore our stokes drift is purely zonal, just as demonstrated in Kamenkovich et al. (2009). This agrees with our observations in fig. F.5 and fig. F.6 where we see enhanced zonal spreading due to analytic Rossby half waves. The form of the velocity used to derive the Stokes' drift resembles that used in Constantin & Villari (2008), except instead of sech^2, they used the exponential, where it was verified that in deep water, using linear water wave theory, particle trajectories were not closed but exhibited a net drift. Though, similarly to most other Stokes' drift studies, the velocities of interested were zonal and vertical.

Fig. 5.15a plots the stokes drift profile against y, $\overline{u_S}$ as defined in eq. (5.5) and eq. (5.6), and fig. 5.15b plots the mean location of particles after 1000 days which have been advected by the kinematic Rossby half waves, as defined in eq. (5.3). The profile in fig. 5.15a is quantitatively

the same as that derived in Weber (2017), despite the formulation being very different. Weber (2017) derived Stokes' drift for equatorial Rossby waves on a β-plane. The figure in question was for the first baroclinic mode at the surface. They also don't account for background flows. It is also qualitatively similar to the meridional profiles of Stokes' drift induces by Rossby waves as seen in Li et al. (1996). There is a qualitative agreement between the two figures, in that there is pronounced zonal dispersion on the jet core, and dispersion in the opposite direction around flanks of the jet. However, we do see that the magnitude of transport around the core is slightly more marked than what Stokes' drift would imply. We should be getting about three times the amount of spreading in the jet core in relation to that on the flanks. This may be explained by the fact that the Lagrangian velocities were only approximated by a Taylor expansion to $\mathcal{O}(\xi)$.

Fig. 5.15c plots the same but for particles advected by the actual RossbyHalf EOFs, as in the EOFs produced by decomposition of the dynamical flow field combined with their corresponding PCs. We see qualitatively the same behaviour. We do however see greater dispersion in the return flow in the top layer, in fact it is comparable to jet core dispersion. Though it is very similar quantitatively to the kinematic model. The RossbyHalf EOFs alone are only meant to represent the eddy field, and so the Stokes' drift in this section is meant to emulate the mean spread of the EO Lagrangian particles and so we do not include the relative speed of the wave compared to the background flow.

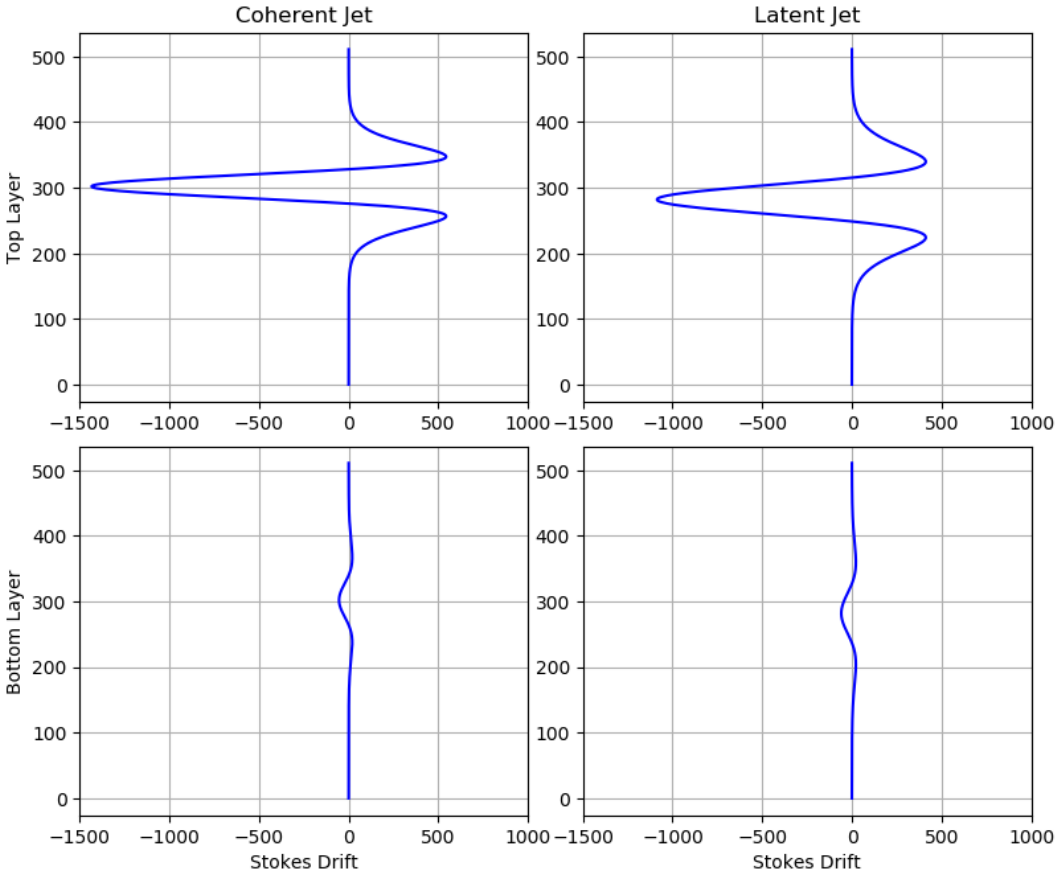

(a) Analytical solution for the stokes drift.

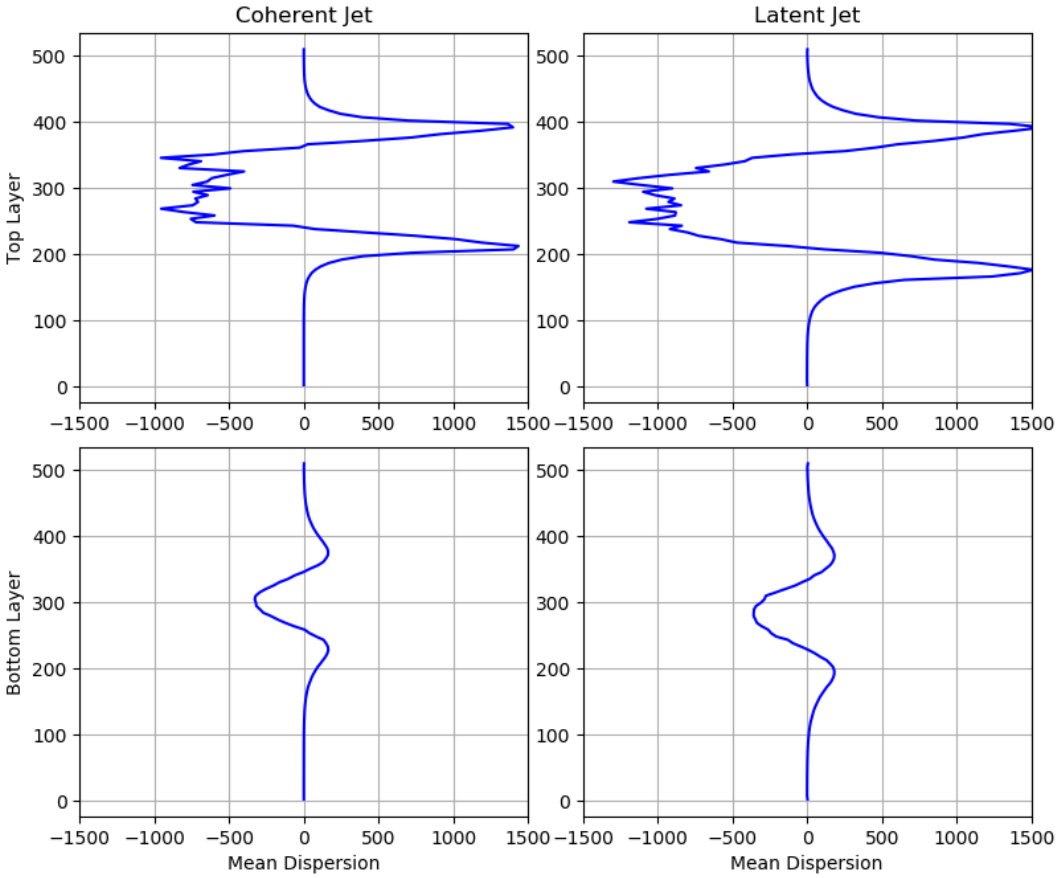

(b) Mean spread of particles for the kinematic model.

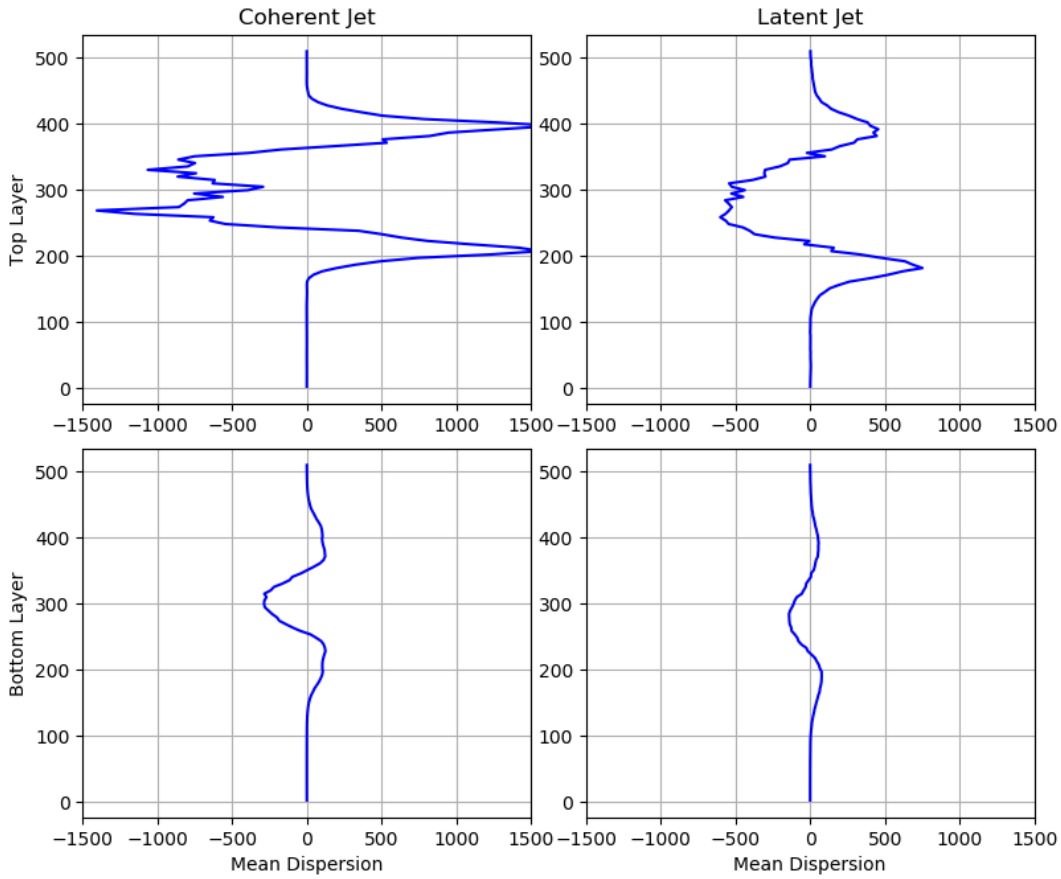

(c) Mean spread of particles for the EOF rossbyHalf modes.

Figure 5.15: Figures comparing the stokes drift and mean spread (km) for the half rossby wave kinematic model and the rossby half eof modes. They all show qualitatively similar results.

5.4 Summary and Conclusion

Our first step in establishing whether we could motivate a kinematic model to appropriately simulate Lagrangian transport, was to verify if a finite number of EOFs could capture Lagrangian transport. We found that zonal dispersion could be simulated well in both regimes across the whole domain. This prompted us to ask which were the most important patterns in causing this zonal transport.

We categorise the EOFs into different patterns and deducted them in turn from the full flow, and advected particles using the FFE methodology. From this we found that the zonal EOF pattern and half domain length Rossby waves were the most influential EOF patterns.

We proceeded to synthetically reproduce the RossbyHalf waves by constructing an analyt-

ical stream function to represent the Rossby wave and then we analytically advected particles. A combination of the Rossby wave and zonal flow came pretty close to capturing the zonal dispersion across the jet.

By calculating the Stokes' drift as a result of the Rossby wave, we found that the Stokes' drift profile emulated the mean zonal dispersion profile as a result of the actual EOF modes for the half Rossby waves implying that Stokes' drift is the primary mechanism behind enhanced eddy-induced zonal dispersion. Stokes' drift is typically associated with sub-surface drifters advected by travelling gravity waves (van den Bremer & Breivik 2018*a*, van den Bremer & Taylor 2015) and results in vertical oscillations and a mean drift. It has been used for example to explain surface dispersion of micro-plastics (Onink et al. 2019). It is not typically associated with particles being advected purely in the horizontal plane. It results in non-closed circular particle paths. Where there is no wave propagation, there is no mean drift of particles and so particles form closed circular paths (Henry 2019). Fig. 5.16 illustrates this type of drift caused by surface waves. We are seeing the same kind of transport, except flipped from the vertical to the horizontal plane.

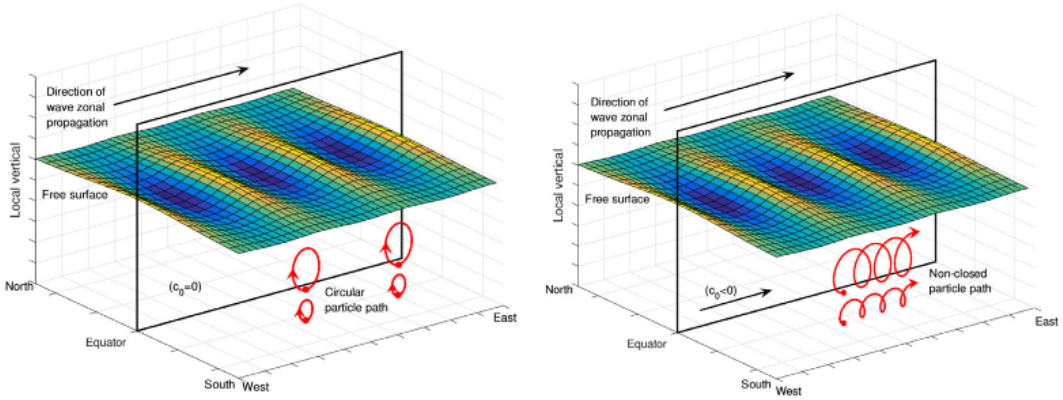

Figure 5.16: Figure illustrating Stokes drift resulting from free-surface waves with and without a current. Courtesy of Henry (2019)

Traditionally, isolation of Lagrangian coherent structures is used to diagnose kinematic oceanic features that play dominant roles in particle dispersion and mixing (Sinha et al. 2019, Haller & Yuan 2000), so this approach provides a novel method where parameterisation and identification of flow features does not need to be done using Lagrangian methods, but can be done from only Eulerian data. It does however remain to be investigated how to retrieve the

necessary parameters from oceanic or numerical model data to determine the kinematic model.

The story for meridional dispersion is however different. A large number of EOFs (even more than 20) is needed to capture the meridional spreading. This implies that small-scale motions play a big role in meridional transport, and that a deterministic kinematic model is going to struggle to effectively parameterise meridional transport. A large number of modes is needed, which would prove to be quite expensive.

The role of parameters in the derived kinematic model were also investigated. In agreement with Thompson & Kawase (1993), the wave propagation as opposed to the Eulerian mean, is the important role in determining mean drift of particles. It was found that there was a critical eddy propagation speed at which zonal dispersion was enhanced, much like in Ferrari & Nikurashin (2010), but where meridional dispersion was almost completely suppressed. It remains to be answered what determines the value of this critical eddy propagation speed? We hypothesise that the lack of meridional wave number results in suppression of meridional dispersion, but this would need to be further investigated an verified.

Furthermore, Li et al. (1996) states that the combination of waves is what can induce stirring processes in the interior equatorial ocean. Could meridional dispersion be captured by combining several Rossby type waves? Would the cross-jet dispersion still be suppressed at this critical eddy propagation speed?

Chapter 6

Lagrangian Stochastic Models

6.1 Background

Stochasticity has frequently been added to ocean models to represent a variety of phenomena, and is generally used to represent small-scale motions as a result of turbulence which we are unable to capture deterministically. Both ocean mesoscale eddies (Mana & Zanna 2014, Berloff 2005) and eddy-induced transport (Berloff & McWilliams 2002, 2003) have been parameterised by stochastic models. We will go into more in-depth detail outlining some stochastic models and their applicability to the ocean at the end of this chapter.

We will be following the methodology of Berloff & McWilliams (2002), in using Markov models. But firstly, let us outline the theory behind such models. We follow the arguments presented in Rodean (1996) in this section.

Supposing X_t is a stochastic process, we can write a 1D stochastic differential equation for X_t, known as a Generalised Langevin Equation, as follows:

$$dX_t = a(X_t, t)dt + b(X_t, t)dW_t, \tag{6.1}$$

where a and b are continuous functions, dW_t is a random increment, and $W(t)$ is a Wiener Process related to white noise, ξ, as follows (Rodean 1996):

$$W(t) = \int_0^t \xi(s)ds, \tag{6.2}$$

$W(t)$ represents the particle location advected due to Brownian motion at time t. Therefore we can express $dW(t) = W(t + dt) - W(t) = \xi(t)dt$. The incremental Wiener process $dW(t)$ has mean and variance:

$$\langle dW(t) \rangle = 0 \tag{6.3}$$

$$\left\langle (dW(t))^2 \right\rangle = dt, \tag{6.4}$$

and is normally distributed: $dW_k(t) \sim \mathcal{N}(0, dt)$.

We shall consider Markovian models, where the probability distribution of the stochastic variable at the current time step, X_t, is only dependent on the previous time step, that is:

$$\mathrm{p}(X_t = x_t | X_{t-1} = x_{t-1}, \cdots, X_0 = x_0) = \mathrm{p}(X_t = x_t | X_{t-1} = x_{t-1}). \tag{6.5}$$

We can express the evolution of probability density, p, for a Markovian process with the Fokker-Planck Equation:

$$\frac{\partial p(\mathbf{x}, t)}{\partial t} = -\sum_{i=1}^{N} \frac{\partial}{\partial x_i} \left[a_i(\mathbf{x}, t) p(\mathbf{x}, t) \right] + \sum_{i=1}^{N} \sum_{j=1}^{N} \frac{\partial^2}{\partial x_i \partial x_j} \left[\frac{1}{2} b_{ij} b_{jk} p(\mathbf{x}, t) \right]. \tag{6.6}$$

$p(\mathbf{x}, t)$ is the probability density of the random variable $\mathbf{x}$. In a zeroth-order Markov model, this would be the particle position. In Markov models of higher successive integer orders, the variable to which stochasticity is applied is the successive higher order derivative of the particle position. We refer to $a(\mathbf{x}, t)$ as the drift correction term and $b(\mathbf{x}, t)$ as the diffusion term.

We aim to find solutions for a and b for each Markov model that obey the well-mixedness condition. The well-mixedness constraint states that the Lagrangian probability density function is equivalent to the Eulerian probability density function. This means that uniformly distributed particles remain uniformly distributed. We derive the stochastic differential equations defining Markov-models of successive orders referring to eq. (6.6). We will also be assuming

that the x and y directions are independent of each other, as in there is no cross-correlation, as the flow is zonally dominated and off diagonal components of the diffusivity tensor are negligible. We will briefly visit the case where we do assume that there is cross-correlation at the end of this chapter.

6.2 Model 1: 0th-Order Markov (Random Walk)

This is the simplest stochastic model in our hierarchy, alternatively known as a Markov displacement process. Here, a stochastic term is added to the particle position $\mathbf{x}$ resulting in the 1D stochastic differential equation, derived in appendix chapter H:

$$x_i(t+dt) = x_i(t) + \left(\overline{u_i} + \frac{\partial K_i}{\partial x_i}\right) dt + \sqrt{2K_i} dW(t). \tag{6.7}$$

This somewhat differs from the classical homogeneous diffusion model (as seen in Griffa (1996)) due to the presence of the diffusivity derivative term. This term is what is known as the 'drift term'. This arises due to the spatial inhomogeneity of the diffusivity, i.e. the process is not isotropic. Due to the zonal structure of our flow field, we have estimated the diffusivity in zonal bins, and therefore assumed that the diffusivity does not vary in the x-direction. Therefore, this drift term will be introduced in the y-direction and there will therefore be a dependence on the y coordinate.

This model is only able to model the far-field, where the far-field eddy diffusivity coefficient is $K_{ii} = \sigma_{ii}^2 t$ (see eq. (4.10) and Thomson & Wilson (2013)). So by construction, this model will only be able to model diffusive processes with a constant eddy-diffusion coefficient. We therefore expect this model to not be able to accurately parameterise the non-diffusive material transport present in the meandering jet.

The use of the diffusivity tensor will evidently be quite crude because, as seen before, this process is inherently non-diffusive and so $\mathbf{K}$ changes in time. Therefore, we choose a 'best' guess diffusivity. We know that we see initial ballistic dispersion, so we know that we will not capture this behaviour, and so no attempt is made to fit the diffusivity over the ballistic

time-scale, but rather to fit the long-term, or far-field, asymptotic behaviour.

Description of the Numerical Model

As with the transport model described in section 3, we must perform numerical time integration and spatial interpolation.

The time-averaged velocity, diffusivity and diffusivity derivative must be interpolated. We calculate the time-averaged velocity (and flow derived variables such as the velocity variance) using the same 2D-cubic interpolation method as applied in the transport model. As diffusivity only varies in y, we only need to perform 1D spatial interpolation. One dimensional cubic Lagrange polynomial spatial interpolation, from which 2D-cubic interpolation was derived, was used to estimate the diffusivity. In order to estimate the derivative, a first order finite difference scheme was used to numerically differentiate interpolated diffusivities.

A first order Euler method was used for time-integration and, as the flow variables are of the same scale as for the dynamical model, a time step of 3600 seconds was used.

6.2.1 Comparing different estimates of K_{ii}

We use two methods of calculating the diffusivity:

$$K_i = \frac{1}{2}\frac{\partial D_{ii}}{\partial t}, \tag{6.8}$$

$$= \sigma_{ii}^2 T_L. \tag{6.9}$$

and compare the results in fig. 6.1 for the two jet regimes and bins 2 and 5 to compare the surf zone and jet core respectively. We include the figures for all bins and layers for both regimes in appendix J.

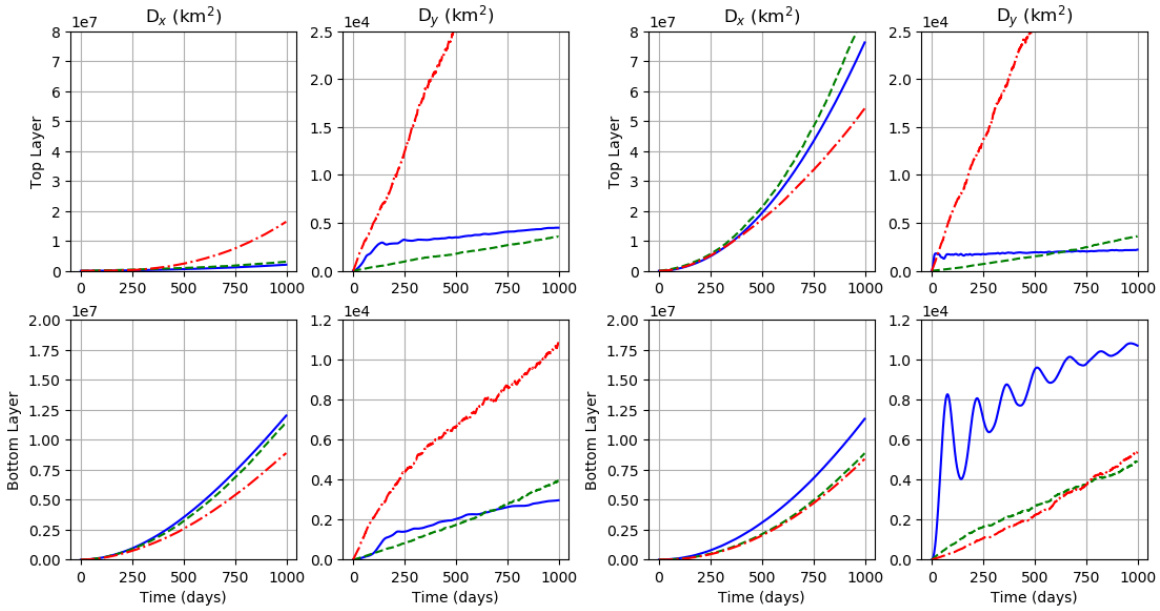

(a) Bin 2 - Coherent Jet

(b) Bin 5 - Coherent Jet

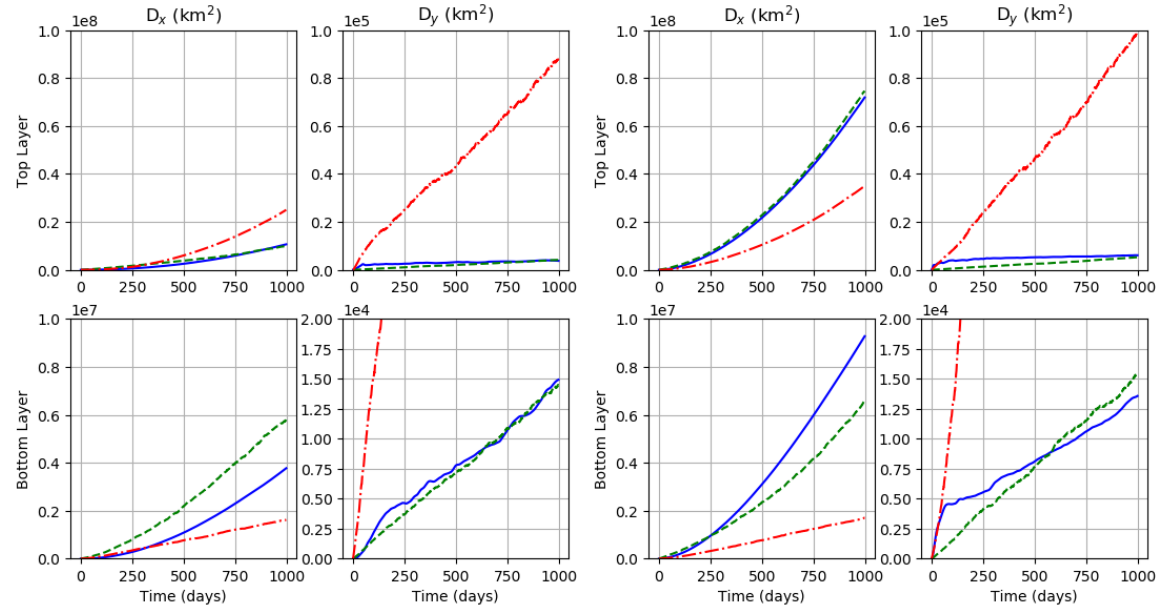

(c) Bin 2 - Latent Jet

(d) Bin 5 - Latent Jet

Figure 6.1: Single-Particle Dispersion (km^2) against time (days) for the Diffusion Model for the two jets comparing use of diffusivity calculated from the SPD or from $\sigma_{ii}^2 T_L^{(i)}$. Demonstrates SPD gives a more accurate asymptotic diffusivity estimate.

When calculating the diffusivity from the SPD, we assume the SPD to be linear, which evidently it is not, and therefore the diffusivity will be over-fitted. Hence, as expected, the SPD approximation underestimates the zonal dispersion as the diffusivity is overestimated due to super-diffusivity, and conversely, dispersion is underestimated meridionally due to sub-diffusivity. The converse is true for using σ. In particular, the meridional dispersion is drasti-

cally overestimated. It appears to only be capturing the ballistic growth rate.

We will use the SPD diffusivity approximation for the following diffusion models. The SPD method is also slightly more accurate in the zonal direction.

6.2.2 Comparing PV-mapped Diffusion K_{PV} to K_{ii}

Now we run the diffusion model, except using the PV-mapped diffusivity. The PV-mapped diffusivity K_{PV} is stored in the PV bins, and interpolated at the particle location, and particles are released in non-uniform bins, where the zonally-averaged and time-averaged PV has been binned uniformly and then mapped to its y coordinate. The particles are then released according to the y coordinate.

We plot the single-particle dispersion as obtained from diffusion models in fig. 6.2 for both jet regimes. For the coherent jet, K_{PV} results in faster growth, however the converse is true for the latent jet. The PV-mapped diffusion model overestimates growth in the coherent jet, however for the latent jet, the growth rate appears to be similar once the ballistic time-scale is passed.

From fig. 4.19, PV-mapped dispersion shows clear maxima in the diffusivity around the jet core, in bins 5, 6 and 7. Restricting our attention to those bins in fig. 6.2, we can see that initially, K_{PV} comes closer to capturing that rapid growth in dispersion. However, as the bins are very narrow and the locality time-scale is quite small, particles leave the bin quickly and so are then advected using K_{PV} for the mixing regions, which is underestimated, and hence results in slower growth.

However, we are not capturing the initial ballistic growth. Both diffusivity measures have been fitted to a non-linear dispersion plot, and so can only expect to fit the gradient for a finite period. This leads us to consider the next model in the hierarchy.

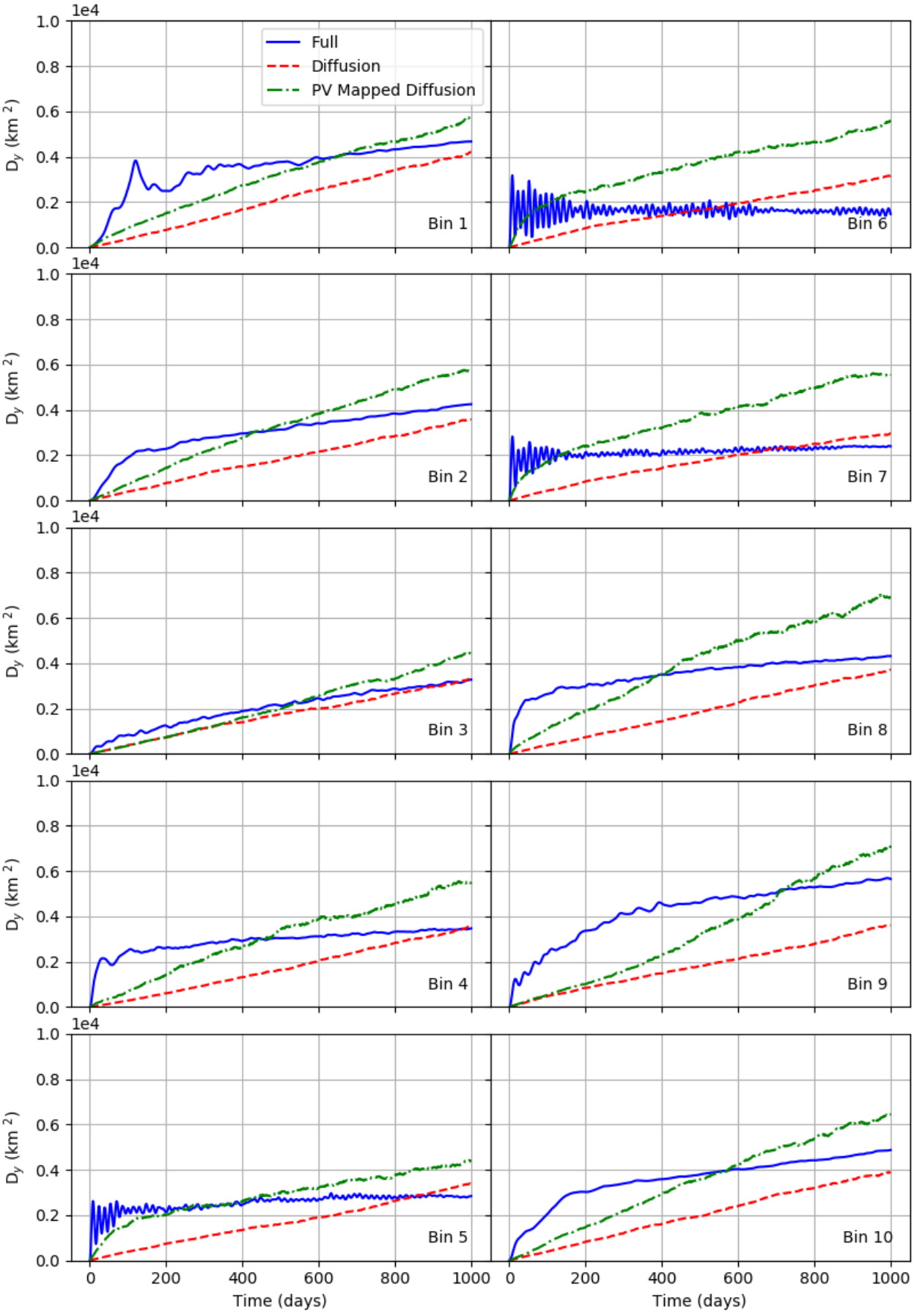

(a) Coherent Jet.

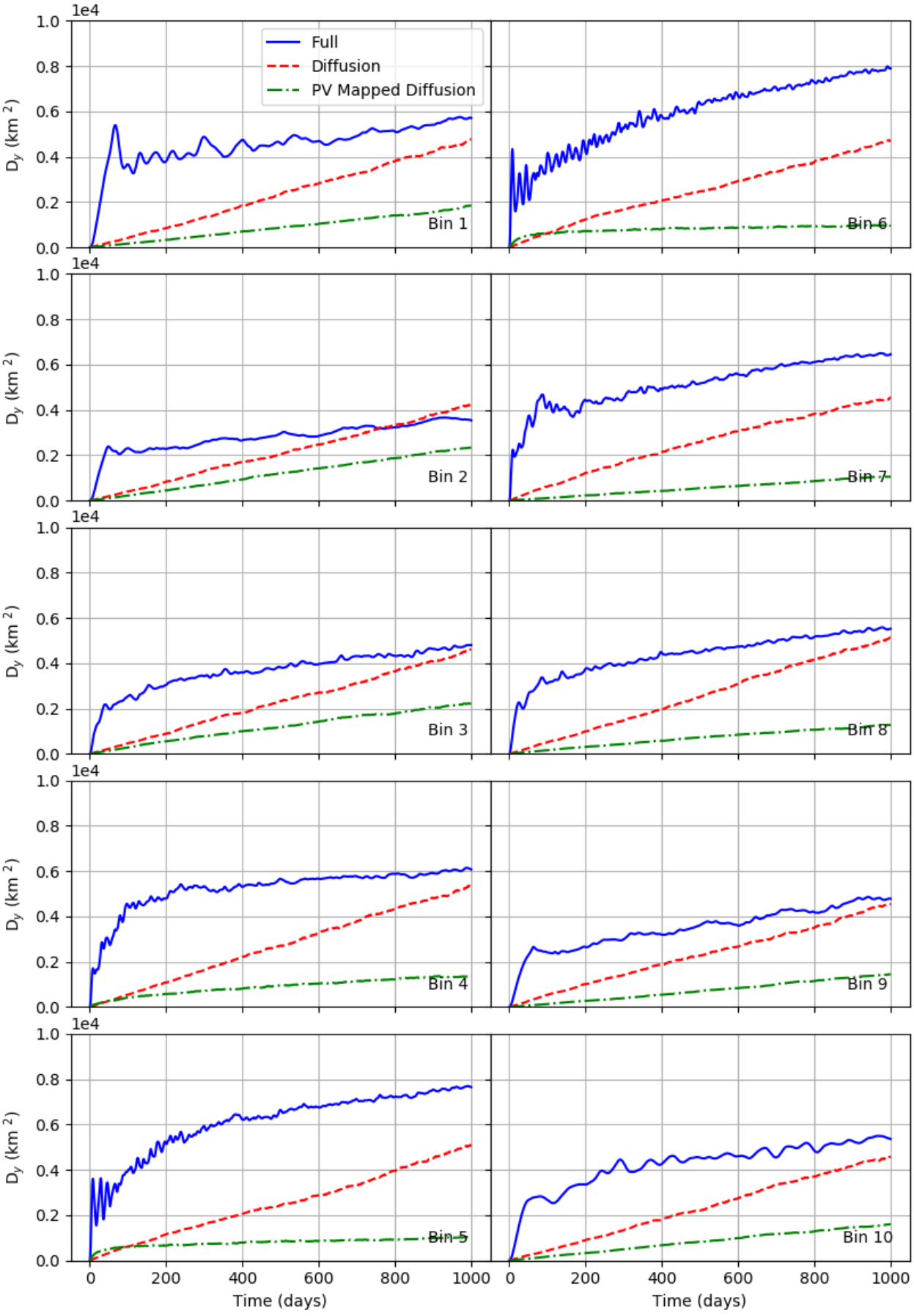

(b) Latent Jet.

Figure 6.2: Single-Particle Dispersion (km^2) against time (days) for a diffusion model using diffusivities calculated using both the regular method and the PV-mapped method. PV-mapped is only more accurate in the immediate vicinity of the jet core.

6.3 Model 2: 1st-Order Markov (Random Flight)

The limitations demonstrated by the diffusion model, in particular its failure to capture the short-term ballistic behaviour, $D \sim t^2$, we hope to capture in the 1st-order model. Random flight models have been used in oceanic literature before (Berloff & McWilliams 2002, Griffa et al. 1995, Griffa 1996), and are now quite common practice in use as a parametrisation method favourable to the traditional diffusion approach. An advantage of this model, is that it only requires one additional parameter and so is relatively simple to implement.

The governing equations for the Markov-1 Model are derived in appendix I following the methodology as described in Thomson (1987):

$$x_i(t+dt) = x_i(t) + (\overline{u}_i(t) + u_i'(t))\,dt, \tag{6.10}$$

$$u_i'(t+dt) = u_i'(t) - \frac{u_i'}{T_L^{(i)}}dt + \frac{1}{2}\left(1 + \left(\frac{u_i'}{\sigma_{ii}}\right)^2\right)\frac{\partial \sigma_{ii}^2}{\partial x_i}dt + \left(\frac{2\sigma_{ii}^2}{T_L^{(i)}}\right)^{1/2} dW_i(t). \tag{6.11}$$

So we have two parameters of interest in this model: σ_{ii} and $T_L^{(i)}$, which is the Lagrangian integral time-scale, as discussed in section 4.3.3. Much like with the diffusion model, we will compare which combination of parameters provide the best results.

The diffusion model results in a δ-function for $R(\tau)$, which implies an immediate loss of memory. A Markov-1 model however gives $R(\tau) = e^{-\tau/T_L}$ (Griffa et al. 1995). As we have already seen, this does not quite fit R as obtained from our data, especially in the meridional direction, though R_x does fit an exponential decay quite closely.

The velocity fluctuation will be initialised as a Gaussian distribution with mean 0 and variance σ^2.

6.3.1 Description of the numerical model

Similarly to the 0-th order Markov model, we will use a time step of 3600 seconds, the Euler time-integration scheme, and cubic interpolation. We however have more variables to consider.

$T_L(i)$ and σ_{ii} are estimated per zonal bin. We assume it is constant in x and is defined and the mid-point of the bin. We then perform 1D cubic lagrange interpolation to find the value at the particle location.

6.3.2 Comparing different σ estimates

We compare two different ways of retaining the Lagrangian velocity variance: σ^2. First is directly from the Lagrangian trajectory data and the second is from the diffusivity: $\sigma_{ii}^2 = K_{ii}/T_i^L$. As we saw in the diffusion model, these different methods can produce vastly different results. They would only produce the same result if the process was purely diffusive. The resulting SPD is plotted in fig. 6.4 for the two jet regimes for bins 2 and 5. Figures for all bins are included in appendix J. Calculating σ from the diffusivity consistently results in better results, just as with the diffusion model, so now we will compare this with the PV-mapped diffusivity.

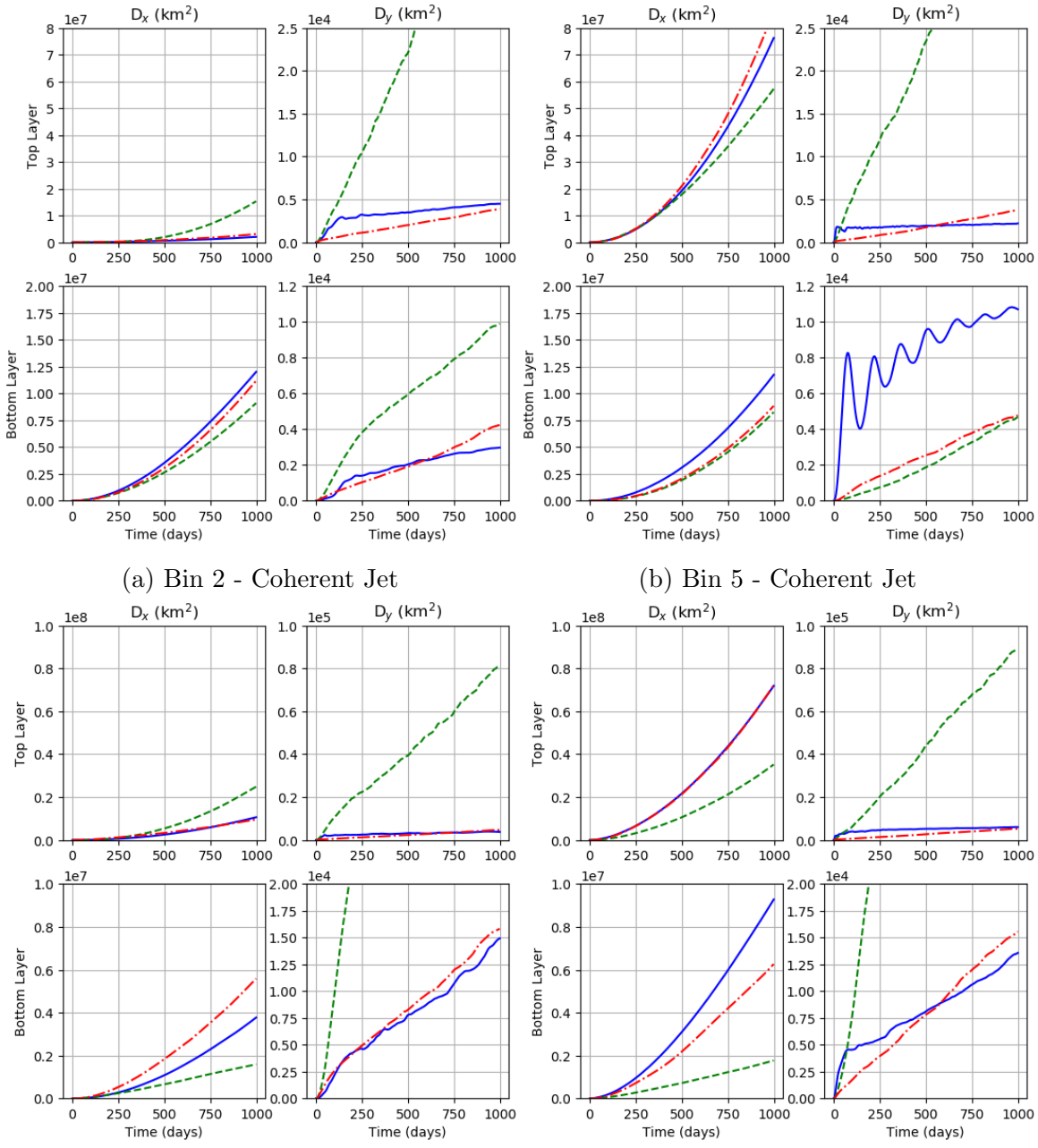

(a) Bin 2 - Coherent Jet

(b) Bin 5 - Coherent Jet

(c) Bin 2 - Latent Jet

(d) Bin 5 - Latent Jet

Figure 6.3: Single-Particle Dispersion (km^2) against time (days) for the Diffusion Model for the two jets comparing use of diffusivity calculated from the SPD or from the as $\sigma_{ii}^2 T_L^{(i)}$. Demonstrates SPD gives a more accurate asymptotic diffusivity estimate.

6.3.3 Comparing PV-mapped Markov-1 to Regular Markov-1

Now we see if K_{PV} gives us better results. Instead of using σ_{PV}, we use K_{PV}, and the SPD T_L. The PV-mapped dispersion underestimates the ballistic time-scale, and as this is what we are interested in capturing, it is important to consider the 'true' ballistic time-scale. The dispersion

is plotted in fig. 6.4 for PV bins. Much like for the diffusion model, PV-mapped dispersion more closely captures the initial growth in bins 5, 6 and 7 around the jet core. Though, in the latent jet it performs much worse at later times.

Over the whole time period, the Markov-1 model performs slightly better than the diffusion model, however as theory suggests, sub-diffusivity is not effectively modelled and dispersion is over-estimated in the intermediate-time range by both diffusivities.

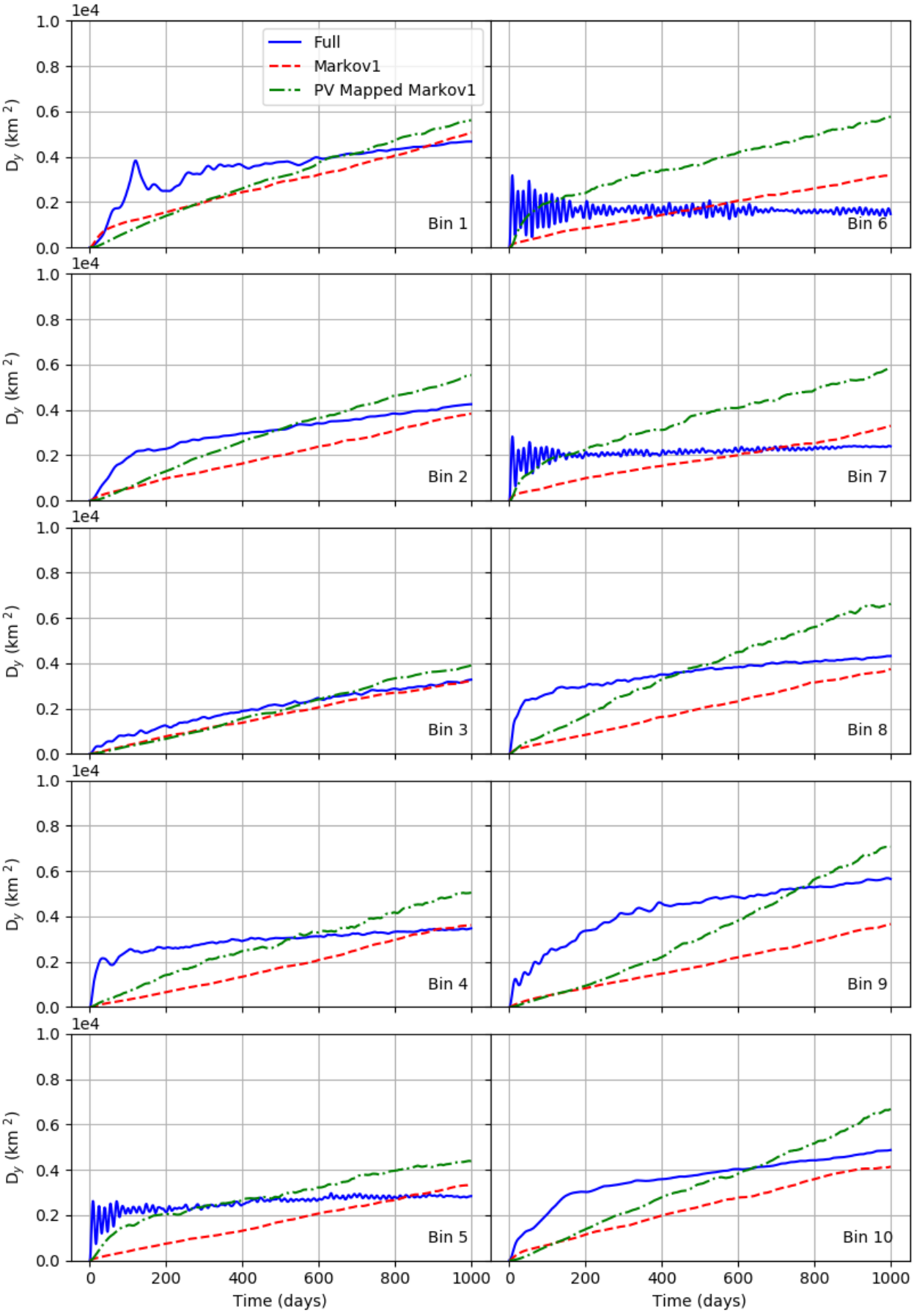

(a) Coherent Jet.

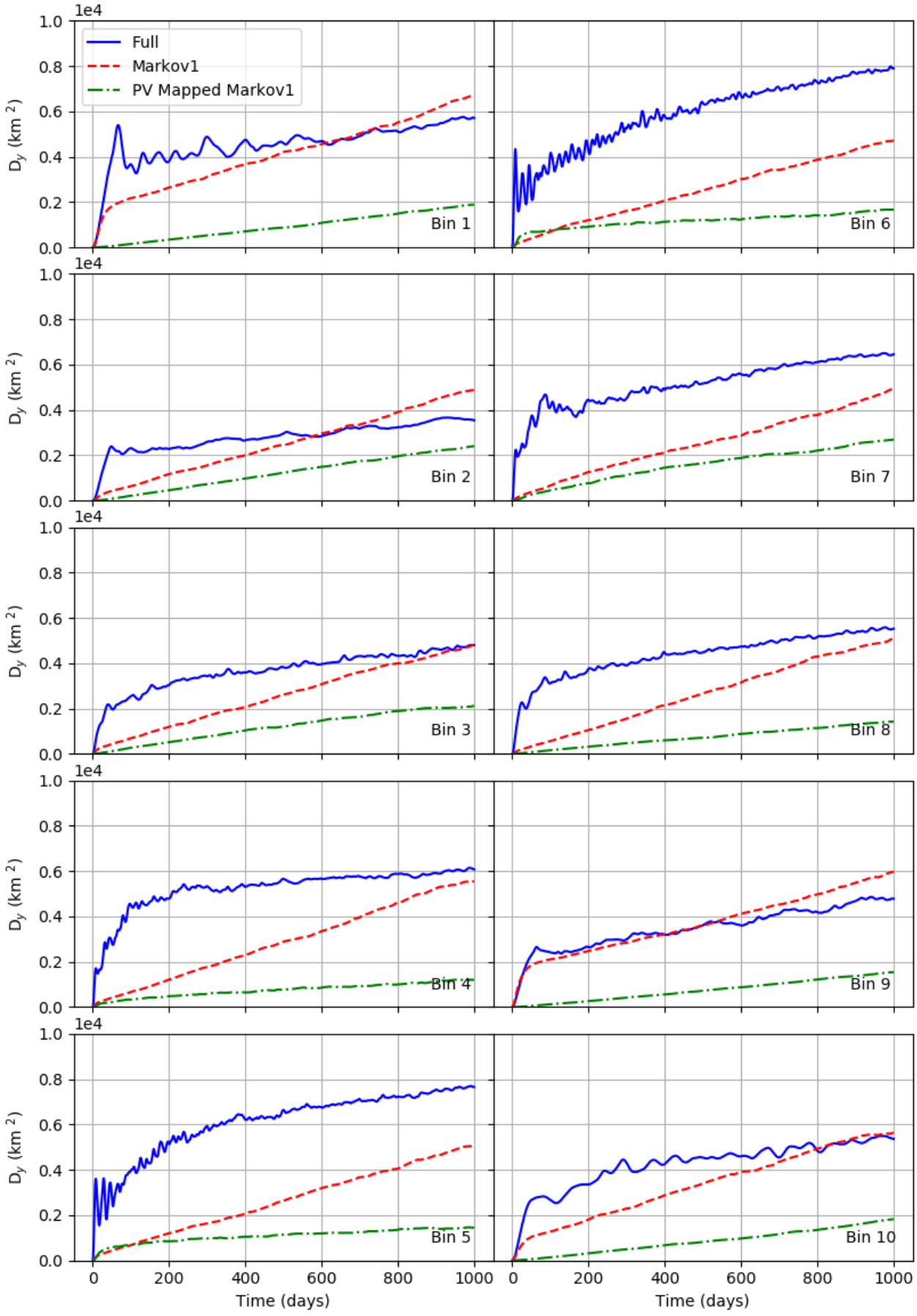

(b) Latent Jet.

Figure 6.4: Meridional single-particle dispersion (km^2) in the top layer against time (days) for the random flight model using diffusivities calculated using both the regular method and the PV-mapped method.

6.4 Model 3: 1st-Order Markov with Looping

An exponential fit for the LACF does not always give an appropriate value for $T_L^{(i)}$. It is frequently less than the time at which R reaches its first zero. Furthermore, as R is often oscillatory, it does not fit well to an exponential curve.

Veneziani et al. (2005), suggested a different 1st-order stochastic model which accounts for this oscillatory behaviour that is produced by looping trajectories. It is also able to simulate sub-diffusive behaviour. They achieve this by introducing a spin parameter Ω. The new stochastic differential equations (for homogeneous flows) are:

$$du' = -\frac{u'}{T_L^{(x)}}dt - \Omega v' dt + \left(\frac{2\sigma_{xx}^2}{T_L^{(x)}}\right)^{1/2} dW(t), \tag{6.12}$$

$$dv' = -\frac{v'}{T_L^{(y)}}dt + \Omega u' dt + \left(\frac{2\sigma_{yy}^2}{T_L^{(y)}}\right)^{1/2} dW(t), \tag{6.13}$$

$$\Omega = \frac{\langle u'dv' - v'du' \rangle}{2dtE_k}, \tag{6.14}$$

where $E_k = 1/2\left(\sigma_{ii}^2 + \sigma_{jj}^2\right)$ is the Eddy Kinetic Energy.

For this SLM, we get that (Veneziani et al. (2004)):

$$R_i = \exp\left(-\frac{t}{T_L^{(i)}}\right)\cos(\Omega t), \tag{6.15}$$

which is what Dosio et al. (2005) suggested, and can more appropriately fit the observed oscillatory Lagrangian autocorrelation functions.

According to Veneziani et al. (2004), looping trajectories are most frequently observed in the return flow regions, that consist of vortices and eddies. The jet core region has a dominant zonal flow, so we would not expect to see looping full trajectories.

We plot the ensemble-averaged Ω in fig. 6.5 for the two jet regimes for the FFE case. We see that in the coherent jet, looping trajectories are found in the return flows. In the top layer, cyclonic trajectories are found beneath the jet and anti-cyclonic trajectories above the jet. The reverse is true for the bottom layer. The coherent jet however seems to have much

fewer cyclonic trajectories as a much smaller Ω is found across the domain. The structure is also very different. Cyclonic trajectories are found around the jet core and anti-cyclonic in the mixing regions.

However, our values of Ω are much smaller than what was found in Veneziani et al. (2005), by a whole order of magnitude. A typical value of Ω for cyclonic trajectories is 0.25 days^{-1}. Even when we plot the full distribution of Ω, we only achieve maximum values of around 0.06 days^{-1}.

The velocity autocorrelation functions plotted in Veneziani et al. (2005) differ to those found in our simulation. Their zonal and meridional autocorrelation functions don't differ as much from each other. That is, the zonal autocorrelation does sometimes oscillate and it frequently decays to zero within a time-lag of 20 days. Our zonal autocorrelation, however, does not. Therefore, we conclude that there is insufficient cross-correlation between the zonal and meridional directions to warrant using a Markov model with looping.

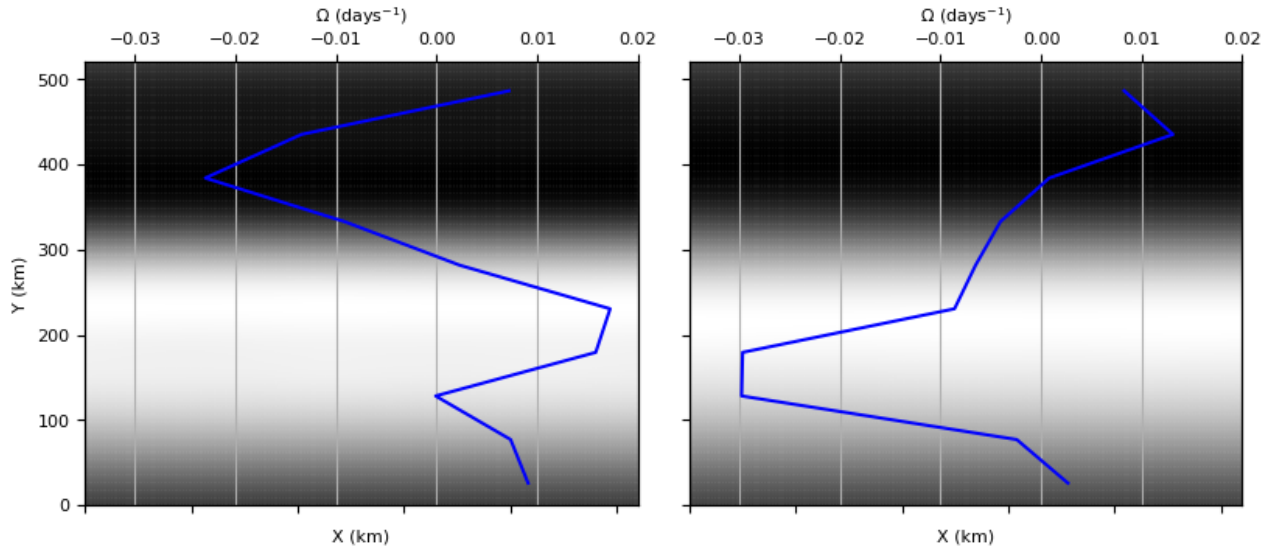

(a) Coherent Jet

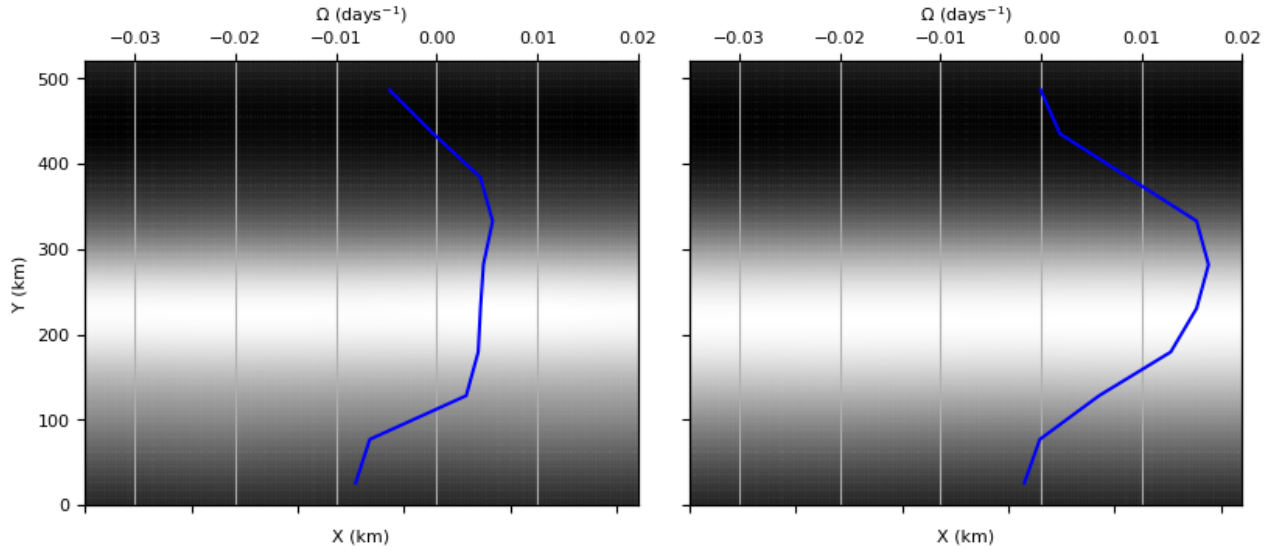

(b) Latent Jet

Figure 6.5: Ω (days^{-1}) for each uniform bin as calculated from the FFE trajectories for each jet regime superimposed on the time-averaged stream function. The left panel is the top layer and the right is the bottom layer.

6.5 Summary and Conclusion

In this chapter we examine three different stochastic models in which we use different parameters obtained from both the standard FFE trajectories and the PV-mapped trajectories. In running these models, it is assumed that statistics are stationary. With the exception of the Markov-1 model with looping, the velocity components are considered as independent from each other.

Firstly, we examine the diffusion model, which is otherwise known as a 0th-order Markov model as stochasticity is only added to the particle location. We know that since material transport is not diffusive, we will not obtain particularly accurate results, however it does give us a good indication of the importance of the method chosen to estimate the diffusivity. We find that, particularly for the meridional direction, it matters whether the diffusivity is calculated from the dispersion or from the Lagrangian velocity variance. The Lagrangian velocity variance drastically overestimates meridional dispersion particularly around the jet core and the bottom layer. This can be attributed to significant non-diffusive behaviour.

We do however find that zonal dispersion is quite well captured. We know that the time-averaged flow is purely zonal and is of a greater magnitude than the eddying flow. Our results suggest that the mean flow is still very much the dominant effect in driving zonal dispersion. We therefore focus on meridional dispersion for the remainder of chapter.

We then run the diffusion model for particles released in PV bins also using the PV-mapped dispersion. K_{PV} does slightly better at the immediate time-scale at accurately capturing dispersion near the jet core, particularly in the coherent jet.

We then proceed to a 1st-order Markov Model where stochasticity is added to the velocity. Particles exhibit a memory over the decorrelation time-scale and hence we are able to simulate ballistic behaviour. We compare different diffusivity estimates and find again that using the diffusivity as estimated from the SPD produces better results.

We obtain similar results as to the diffusion model when considering PV bins and the PV-mapped and SPD diffusivity estimates, and up to about 100 days in bins 5, 6 and 7 (i.e. the jet core) the PV-mapped Markov-1 model is slightly better at capturing the enhanced dispersion seen in the jet core. However in the latent jet this is much less pronounced. Away from the jet core, the regular method performs better. Take particular note of bins 1, 9 and 10 in the latent jet where the SPD Markov-1 model managed to capture some ballistic growth.

To summarise, it appears that where there is little PV mixing and a strong PV gradient (such as in the jet core of the coherent jet) the PV-mapped diffusivity is a more appropriate measure. In mixing regions, the SPD diffusivity is more appropriate. K_{PV} effectively captures a

diffusivity maximum around the jet core where there is a significant meandering PV isoline, and so can aptly capture the 'true' dispersion of a particle from its initial location. It underestimates, however, the diffusivity elsewhere. Perhaps a spatial mixture of the two measures may prove to provide better results.

It is however important to note that in the meridional direction, after the ballistic time-scale, transport is sub-diffusive, a phenomenon that a Markov-1 model is unable to capture. This leads us to our final model. We had two options to choose from to introduce sub-diffusivity into a stochastic model. One is by going up an order in the hierarchy of stochastic models by introducing white noise to the acceleration. The other, which we study in this chapter, which is slightly simpler, is to introduce cross-correlation between the meridional and zonal velocities.

Veneziani et al. (2005) states that in regions surrounding jets, where coherent structures such as vortices are found, which are associated with the trapping of particles and hence sub-diffusivity, particles typically exhibit a looping behaviour, resulting in a non-zero velocity cross-correlation. We also see such behaviour, particularly in the latent jet, where vortices are frequently shed as a result of pinching of jet meanders. Such a model results in an oscillatory LACF for both the zonal and meridional directions. However, only our meridional autocorrelation is strongly oscillatory. As a result, we obtain values of Ω that are too small to be considered looping. We conclude that this method is not suitable for flows that have a strong zonal component even in the absence of the mean flow.

We choose to not proceed with models that can capture super-diffusivity, as firstly, this is not behaviour that we see in the meridional direction; and while we do see this behaviour in the zonal direction, zonal dispersion is mostly accounted for by the mean zonal flow, and we also outline another simpler and deterministic approach to parameterise zonal dispersion in the next chapter. We will however briefly outline some more stochastic models that can be used and their potential advantages.

6.5.1 Further Possible Stochastic Models

Berloff & McWilliams (2002) investigated the applicability of Markov models of higher orders

in a double-gyre model. We will firstly discuss the next two models in the hierarchy.

Reynolds (1999) introduced the second-order Lagrangian stochastic model where the random perturbation is added to the acceleration. An additional time-scale is introduced, which is the Markov-2 fading memory time tensor $T_L^{(2)}$. In this case the autocorrelation oscillates on one T_L and the oscillation decays exponentially with a time-scale of $T_L^{(2)}$. This would result in an autocorrelation function similar to what we see in our data and the same as what the Markov-1 looping model gives. A key benefit of this method is its ability to simulate intermediate-time sub-diffusive behaviour. It produced promising results in Berloff & McWilliams (2002), which is also a jet dominated flow, and therefore may be more appropriate for use in our flow regime than by introducing a looping parameter. Much like the first two models in our hierarchy, it assumes that the two velocity components are independent, and in essence, $T_L^{(2)}$ is equivalent to Ω, except defined independently for each velocity component.

Reynolds (2003) introduced the idea of a third-order Lagrangian stochastic model, where the random perturbation is added to the hyper-acceleration, the derivative of the acceleration. A third time-scale parameter is introduced, referred to as the Markov-3 fading time-scale. This can simulate intermediate-time super-diffusive spreading. The resulting autocorrelation function oscillates while decaying to zero, that is, the oscillations are not centred around zero. This is the behaviour we observe for R_x in figs. E.5 and E.6.

Other models that fall outside the typical Markov model hierarchy that have been used in oceanographic and atmospheric applications include fractional Brownian motion (fBm), the Matèrn process and the Ornstein-Uhlenbeck (OU) process. A major limitation of fBm is its inability to capture diffusion, which is the long-time range behaviour exhibited by oceanic Lagrangian trajectories (Lilly et al. 2017), and so will not be of much use. Instead, Lilly et al. (2017) outlines the theory behind the Matèrn process and Sykulski et al. (2016) applies it to an oceanographic setting in an attempt to simulate surface drifters which exhibit inertial oscillations. The inertial oscillations are modelled using an OU process, and transport due to the turbulent background flow is captured using a Matèrn process. It successfully accounts for non-stationarity of statistics by allowing the parameters needed to define the stochastic model to vary in space and time. A key feature of the Matèrn process, is that where the models we

have considered in our Markov model hierarchy all have integer orders, in that stochasticity is added to an integer order derivative of particle displacement, the Matérn process (and fBm) does not. As this model can account for non-stationarity and anisotropy, as well as capture short- and medium-time range behaviour, without non-physical long-time range behaviour, the Matérn process may be a more appropriate stochastic model than a Markov-3 model.

Another stochastic approach that we have not mentioned is to add stochasticity to parameters in addition to or instead of adding stochasticity to Lagrangian variables .e.g. Lagrangian displacement, velocity etc. This is something that was experimented with in Berloff & McWilliams (2003), Sykulski et al. (2016) and Veneziani et al. (2005). The idea behind this is to try and capture the distribution of parameter values, as model parameters are typically determined as an ensemble average even though there may be a relatively large variance. Lagrangian trajectories simulated using averaged statistics may not produce the full range of behaviours observed.

Firstly, let's focus on the application of this method in the looping Markov-1 model in Veneziani et al. (2005). As there is a trimodal distribution of Ω, consisting of non-loopers, cyclonic and anti-cyclonic loopers, it is important to capture all these types of behaviours. However, it is possible that a Lagrangian trajectory can transition from one behaviour to another. A transition probability P_{nm} is defined, where n and m denote the transition start type and destination type. Vortices evolve in time, and the strong PV gradient is only a partial barrier to transport, and so particles can escape and hence become non-looping. P_{nm} represents the probability of this occurrence. $P_{nm} = P_{mn}$ to ensure that the percentage of looping and non-looping trajectories remains constant.

Berloff & McWilliams (2003) focuses on introducing a distributed first kinematic time-scale:

$$T^{(1)}_{ik} T^{(1)}_{kj} = \sigma_{ik} [\xi]^{-1}_{kj}, \tag{6.16}$$

where ξ_{ij} is the Lagrangian acceleration variance, to the Markov-2 model. The distribution of $T^{(1)}_{ii}$ is found from Lagrangian data obtained from particles advected by the QG double gyre model. It was shown to result in more realistic Lagrangian autocorrelation functions than the

standard Markov-2 model. This approach however will need to be extended so randomness can be added to other model parameters.

Chapter 7

Conclusion and Future Work

The first chapters in this thesis were concerned with the model set-up of the dynamical and transport models. We used a 2 layer doubly-periodic QG ocean model as described in Karabasov et al. (2009). We varied the bottom friction to generate two different meandering jet regimes. Bottom friction is used in an effort to resolve the bottom boundary layer (Rivire et al. 2004) and acts as a drag, dampening vorticity in the bottom layer (Berloff et al. 2011). It is known that the bottom friction has a role in controlling the influence of large-scales and mesoscales. Rivire et al. (2004) states that a small bottom friction results in flows with large horizontal (i.e. zonal) scales, and that the mesoscale is more energetic with a greater bottom friction. We refer to these jets as coherent and latent, using similar terminology to that used in Berloff et al. (2011). A key property differentiating these two regimes is the frequency of jet break-up. Both jets are defined by strong potential vorticity gradients surrounded by regions of PV mixing and return flows. The coherent jet exhibits an almost periodic propagating meander that remains relatively stable throughout the simulation. The latent jet, however, frequently undergoes disruption of the PV gradient and sheds vortices as a result. Therefore, there is more PV mixing on the jet flanks. Furthermore, the time-averaged zonal velocity demonstrates that the coherent jet shows less positional variability. This is indicated by a narrower band of enhanced positive zonal velocity. This is in agreement with Berloff et al. (2011) and Khatri & Berloff (2018), where smaller bottom friction values are associated with a more PV staircase like structure as described by Dritschel & McIntyre (2008). They also found that increasing

the bottom friction results in greater eddy kinetic energy and weaker mean flows.

Chapter 3 focused on building and testing the transport model that will be used to advect particles. We built a transport model especially for use in our dynamical model that made use of the uniform grid, double-periodicity and non-divergence. We derived and tested the accuracy and performance times of two novel spatial interpolation methods: 2D-cubic and bicubic. They are both motivated by finding a polynomial approximation for the stream function that can then be differentiated to find the velocity using the non-divergence principle. It was found that the 2D-cubic method was both more accurate and faster than the bicubic method. The bicubic method was limited by matrix inversion. However the 2D-cubic method is un-symmetric and so the advantages in accuracy gained by the 2D-cubic method may be due to the un-symmetry of our flow, or in other words, that it is zonally dominated. The 2D-cubic algorithm may need to be flipped for a meridionally dominated flow. These are questions that would need to be answered before applying these spatial interpolation methods to other flow fields. We then compare two different time integration schemes: euler and Runge-Kutta fourth-order (RK4) methods and found that RK4 dramatically increased the accuracy of the transport model.

In chapter 4 we both investigate the work carried out in Ferrari & Nikurashin (2010) and use the transport model built in chapter 3 to advect particles by the flow fields generated by the dynamical model.

The first thing we consider is how to appropriately isolate eddying effects on Lagrangian transport. We follow the reasoning of Rypina et al. (2012) by introducing the concept of full-following-eddy (FFE) trajectories. Real floats and drifters in the ocean will be advected by the full flow, not the eddying flow, therefore it is more relevant to ask what the eddying effects are on the full trajectory. We find that the most significant difference between the two eddying trajectories is in the meridional direction. The eddying flow on its own over-estimates top layer meridional diffusivity and suggests there is much more meridional mixing than is actually present. This implies that the zonal jets acts to suppress eddy-induced meridional mixing.

We advected particles using a simplified version of the kinematic model used in Ferrari & Nikurashin (2010) to verify that FFE meridional dispersion is maximised when the eddy propagation speed equals the uniform background velocity. We also find that the same behaviour is

observed in the zonal direction. We repeat this experiment but with a Gaussian jet, and find that dispersion is maximised when the eddy propagation speed equals the average background zonal velocity. We also find that sub diffusion occurs when the background velocity differs from the eddy propagation speed and that super diffusion occurs otherwise.

We also verify that the diffusive and isotropic estimate is not appropriate to parameterise material transport. Meridional transport is consistently sub-diffusive, behaviour which is typically associated with trapping of particles inside vortices (Berloff et al. 2002, Veneziani et al. 2005). Even in the absence of the mean zonal flow, zonal transport is super-diffusive.

However, the obtained Lagrangian statistics are smeared. Uniformly binning the domain zonally results in bins that may not capture the whole jet as it meanders, so the jet may occupy several bins. A single bin may also describe several distinct regions, such as a transport barrier associated with the jet core, and the flanks for the jet core which may be associated with enhanced mixing. Furthermore, due to the large meridional variation in the jet core, particles that remain on the jet core will exhibit a large oscillatory meridional dispersion, even though they may not have dispersed relative to the jet core. Therefore we introduce a meridionally monotonic coordinate derived from flow properties. We map and uniformly bin the zonally and temporally averaged PV to the y coordinate. Our new dispersion measure is referred to as PV-mapped dispersion. This new PV-mapped dispersion method more aptly captures a meridional diffusivity maximum around the jet core for both jet regimes. The coherent jet, however, also has a slight minimum in the jet core. This demonstrates enhanced dispersion on the jet flanks, but that the jet core is a barrier to transport. We however find that in regions of high PV mixing in the surf zones, the PV-mapped diffusivity is underestimated. The PV-mapped locality time-scale in the latent jet clearly demonstrates how particles are leaving the PV isoline around the jet core, but stay closer to their PV isoline for a longer period of time in the jet flanks. This is in contrast to the regular locality time-scale in the latent jet which showed little variation across the domain.

There are, however, limitations to this method. Firstly, it relies on being able to find a flow variable that varies monotonically against y, or some other spatial coordinate. This means that there must be some kind of PV staircase like structure, and we can only obtain statistics

in one direction. Furthermore, in order to obtain a monotonic variable, we perform both zonal and temporal averaging and therefore results in some smearing. Perhaps even sharper statistics could be obtained with another less averaged variable.

One Lagrangian statistical measure that we did not explore that has been of use in diagnosing mixing barriers and Lagrangian coherent structures is that of Lyapunov exponents (Haller & Yuan 2000). A Lyapunov exponent quantifies the rate of separation of infinitesimally close particles. This may provide a better diagnosis for the partial transport barrier and allow us to more aptly compare the nature of the two jet regimes. However, it is a two-particle statistic that diagnoses mixing as opposed to transport and so would not provide useful statistics to be used for parameterising Lagrangian transport. Furthermore, calculating the jet core crossing-rate of particles, similarly to that done in Berloff et al. (2002), may provide further insight into whether particles are being repelled away from the jet core, or are in fact crossing the jet.

In the chapter 5 we attempt a kinematic approach to parameterisation by decomposing the flow into Empirical Orthogonal Functions. We firstly carry out some analysis to establish if we can reproduce the observed Lagrangian statistics with a reasonable number of EOFs, and then deduce the role of EOFs in Lagrangian dispersion before motivating a kinematic model.

We find that even with the 20 EOFs, we don't fully capture meridional spreading, illustrating that a kinematic model will not be appropriate for meridional transport parameterisation. Zonal dispersion however is almost entirely captured by 20. Our following analysis reveals that a single row of zonally propagating eddies with a wavelength of half the domain accounts for most of the zonal dispersion in the top layer. We then synthetically reproduce these EOFs to recapture the zonal dispersion. We also establish a critical eddy propagation speed that maximises zonal transport and minimises meridional transport as induced by the analytic flow field. This analytic flow field also induces a zonal Stokes' drift. It however remains to establish a relationship between the large-scale flow and the parameters that determine the Stokes' drift before a kinematic model can be used in oceanic parameterisations.

In chapter 6 we explore the applicability of a hierarchy of Markov models of integer orders using Lagrangian statistics as calculated in chapter 4. We find that the method used to calculate the diffusivity, whether from the dispersion or the Lagrangian velocity variance, is important

due to significantly non-diffusive transport. We find that the zonal dispersion is relatively well captured by the Markov-1 model as dispersion is dominated by mean flow effects. Markov-1 also performs slightly better than the diffusive model in the meridional direction, though it still does not capture sub-diffusive spreading.

Instead of taking the approach in Berloff & McWilliams (2002) by introducing randomness to the acceleration, we introduce a cross-correlation parameter Ω, motivated by Veneziani et al. (2005). This will result in oscillatory Lagrangian autocorrelation functions. We however find, that as our zonal dispersion is strongly super-diffusive and so doesn't exhibit a strongly oscillatory autocorrelation function, this model is not appropriate for use in jet dominated flows.

We also test the use of PV-mapped diffusivity in the Markov-0 and Markov-1 model. We find that it results in a slightly more accurate dispersion in the immediate jet core vicinity. Though this area of improved accuracy is quite limited as the diffusivity is substantially underestimated elsewhere, particularly for the latent jet. We suggest that perhaps a spatial mixture of the two measures may be more appropriate, however it remains to establish the criteria that must be met in order for the PV-mapped diffusivity to be relevant. We hypothesise that in regions near a strong PV gradient it may be of use, though this remains to be verified.

7.1 Summary of Findings

In this thesis we clearly establish anisotropic and non-diffusive Lagrangian transport is consistently observed and therefore novel parameterisation techniques must be examined. By introducing a flow based dispersion measure, we are able to capture a diffusivity maximum at the jet core and verify that particles are less likely to stick to their PV isoline in the jet core, but remain closer to their PV isoline on the flanks. Furthermore, the latent jet appears to be a weaker barrier to transport, exhibited by smaller diffusivity estimates. We also find that zonal and meridional transport are sufficiently un-correlated, illustrated by small values for Ω, that it makes sense to treat the two directions as independent. The mechanism behind zonal dispersion is much better understood through the dominance of the mean flow and by representing the

eddying-component of Lagrangian transport as a Stokes' drift. Therefore, more complicated techniques may not be needed to capture the zonal dispersion. More work needs to be done, however, to understand the mechanisms behind meridional dispersion. It is not captured by a large number of EOF modes, so we can conclude that very small flow variabilities play a significant role in meridional dispersion. Therefore, we hypothesise that we cannot capture meridional Lagrangian transport deterministically. We must resort to Stochastic methods.

We find a significant time period where sub-diffusivity is captured, for which at least a Markov-2 model is needed. We argue, however, that we should not need to exceed a Markov-2 model and that zonal dispersion can be understood by other means. van Sebille et al. (2018) also reiterates that Markov models can be used to account for velocity correlations that are as a result of eddy processes.

7.2 Summary of Further Work

A key property of the 2D-cubic spatial interpolation method is that, as it calculates cubic polynomials at the y coordinates first, it is antisymmetric. Would the 2D-cubic regime still be more accurate if the method was rotated 90 degrees to calculate cubic polynomials in x first? Also, what is the threshold of the ratio of number of Lagrangian particles to number of time steps at which the bicubic method starts to perform faster than the 2D-cubic method?

It is not completely clear whether particles are diverging away from the jet core, or are crossing the jet core. Therefore it remains to explore jet core crossing-rates similarly to that done in Berloff et al. (2002). Two-particle statistics such as Lyapunov exponents can also illustrate whether particles are diverging from each other. A maximum Lyapunov exponent illustrates chaotic mixing and a rapid divergence of particles.

More investigation of the PV-mapped dispersion method should be carried out. The idea of trying to obtain less smeared and more flow based dispersion statistics would be useful in order to calculate more local diagnostics. If we were to simulate an even more latent jet by further increasing the bottom friction, would we still see a K_{PV} maximum? Or would the instantaneous PV be too mixed meridionally that PV binned particles would not form any spatial structure?

How would the idea of PV-mapped dispersion apply to real data? Can we obtain sufficiently high-resolution data to calculate the PV at the particle location accurately enough? Also, could a monotonic flow based coordinate be determined? It may be necessary to diagonalise the flow field before performing such analysis so that the flow appears zonal. This would have to be performed in regions with a sufficiently high PV gradient, such as near the separation point of the Gulf Stream or the ACC.

In order to apply a Stokes' drift based kinematic model to an OGCM, it is necessary to find the relationship between the coarse-grained large-scale flow and the half Rossby wave parameters, such as wave width, amplitude and period. It also remains to establish what the relationship between the critical eddy propagation speed, that maximises zonal transport and minimises meridional transport, and flow variables is, and whether it is the lack of meridional wave number that results in the cross-jet transport suppression.

We have verified that sub-diffusivity needs to be able to be simulated in order to effectively parameterise meridional transport, therefore it remains to test the accuracy of a Markov-2 model. This is the minimum order model that we would need. The Matèrn process may also prove effective, though it is slightly less simple.

Bibliography

Abernathey, R. P. & Marshall, J. (2013), 'Global surface eddy diffusivities derived from satellite altimetry', *Journal of Geophysical Research: Oceans* **118**(2), 901–916.
URL: *https://agupubs.onlinelibrary.wiley.com/doi/abs/10.1002/jgrc.20066*

Berloff, P., Karabasov, S., Farrar, J. T. & Kamenkovich, I. (2011), 'On latency of multiple zonal jets in the oceans', *Journal of Fluid Mechanics* **686**, 534567.

Berloff, P. & McWilliams, J. C. (2002), 'Material transport in oceanic gyres. part ii: Hierarchy of stochastic models', *Journal of Physical Oceanography* **32**(3), 797–830.
URL: *http://dx.doi.org/10.1175/1520-0485(2002)032¡0797:MTIOGP¿2.0.CO;2*

Berloff, P. & McWilliams, J. C. (2003), 'Material Transport in Oceanic Gyres. Part III: Randomized Stochastic Models', *Journal of Physical Oceanography* **33**(7), 1416–1445.
URL: *http://dx.doi.org/10.1175/1520-0485(2003)033¡1416:MTIOGP¿2.0.CO;2*

Berloff, P. S. (2005), 'Random-forcing model of the mesoscale oceanic eddies', *Journal of Fluid Mechanics* **529**, 7195.

Berloff, P. S., McWilliams, J. C. & Bracco, A. (2002), 'Material Transport in Oceanic Gyres. Part I: Phenomenology', *Journal of Physical Oceanography* **32**(3), 764–796.
URL: *https://doi.org/10.1175/1520-0485(2002)032¡0764:MTIOGP¿2.0.CO;2*

Boland, E. J. D., Thompson, A. F., Shuckburgh, E. & Haynes, P. H. (2012), 'The Formation of Nonzonal Jets over Sloped Topography', *Journal of Physical Oceanography* **42**(10), 1635–1651.
URL: *https://doi.org/10.1175/JPO-D-11-0152.1*

Booth, J. & Kamenkovich, I. (2008), 'Isolating the role of mesoscale eddies in mixing of a passive tracer in an eddy resolving model', *Journal of Geophysical Research: Oceans* **113**(C5).

Boughton, B. A., Delaurentis, J. M. & Dunn, W. E. (1987), 'A stochastic model of particle dispersion in the atmosphere', *Boundary-Layer Meteorology* **40**(1), 147–163.
URL: *https://doi.org/10.1007/BF00140073*

Bower, A. S. (1991), 'A Simple Kinematic Mechanism for Mixing Fluid Parcels across a Meandering Jet', *Journal of Physical Oceanography* **21**(1), 173–180.
URL: *http://dx.doi.org/10.1175/1520-0485(1991)021¡0173:ASKMFM¿2.0.CO;2*

Bower, A. S. & Lozier, M. S. (1994), 'A Closer Look at Particle Exchange in the Gulf Stream', *Journal of Physical Oceanography* **24**(6), 1399–1418.
URL: *http://dx.doi.org/10.1175/1520-0485(1994)024¡1399:ACLAPE¿2.0.CO;2*

Bower, A. S., Rossby, H. T. & Lillibridge, J. L. (1985), 'The gulf streambarrier or blender?', *Journal of Physical Oceanography* **15**(1), 24–32.
URL: *https://doi.org/10.1175/1520-0485(1985)015¡0024:TGSOB¿2.0.CO;2*

Bower, A. S. & Rossby, T. (1989), 'Evidence of Cross-Frontal Exchange Processes in the Gulf Stream Based on Isopycnal RAFOS Float Data', *Journal of Physical Oceanography* **19**(9), 1177–1190.
URL: *http://dx.doi.org/10.1175/1520-0485(1989)019¡1177:EOCFEP¿2.0.CO;2*

Brach, L., Deixonne, P., Bernard, M.-F., Durand, E., Desjean, M.-C., Perez, E., van Sebille, E. & ter Halle, A. (2018), 'Anticyclonic eddies increase accumulation of microplastic in the north atlantic subtropical gyre', *Marine Pollution Bulletin* **126**, 191 – 196.
URL: *http://www.sciencedirect.com/science/article/pii/S0025326X17309232*

Chapman, C. C. & Morrow, R. (2014), 'Variability of southern ocean jets near topography', *Journal of Physical Oceanography* **44**(2), 676–693.
URL: *https://doi.org/10.1175/JPO-D-13-0182.1*

Chen, R. & Waterman, S. (2017), 'Mixing nonlocality and mixing anisotropy in an idealized

western boundary current jet', *Journal of Physical Oceanography* **47**(12), 3015–3036.
URL: *https://doi.org/10.1175/JPO-D-17-0011.1*

Constantin, A. & Villari, G. (2008), 'Particle trajectories in linear water waves', *Journal of Mathematical Fluid Mechanics* **10**, 1–18.

Davis, R. E. (1987), 'Modeling eddy transport of passive tracers', *Journal of Marine Research* **45**(3), 635–666.
URL: *https://www.ingentaconnect.com/content/jmr/jmr/1987/00000045/00000003/art00006*

Dosio, A., Guerau de Arellano, J. V., Holtslag, A. A. M. & Builtjes, P. J. H. (2005), 'Relating eulerian and lagrangian statistics for the turbulent dispersion in the atmospheric convective boundary layer', *Journal of the Atmospheric Sciences* **62**(4), 1175–1191.
URL: *https://doi.org/10.1175/JAS3393.1*

Dritschel, D. G. & McIntyre, M. E. (2008), 'Multiple jets as pv staircases: The phillips effect and the resilience of eddy-transport barriers', *Journal of the Atmospheric Sciences* **65**(3), 855–874.
URL: *https://doi.org/10.1175/2007JAS2227.1*

Dritschel, D. G. & Scott, R. K. (2011), 'Jet sharpening by turbulent mixing', *Philosophical Transactions of the Royal Society A: Mathematical, Physical and Engineering Sciences* **369**(1937), 754–770.
URL: *https://royalsocietypublishing.org/doi/abs/10.1098/rsta.2010.0306*

Drouin, K., Mariano, A., Ryan, E. & Laurindo, L. (2019), 'Lagrangian simulation of oil trajectories in the florida straits', *Marine Pollution Bulletin* **140**, 204 – 218.
URL: *http://www.sciencedirect.com/science/article/pii/S0025326X19300414*

Everett, J. D., van Sebille, E., Taylor, M. D., Suthers, I. M., Setio, C., Cetina-Heredia, P. & Smith, J. A. (2017), 'Dispersal of eastern king prawn larvae in a western boundary current: New insights from particle tracking', *Fisheries Oceanography* **26**(5), 513–525.

Ferrari, R. & Nikurashin, M. (2010), 'Suppression of eddy diffusivity across jets in the southern

ocean', *Journal of Physical Oceanography* **40**(7), 1501–1519.
URL: *https://doi.org/10.1175/2010JPO4278.1*

Fox-Kemper, B., Danabasoglu, G., Ferrari, R., Griffies, S., Hallberg, R., Holland, M., Maltrud, M., Peacock, S. & Samuels, B. (2011), 'Parameterization of mixed layer eddies. iii: Implementation and impact in global ocean climate simulations', *Ocean Modelling* **39**(1), 61 – 78. Modelling and Understanding the Ocean Mesoscale and Submesoscale.
URL: *http://www.sciencedirect.com/science/article/pii/S1463500310001290*

García-Garrido, V. J., Curbelo, J., Mechoso, C. R., Mancho, A. M. & Wiggins, S. (2017), 'A simple kinematic model for the lagrangian description of relevant nonlinear processes in the stratospheric polar vortex', *Nonlinear Processes in Geophysics* **24**(2), 265–278.
URL: *https://www.nonlin-processes-geophys.net/24/265/2017/*

Greenslade, M. D. & Haynes, P. H. (2008), 'Vertical transition in transport and mixing in baroclinic flows', *Journal of the Atmospheric Sciences* **65**(4), 1137–1157.
URL: *https://doi.org/10.1175/2007JAS2236.1*

Griffa, A. (1996), Stochastic modelling in physical oceanography, Birkhauser Boston Inc., Cambridge, MA, USA, chapter Applications of Stochastic Particle Models to Oceanographic Problems, pp. 113–140.
URL: *http://dl.acm.org/citation.cfm?id=242899.242910*

Griffa, A., Owens, K., Piterbarg, L. & Rozovskii, B. (1995), 'Estimates of turbulence parameters from lagrangian data using a stochastic particle model', *Journal of Marine Research* **53**(3), 371–401.
URL: *https://www.ingentaconnect.com/content/jmr/jmr/1995/00000053/00000003/art00003*

Haller, G. & Yuan, G. (2000), 'Lagrangian coherent structures and mixing in two-dimensional turbulence', *Physica D: Nonlinear Phenomena* **147**(34), 352 – 370.
URL: *http://www.sciencedirect.com/science/article/pii/S0167278900001421*

Hardesty, B. D., Harari, J., Isobe, A., Lebreton, L., Maximenko, N., Potemra, J., van Sebille, E., Vethaak, A. D. & Wilcox, C. (2017), 'Using numerical model simulations to improve

the understanding of micro-plastic distribution and pathways in the marine environment', *Frontiers in Marine Science* **4**, 30.
URL: *https://www.frontiersin.org/article/10.3389/fmars.2017.00030*

Haynes, P. H., Poet, D. A. & Shuckburgh, E. F. (2007), 'Transport and mixing in kinematic and dynamically consistent flows', *Journal of the Atmospheric Sciences* **64**(10), 3640–3651.
URL: *https://doi.org/10.1175/JAS4030.1*

Henry, D. (2019), 'Stokes drift in equatorial water waves, and wavecurrent interactions', *Deep Sea Research Part II: Topical Studies in Oceanography* **160**, 41 – 47. Waves and Currents.
URL: *http://www.sciencedirect.com/science/article/pii/S0967064518301334*

Juckes, M. N. & McIntyre, M. E. (1987), 'A high-resolution one-layer model of breaking planetary waves in the stratosphere', *Nature* **328**(6131), 590–596.
URL: *https://doi.org/10.1038/328590a0*

Kamenkovich, I., Berloff, P. & Pedlosky, J. (2009), 'Anisotropic Material Transport by Eddies and Eddy-Driven Currents in a Model of the North Atlantic', *Journal of Physical Oceanography* **39**(12), 3162–3175.
URL: *http://dx.doi.org/10.1175/2009JPO4239.1*

Kamenkovich, I., Rypina, I. I. & Berloff, P. (2015), 'Properties and Origins of the Anisotropic Eddy-Induced Transport in the North Atlantic', *Journal of Physical Oceanography* **45**(3), 778–791.
URL: *http://dx.doi.org/10.1175/JPO-D-14-0164.1*

Karabasov, S., Berloff, P. & Goloviznin, V. (2009), 'CABARET in the ocean gyres', *Ocean Modelling* **30**(23), 155 – 168.
URL: *http://www.sciencedirect.com/science/article/pii/S1463500309001267*

Khatri, H. & Berloff, P. (2018), 'Role of eddies in the maintenance of multiple jets embedded in eastward and westward baroclinic shears', *Fluids* **3**, 91.

Klocker, A. & Abernathey, R. (2014), 'Global patterns of mesoscale eddy properties and diffusivities', *Journal of Physical Oceanography* **44**(3), 1030–1046.
URL: *https://doi.org/10.1175/JPO-D-13-0159.1*

Klocker, A., Ferrari, R. & LaCasce, J. H. (2012), 'Estimating suppression of eddy mixing by mean flows', *Journal of Physical Oceanography* **42**(9), 1566–1576.
URL: *https://doi.org/10.1175/JPO-D-11-0205.1*

Klocker, A., Ferrari, R., Lacasce, J. & Merrifield, S. (2012), 'Reconciling float-based and tracer-based estimates of eddy diffusivities in the southern ocean', *Journal of Marine Research* **70**, 569–602.

LaCasce, G. I. (2008), 'Statistics from Lagrangian observations', *Progress in Oceanography* **77**(1), 1 – 29.
URL: *http://www.sciencedirect.com/science/article/pii/S0079661108000232*

Lacorata, G., Palatella, L. & Santoleri, R. (2014), 'Lagrangian predictability characteristics of an ocean model', *Journal of Geophysical Research: Oceans* **119**(11), 8029–8038.
URL: *https://agupubs.onlinelibrary.wiley.com/doi/abs/10.1002/2014JC010313*

Li, X., Chang, P. & Pacanowski, R. C. (1996), 'A wave-induced stirring mechanism in the mid-depth equatorial ocean', *Journal of Marine Research* **54**(3), 487–520.
URL: *https://www.ingentaconnect.com/content/jmr/jmr/1996/00000054/00000003/art00005*

Lilly, J. M., Sykulski, A. M., Early, J. J. & Olhede, S. C. (2017), 'Fractional Brownian motion, the Matérn process, and stochastic modeling of turbulent dispersion', *Nonlinear Processes in Geophysics* **24**(3), 481–514.

Liu, Y., Wilson, C., Green, M. A. & Hughes, C. W. (2018), 'Gulf stream transport and mixing processes via coherent structure dynamics', *Journal of Geophysical Research: Oceans* **123**(4), 3014–3037.
URL: *https://agupubs.onlinelibrary.wiley.com/doi/abs/10.1002/2017JC013390*

Lumpkin, R. & Pazos, M. (2007), *Measuring surface currents with Surface Velocity Program*

drifters: the instrument, its data, and some recent results, Cambridge University Press, p. 3967.

Lumpkin, R., Treguier, A.-M. & Speer, K. (2002), 'Lagrangian eddy scales in the northern atlantic ocean', *Journal of Physical Oceanography* **32**(9), 2425–2440.
URL: *https://doi.org/10.1175/1520-0485-32.9.2425*

Mana, P. P. & Zanna, L. (2014), 'Toward a stochastic parameterization of ocean mesoscale eddies', *Ocean Modelling* **79**, 1 – 20.
URL: *http://www.sciencedirect.com/science/article/pii/S1463500314000420*

Marshall, D. P., Vogel, B. & Zhai, X. (2013), 'Rossby rip currents', *Geophysical Research Letters* **40**(16), 4333–4337.
URL: *https://agupubs.onlinelibrary.wiley.com/doi/abs/10.1002/grl.50842*

Marshall, J., Scott, J. R., Romanou, A., Kelley, M. & Leboissetier, A. (2017), 'The dependence of the ocean's moc on mesoscale eddy diffusivities: A model study', *Ocean Model.* **111**, 1–8.

Marshall, J., Shuckburgh, E., Jones, H. & Hill, C. (2006), 'Estimates and implications of surface eddy diffusivity in the southern ocean derived from tracer transport', *Journal of Physical Oceanography* **36**(9), 1806–1821.
URL: *https://doi.org/10.1175/JPO2949.1*

McWilliams, J. C. (1977), 'A note on a consistent quasigeostrophic model in a multiply connected domain', *Dynamics of Atmospheres and Oceans* **1**(5), 427 – 441.
URL: *http://www.sciencedirect.com/science/article/pii/0377026577900021*

Nakamura, N. (1996), 'Two-dimensional mixing, edge formation, and permeability diagnosed in an area coordinate', *Journal of the Atmospheric Sciences* **53**(11), 1524–1537.
URL: *https://doi.org/10.1175/1520-0469(1996)053¡1524:TDMEFA¿2.0.CO;2*

Nakamura, N. (2008), 'Sensitivity of Global Mixing and Fluxes to Isolated Transport Barriers', *Journal of the Atmospheric Sciences* **65**(12), 3800–3818.
URL: *https://doi.org/10.1175/2008JAS2641.1*

Naveira Garabato, A. C., Ferrari, R. & Polzin, K. L. (2011), 'Eddy stirring in the southern ocean', *Journal of Geophysical Research: Oceans* **116**(C9).
URL: *https://agupubs.onlinelibrary.wiley.com/doi/abs/10.1029/2010JC006818*

O'Dwyer, J., Williams, R., LaCasce, J. & Speer, K. (2000), 'Does the Potential Vorticity Distribution Constrain the Spreading of Floats in the North Atlantic?', *Journal of Physical Oceanography* **30**(4), 721–732.
URL: *http://dx.doi.org/10.1175/1520-0485(2000)030¡0721:DTPVDC¿2.0.CO;2*

Onink, V., Wichmann, D., Delandmeter, P. & van Sebille, E. (2019), 'The role of ekman currents, geostrophy, and stokes drift in the accumulation of floating microplastic', *Journal of Geophysical Research: Oceans* **124**(3), 1474–1490.
URL: *https://agupubs.onlinelibrary.wiley.com/doi/abs/10.1029/2018JC014547*

Pierrehumbert, R. T. (1991), 'Largescale horizontal mixing in planetary atmospheres', *Physics of Fluids A* **3**(5), 1250–1260.
URL: *http://scitation.aip.org/content/aip/journal/pofa/3/5/10.1063/1.858053*

Prandtl, L. (1925), '7. bericht ber untersuchungen zur ausgebildeten turbulenz', *ZAMM - Journal of Applied Mathematics and Mechanics / Zeitschrift fr Angewandte Mathematik und Mechanik* **5**(2), 136–139.
URL: *https://onlinelibrary.wiley.com/doi/abs/10.1002/zamm.19250050212*

Reynolds, A. M. (1999), 'A second-order lagrangian stochastic model for particle trajectories in inhomogeneous turbulence', *Quarterly Journal of the Royal Meteorological Society* **125**(557), 1735–1746.
URL: *https://rmets.onlinelibrary.wiley.com/doi/abs/10.1002/qj.49712555713*

Reynolds, A. M. (2003), 'Third-order lagrangian stochastic modeling', *Physics of Fluids* **15**(9), 2773–2777.
URL: *https://doi.org/10.1063/1.1600732*

Riha, S. & Eden, C. (2011), 'Lagrangian and eulerian lateral diffusivities in zonal jets', *Ocean Modelling* **39**(1), 114 – 124. Modelling and Understanding the Ocean Mesoscale and Subme-

soscale.

URL: *http://www.sciencedirect.com/science/article/pii/S1463500311000254*

Rivire, P., Treguier, A. M. & Klein, P. (2004), 'Effects of bottom friction on nonlinear equilibration of an oceanic baroclinic jet', *Journal of Physical Oceanography* **34**(2), 416–432.

URL: *https://doi.org/10.1175/1520-0485(2004)034¡0416:EOBFON¿2.0.CO;2*

Rodean, H. C. (1996), 'Stochastic lagrangian models of turbulent diffusion', *Meteorological Monographs* **48**, 1–84.

URL: *https://doi.org/10.1175/0065-9401-26.48.1*

Roundy, P. E. (2015), 'On the interpretation of eof analysis of enso, atmospheric kelvin waves, and the mjo', *Journal of Climate* **28**(3), 1148–1165.

URL: *https://doi.org/10.1175/JCLI-D-14-00398.1*

Rypina, I. I., Brown, M. G., Beron-Vera, F. J., Koçak, H., Olascoaga, M. J. & Udovydchenkov, I. A. (2007), 'On the Lagrangian Dynamics of Atmospheric Zonal Jets and the Permeability of the Stratospheric Polar Vortex', *Journal of the Atmospheric Sciences* **64**(10), 3595–3610.

URL: *http://dx.doi.org/10.1175/JAS4036.1*

Rypina, I., Kamenkovich, I. I., Berloff, P. & Pratt, L. J. (2012), 'Eddy-Induced Particle Dispersion in the Near-Surface North Atlantic', *Journal of Physical Oceanography* **42**(12), 2206–2228.

URL: *http://dx.doi.org/10.1175/JPO-D-11-0191.1*

Sallee, J. B., Speer, K., Morrow, R. & Lumpkin, R. (2008), 'An estimate of Lagrangian eddy statistics and diffusion in the mixed layer of the Southern Ocean', *Journal of Marine Research* **66**(4), 441–463.

URL: *http://www.ingentaconnect.com/content/jmr/jmr/2008/00000066/00000004/art00002*

Samelson, R. M. (1992), 'Fluid exchange across a meandering jet', *Journal of Physical Oceanography* **22**(4), 431–444.

URL: *https://doi.org/10.1175/1520-0485(1992)022¡0431:FEAAMJ¿2.0.CO;2*

Samelson, R. M. & Wiggins, S. (2006), *Lagrangian transport in geophysical jets and waves: The dynamical systems approach*, Vol. 31, Springer Science & Business Media.

Sinha, A., Balwada, D., Tarshish, N. & Abernathey, R. (2019), 'Modulation of lateral transport by submesoscale flows and inertia-gravity waves', *Journal of Advances in Modeling Earth Systems* **11**(4), 1039–1065.
URL: *https://agupubs.onlinelibrary.wiley.com/doi/abs/10.1029/2018MS001508*

Smith, K. S. (2007), 'Eddy Amplitudes in Baroclinic Turbulence Driven by Nonzonal Mean Flow: Shear Dispersion of Potential Vorticity', *Journal of Physical Oceanography* **37**(4), 1037–1050.
URL: *https://doi.org/10.1175/JPO3030.1*

Spence, P., van Sebille, E., Saenko, O. A. & England, M. H. (2014), 'Using eulerian and lagrangian approaches to investigate wind-driven changes in the southern ocean abyssal circulation', *Journal of Physical Oceanography* **44**(2), 662–675.
URL: *https://doi.org/10.1175/JPO-D-13-0108.1*

Sykulski, A., Olhede, S., Lilly, J. & Danioux, E. (2016), 'Lagrangian time series models for ocean surface drifter trajectories', *Journal of the Royal Statistical Society: Series C (Applied Statistics)* **65**(1), 29–50.

Taylor, G. I. (1922), 'Diffusion by Continuous Movements', *Proceedings of the London Mathematical Society* **s2-20**(1), 196–212.
URL: *http://plms.oxfordjournals.org/content/s2-20/1/196.short*

Thomas, M. D., Trguier, A.-M., Blanke, B., Deshayes, J. & Voldoire, A. (2015), 'A lagrangian method to isolate the impacts of mixed layer subduction on the meridional overturning circulation in a numerical model', *Journal of Climate* **28**(19), 7503–7517.
URL: *https://doi.org/10.1175/JCLI-D-14-00631.1*

Thomas, M. D. & Zhai, X. (2013), 'Eddy-induced variability of the meridional overturning circulation in a model of the north atlantic', *Geophysical Research Letters* **40**(11), 2742–

2747.

URL: *https://agupubs.onlinelibrary.wiley.com/doi/abs/10.1002/grl.50532*

Thompson, A. F. & Salle, J.-B. (2012), 'Jets and topography: Jet transitions and the impact on transport in the antarctic circumpolar current', *Journal of Physical Oceanography* **42**(6), 956–972.

URL: *https://doi.org/10.1175/JPO-D-11-0135.1*

Thompson, L. & Kawase, M. (1993), 'The nonlinear response of an equatorial ocean to oscillatory forcing', *Journal of Marine Research* **51**(3), 467–496.

URL: *https://www.ingentaconnect.com/content/jmr/jmr/1993/00000051/00000003/art00002*

Thomson, D. J. (1987), 'Criteria for the selection of stochastic models of particle trajectories in turbulent flows', *Journal of Fluid Mechanics* **180**, 529556.

Thomson, D. J. & Wilson, J. D. (2013), *History of Lagrangian Stochastic Models for Turbulent Dispersion*, American Geophysical Union (AGU), chapter 3, pp. 19–36.

URL: *https://agupubs.onlinelibrary.wiley.com/doi/abs/10.1029/2012GM001238*

Treguier, A. M., Lique, C., Deshayes, J. & Molines, J. M. (2017), 'The north atlantic eddy heat transport and its relation with the vertical tilting of the gulf stream axis', *Journal of Physical Oceanography* **47**(6), 1281–1289.

URL: *https://doi.org/10.1175/JPO-D-16-0172.1*

Vallis, G. K. (2006), *Atmospheric and Oceanic Fluid Dynamics*, Cambridge University Press, Cambridge, U.K.

van den Bremer, T. & Breivik, O. (2018*a*), 'Stokes drift', *Philosophical Transactions of The Royal Society A Mathematical Physical and Engineering Sciences* **376**, 20170104.

van den Bremer, T. S. & Breivik, Ø. (2018*b*), 'Stokes drift', *Philosophical transactions. Series A, Mathematical, physical, and engineering sciences* **376**(2111), 20170104. 29229803[pmid].

URL: *https://pubmed.ncbi.nlm.nih.gov/29229803*

van den Bremer, T. S. & Taylor, P. H. (2015), 'Estimates of lagrangian transport by surface gravity wave groups: The effects of finite depth and directionality', *Journal of Geophysical Research: Oceans* **120**(4), 2701–2722.

URL: *https://agupubs.onlinelibrary.wiley.com/doi/abs/10.1002/2015JC010712*

Van Roekel, L. P., Ito, T., Haertel, P. T. & Randall, D. A. (2009), 'Lagrangian analysis of the meridional overturning circulation in an idealized ocean basin', *Journal of Physical Oceanography* **39**(9), 2175–2193.

URL: *https://doi.org/10.1175/2009JPO4110.1*

van Sebille, E., Griffies, S. M., Abernathey, R., Adams, T. P., Berloff, P., Biastoch, A., Blanke, B., Chassignet, E. P., Cheng, Y., Cotter, C. J., Deleersnijder, E., Ds, K., Drake, H. F., Drijfhout, S., Gary, S. F., Heemink, A. W., Kjellsson, J., Koszalka, I. M., Lange, M., Lique, C., MacGilchrist, G. A., Marsh, R., Adame, C. G. M., McAdam, R., Nencioli, F., Paris, C. B., Piggott, M. D., Polton, J. A., Rhs, S., Shah, S. H., Thomas, M. D., Wang, J., Wolfram, P. J., Zanna, L. & Zika, J. D. (2018), 'Lagrangian ocean analysis: Fundamentals and practices', *Ocean Modelling* **121**, 49 – 75.

URL: *http://www.sciencedirect.com/science/article/pii/S1463500317301853*

Veneziani, M., Griffa, A., Garraffo, Z. D. & Chassignet, E. P. (2005), 'Parameterizations of lagrangian spin statistics and particle dispersion in the presence of coherent vortices', *Journal of Marine Research* **63**, 1057–1083.

Veneziani, M., Griffa, A., Reynolds, A. M. & Mariano, A. J. (2004), 'Oceanic turbulence and stochastic models from subsurface lagrangian data for the northwest atlantic ocean', *Journal of Physical Oceanography* **34**(8), 1884–1906.

URL: *https://doi.org/10.1175/1520-0485(2004)034¡1884:OTASMF¿2.0.CO;2*

Waterman, S. & Hoskins, B. J. (2013), 'Eddy shape, orientation, propagation, and mean flow feedback in western boundary current jets', *Journal of Physical Oceanography* **43**(8), 1666–1690.

URL: *https://doi.org/10.1175/JPO-D-12-0152.1*

Weber, J. E. H. (2017), 'Equatorial stokes drift and rossby rip currents', *Journal of Geophysical Research: Oceans* **122**(6), 4819–4828.

URL: *https://agupubs.onlinelibrary.wiley.com/doi/abs/10.1002/2016JC012653*

Weijer, W. & van Sebille, E. (2014), 'Impact of agulhas leakage on the atlantic overturning circulation in the ccsm4', *Journal of Climate* **27**(1), 101–110.

URL: *https://doi.org/10.1175/JCLI-D-12-00714.1*

Ying, Y., Maddison, J. & Vanneste, J. (2019), 'Bayesian inference of ocean diffusivity from lagrangian trajectory data', *Ocean Modelling* **140**, 101401.

URL: *http://www.sciencedirect.com/science/article/pii/S1463500318303871*

Appendices

Appendix A

Derivation of 2D-cubic spatial interpolation

First, we construct the four one dimensional cubic polynomials that approximate the stream function on the blue dashed lines in fig. 3.1. That is

$$\psi_{y_k}(x) = \psi_{y_k}(a) = A_k + B_k a + C_k a^2 + D_k a^3, \tag{A.1}$$

where $a = x - x_i$, $\psi_{y_k}(a) = \psi(y_k, x)$ and $k = i-1, \cdots, i+2$.

These coefficients can be found analytically by constructing cubic Lagrange polynomials. A one dimensional cubic Lagrange polynomial $P(x)$ is expressed as follows:

$$P(x) = \sum_{k=i-1}^{i+2} \psi(x_k) L_k(x), \tag{A.2}$$

where

$$L_k(x) = \prod_{\substack{i-1 \le m \le i+2 \\ m \neq k}} \frac{x - x_m}{x_k - x_m}. \tag{A.3}$$

Hence,

$$
\begin{aligned}
L_{i-1}(x) &= \frac{x-x_i}{x_{i-1}-x_i}\frac{x-x_{i+1}}{x_{i-1}-x_{i+1}}\frac{x-x_{i+2}}{x_{i-1}-x_{i+2}}, \\
&= \frac{a}{-1}\frac{a-1}{-2}\frac{a-2}{-3}, \\
&= \frac{-a(a-1)(a-2)}{6}, \\
&= \frac{-a^3+3a^2-2a}{6}. \\
L_i(x) &= \frac{x-x_{i-1}}{x_i-x_{i-1}}\frac{x-x_{i+1}}{x_i-x_{i+1}}\frac{x-x_{i+1}}{x_i-x_{i+2}}, \\
&= \frac{1+a}{1}\frac{a-1}{-1}\frac{a-2}{-2}, \\
&= \frac{(1+a)(a-1)(a-2)}{2}, \\
&= \frac{a^3-2a^2-a+2}{2}. \\
L_{i+1}(x) &= \frac{x-x_{i-1}}{x_{i+1}-x_{i-1}}\frac{x-x_i}{x_{i+1}-x_i}\frac{x-x_{i+2}}{x_{i+1}-x_{i+2}}, \\
&= \frac{1+a}{2}\frac{a}{1}\frac{a-2}{-1}, \\
&= \frac{-a(1+a)(a-2)}{2}, \\
&= \frac{-a^3+a^2+2a}{2}. \\
L_{i+2}(x) &= \frac{x-x_{i-1}}{x_{i+2}-x_{i-1}}\frac{x-x_i}{x_{i+2}-x_i}\frac{x-x_{i+1}}{x_{i+2}-x_{i+1}}, \\
&= \frac{1+a}{3}\frac{a}{2}\frac{a-1}{1}, \\
&= \frac{a(1+a)(a-1)}{6}, \\
&= \frac{a^3-a}{6}.
\end{aligned}
$$

Substituting these values into the expression for $P(x)$ gives:

$$
\begin{aligned}
P(x) &= \psi(x_{i-1})\frac{-a^3+3a^2-2a}{6} + \psi(x_i)\frac{a^3-2a^2-a+2}{2} \\
&+ \psi(x_{i+1})\frac{-a^3+a^2+2a}{2} + \psi(x_{i+2})\frac{a^3-a}{6}, \\
&= \psi(x_i) + a\left(-\frac{1}{3}\psi(x_{i-1}) - \frac{1}{2}\psi(x_i) + \psi(x_{i+1}) + \frac{1}{6}\psi(x_{i+2})\right) \\
&+ a^2\left(\frac{1}{2}\psi(x_{i-1}) - \psi(x_i) + \frac{1}{2}\psi(x_{i+1})\right)
\end{aligned}
$$

$$+ a^3 \left(-\frac{1}{6}\psi(x_{i-1}) + \frac{1}{2}\psi(x_i) - \frac{1}{2}\psi(x_{i+1}) + \frac{1}{6}\psi(x_{i+2}) \right).$$

We wish to find four polynomials of this type that approximate ψ along the lines $y = y_{j-1}, \cdots, y_{j+2}$. So replacing $\psi(x)$ with $\psi(x, y_k), k = j-1, \cdots j+2$ gives,

$$A_k = \psi(x_i, y_k), \tag{A.4}$$

$$B_k = -\frac{1}{3}\psi(x_{i-1}, y_k) - \frac{1}{2}\psi(x_i, y_k) + \psi(x_{i+1}, y_k) - \frac{1}{6}\psi(x_{i+2}, y_k), \tag{A.5}$$

$$C_k = \frac{1}{2}\psi(x_{i-1}, y_k) - \psi(x_i, y_k) + \frac{1}{2}\psi(x_{i+1}, y_k), \tag{A.6}$$

$$D_k = -\frac{1}{6}\psi(x_{i-1}, y_k) + \frac{1}{2}\psi(x_i, y_k) - \frac{1}{2}\psi(x_{i+1}, y_k) + \frac{1}{6}\psi(x_{i+2}, y_k). \tag{A.7}$$

Now we wish to construct a one dimensional polynomial along the red dashed line that will be expressed in terms of the above four cubic polynomials, that is

$$\psi(x, y) = \alpha + \beta b + \gamma b^2 + \delta b^3, \tag{A.8}$$

where $b = y - y_j$ and $\alpha = \alpha(\psi(x, y_{j-1}), \cdots, \psi(x, y_{j+2}))$, similarly for β, γ, δ. These coefficients are constructed in exactly the same way as above, by using cubic Lagrange polynomials.

$$\alpha = \psi(x, y_j) = \psi_{y_j}(x), \tag{A.9}$$

$$\beta = -\frac{1}{3}\psi_{y_{j-1}}(x) - \frac{1}{2}\psi_{y_j}(x) + \psi_{y_{j+1}}(x) - \frac{1}{6}\psi_{y_{j+2}}(x), \tag{A.10}$$

$$\gamma = \frac{1}{2}\psi_{y_{j-1}}(x) - \psi_{y_j}(x) + \frac{1}{2}\psi_{y_{j+1}}(x), \tag{A.11}$$

$$\delta = -\frac{1}{6}\psi_{y_{j-1}}(x) + \frac{1}{2}\psi_{y_j}(x) - \frac{1}{2}\psi_{y_{j+1}}(x) + \frac{1}{6}\psi_{y_{j+2}}(x), \tag{A.12}$$

where we substitute in the expressions provided by eq. (A.1).

Now we have a polynomial approximation for ψ and can analytically differentiate it to find u and v at (x, y):

$$u = -\frac{\partial \psi}{\partial y} = -\frac{\partial \psi}{\partial b} = -\beta - 2\gamma b - 3\delta b^2, \tag{A.13}$$

$$v = \frac{\partial \psi}{\partial x} = \frac{\partial \psi}{\partial a} = \frac{\partial \alpha}{\partial a} + b\frac{\partial \beta}{\partial a} + b^2\frac{\partial \gamma}{\partial a} + b^3\frac{\partial \delta}{\partial a}. \tag{A.14}$$

Appendix B

2D-cubic code

B.1 Calculating the first set of coefficients

The subroutine calculating 1D cubic polynomial coefficients across the ii × jj grid. Each set of cubic polynomial coefficients a,b,c,d are calculated for each grid coordinate of y. (i.e. we get ii × jj 1D cubic polynomials defined in the y-direction)

```
      subroutine cubic_coeff_x(ii,jj,psi,a,b,c,d)

c INPUT : ii,jj : grid size
c INPUT : psi(ii,jj) : stream function snapshot
c OUTPUT : a(ii,jj),b(ii,jj),c(ii,jj),d(ii,jj) : polynomial coefficients

      implicit none

      integer ii,jj,i,j,n,ic(4)
      real*8 psi(ii,jj)
     &,a(ii,jj),b(ii,jj)
     &,c(ii,jj),d(ii,jj)
```

```
      do i = 1,ii
c i denotes the grid point to the left of the interpolation point in x
      do j = 1,jj
c j denotes the grid point above the interpolation point in y
c determine the 4 data points used to calculate the cubic polynomial

            do n = 1,4
                ic(n) = i - 2 + n
                      if (ic(n) <= 0) then
                            ic(n) = ii + ic(n)
                      elseif (ic(n) > ii) then
                            ic(n) = ic(n) - ii
                      endif
            enddo

c coefficients for the 4 1-D polynomials defined on the grid lines
c j =jc(1), jc(2), jc(3), jc(4)

                a(i,j) = psi(ic(2),j)
                b(i,j)= -psi(ic(1),j)/3 - psi(ic(2),j)/2
     &            +psi(ic(3),j) - psi(ic(4),j)/6
                c(i,j) = psi(ic(1),j)/2 - psi(ic(2),j)
     &            + psi(ic(3),j)/2
                d(i,j) = -psi(ic(1),j)/6 + psi(ic(2),j)/2
     &            -psi(ic(3),j)/2 + psi(ic(4),j)/6

      enddo
      enddo
      end subroutine
```

B.2 Finding cubic polynomials in terms of x at each y coordinate

The subroutine that takes the grid size: ii x jj, the snapshot streamfunction and the x coordinate of the interpolation point and returns the cubic polynomials approximated along x across the whole y direction in all possible locations of the y coordinate of the interpolation point. It takes a, b ,c and d from the previous subroutine as input (it avoids having to continuously recalculate the coefficients).

```
      subroutine cubic_poly_x(ii,jj,x,y,a,b,c,d,psi_interp_x)

c INPUT : ii,jj : grid size
c INPUT : x,y : the interpolation point values
c INPUT : a(ii,jj),b(ii,jj),c(ii,jj),d(ii,jj) : coefficients
c OUTPUT : psi_interp_x(4) : evaluated polynomial at the 4
c          surrounding y coordinates

      implicit none

      integer ii,jj,i,j,xc,jc(4),yc
      real*8 x, psi_interp_x(4),ax,y
      real*8 a(ii,jj),b(ii,jj)
     & ,c(ii,jj),d(ii,jj)

c grid point to the left of the interpolation point
      xc = int(x) + 1

      ax = x - int(x)
```

```
      yc = int(y) + 1


      do i = 1,4
           jc(i) = yc - 2 + i
           if (jc(i)>jj) then
                jc(i) = jc(i) - jj
           endif
           if(jc(i)<=0) then
                jc(i) = jc(i) + jj
           endif


      enddo


      do i = 1,4
           psi_interp_x(i) = a(xc,jc(i)) + b(xc,jc(i))*ax
     &        + c(xc,jc(i))*ax**2
     & + d(xc,jc(i))*ax**3
      enddo


      return


      end subroutine
```

B.3 Finding the second set of coefficients defined in terms of x

The subroutine that takes the grid size, `psi_x`, from the previous subroutine and the x coordinate of the interpolation point and constructs the coefficients for the cubic polynomial that

approximates the streamfunction on the line x.

```
      subroutine cubic_coeff_y(ii,jj,psi_x,alpha,beta,gamma,delta)

c INPUT: ii,jj : grid size
c INPUT: psi_x(4) : output of cubic_poly_x
c OUTPUT : alpha,beta,gamma,delta : cubic polynomial coefficients
c          of the final 2D cubic polynomial

      implicit none

      integer ii,jj,i,j,n,jc(4)
      real*8 psi_x(4)
     &      ,alpha,beta,gamma,delta

        alpha = psi_x(2)

        beta = - psi_x(1)/3 - psi_x(2)/2 + psi_x(3)
     &        -psi_x(4)/6

        gamma = psi_x(1)/2 - psi_x(2) + psi_x(3)/2

        delta = - psi_x(1)/6 + psi_x(2)/2
     &          - psi_x(3)/2 + psi_x(4)/6

      return

      end subroutine
```

B.4 Evaluating the 2D cubic polynomial to find the stream function

The subroutine that returns the value of psi approximated at the interpolation point (x,y) called `psi_interp`.

```
      subroutine cubic_interp(ii,jj,psi_x,y,psi_interp)

c INPUT : ii,jj : grid size
c INPUT : psi_x(4) : output of cubic_poly_x
c INPUT : y : value of interpolation point y
c OUTPUT : psi_interp : psi(x,y) interpolated at x,y

      implicit none

      integer ii,jj,yc
      real*8 psi_x(4),x,y,psi_interp,ay
      real*8 alpha,beta,gamma,delta

      ay = y - int(y)
      yc = int(y) + 1

      call cubic_coeff_y(ii,jj,psi_x,alpha,beta,gamma,delta)

      psi_interp = alpha + beta*ay + gamma*ay**2
     &    + delta*ay**3

      return
```

```
      end subroutine
```

B.5 Finding the velocity

The subroutine that returns the velocities given the coefficients.

```
      subroutine vel(ii,jj,psi_x,a,b,c,d,x,y,u,v)

      implicit none

c INPUT : ii,jj : grid size
c INPUT : psi_x : output of cubic_poly_x
c INPUT : a,b,c,d : polynomial coefficients
c INPUT : x,y : interpolation points
c OUTPUT : u,v : velocity approximated at x,y

      integer ii,jj,yc,xc,jc(4),i
      real*8 x,y,u,v,psi_x(4),ay,ax
      real*8 a(ii,jj),b(ii,jj)
     &      ,c(ii,jj),d(ii,jj)
      real*8 alpha,beta,gamma,delta
      real*8 d_alpha,d_beta,d_gamma,d_delta

      call cubic_coeff_y(ii,jj,psi_x,alpha,beta,gamma,delta)

      yc = int(y) + 1
      ay = y - int(y)

      xc = int(x) + 1
```

```
      ax = x - int(x)

      do i = 1,4
         jc(i) = yc - 2 + i
         if (jc(i) <= 0) then
            jc(i) = jj + jc(i)
         elseif (jc(i) > jj) then
            jc(i) = jc(i) - jj
         endif
      enddo

      u = -(beta + 2*gamma*ay + 3*delta*ay**2)

      d_alpha = b(xc,jc(2)) + 2*c(xc,jc(2))*ax + 3*d(xc,jc(2))*ax**2

      d_beta = (-b(xc,jc(1))/3 - b(xc,jc(2))/2
     &    + b(xc,jc(3))-b(xc,jc(4))/6)
     & + 2*(-c(xc,jc(1))/3 - c(xc,jc(2))/2
     & + c(xc,jc(3)) - c(xc,jc(4))/6)*ax
     & + 3*(-d(xc,jc(1))/3 - d(xc,jc(2))/2
     & + d(xc,jc(3)) - d(xc,jc(4))/6)*ax**2

      d_gamma = (b(xc,jc(1))/2 - b(xc,jc(2)) + b(xc,jc(3))/2)
     & + 2*(c(xc,jc(1))/2 - c(xc,jc(2)) + c(xc,jc(3))/2)*ax
     & + 3*(d(xc,jc(1))/2 - d(xc,jc(2)) + d(xc,jc(3))/2)*ax**2

      d_delta = (-b(xc,jc(1))/6 + b(xc,jc(2))/2
     &   - b(xc,jc(3))/2 + b(xc,jc(4))/6)
```

```
& + 2*(-c(xc,jc(1))/6 + c(xc,jc(2))/2
& - c(xc,jc(3))/2 + c(xc,jc(4))/6)*ax
& + 3*(-d(xc,jc(1))/6 + d(xc,jc(2))/2
& - d(xc,jc(3))/2 + d(xc,jc(4))/6)*ax**2

    v = (d_alpha + ay*d_beta + d_gamma*ay**2 + d_delta*ay**3)

    return

    end subroutine
```

B.6 Algorithm

1. At each time step, call `cubic_coeff_x` for the instantaneous stream function to return the coefficients a, b, c and d which are defined for every grid point.

2. For each particle:

   (a) Call `cubic_poly_x` taking the interpolation point and cubic coefficients as input, and returning $\psi_{y_j}(x)$ where $y_j, j = 1, \cdots, 4$ are the grid points in y that surround the interpolation point.

   (b) Call `vel` taking $\psi_{y_j}(x)$, the cubic coefficients and the interpolation point as input to return the velocity approximated at the interpolation point.

Appendix C

Derivation of bicubic spatial interpolation

Let $\mathbf{A}, \mathbf{\Psi}, \mathbf{X}, \mathbf{Y}$ all be 4×4 matrices where

$$[\mathbf{A}]_{k,l} = a_{kl} \tag{C.1}$$

$$\mathbf{X} = \begin{bmatrix} 1 & x_{i-1} & x_{i-1}^2 & x_{i-1}^3 \\ 1 & x_i & x_i^2 & x_i^3 \\ 1 & x_{i+1} & x_{i+1}^2 & x_{i+1}^3 \\ 1 & x_{i+2} & x_{i+2}^2 & x_{i+2}^3 \end{bmatrix}, \mathbf{Y} = \begin{bmatrix} 1 & 1 & 1 & 1 \\ y_{j-1} & y_j & y_{j+1} & y_{j+2} \\ y_{j-1}^2 & y_j^2 & y_{j+1}^2 & y_{j+2}^2 \\ y_{j-1}^3 & y_j^3 & y_{j+1}^3 & y_{j+2}^3 \end{bmatrix},$$

$$[\mathbf{\Psi}]_{k,l} = \psi(x_{i+k-2}, y_{j+l-2}). \tag{C.2}$$

We get the following matrix equation:

$$\mathbf{\Psi} = (\mathbf{XA})\mathbf{Y}, \tag{C.3}$$

which approximates the streamfunction as a bicubic polynomial. In order to find $\mathbf{A}$, we rearrange to get:

$$\mathbf{A} = \mathbf{X}^{-1}(\mathbf{\Psi}\mathbf{Y}^{-1}). \tag{C.4}$$

As before, we can now analytically differentiate these polynomials to find the velocity components:

$$u(x,y) = -\begin{pmatrix} 1 & x & x^2 & x^3 \end{pmatrix} \mathbf{A} \begin{pmatrix} 0 & 1 & 2y & 3y^2 \end{pmatrix}^{\mathsf{T}}, \tag{C.5}$$

$$v(x,y) = \begin{pmatrix} 0 & 1 & 2x & 3x^2 \end{pmatrix} \mathbf{A} \begin{pmatrix} 1 & y & y^2 & y^3 \end{pmatrix}^{\mathsf{T}}. \tag{C.6}$$

Appendix D

Bicubic code

D.1 Calculating the matrix A of coefficients

The subroutine that returns ii × jj, 4 × 4 matrices of bicubic polynomial coefficients.

```
      subroutine A_matrix(ii,jj,psi,A_mat)

c INPUT : ii,jj : grid size
c INPUT : psi(ii,jj) : stream function
c OUTPUT : A_mat(ii,jj,4,4) : 4 X 4 matrix of coefficients stored at each
c                             grid point

      implicit none

      integer ii,jj,i,j,k,n,m,ic(4),jc(4)

      real*8 A_mat(ii,jj,4,4)
     &  , x_mat(4,4),y_mat(4,4),psi_mat(4,4)
     &  ,yc(4),xc(4),x_inv(4,4),y_inv(4,4),psi_grid(4,4)
     &  ,psi(ii,jj)
```

```
&  ,B(4,4)

  do i = 1,ii
  do j = 1,jj

    do k = 1,4
        ic(k) = i + k - 2
        jc(k) = j + k - 2

        xc(k) = dfloat(ic(k))
        if(ic(k)<=0) then
            ic(i) = ii+ic(k)
        endif
        if(ic(k)>ii) then
            ic(k) = ic(k) - ii
        endif

        yc(k) = dfloat(jc(k))
        if(jc(k)<=0) then
            jc(k) = jj + jc(k)
        endif
        if(jc(k) > jj) then
            jc(k) = jc(k) - jj
        endif

    enddo

    do n = 1,4
    do m = 1,4
```

```
        X_mat(n,m) = xc(n)**(m-1)
        Y_mat(n,m) = yc(m)**(n-1)

    enddo
    enddo

    X_inv = inv(X_mat)
    Y_inv = inv(Y_mat)

    do n = 1,4
    do m = 1,4

        psi_grid(m,n) = psi(ic(m),jc(n))

    enddo
    enddo

    B = matmult(psi_grid,Y_inv)
    A_mat(i,j,:,:) = matmult(X_inv,B)

enddo
enddo

end subroutine
```

D.2 Finding the velocity

The subroutine that returns the velocity at the interpolation point by taking the matrix of coefficients as input.

```
      subroutine bicubic(ii,jj,A_mat,x,y,u,v)

c INPUT : ii,jj
c INPUT : A_mat(ii,jj,4,4)
c INPUT : x,y : interpolation point
c OUPUT : u,v : velocities

      implicit none

      integer ii,jj,i,j,k
      real*8 A_mat(ii,jj,4,4)
     &   ,x,y,u,v,x_col(1,4),y_col(4),diff_y(4)
     & ,diff_x(1,4), XA(1,4), diff_XA(1,4)

      do k =1,4

            x_col(1,k) = x**(k-1)
            y_col(k) = y**(k-1)

      enddo

      diff_y(1) = 0.
      diff_x(1,1) = 0.
```

```
    do k = 2,4

        diff_y(k) = (k-1)*y**(k-2)
        diff_x(1,k) = (k-1)*x**(k-2)

    enddo

  XA = matmul(x_col,A_mat(int(x)+1,int(y)+1,:,:))
  diff_XA = matmul(diff_x,A_mat(int(x)+1,int(y)+1,:,:))

  u = -dot_product(XA(1,:),diff_y)
  v = dot_product(diff_XA(1,:),y_col)

  end subroutine

  end module MOD_bicubic
```

D.3 Algorithm

1. For each time step, call `A_matrix`, taking the instantaneous stream function as input, to return A.

2. For each particle, call `bicubic`, taking the matrix A as input, and the interpolation points (x, y) to return the approximated velocity (u, v) at the interpolation point.

Appendix E

Lagrangian Statistics Figures

In this appendix we include multi-panel figures referenced in Chapter 4.

E.1 Single Particle Dispersion

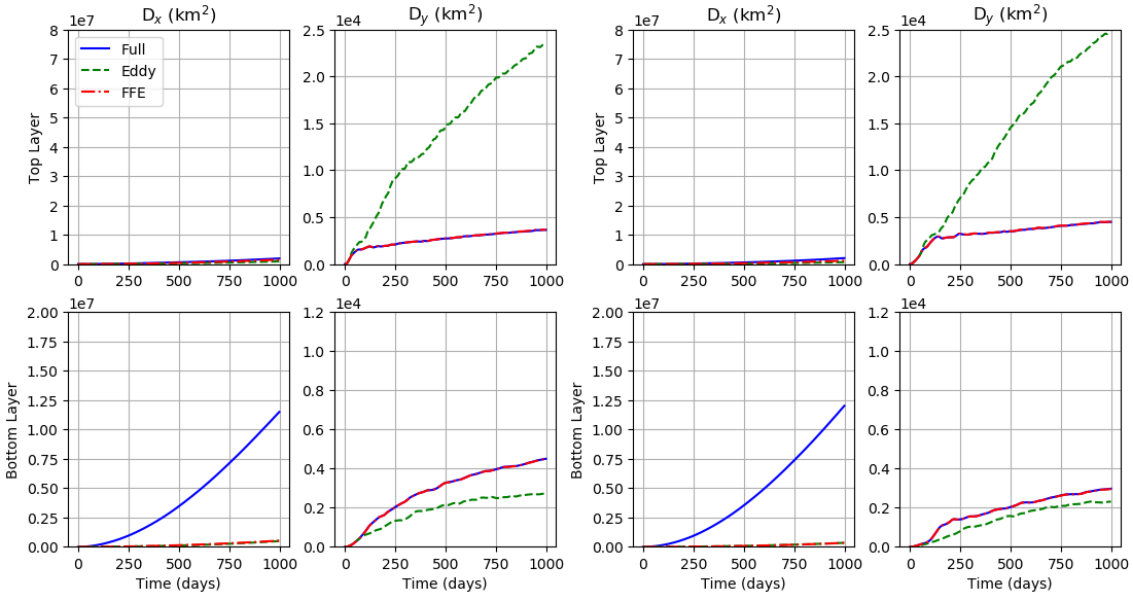

(a) Bin 1

(b) Bin 2

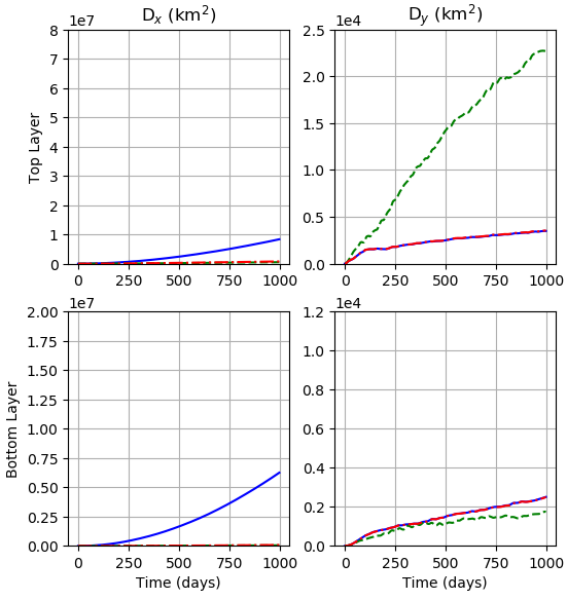

(c) Bin 3

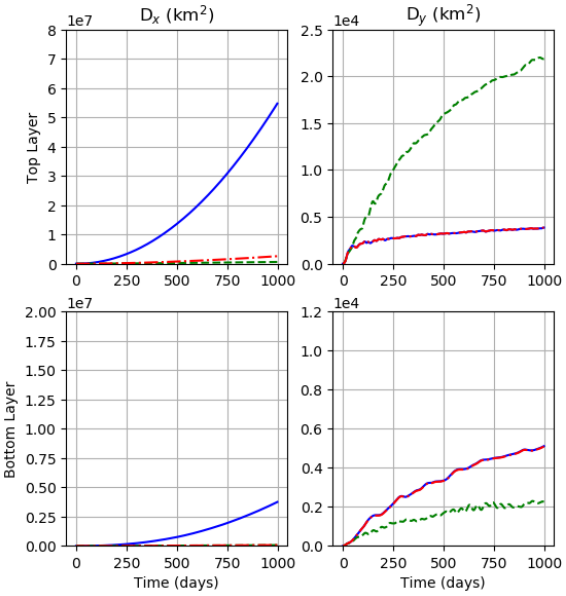

(d) Bin 4

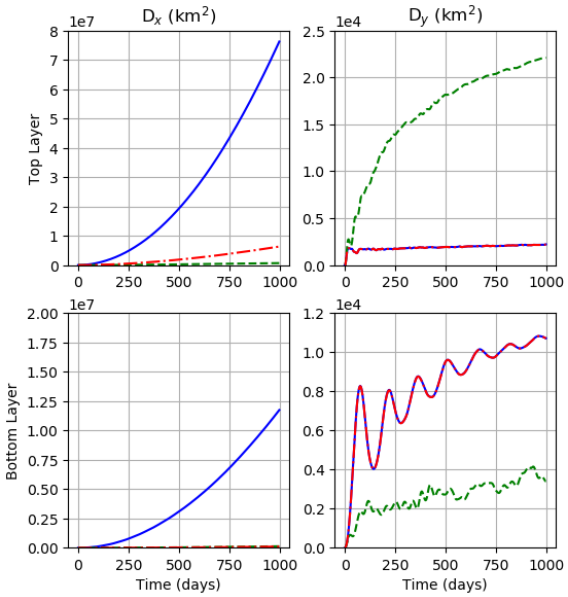

(e) Bin 5

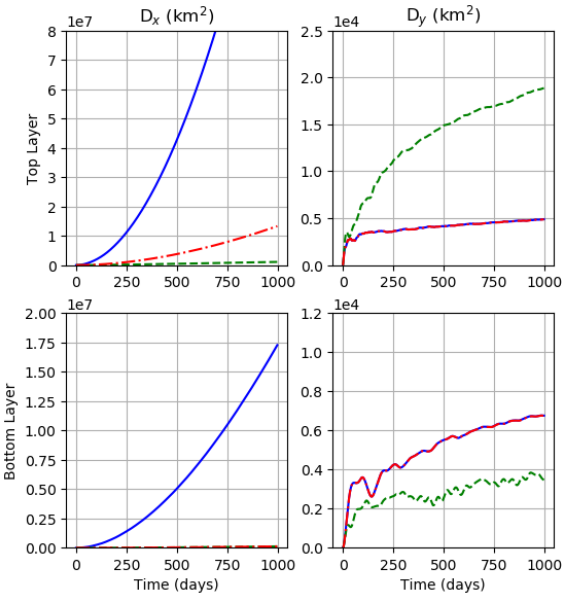

(f) Bin 6

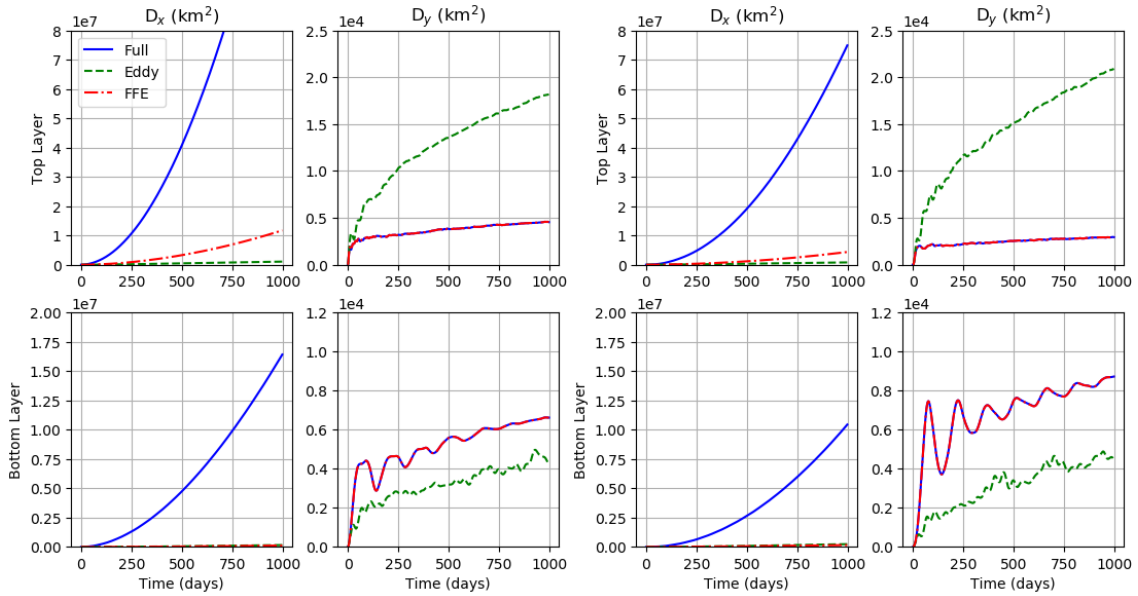

(g) Bin 7 (h) Bin 8

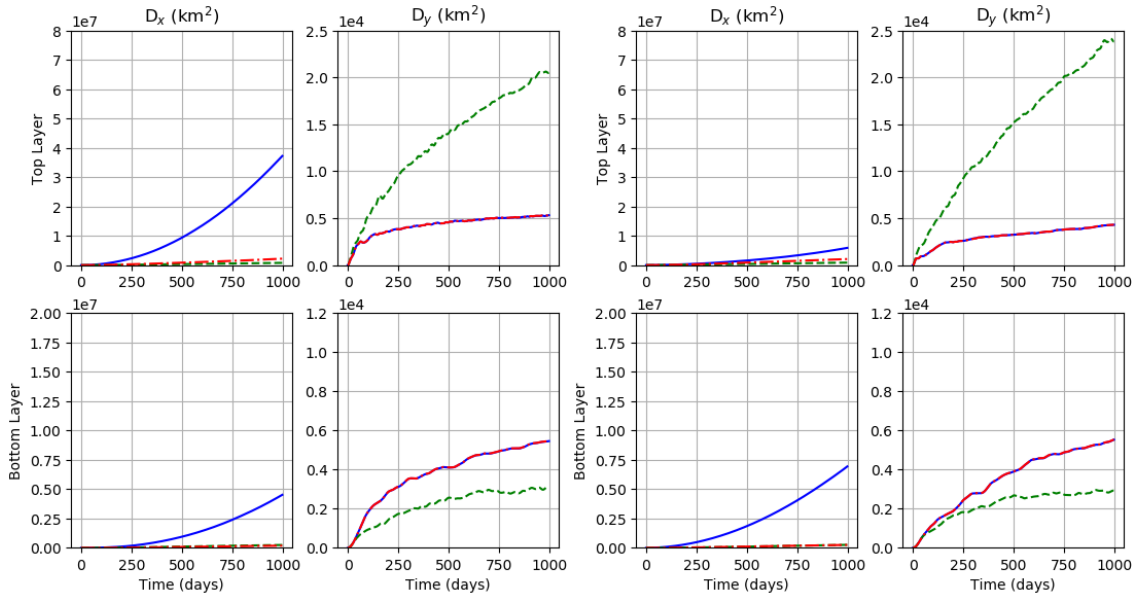

(i) Bin 9 (j) Bin 10

Figure E.1: Single-Particle Dispersion (km^2) against time (days) for Full, EO and FFE trajectories in the coherent jet. The top row of each panel is the top layer and the bottom row is the bottom layer. The left column of each panel is the zonal dispersion and the right is the meridional dispersion. Each figure panel represents a uniform zonal bin, where bin 1 indicates the bin starting at $y = 0$.

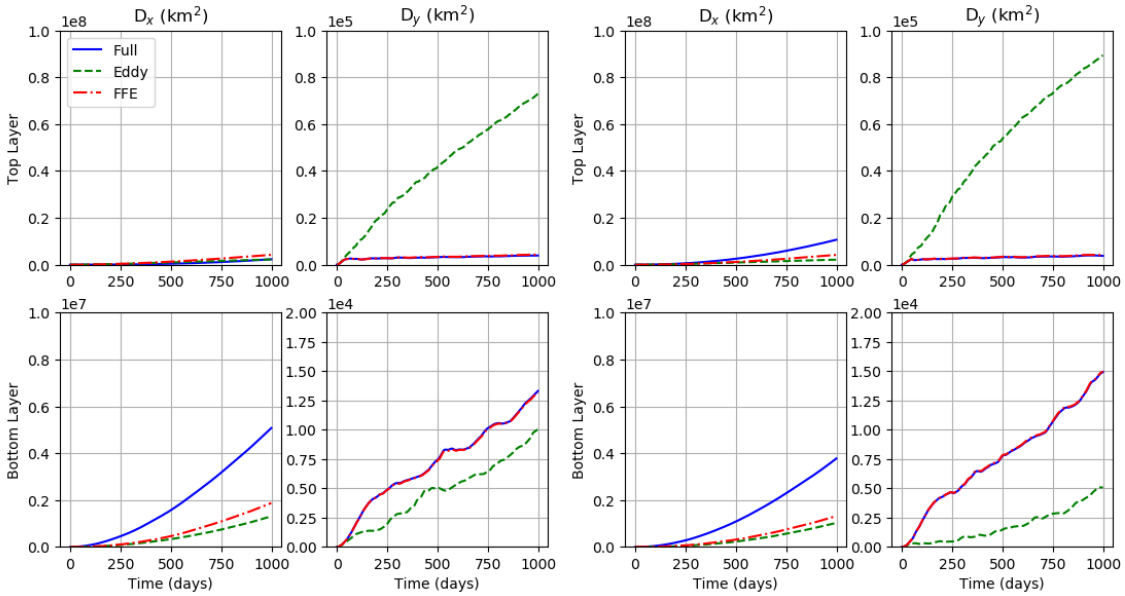

(a) Bin 1

(b) Bin 2

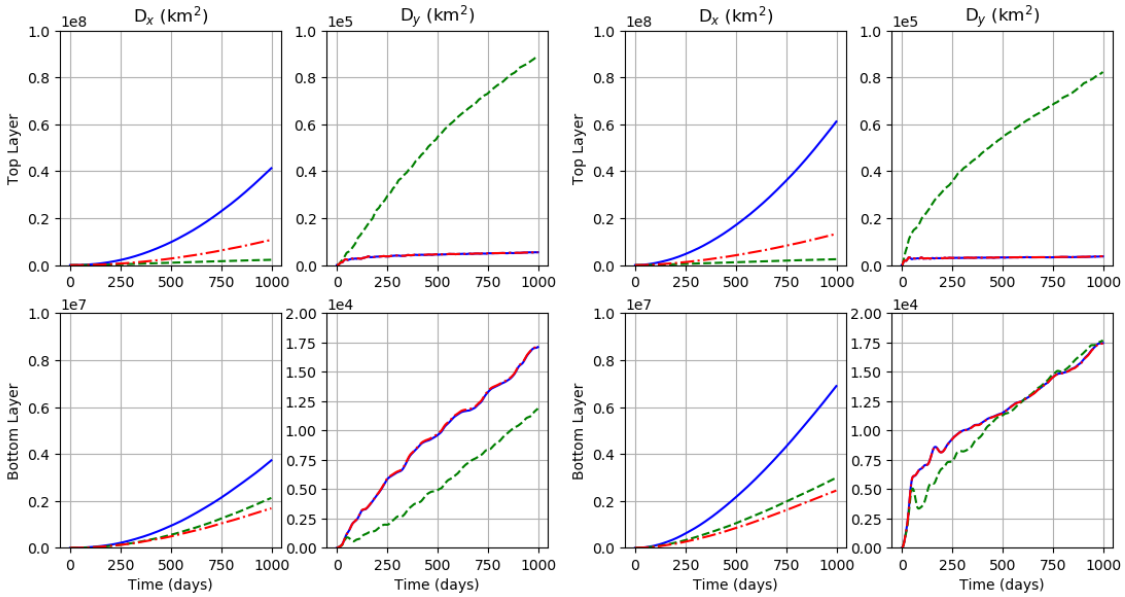

(c) Bin 3

(d) Bin 4

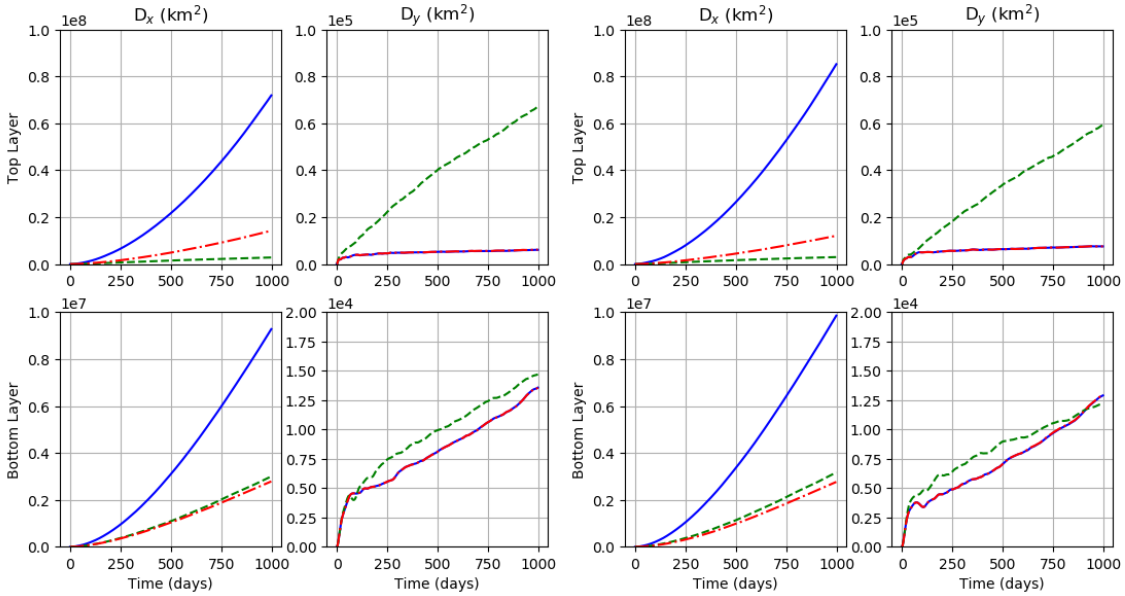

(e) Bin 5

(f) Bin 6

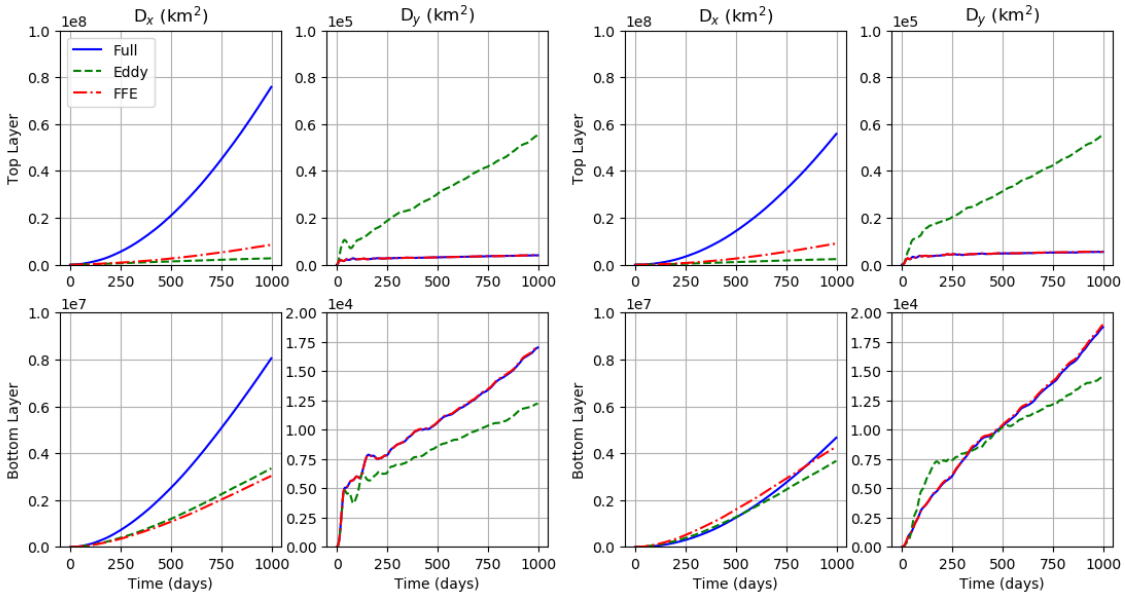

(g) Bin 7

(h) Bin 8

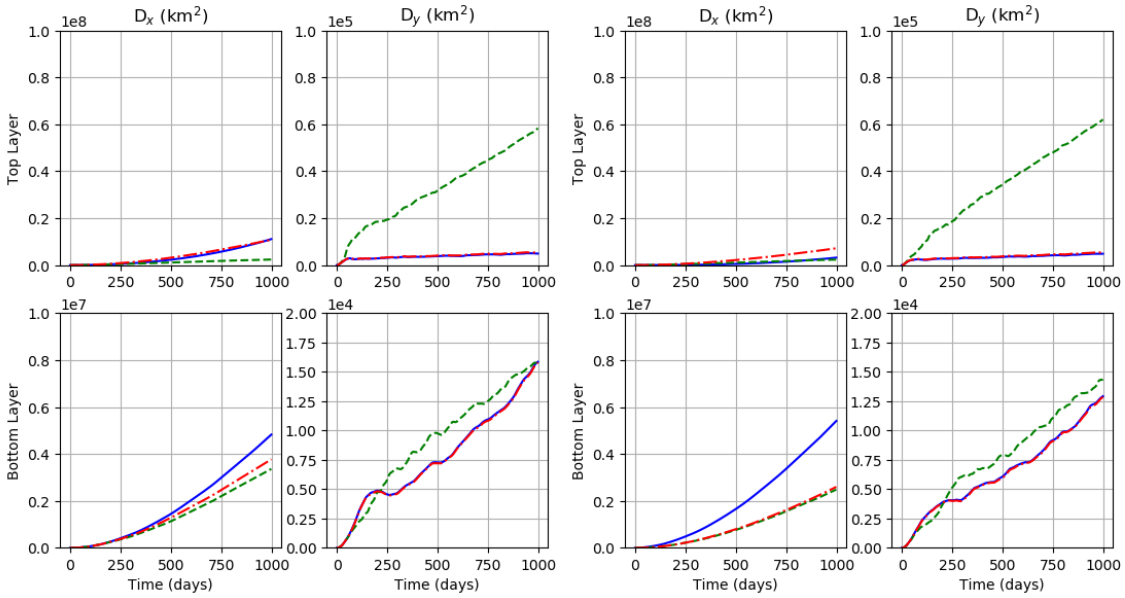

(i) Bin 9

(j) Bin 10

Figure E.2: The same as fig. E.1 but for the latent jet.

E.2 Log-log Plots of Single Particle Dispersion

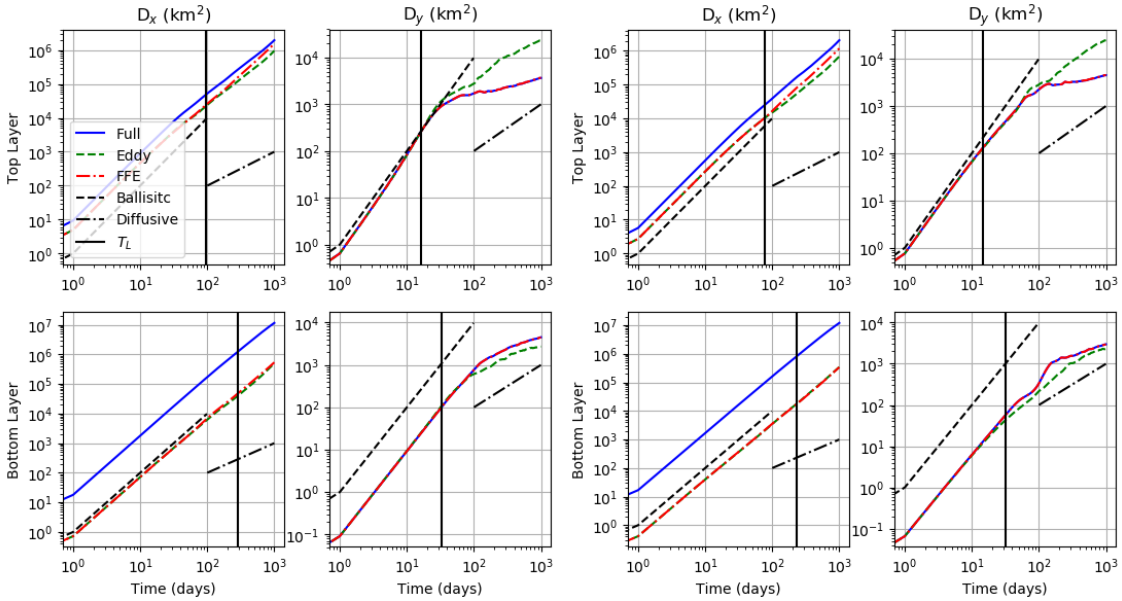

(a) Bin 1

(b) Bin 2

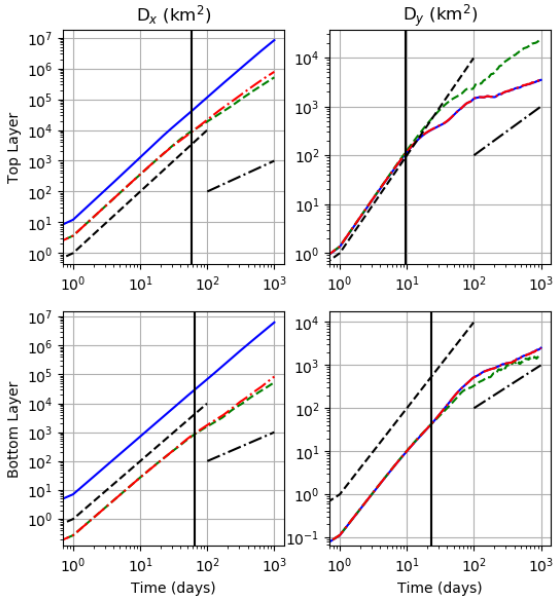

(c) Bin 3

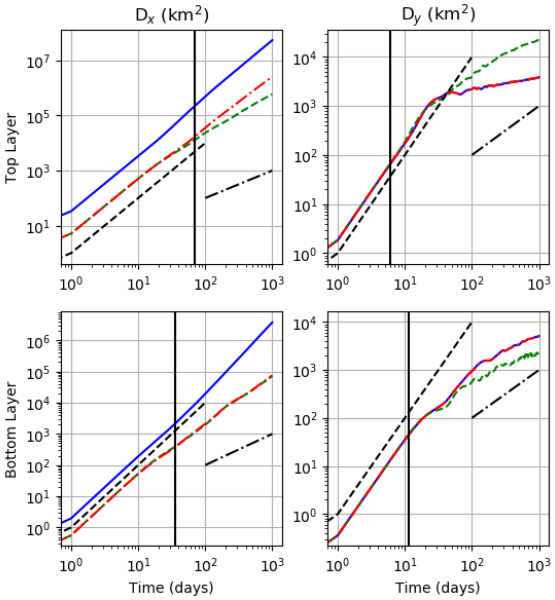

(d) Bin 4

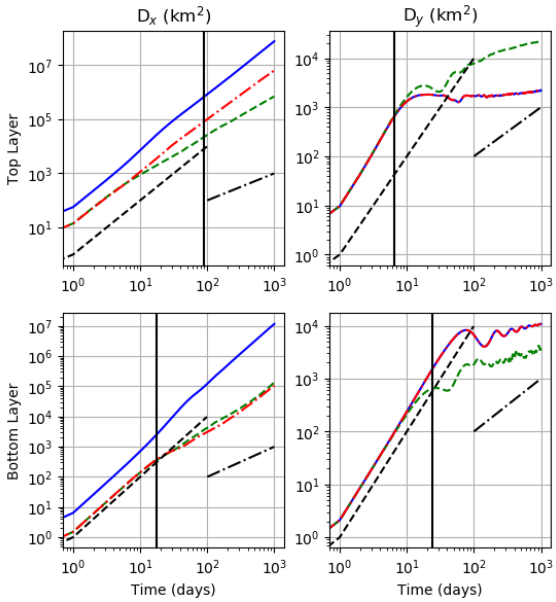

(e) Bin 5

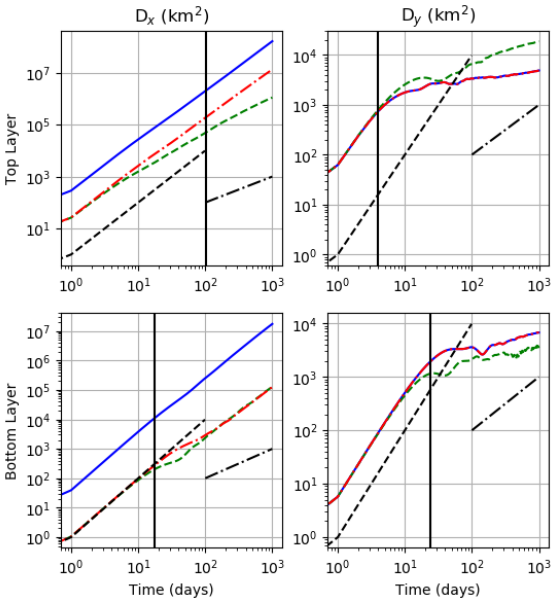

(f) Bin 6

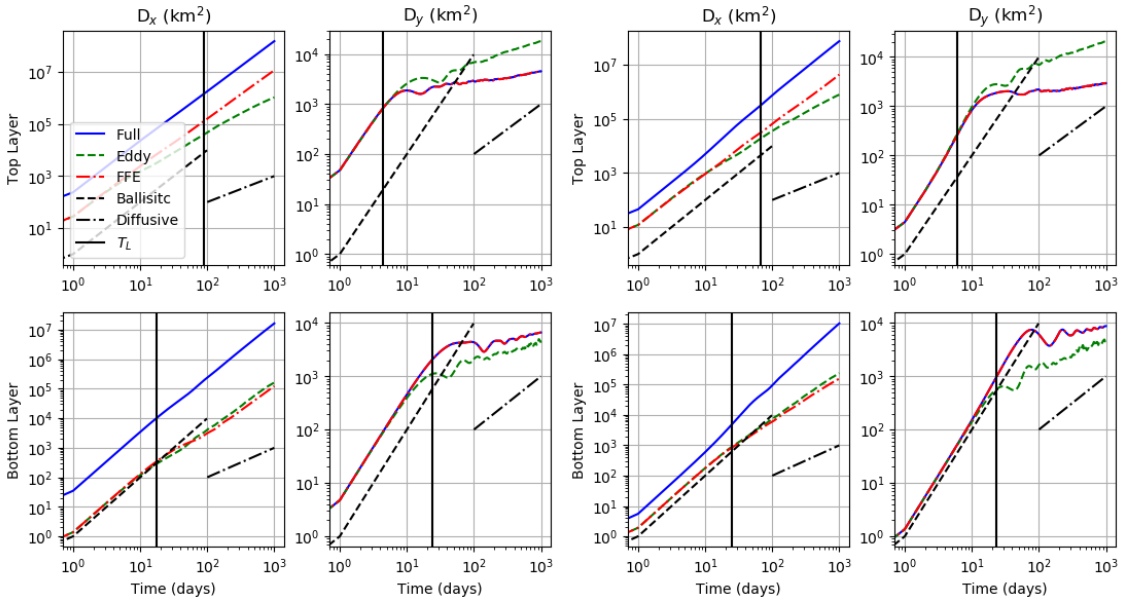

(g) Bin 7 (h) Bin 8

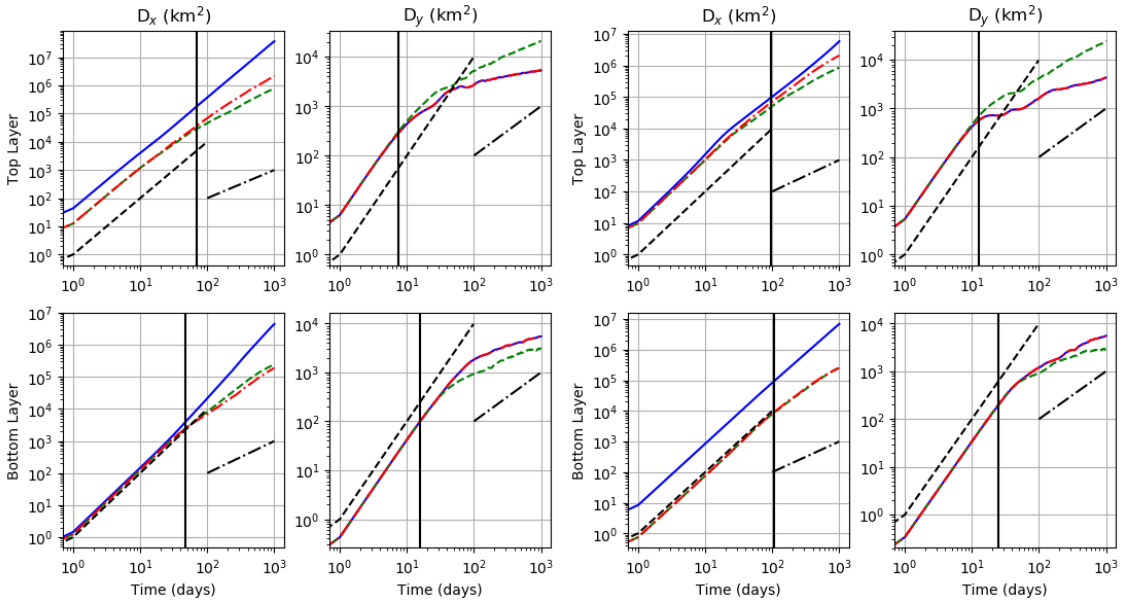

(i) Bin 9 (j) Bin 10

Figure E.3: A log-log plot for the Single-Particle Dispersion (km^2) against time (days) for Full, EO and FFE trajectories in the coherent jet. The figure layout is the same as fig. E.1. The dashed black lines representing diffusive and ballistic growth are included for comparison. The solid vertical black line is T_L, which is meant to represent a rough separation between the two growth rates.

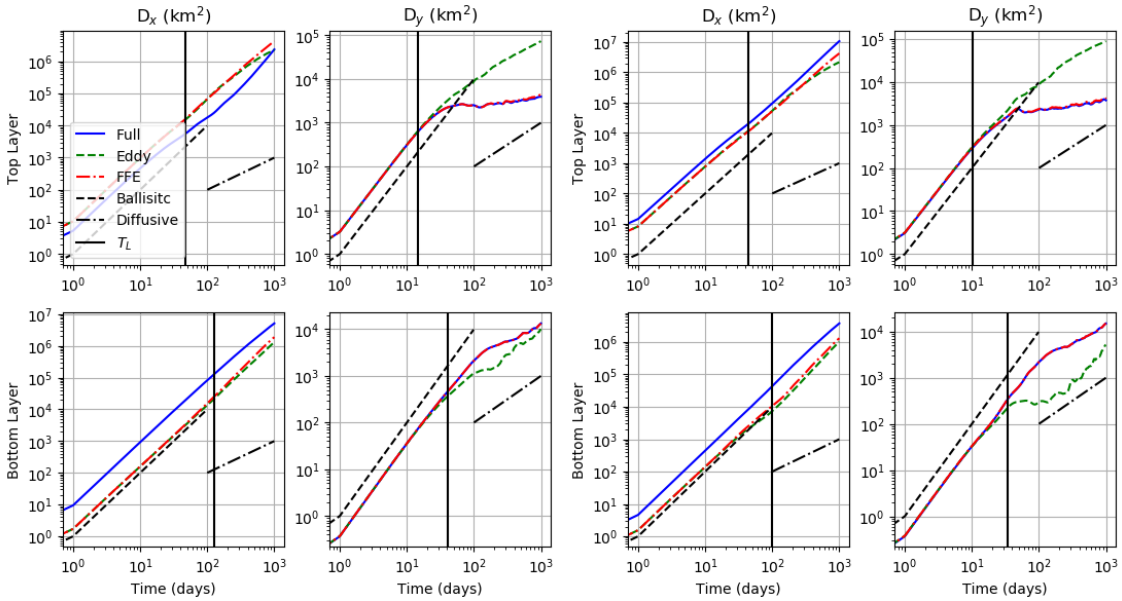

(a) Bin 1

(b) Bin 2

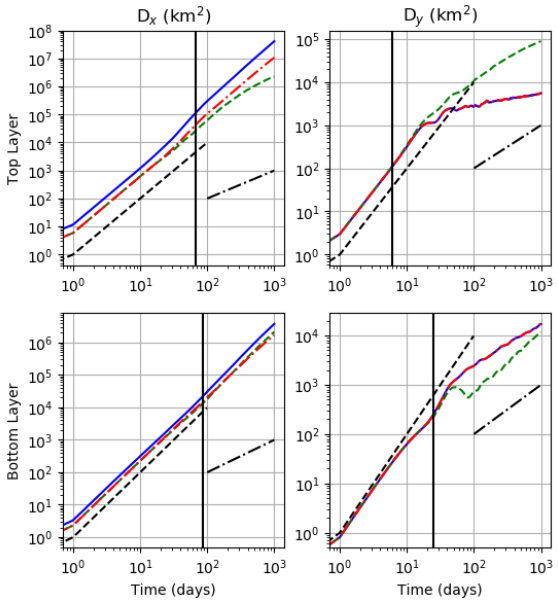

(c) Bin 3

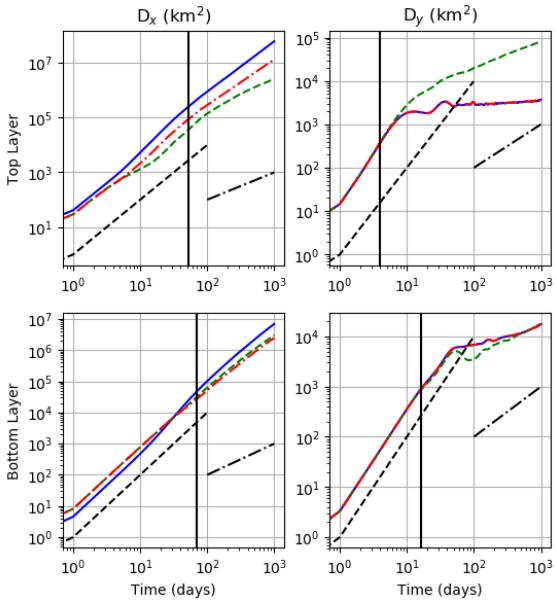

(d) Bin 4

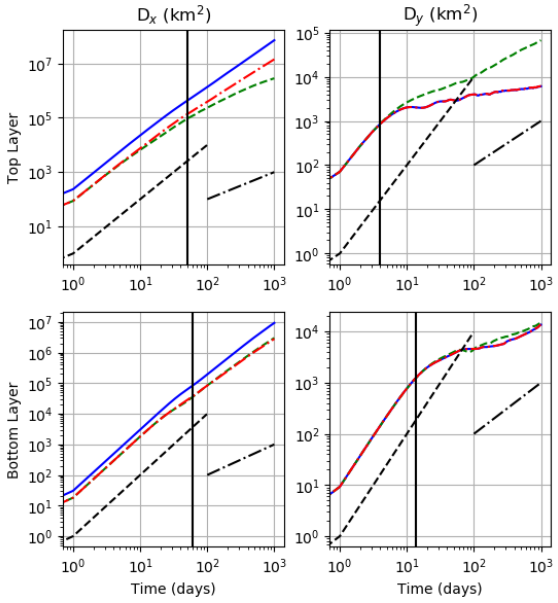

(e) Bin 5

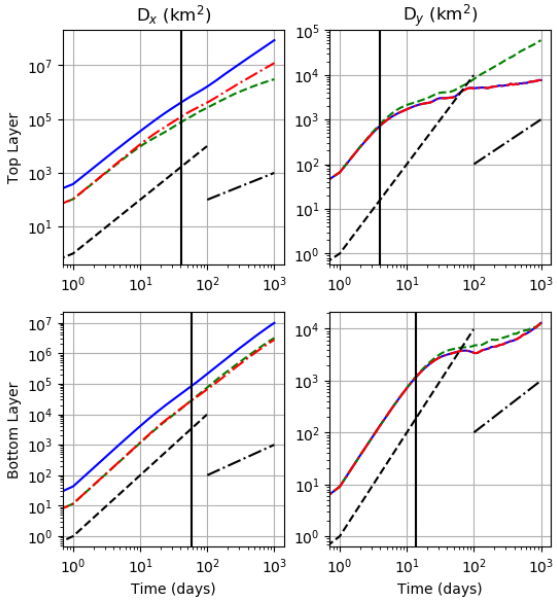

(f) Bin 6

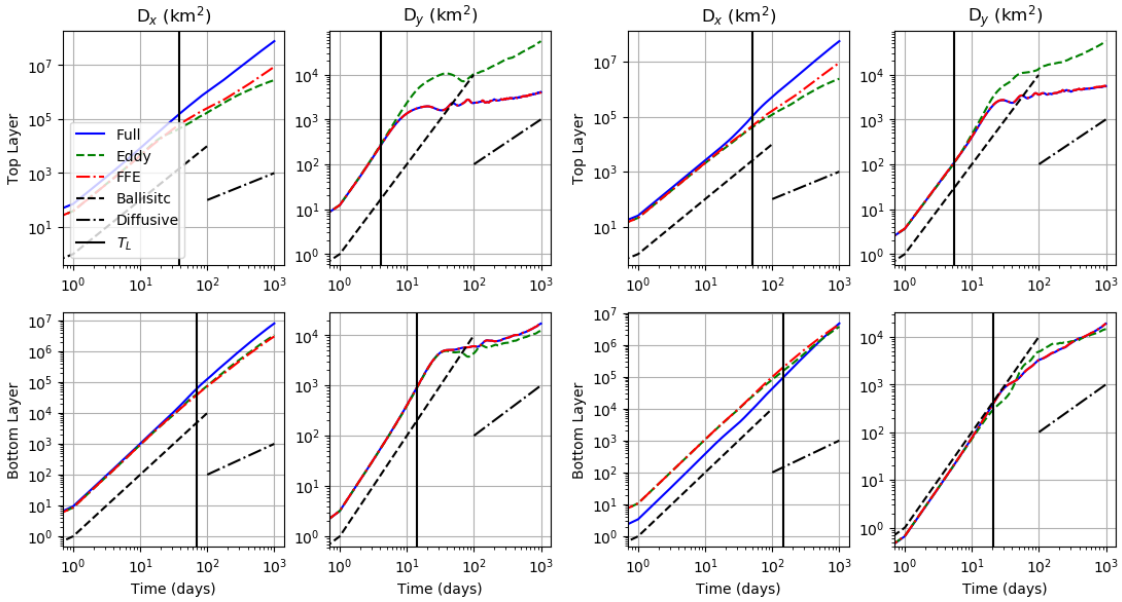

(g) Bin 7 (h) Bin 8

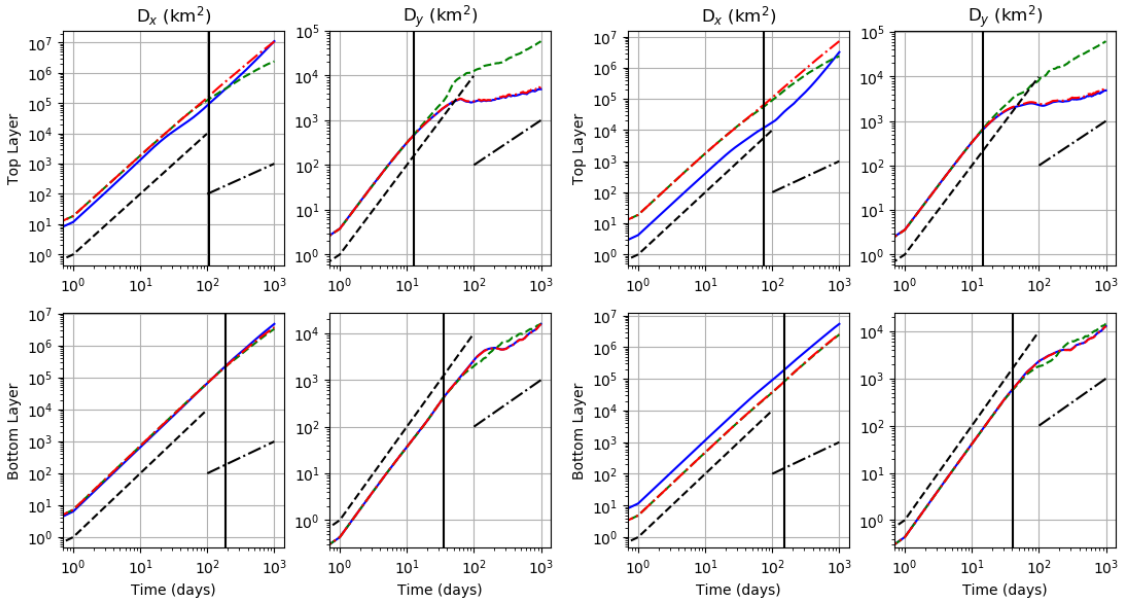

(i) Bin 9 (j) Bin 10

Figure E.4: The same as fig. E.3 but for the latent jet.

E.3 Lagrangian Autocorrelation function

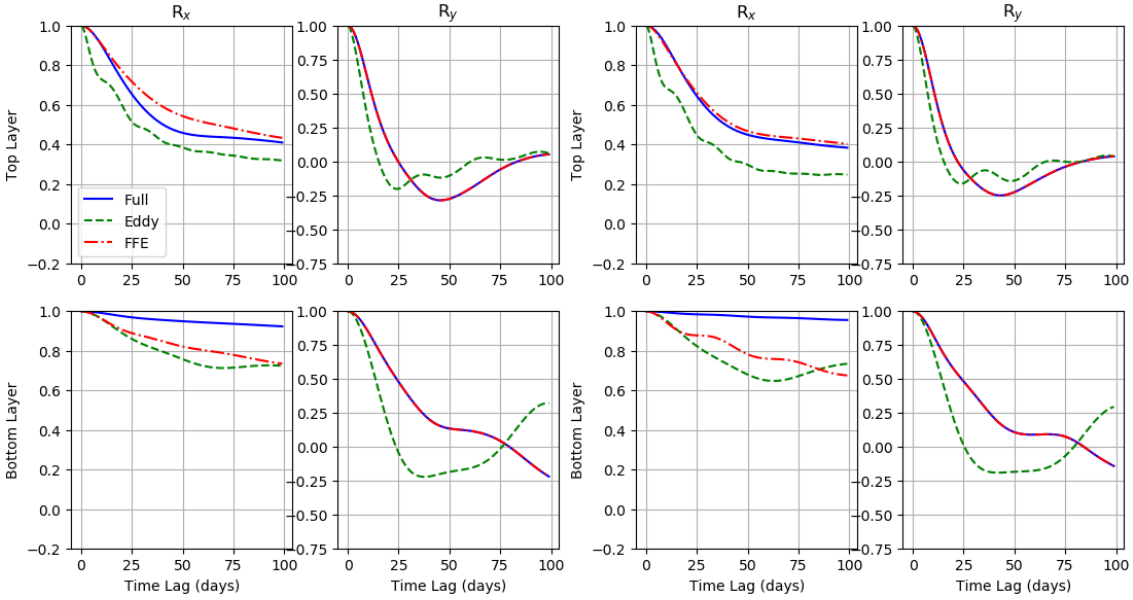

(a) Bin 1

(b) Bin 2

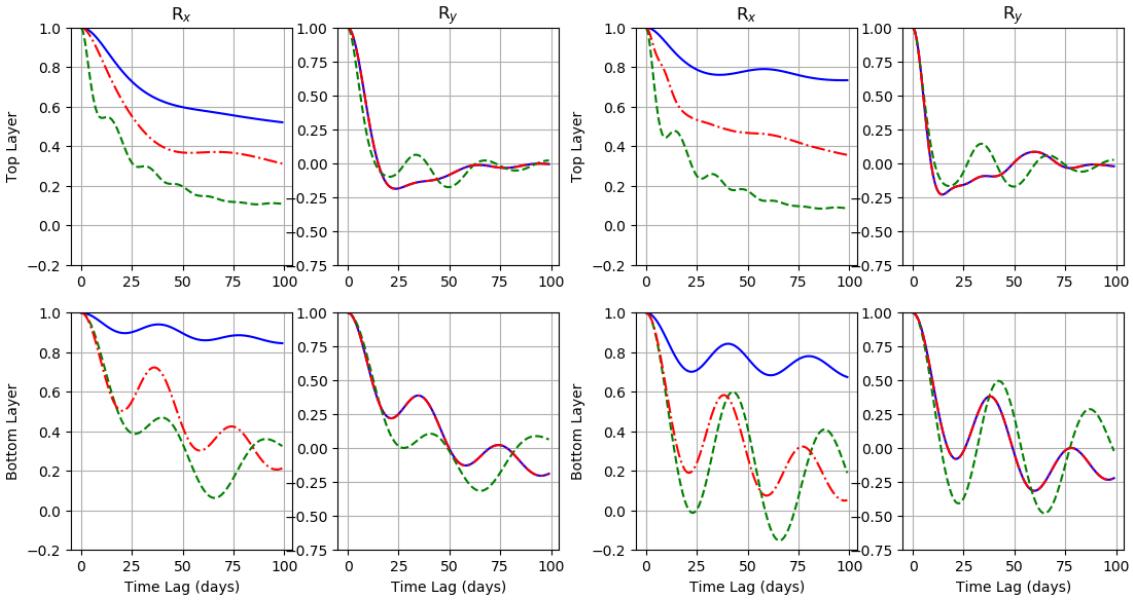

(c) Bin 3

(d) Bin 4

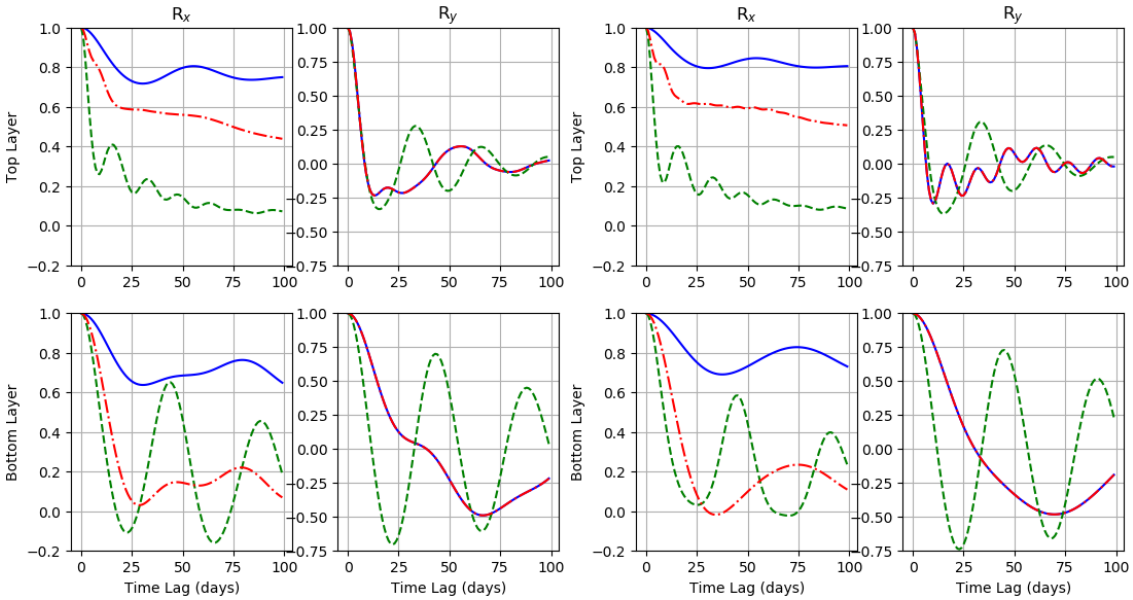

(e) Bin 5

(f) Bin 6

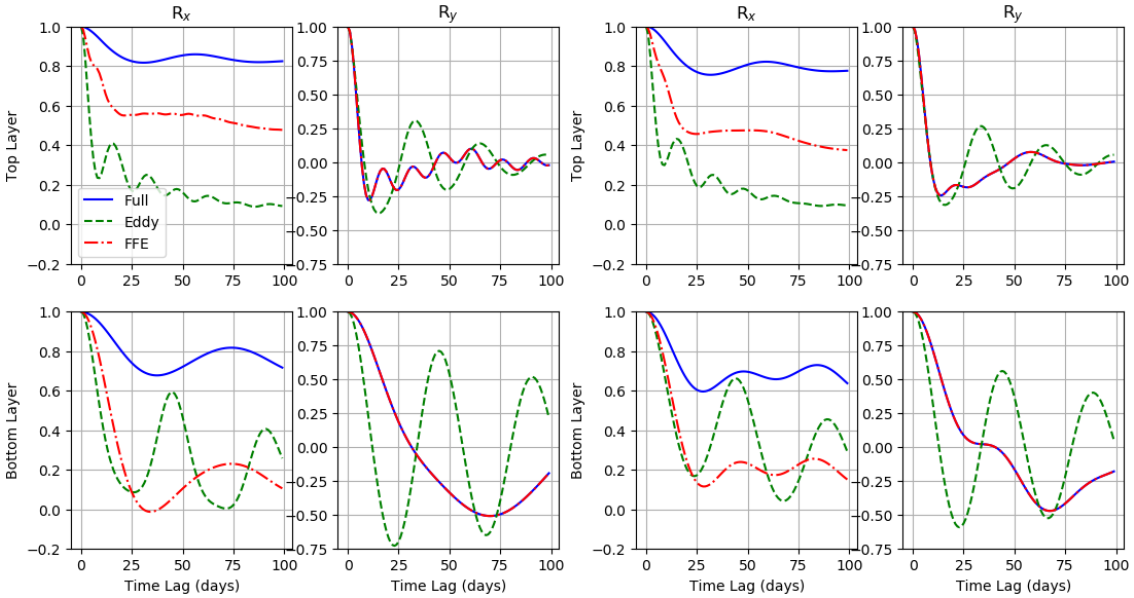

(g) Bin 7 (h) Bin 8

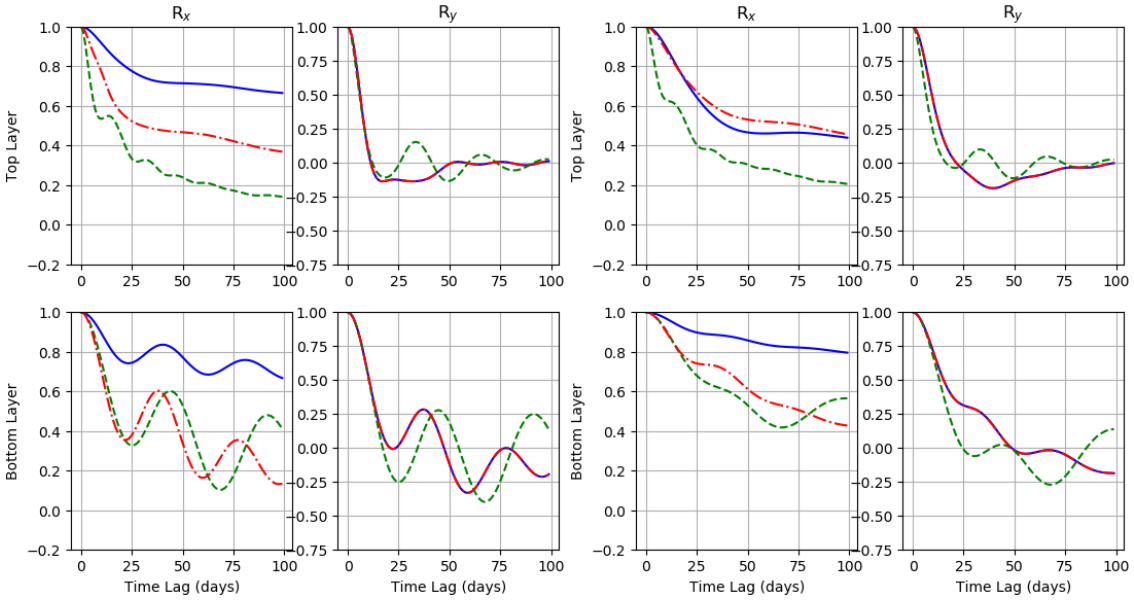

(i) Bin 9 (j) Bin 10

Figure E.5: The normalised Lagrangian Autocorrelation Function for Full, EO and FFE trajectories in the coherent jet. The Figure panels are laid out the same way as in fig. E.1.

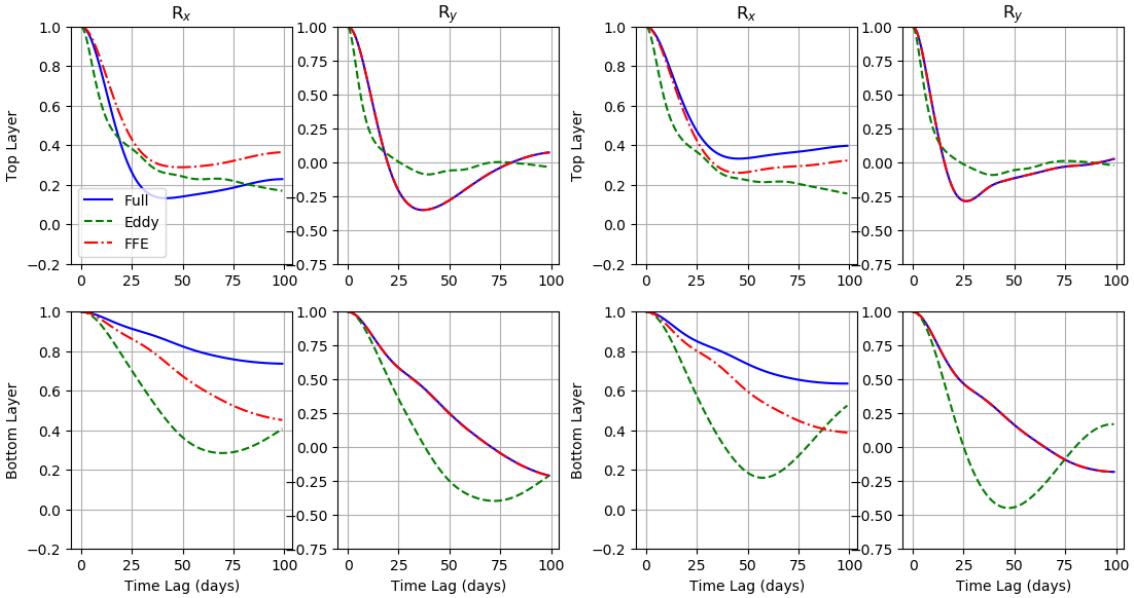

(a) Bin 1

(b) Bin 2

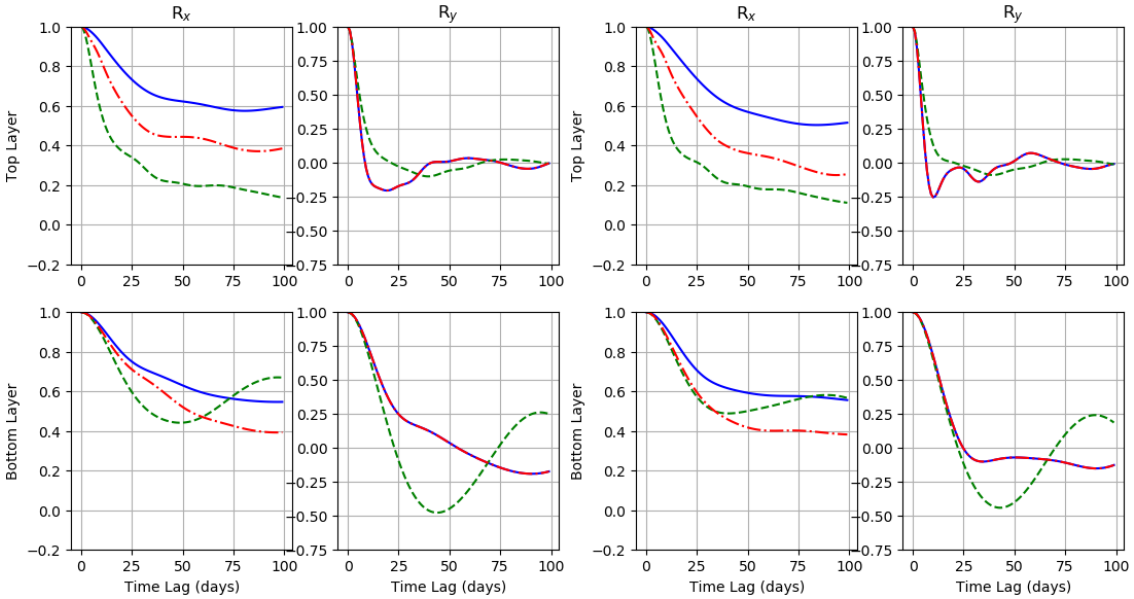

(c) Bin 3

(d) Bin 4

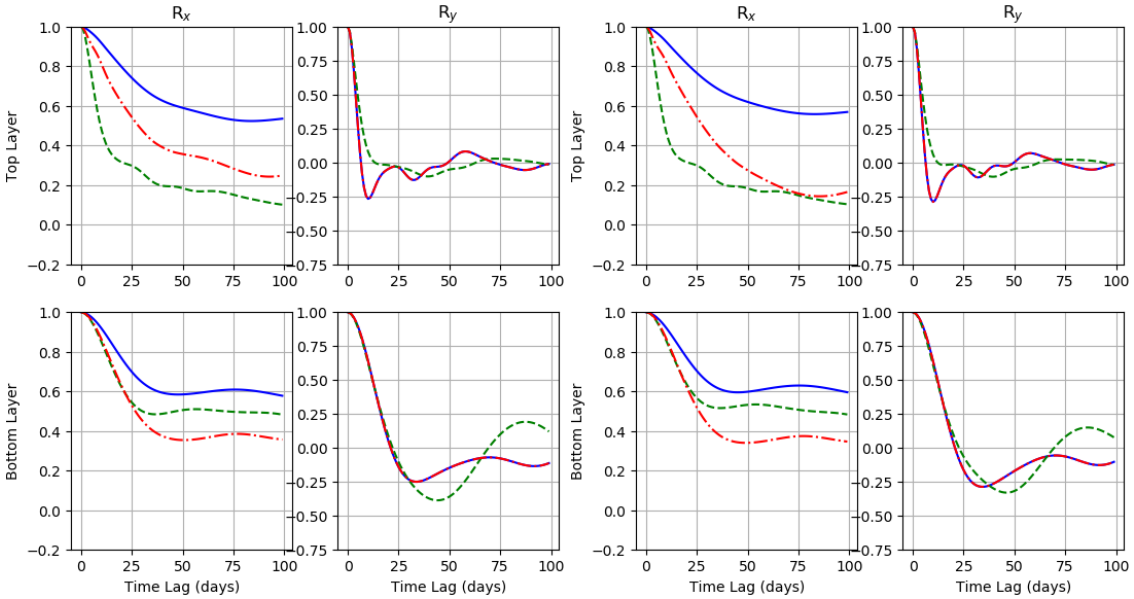

(e) Bin 5

(f) Bin 6

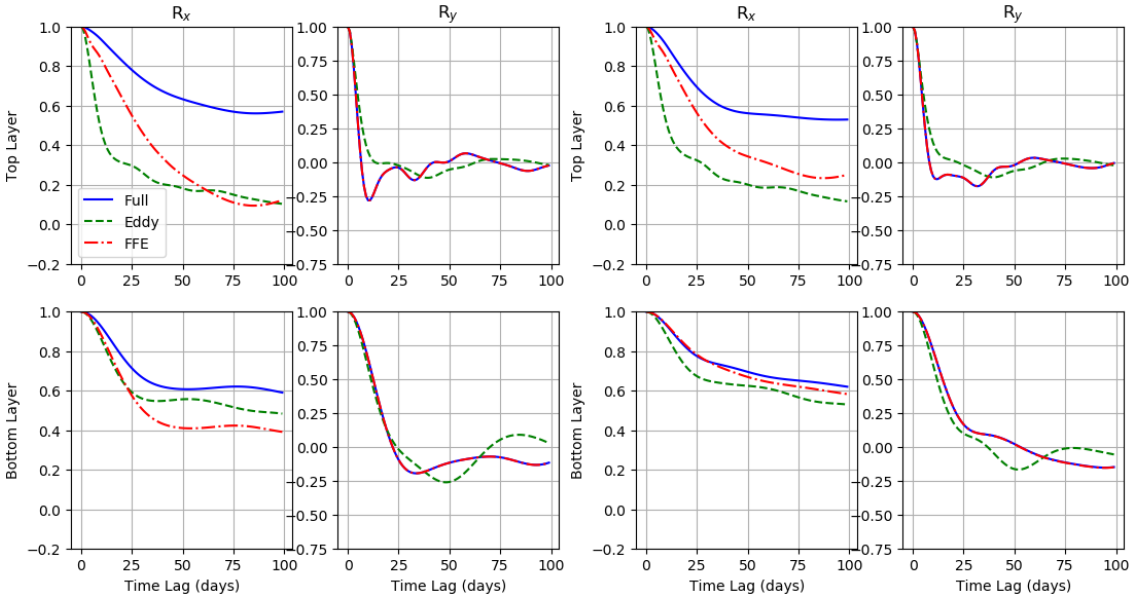

(g) Bin 7 (h) Bin 8

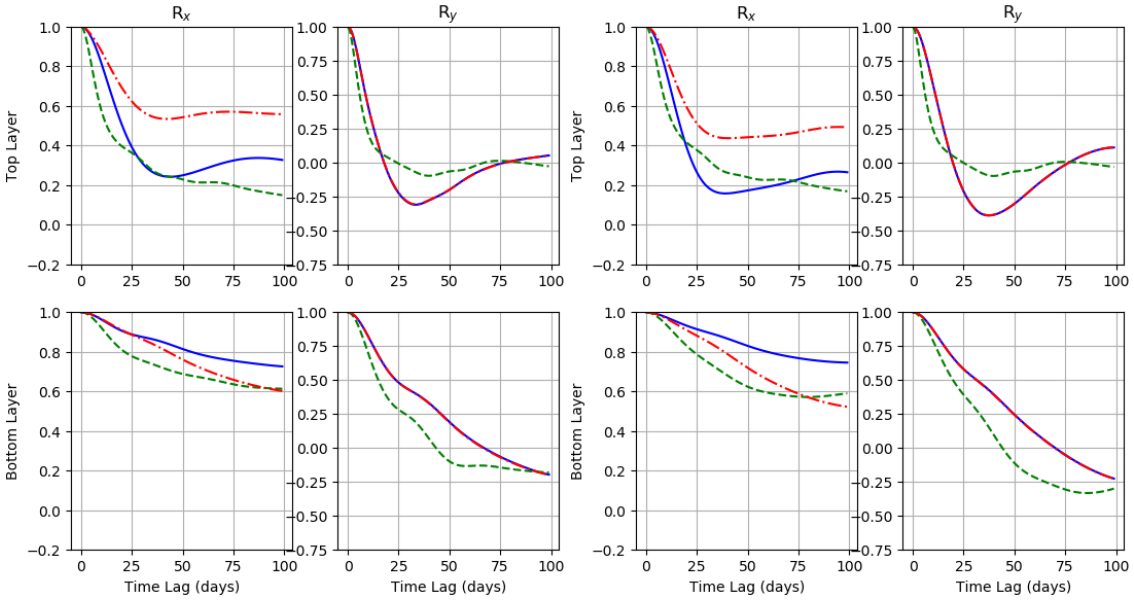

(i) Bin 9 (j) Bin 10

Figure E.6: The same as fig. E.5 but for the latent jet.

E.4 Calculation of T_L

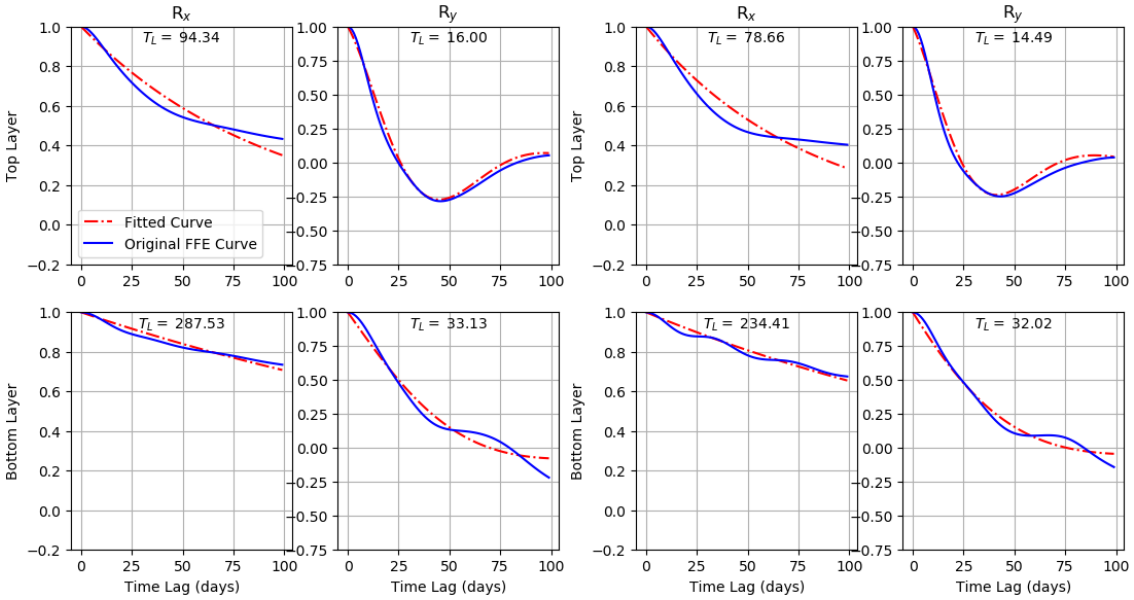

(a) Bin 1 (b) Bin 2

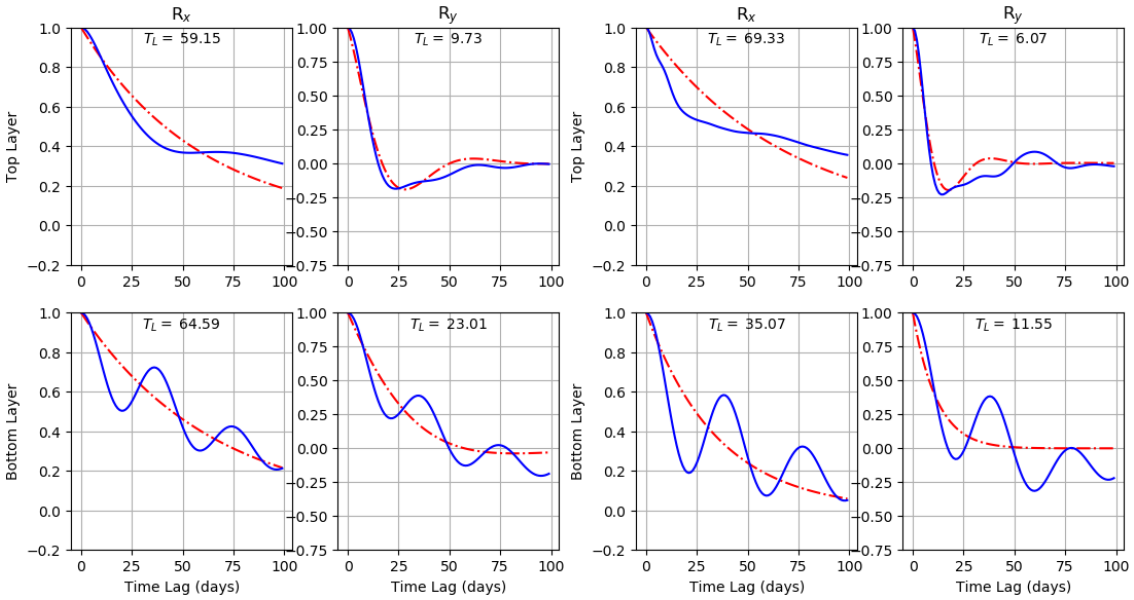

(c) Bin 3 (d) Bin 4

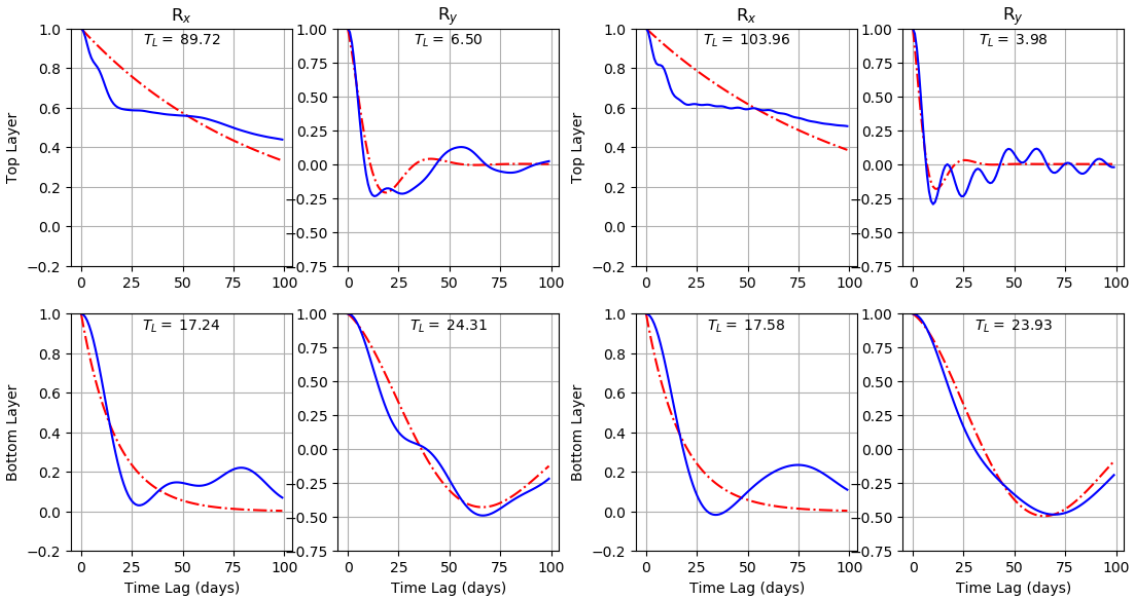

(e) Bin 5 (f) Bin 6

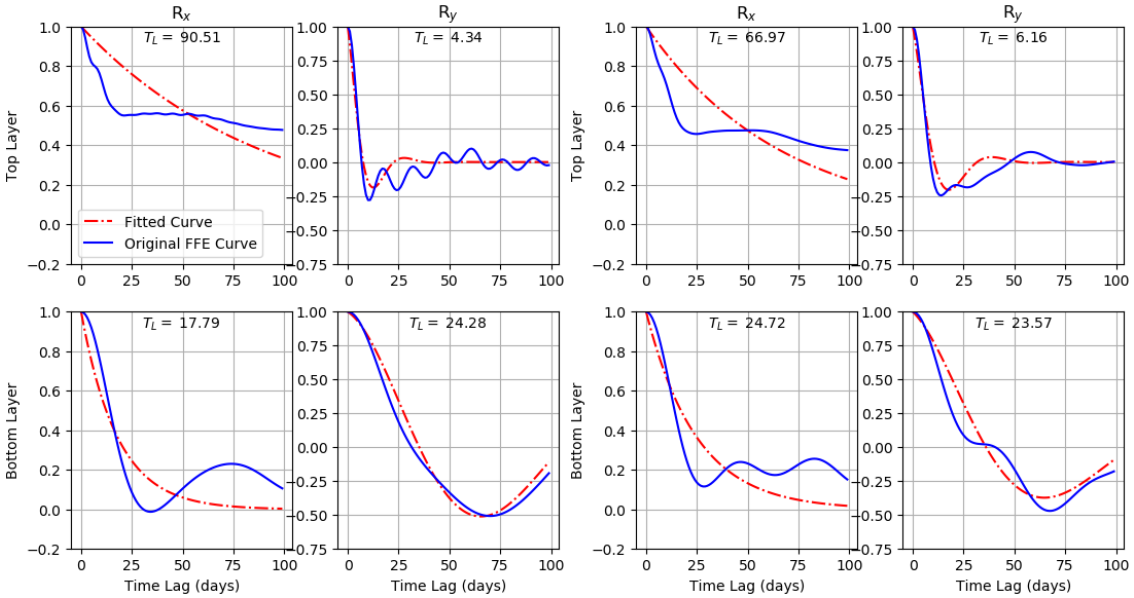

(g) Bin 7 (h) Bin 8

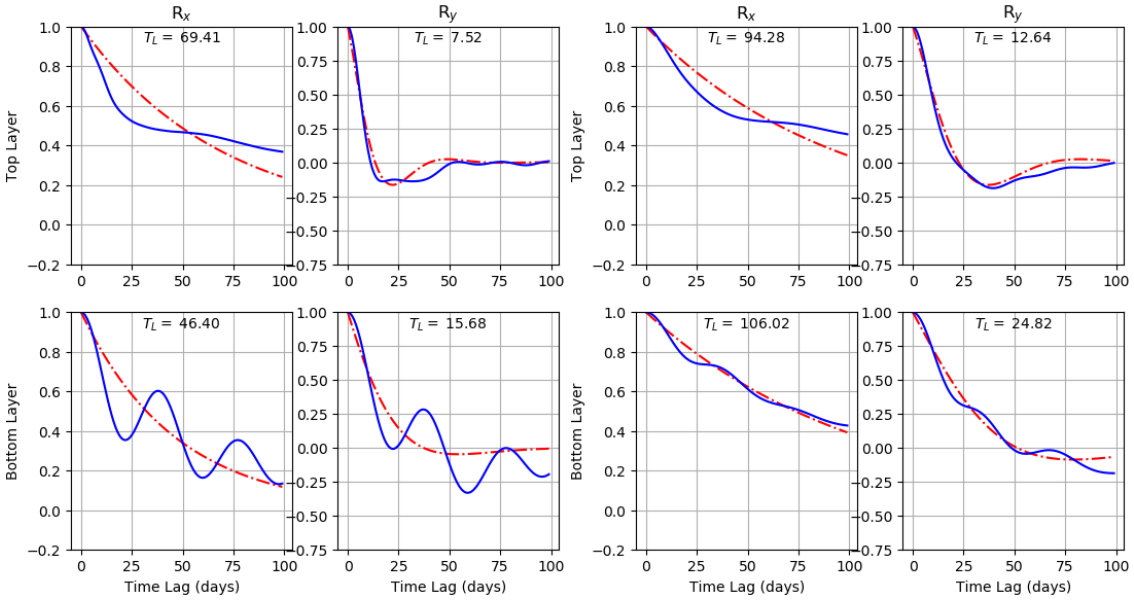

(i) Bin 9 (j) Bin 10

Figure E.7: R fitted to exponential decay for FFE trajectories in the coherent jet. Figure layout is the same as in fig. E.1. The resulting estimated Lagrangian integral time-scale (days) is printed for each figure, estimated as the time at which the fitted curve reaches e^{-1}.

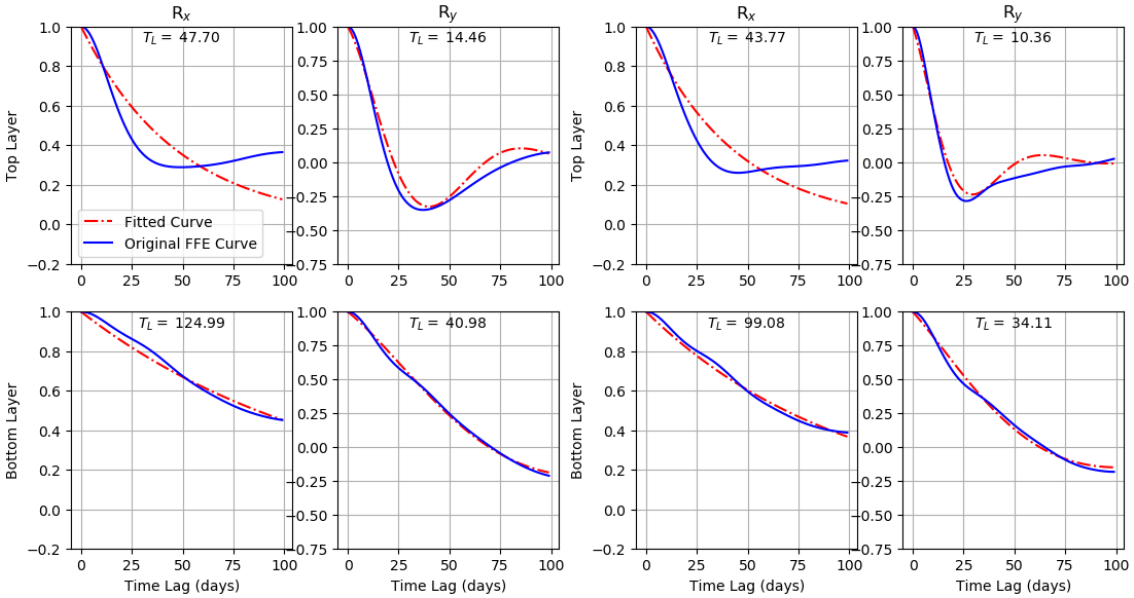

(a) Bin 1

(b) Bin 2

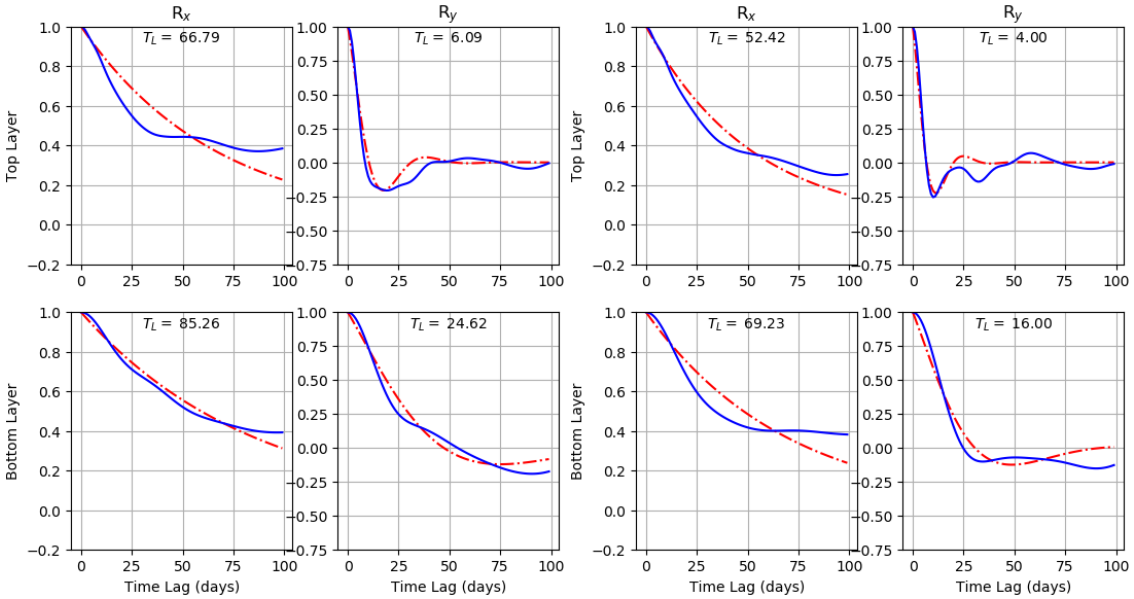

(c) Bin 3

(d) Bin 4

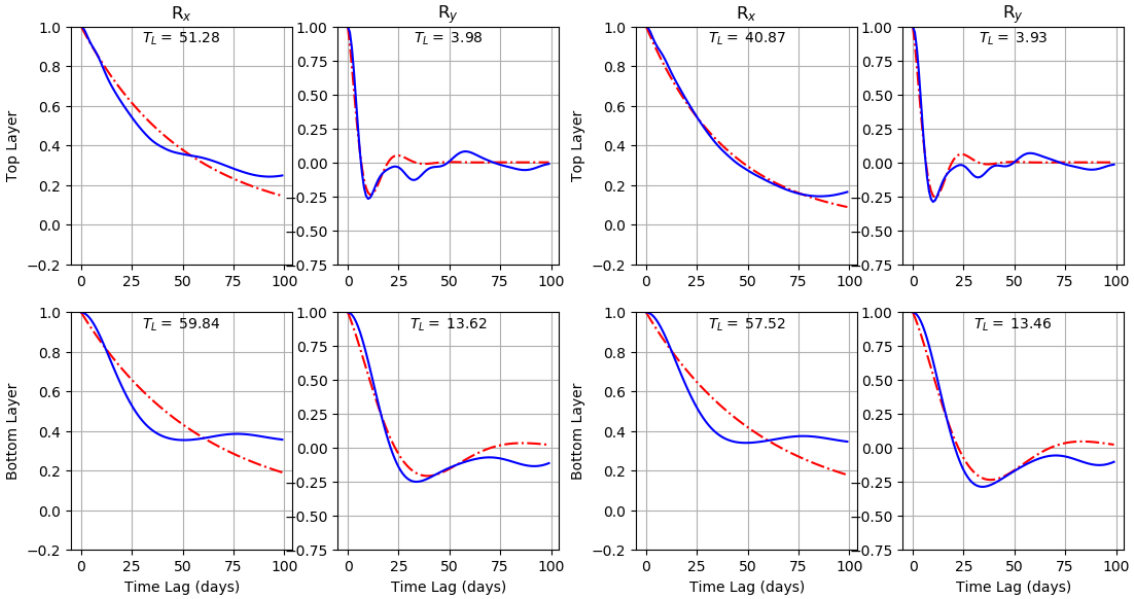

(e) Bin 5

(f) Bin 6

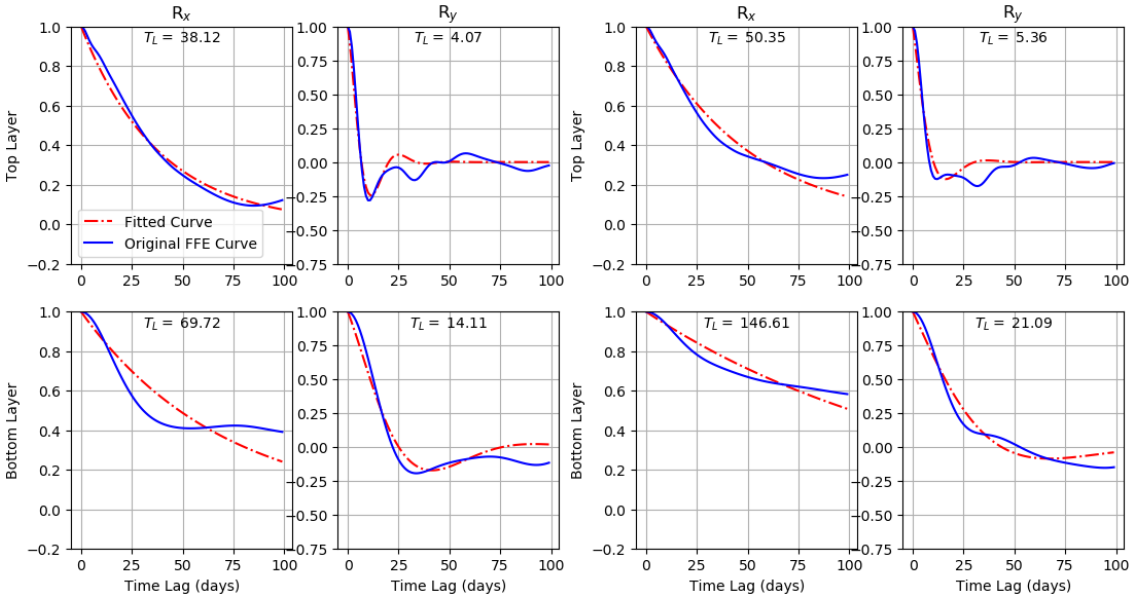

(g) Bin 7 (h) Bin 8

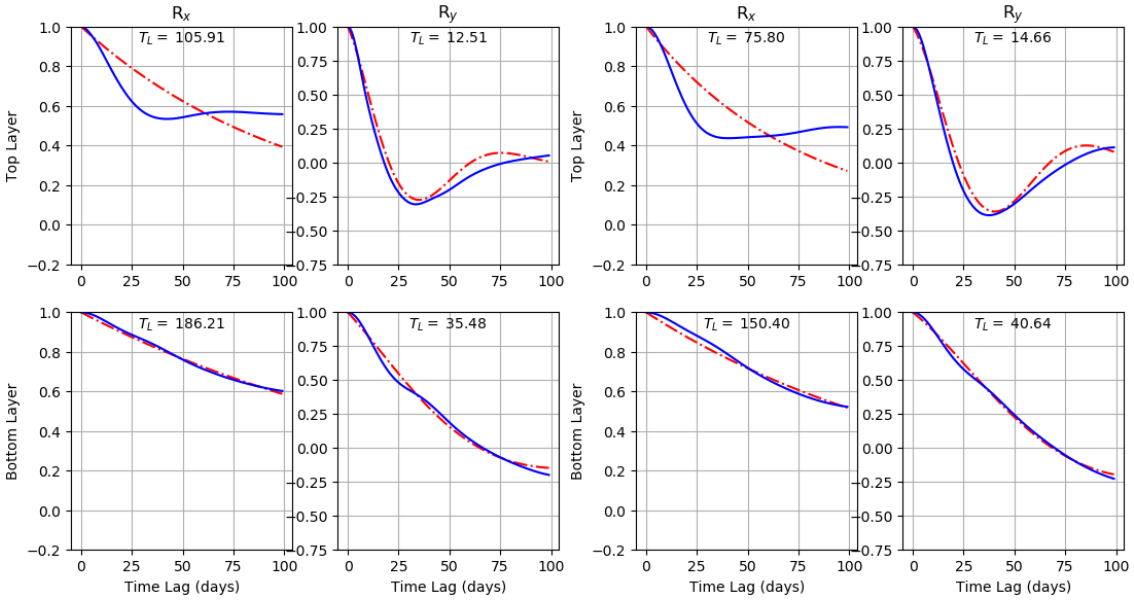

(i) Bin 9 (j) Bin 10

Figure E.8: The same as fig. E.7 but for the latent jet.

E.5 PV-Mapped Dispersion

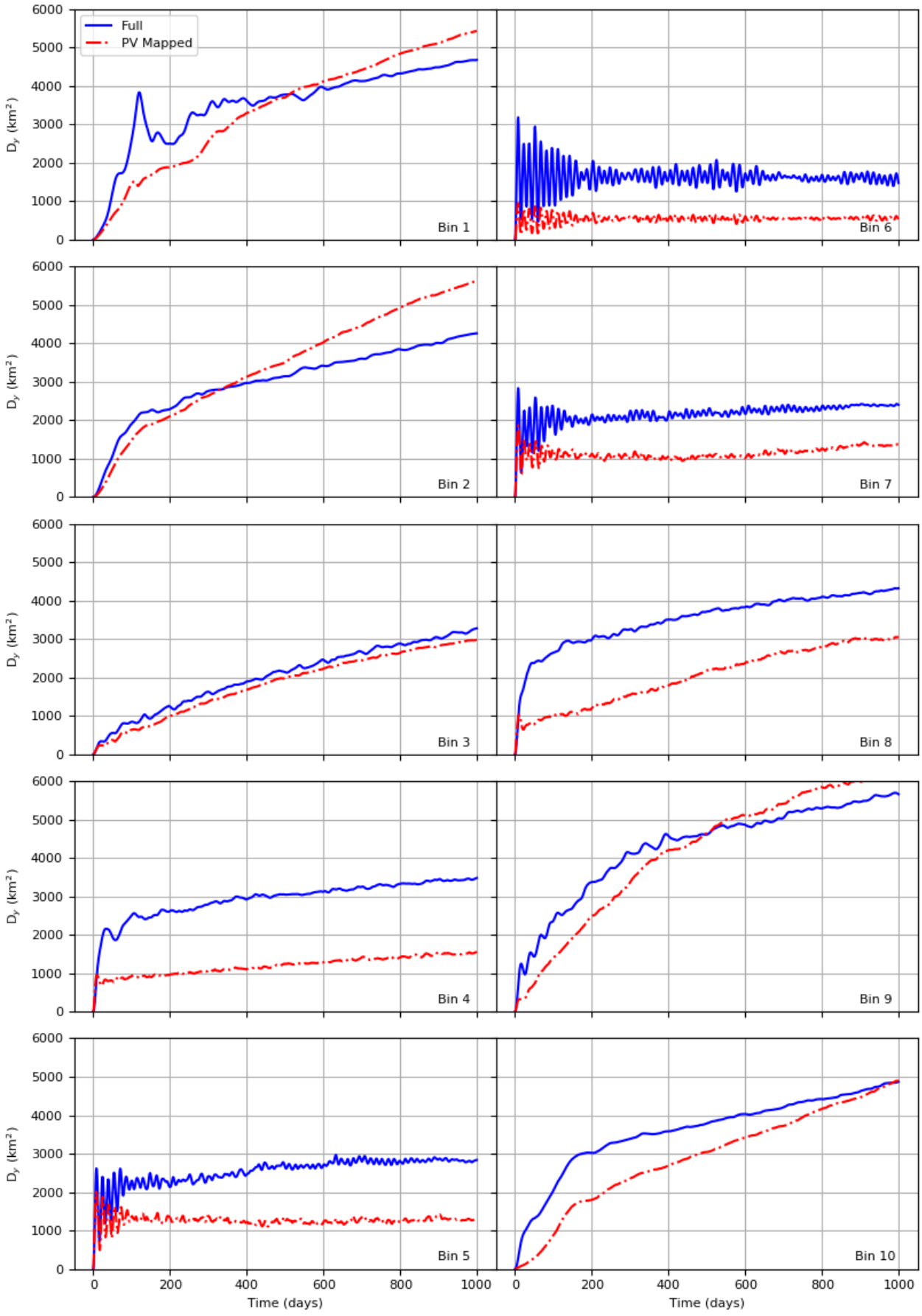

(a) Coherent jet.

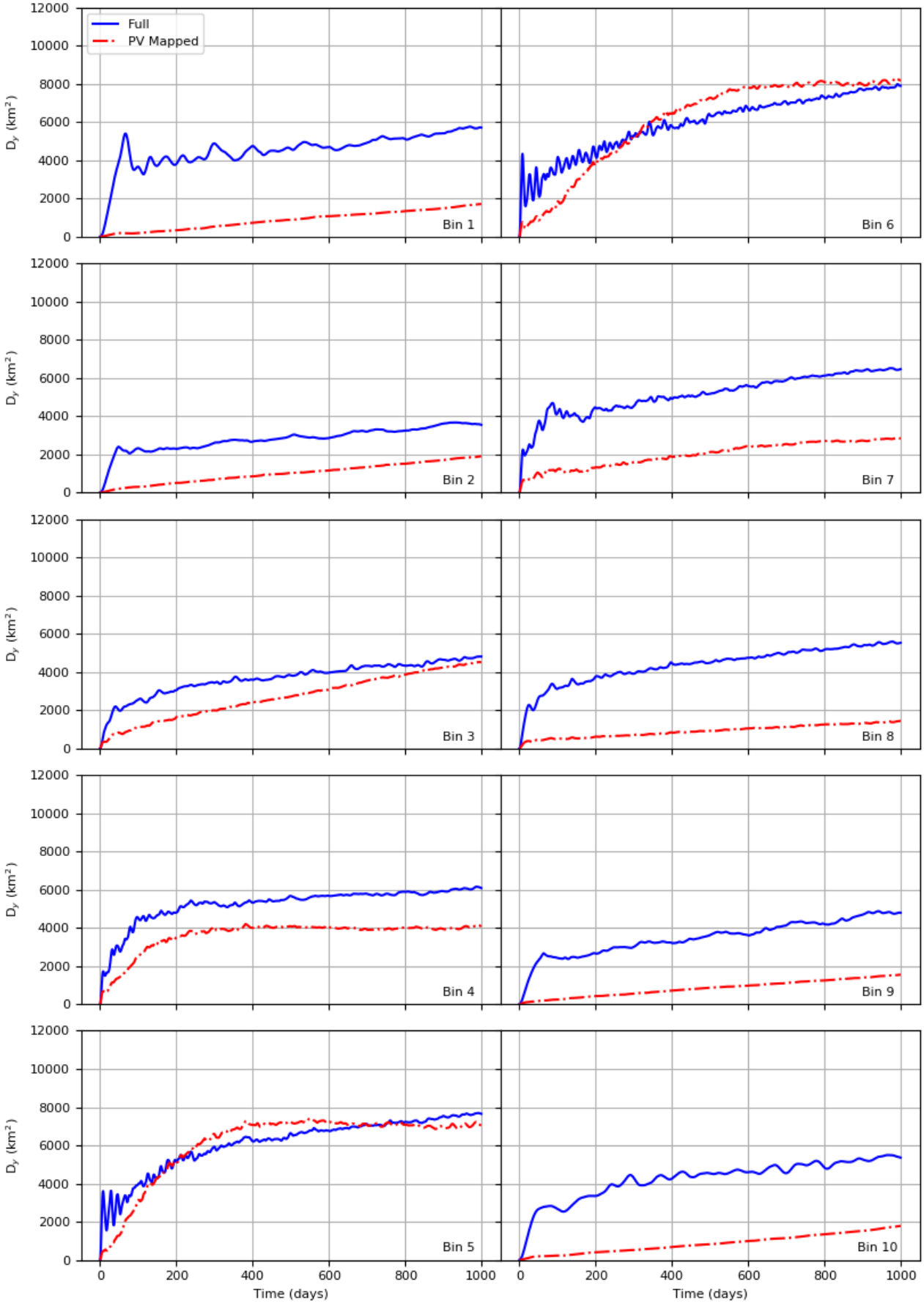

(b) Latent jet.

Figure E.9: Comparison of $D_y(t)$ (km^2) against the PV-mapped dispersion against time (days) for the two jet regimes for each bin. Only the top layer and meridional direction are shown.

E.6 PV-Mapped Lagrangian Autocorrelation Function

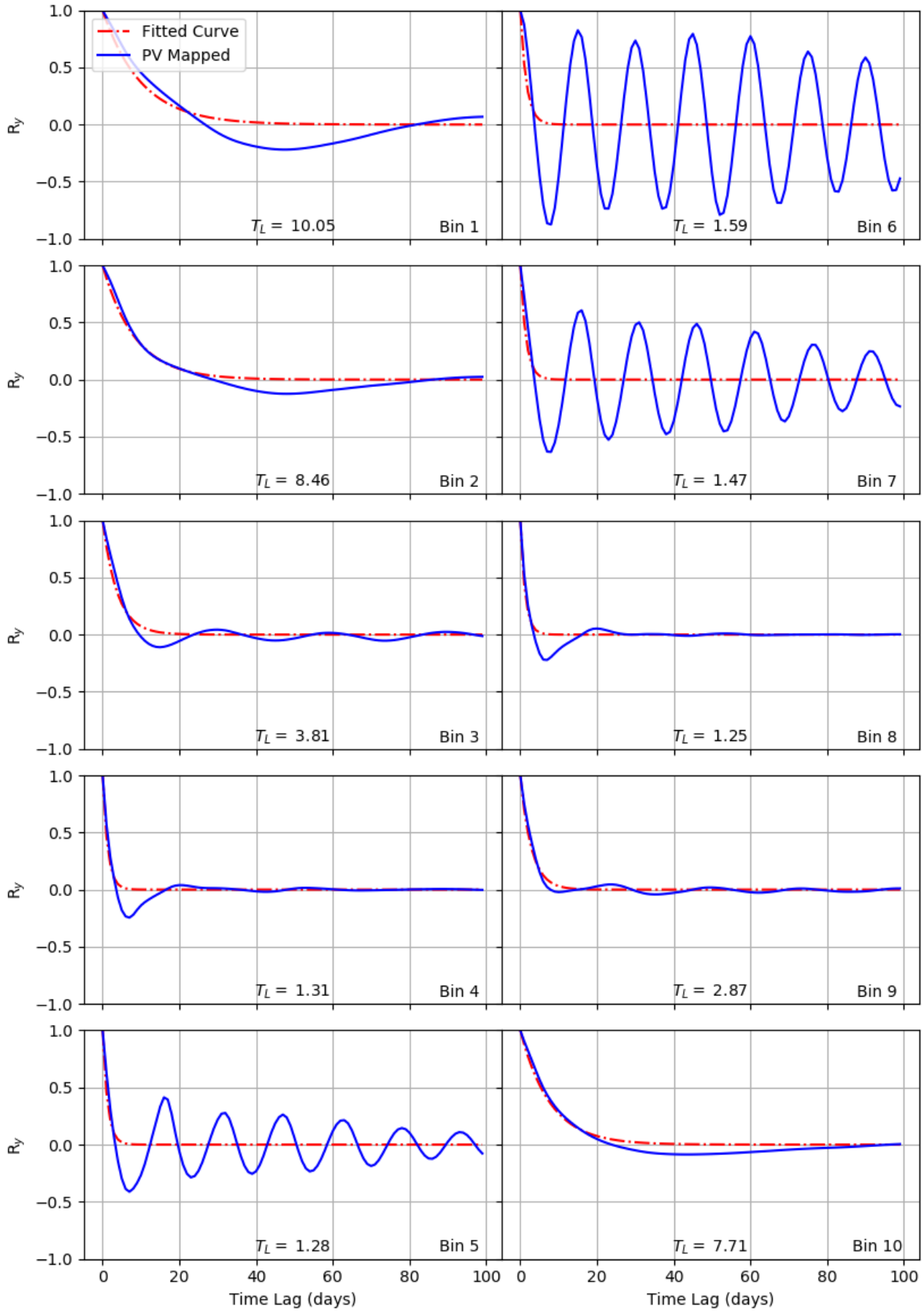

(a) Coherent Jet

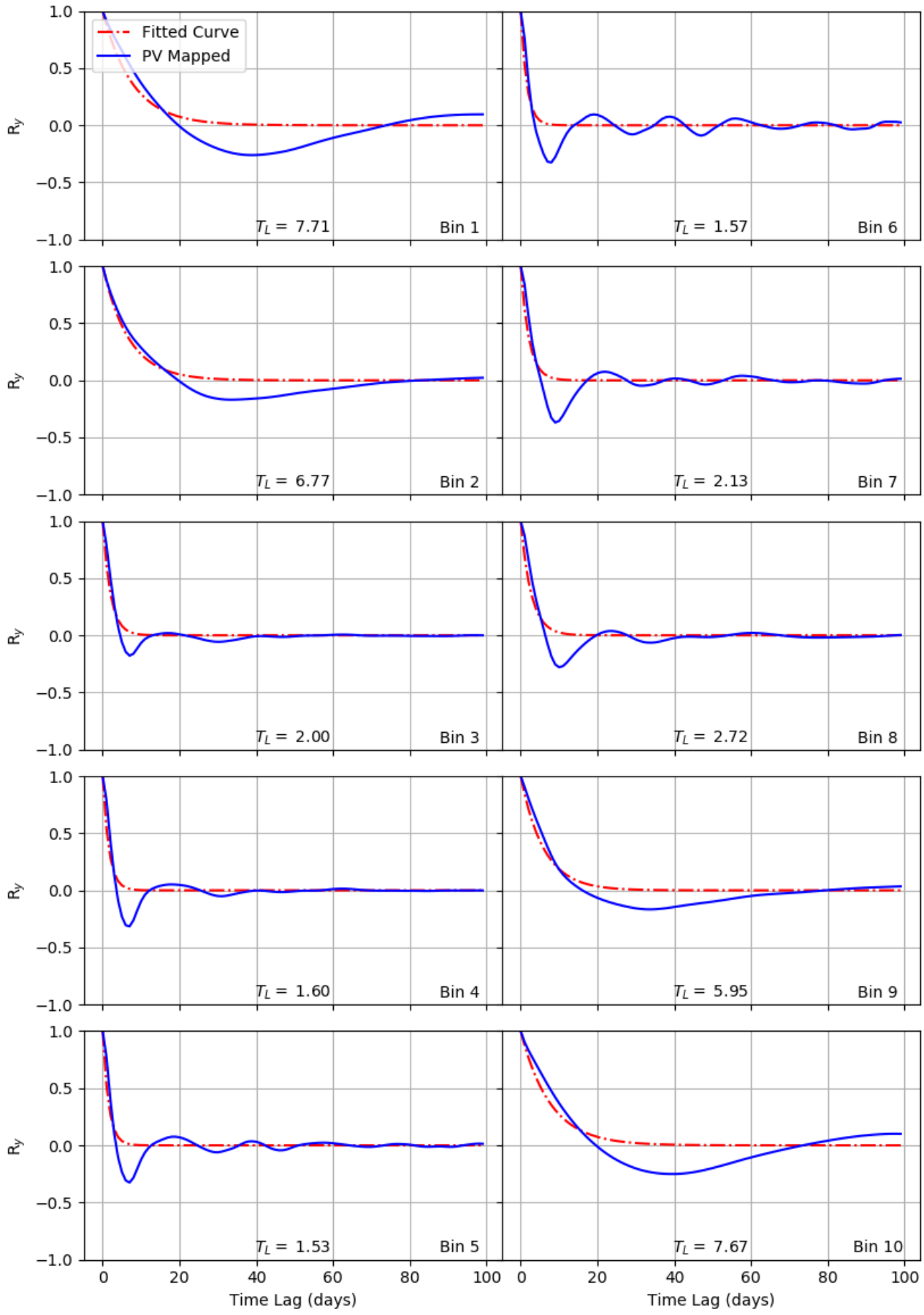

(b) Latent Jet

Figure E.10: The normalised PV-mapped autocorrelation function for each bin for the two jet regimes plotted against the time lag (days). It is compared against a fitted exponential with the Lagrangian integral time-scale, calculated as the decay rate, displayed for each figure. Only the top layer and meridional direction are shown.

Appendix F

Kinematic Model Figures

F.1 Single Particle Dispersion for 'How Many EOFs do we Need to Capture Lagrangian Dispersion?'

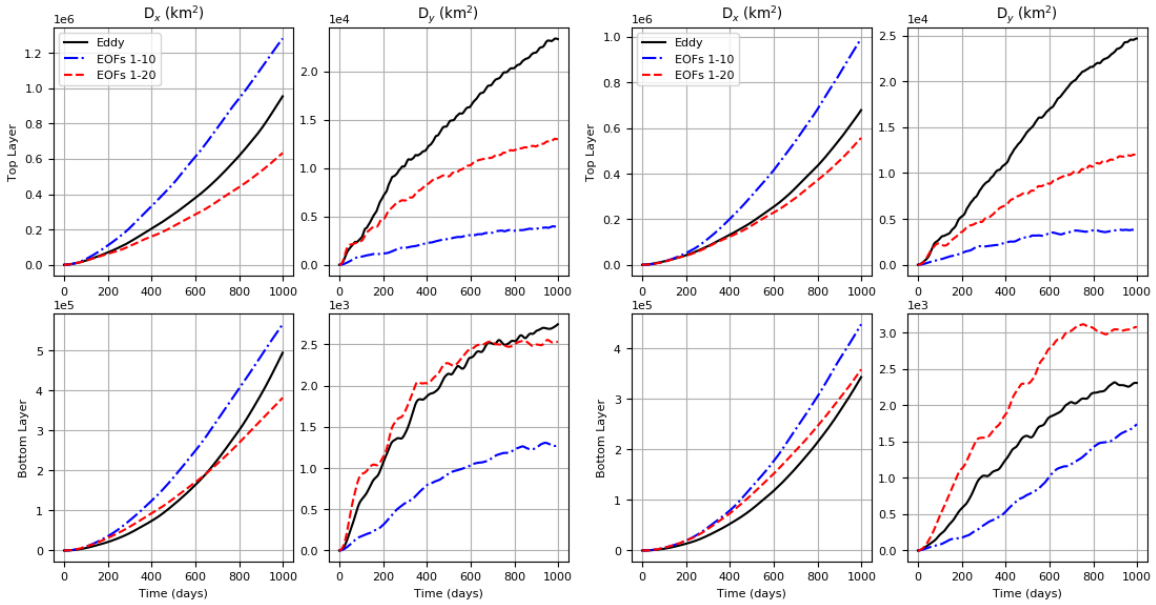

(a) Bin 1

(b) Bin 2

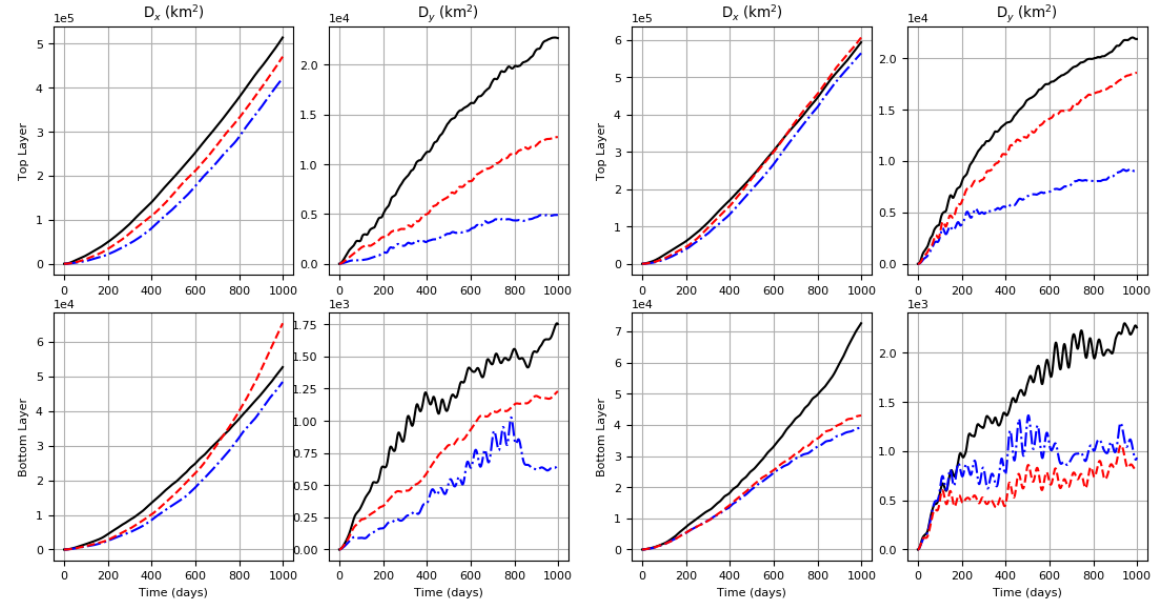

(c) Bin 3

(d) Bin 4

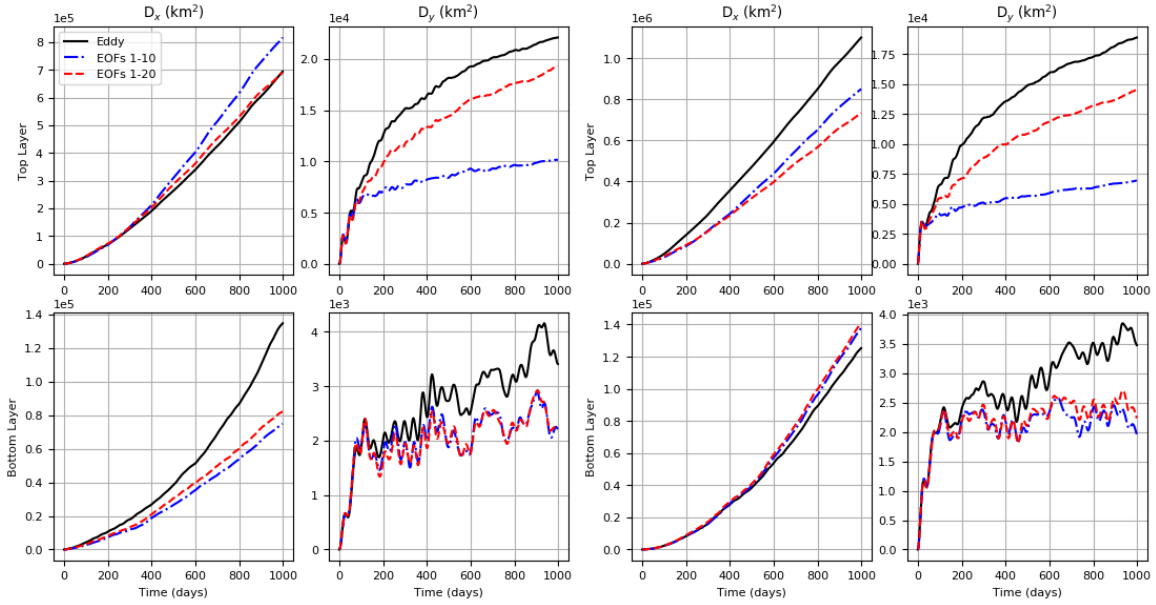

(e) Bin 5

(f) Bin 6

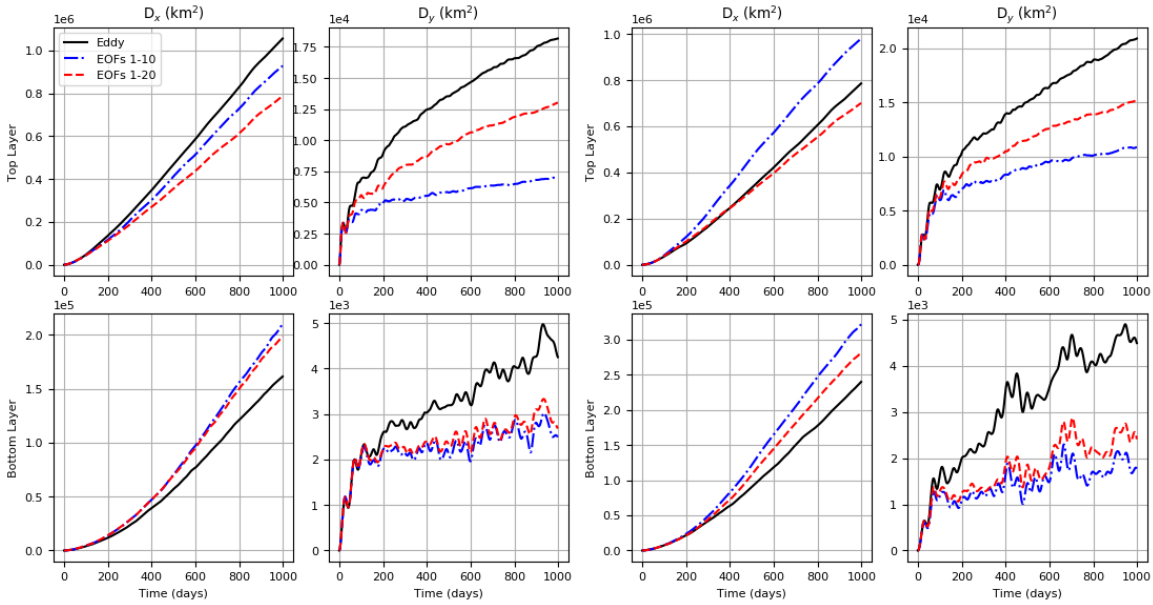

(g) Bin 7 (h) Bin 8

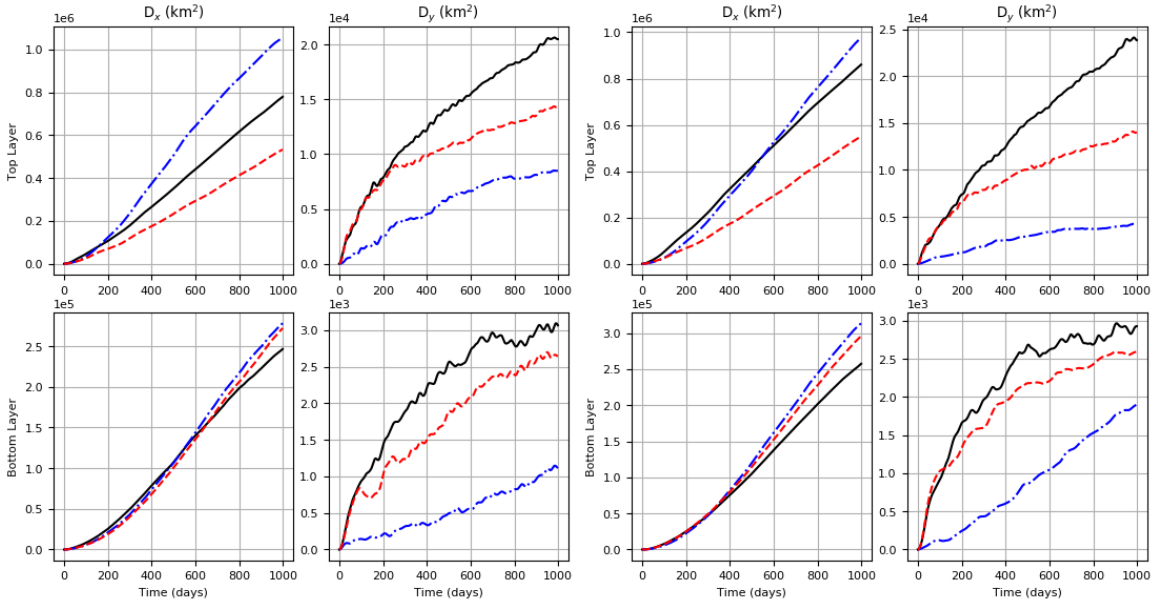

(i) Bin 9 (j) Bin 10

Figure F.1: Single-Particle Dispersion (km^2) against time (days) for each bin for different numbers of EOFs for the coherent jet.

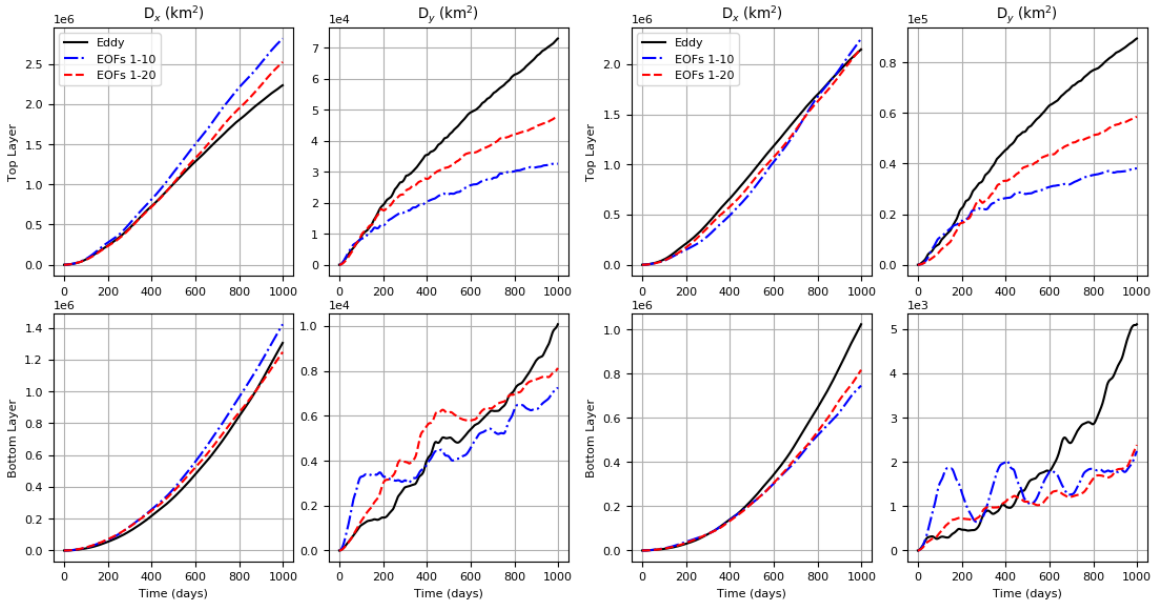

(a) Bin 1

(b) Bin 2

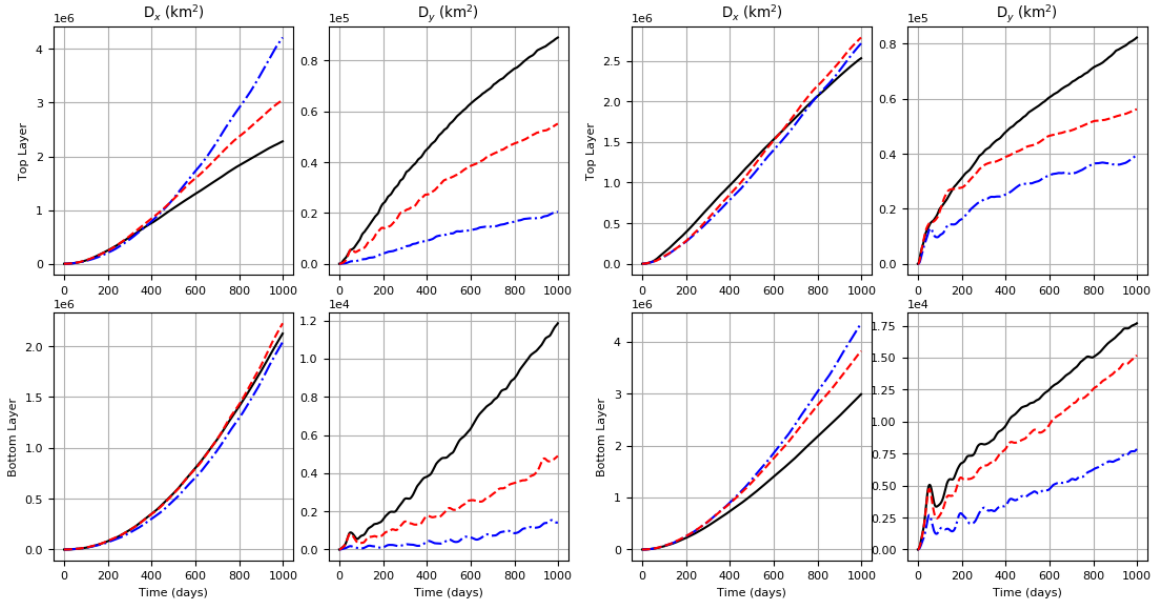

(c) Bin 3

(d) Bin 4

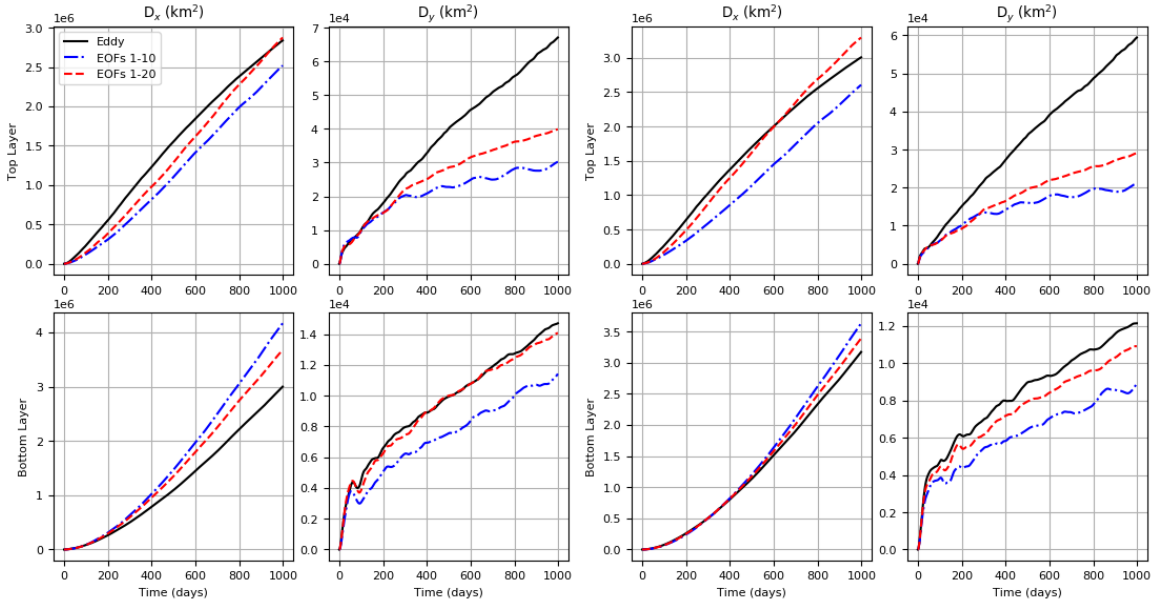

(e) Bin 5

(f) Bin 6

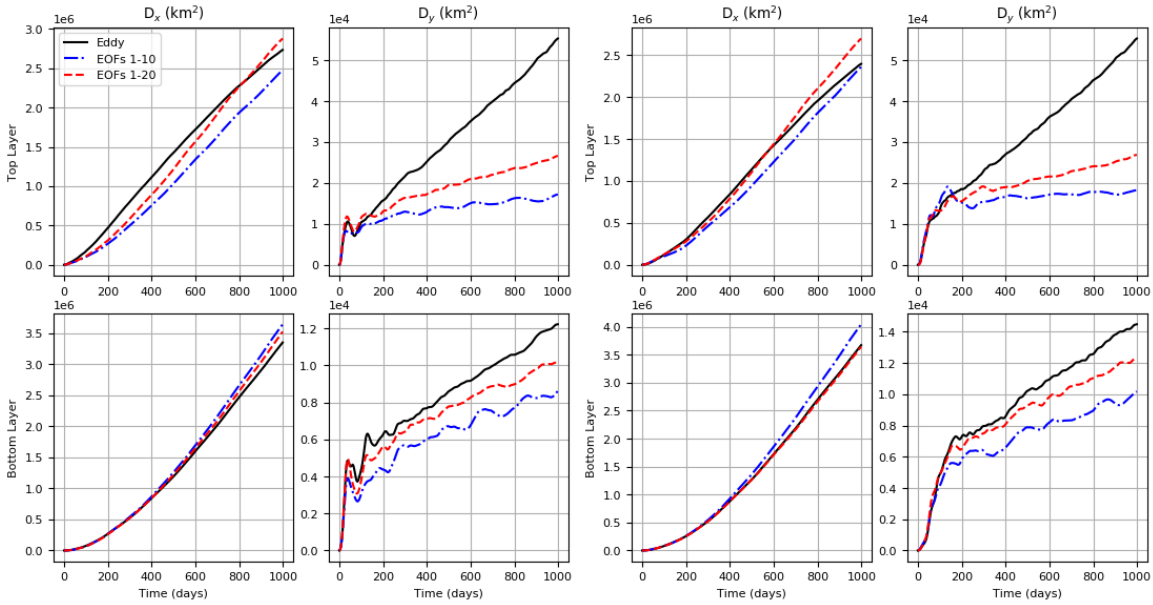

(g) Bin 7 (h) Bin 8

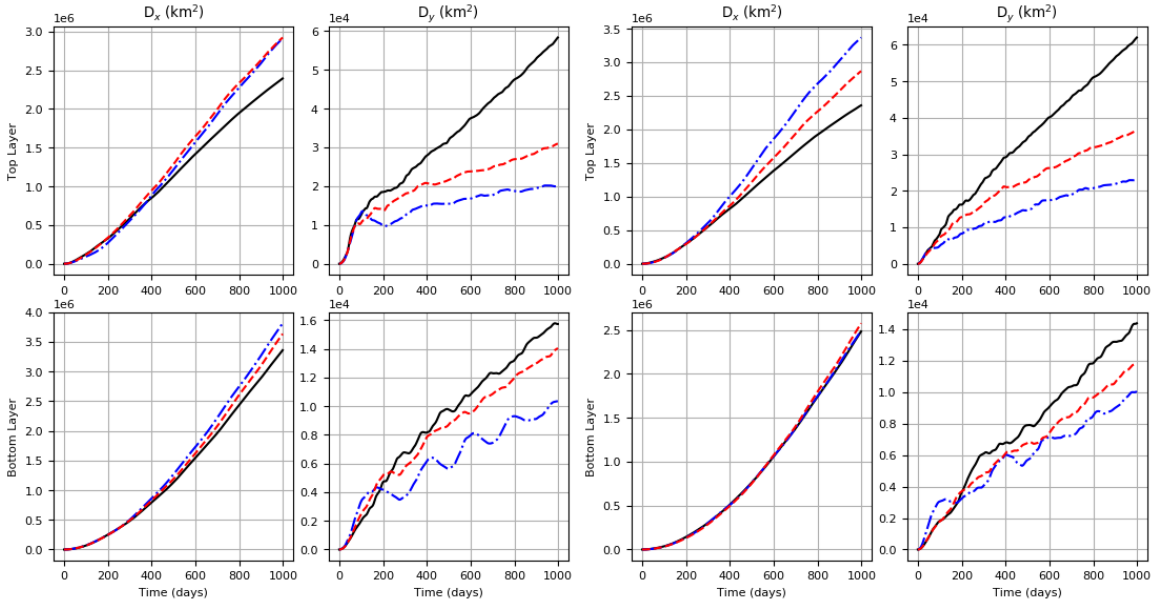

(i) Bin 9 (j) Bin 10

Figure F.2: Single-Particle Dispersion (km^2) against time (days) for each bin for different numbers of EOFs for the latent jet.

F.2 Single Particle Dispersion for 'Deducing the Role of EOF Patterns in Lagrangian Dispersion'.

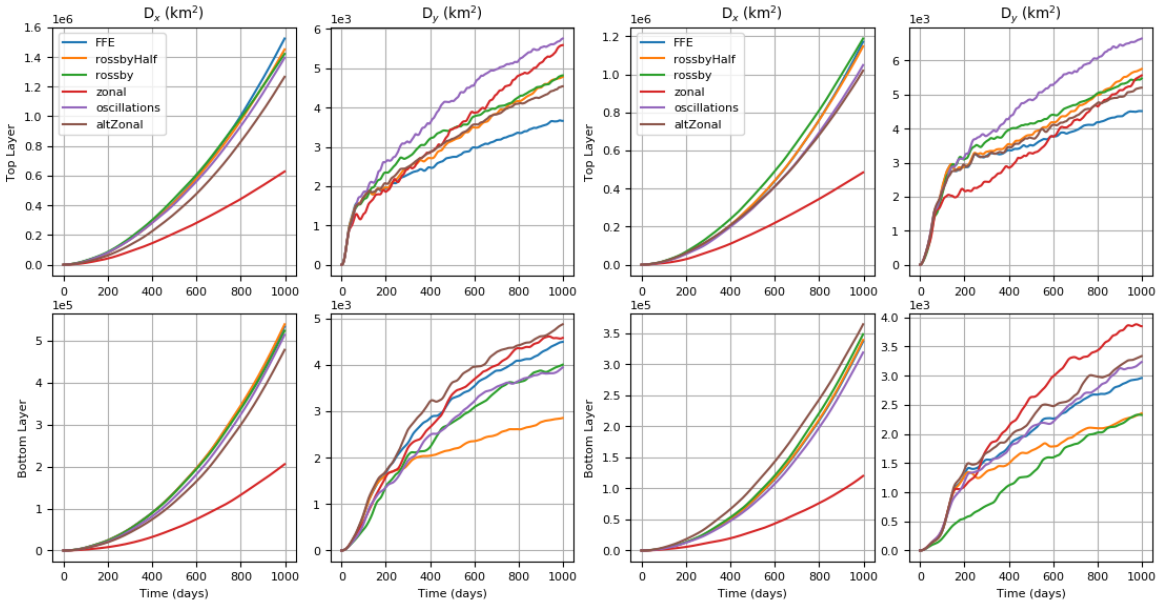

(a) Bin 1

(b) Bin 2

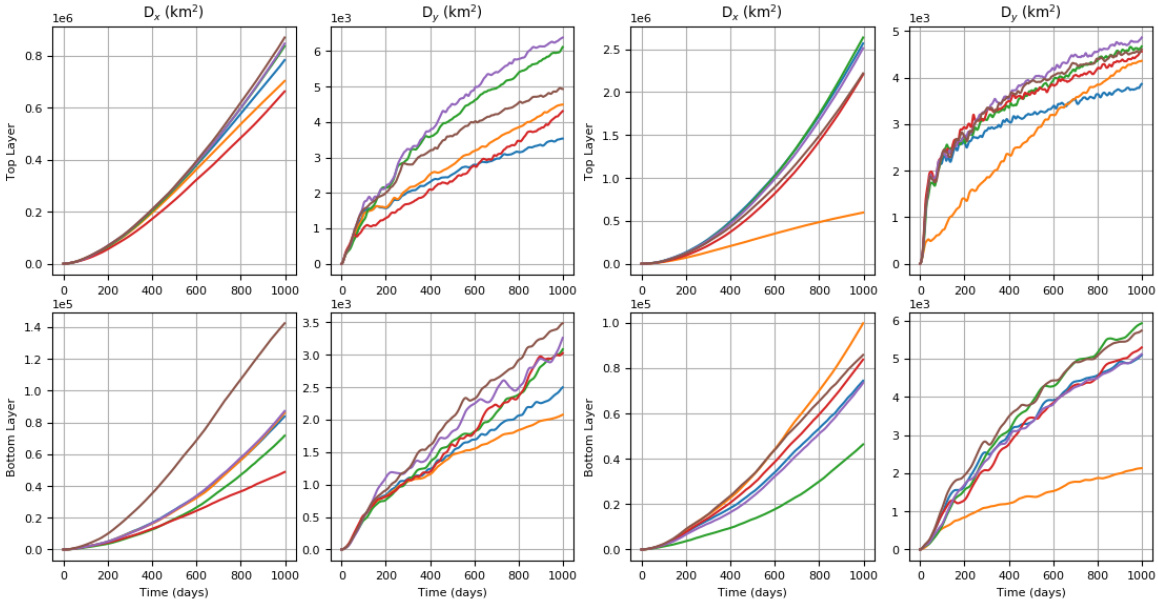

(c) Bin 3

(d) Bin 4

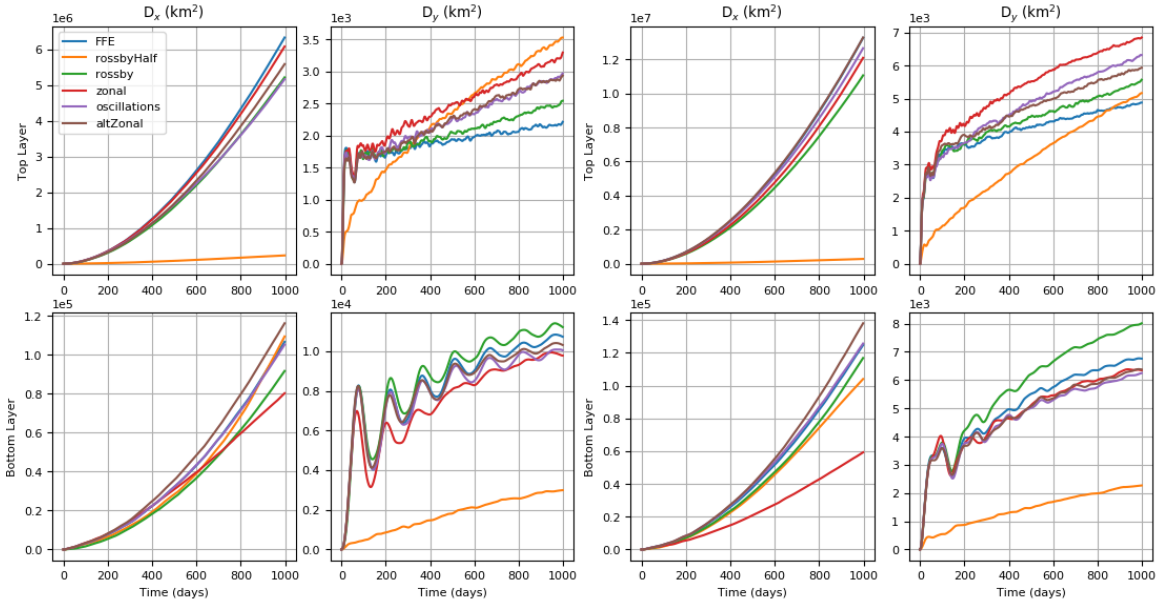

(e) Bin 5

(f) Bin 6

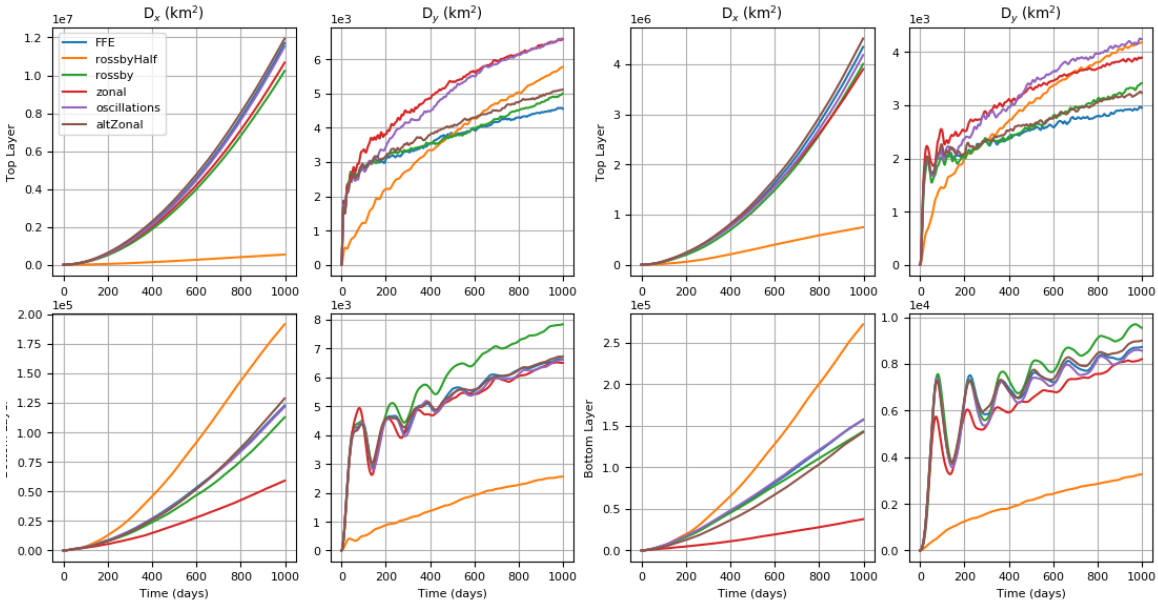

(g) Bin 7 (h) Bin 8

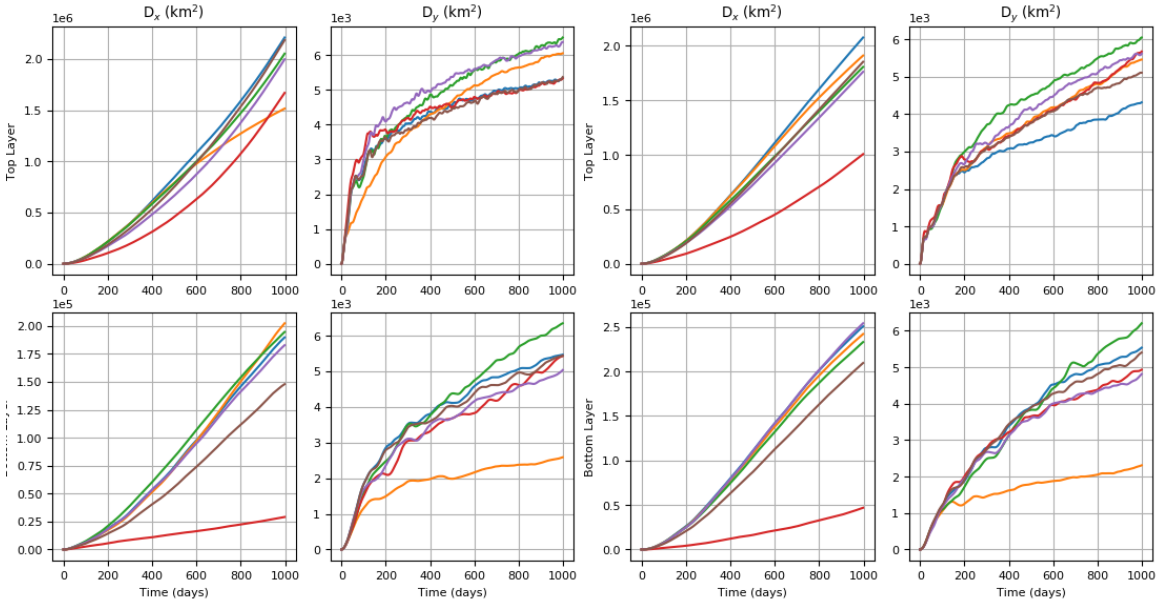

(i) Bin 9 (j) Bin 10

Figure F.3: Single-Particle Dispersion (km^2) against time (days) for each bin where different EOF pairs are deducted from the full field in the coherent jet.

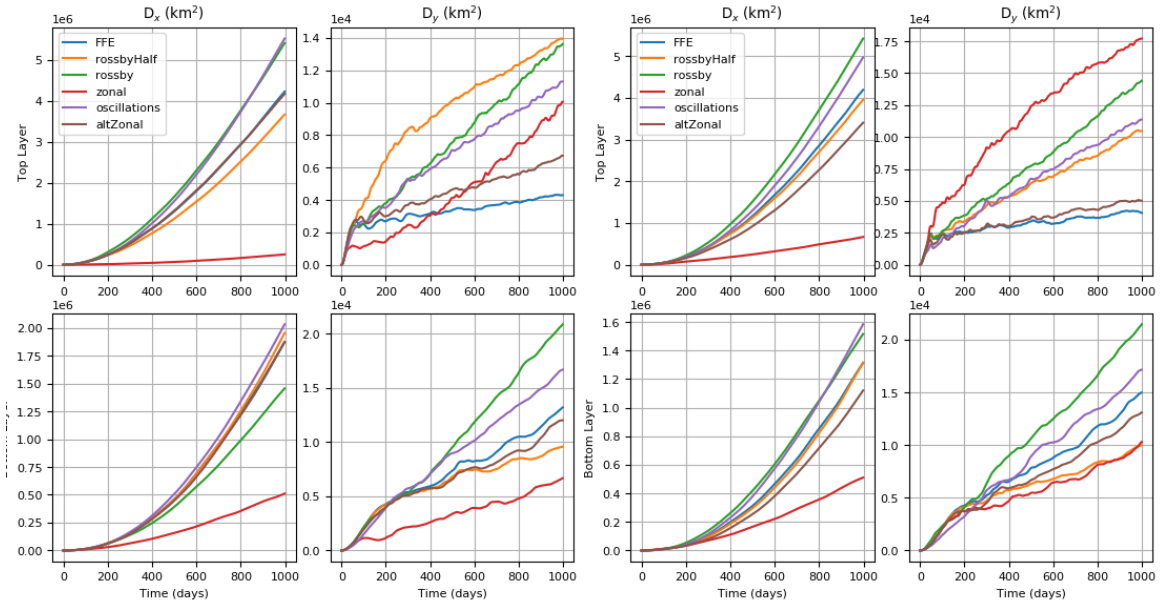

(a) Bin 1

(b) Bin 2

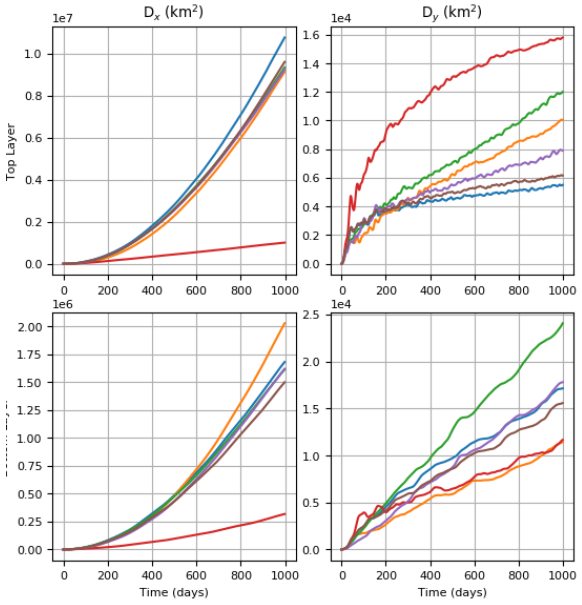

(c) Bin 3

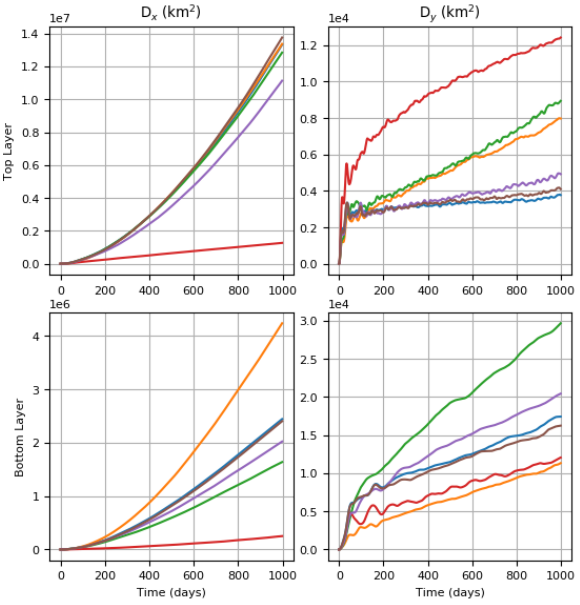

(d) Bin 4

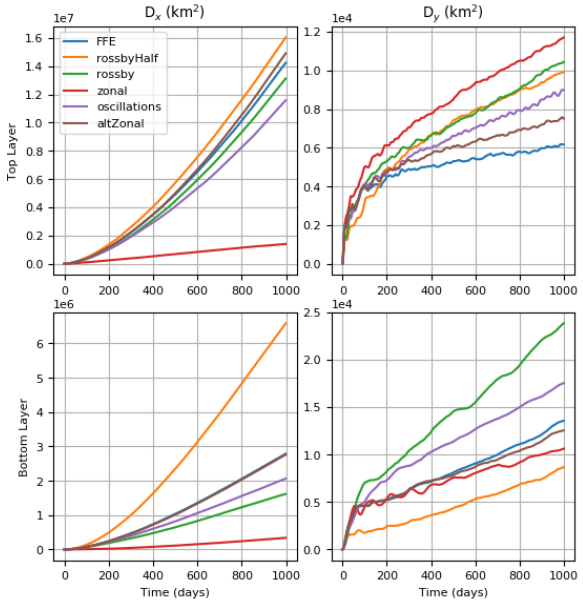

(e) Bin 5

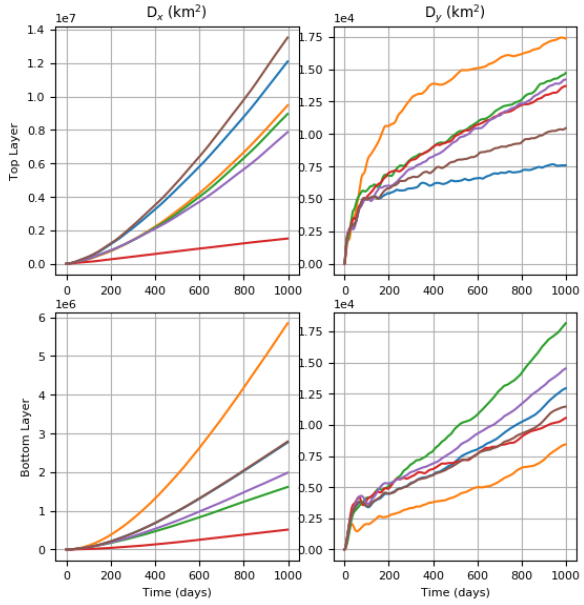

(f) Bin 6

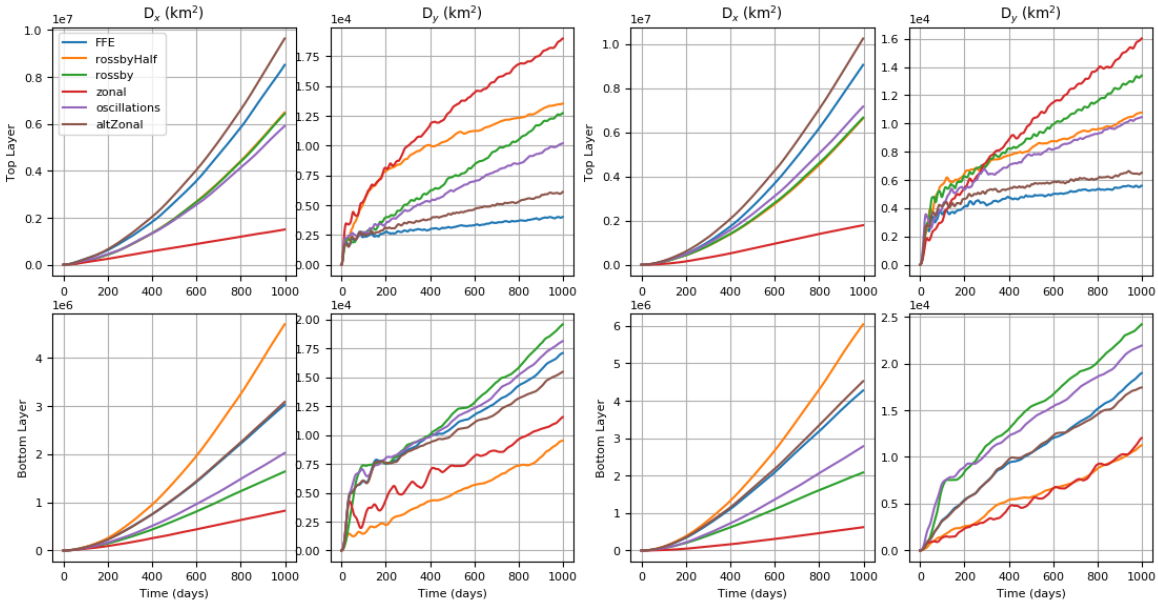

(g) Bin 7

(h) Bin 8

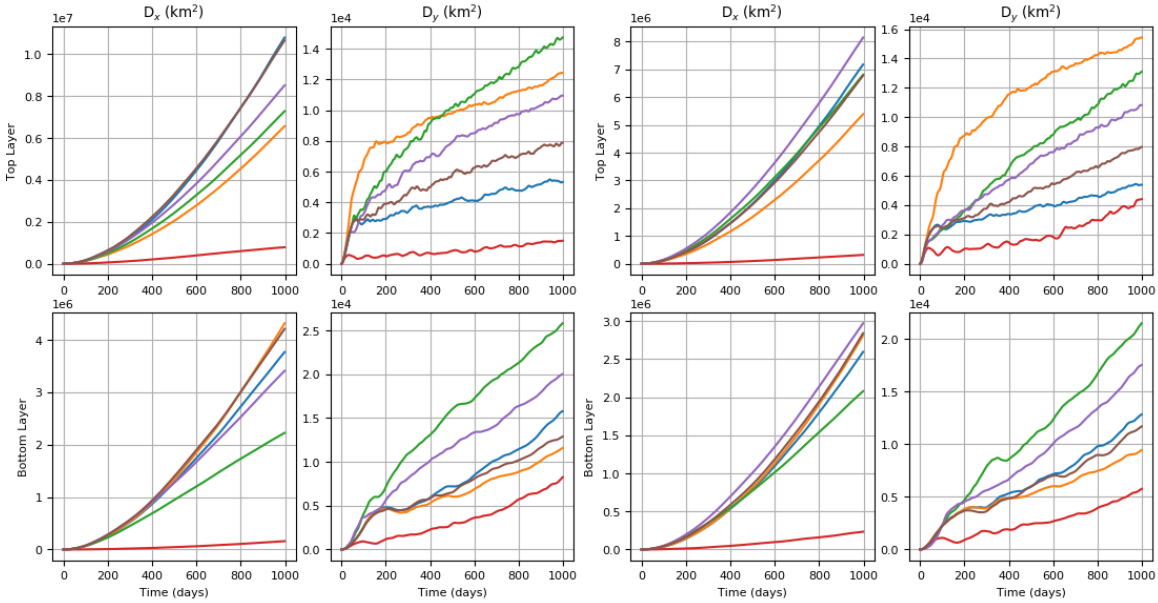

(i) Bin 9

(j) Bin 10

Figure F.4: Single-Particle Dispersion (km^2) against time (days) for each bin where different EOF pairs are deducted from the full field in the latent jet.

F.3 Figure for 'Investigating the Role of Half-Wavelength Rossby Waves'

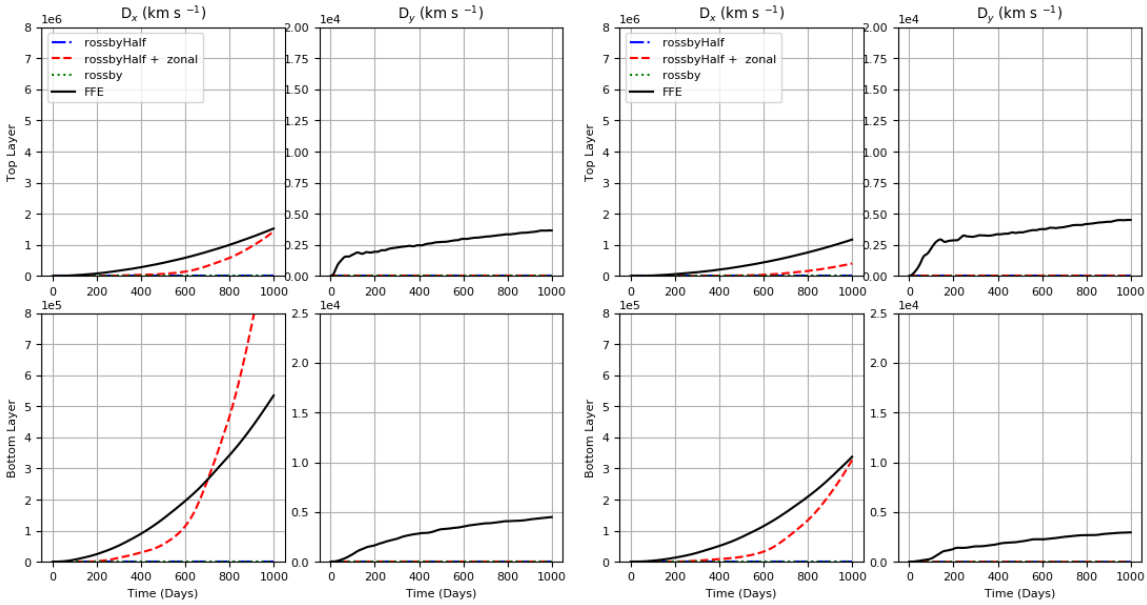

(a) Bin 1

(b) Bin 2

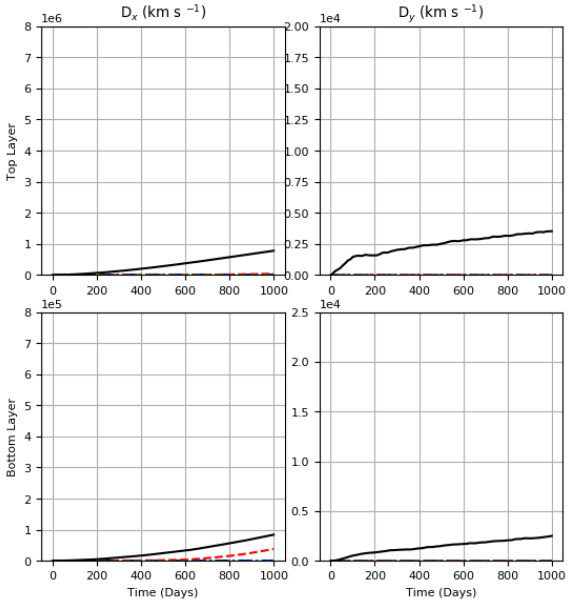

(c) Bin 3

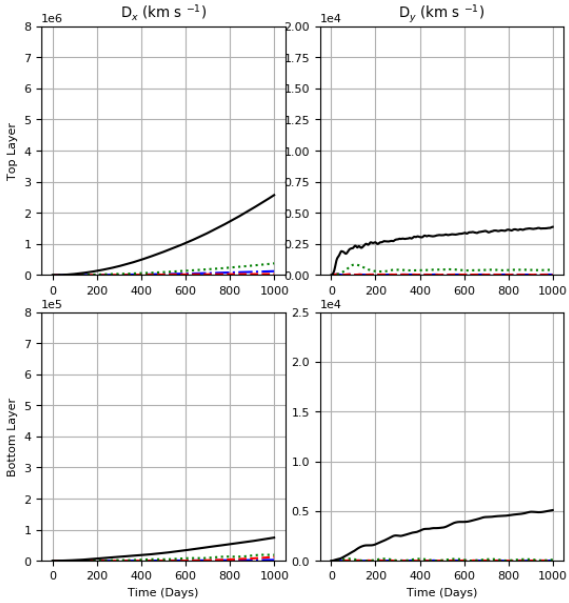

(d) Bin 4

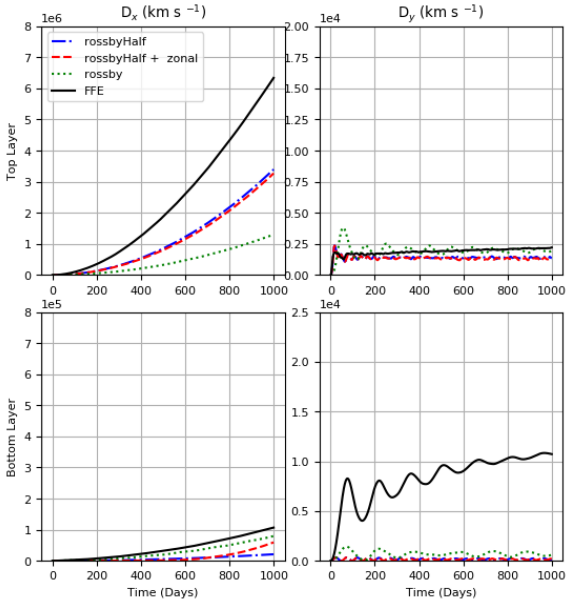

(e) Bin 5

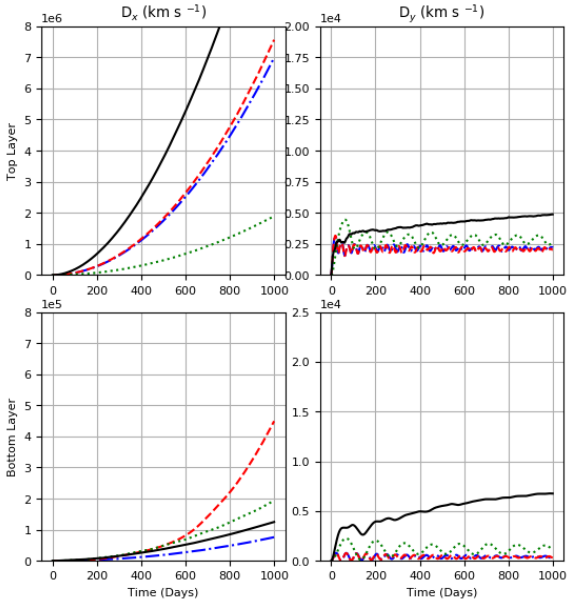

(f) Bin 6

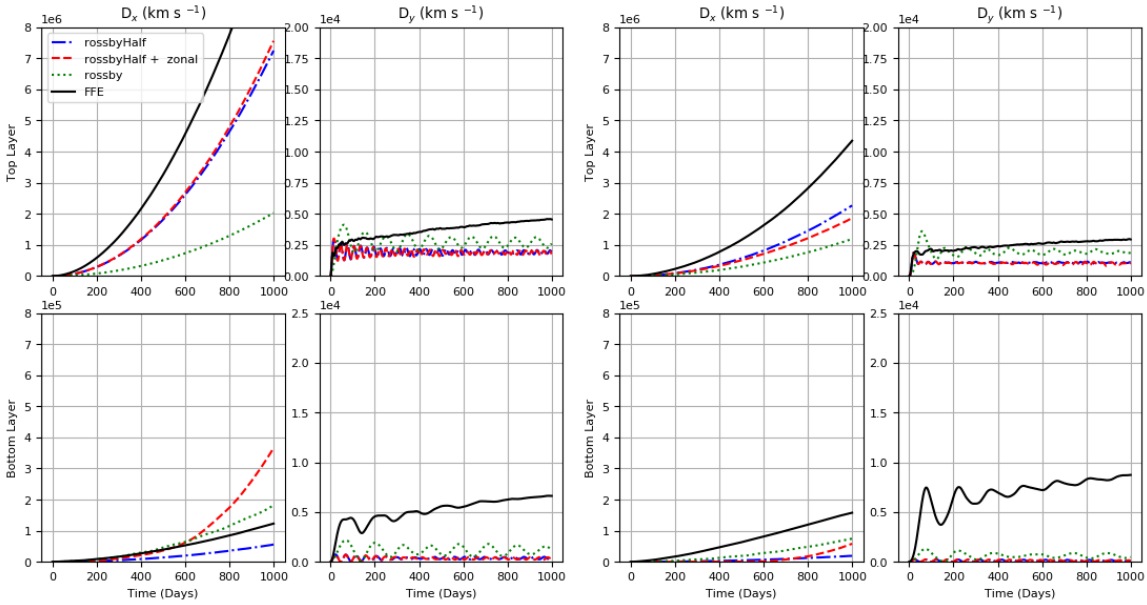

(g) Bin 7

(h) Bin 8

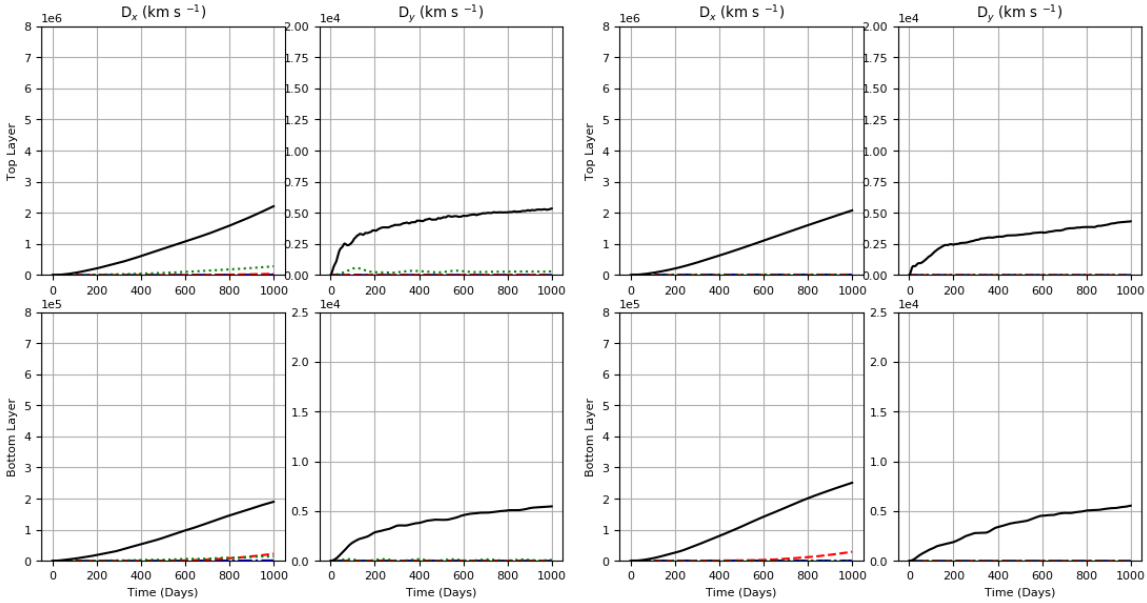

(i) Bin 9

(j) Bin 10

Figure F.5: Comparing the single-particle dispersion (km^2) against time (days) for each bin for the kinematic field with and without the background flow for the coherent jet.

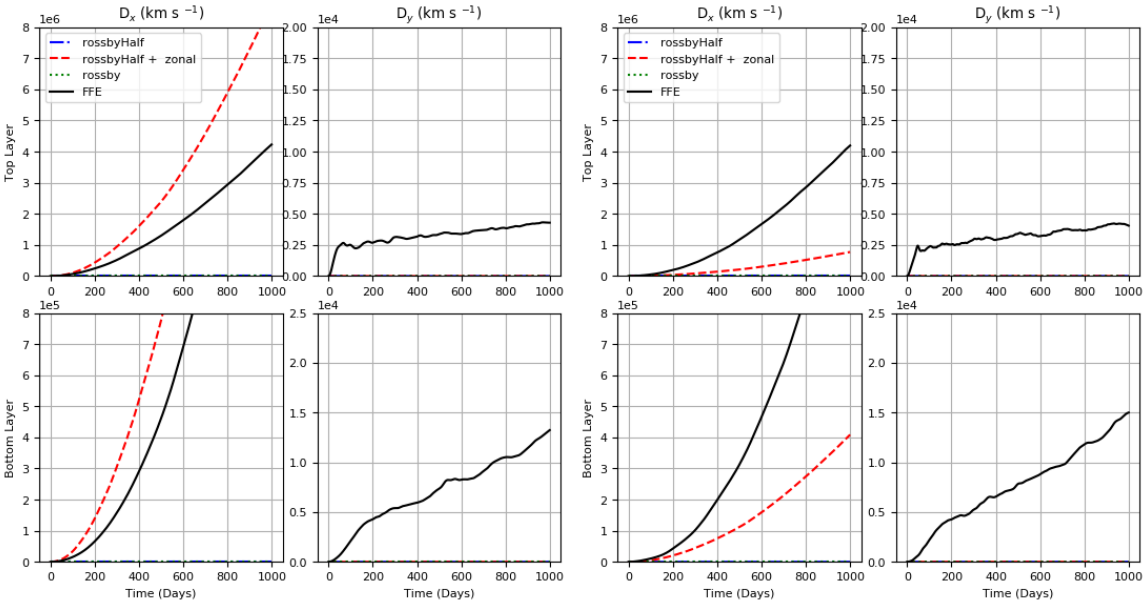

(a) Bin 1

(b) Bin 2

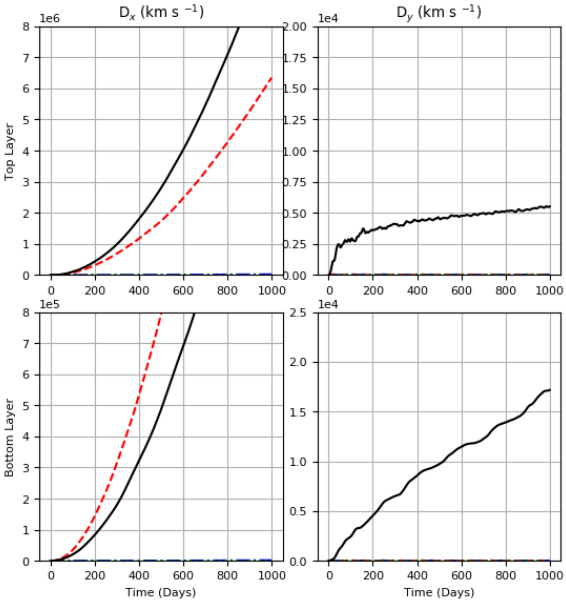

(c) Bin 3

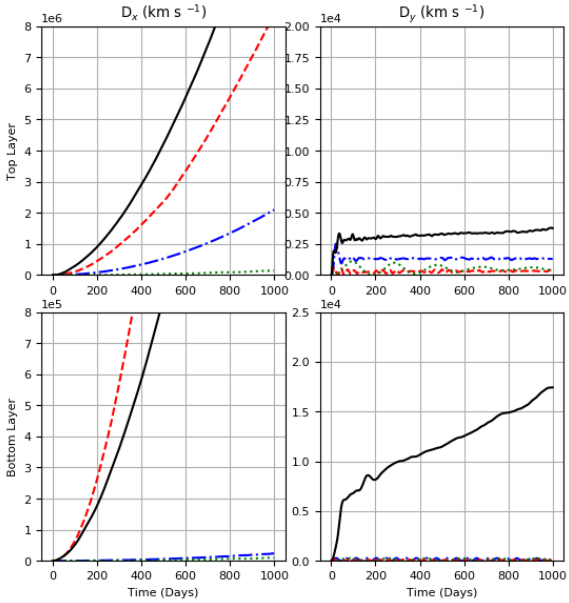

(d) Bin 4

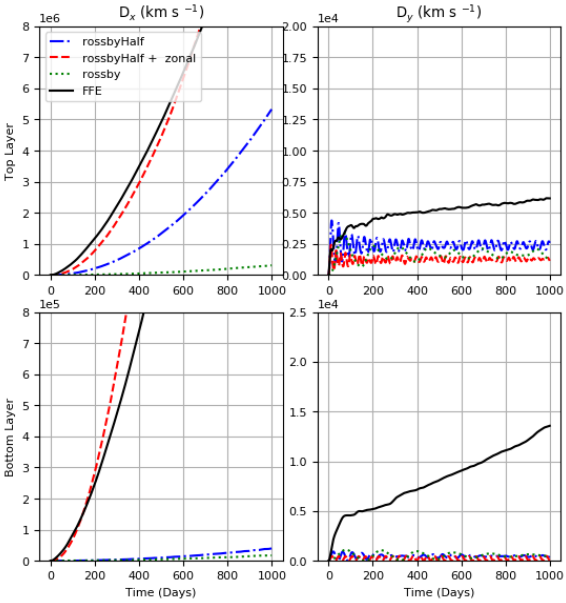

(e) Bin 5

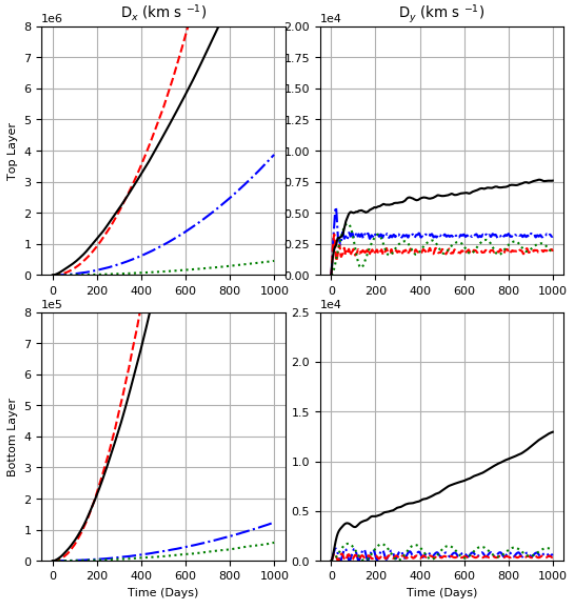

(f) Bin 6

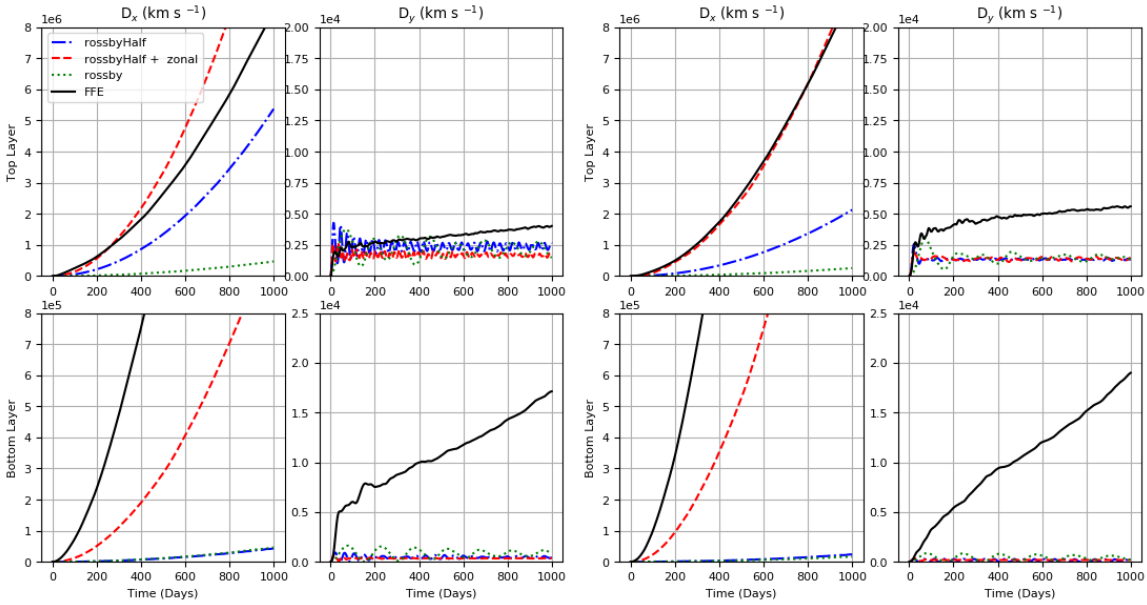

(g) Bin 7 (h) Bin 8

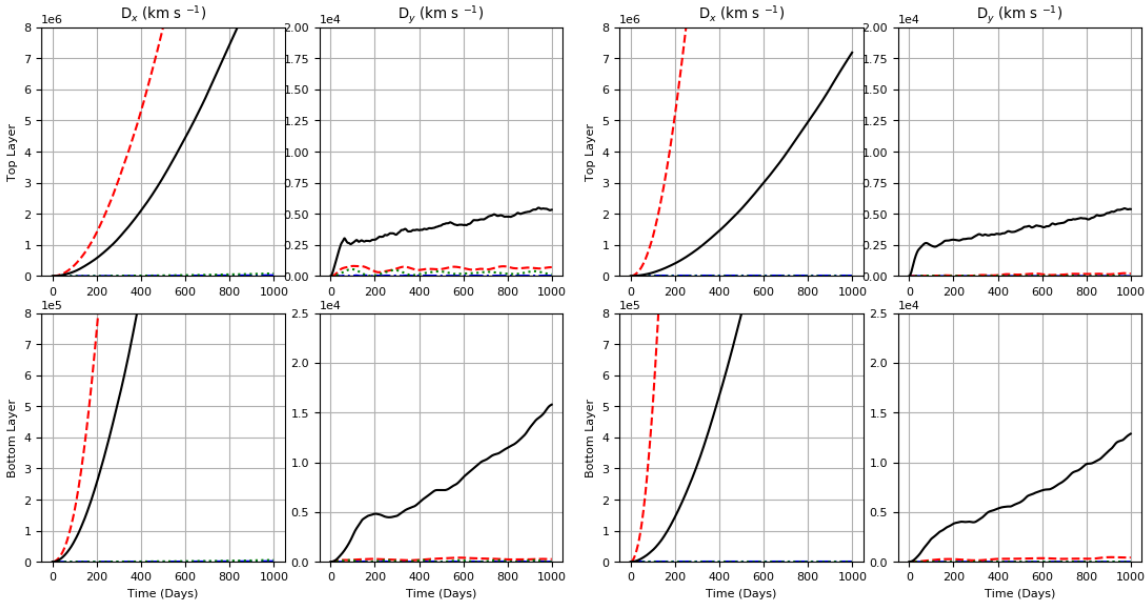

(i) Bin 9 (j) Bin 10

Figure F.6: Comparing the single-particle dispersion (km^2) against time (days) for each bin for the kinematic field with and without the background flow for the latent jet.

Appendix G

Deriving the Stokes Drift for Half Rossby Waves

The Stokes' Drift velocity is given by (van den Bremer & Breivik 2018*a*):

$$\mathbf{u}_S = \bar{\mathbf{u}}_L - \bar{\mathbf{u}}_E, \tag{G.1}$$

where the overbar denotes the average, $\bar{\mathbf{u}}_L$ denotes the Lagrangian velocity and $\bar{\mathbf{u}}_E$ denotes the Eulerian velocity.

For simplicity let's express the half Rossby wave stream functioneq. (5.3) as follows:

$$\psi(x, y, t) = f(x, y)\cos(kx - \omega t), \tag{G.2}$$

where $f(x, y)$ represents the amplitude of the Rossby wave and $kc = \omega$. We get the eulerian velocity components by using the non-divergent property of the stream function:

$$u_E = -\frac{\partial f(x, y)}{\partial y}\cos(kx - \omega t), \tag{G.3}$$

$$v_E = \frac{\partial f(x, y)}{\partial x}\cos(kx - \omega t) - f(x, y)k\sin(kx - \omega t). \tag{G.4}$$

We can approximate the Lagrangian velocity of a particle located at $\boldsymbol{\xi} = (\xi_x, \xi_y)$ using a Taylor expansion about $\boldsymbol{\xi}$:

$$u_L \approx u_E + \frac{\partial u_E}{\partial x}(\xi_x - x_0) + \frac{\partial u_E}{\partial y}(\xi_y - y_0), \tag{G.5}$$

$$v_L \approx v_E + \frac{\partial v_E}{\partial x}(\xi_x - x_0) + \frac{\partial v_E}{\partial y}(\xi_y - y_0). \tag{G.6}$$

$$\tag{G.7}$$

We can find the particle displacements ξ_x and ξ_y as follows:

$$\frac{d\xi_x}{dt} = u_E(\mathbf{x}, t), \implies \tag{G.8}$$

$$\xi_x = x_0 + \frac{1}{\omega}\frac{\partial f}{\partial y}\sin(kx - \omega t). \tag{G.9}$$

and

$$\frac{d\xi_y}{dt} = v_E(\mathbf{x}, t), \implies \tag{G.10}$$

$$\xi_y = y_0 - \frac{1}{\omega}\frac{\partial f}{\partial x}\sin(kx - \omega t) - \frac{1}{\omega}f(x, y)k\cos(kx - \omega t). \tag{G.11}$$

Focusing on the zonal direction, and substituting ξ_x and u_L into eq. (G.1):

$$\overline{u_S} = \overline{\frac{\partial^2 \xi_x}{\partial x \partial t}(\xi_x - x_0)} + \overline{\frac{\partial^2 \xi_x}{\partial y \partial t}(\xi_y - y_0)} \tag{G.12}$$

$$= \overline{\frac{\partial^2 \xi_x}{\partial x \partial t}\left(\frac{1}{\omega}\frac{\partial f}{\partial y}\sin(kx - \omega t)\right)} + \overline{\frac{\partial^2 \xi_x}{\partial y \partial t}\left(-\frac{1}{\omega}\frac{\partial f}{\partial x}\sin(kx - \omega t) - \frac{1}{\omega}f(x, y)k\cos(kx - \omega t)\right)}. \tag{G.13}$$

Firstly, let's evaluate the partial derivatives of ξ_x:

$$\frac{\partial^2 \xi_x}{\partial x \partial y} = -\frac{\partial^2 f}{\partial t \partial x}\cos(kx - \omega t) + k\frac{\partial f}{\partial y}\sin(kx - \omega t), \tag{G.14}$$

$$\frac{\partial^2 \xi_x}{\partial y \partial t} = -\frac{\partial^2 f}{\partial y^2}\cos(kx - \omega t). \tag{G.15}$$

The long time average of $\cos(g(x,y))\sin(h(x,y))$ is 0, so we can simplify $\overline{u_S}$ as follows:

$$\overline{u_S} = \overline{-\frac{k}{\omega}\left(\frac{\partial f}{\partial y}\right)^2 \sin^2(kx - \omega t)} + \overline{\frac{k}{\omega} f(x,y)\frac{\partial^2 f}{\partial y^2}\cos^2(kx - \omega t)}. \tag{G.16}$$

As $t \to \infty, \overline{\sin^2(kx - \omega t)} \to \frac{1}{2}$, hence:

$$\overline{u_S} = \frac{k}{2\omega}\left(\frac{\partial f}{\partial y}\right)^2 + \frac{k}{2\omega} f(x,y)\frac{\partial^2 f}{\partial y^2}, \tag{G.17}$$

$$= \frac{k}{4\omega}\frac{\partial^2}{\partial y^2} f^2. \tag{G.18}$$

Similarly for the meridional direction, we obtain:

$$\overline{v_S} = \frac{k}{4\omega}\frac{\partial^2}{\partial y \partial x} f^2. \tag{G.19}$$

Appendix H

Derivation of the Markov-0 Model

This is the simplest stochastic model in our hierarchy, alternatively known as a Markov displacement process. Here, a stochastic term is added to the particle position $\mathbf{x}$ only resulting in the 1D stochastic differential equation:

$$dx_i = a_i(\mathbf{x}, t)dt + b_{ii}(\mathbf{x}, t)dW_j(t). \tag{H.1}$$

We follow the methodology in Boughton et al. (1987).

Using eq. (6.3), we obtain:

$$\frac{d\left\langle x_i \right\rangle}{dt} = a_i(\mathbf{x}, t), \tag{H.2}$$

and using eq. (6.4):

$$\frac{\left\langle (dx_i - \left\langle dx_i \right\rangle)^2 \right\rangle}{dt} = 2K_{ii} = b_{ii}^2. \tag{H.3}$$

We only need to consider the zonal and meridional 1D fokker-planck equations independently, as we are assuming that our dispersion tensor is strictly diagonal, that is, the off-diagonal components of K_{ij} are zero. Therefore, let us rewrite eq. (6.6) for the 1D case for the Markov displacement process:

$$\frac{\partial p(\mathbf{x}, t)}{\partial t} + \frac{\partial}{\partial x_i}\left(a_i p(\mathbf{x}, t)\right) - \frac{1}{2}\frac{\partial^2}{\partial x^2}\left(b_{ii}^2 p(\mathbf{x}, t)\right) = 0. \tag{H.4}$$

We know that the diffusion term, $b_{ii} = \sqrt{2K_{ii}}$. It still remains to find the drift term $a_i(\mathbf{x}, t)$. We note that the ensemble mean of the tracer concentration, $\langle c \rangle$, from4.3 satisfies eq. (H.4), where

$$a_i(\mathbf{x}, t) = \frac{\partial K_i}{\partial x_i} + \overline{u_i}. \tag{H.5}$$

Therefore the 1D SDE for the 0th order Markov Model is:

$$x_i(t + dt) = x_i(t) + \left(\overline{u_i} + \frac{\partial K_i}{\partial x_i} \right) dt + \sqrt{2K_i} dW(t). \tag{H.6}$$

Appendix I

Derivation of the Markov-1 Model

We follow the methodology described in Rodean (1996) in order to derive the first order Markov model. Much like for the diffusion model, we start with a 1D SDE, however in this case the stochastic process is the velocity:

$$du_i = a_i(\mathbf{u}, \mathbf{x}, t)dt + b_i(\mathbf{u}, \mathbf{x}, t)dW_j(t). \tag{I.1}$$

The 1D Fokker-Planck equation for the Markov-1 model is:

$$\frac{\partial p}{\partial t} + \frac{\partial (u_i p)}{\partial x_i} = -\frac{\partial (a_i p)}{\partial u_i} + \frac{\partial^2}{\partial u_i^2}\left(\frac{1}{2} b_i^2 p\right). \tag{I.2}$$

The Gaussian 1D Eulerian probability distribution for the velocity is:

$$p_E(u_i, x_i, t) = \frac{1}{\sqrt{2\pi}\sigma_{ii}} \exp\left(-\frac{1}{2}\left(\frac{u_i}{\sigma_{ii}}\right)^2\right). \tag{I.3}$$

In order for the well-mixedness condition to be satisfied, the Lagrangian and Eulerian probability distributions for the velocity must be equivalent, that is, $p_E \sim p_L$. From now on, we write p to express p_E, and $p_i = p(u_i, x_i, t)$.

Taking the logarithm of eq. (I.3) we get:

$$\ln(p_i) = -\frac{1}{2}\ln(2\pi) - \ln(\sigma_{ii}) - \frac{1}{2}\left(\frac{u_i}{\sigma_{ii}}\right)^2. \tag{I.4}$$

then taking the derivative with respect to the velocity u_i, with respect to time and with respect to x_i respectively:

$$\frac{\partial \ln p_i}{\partial u_i} = -\frac{u_i}{\sigma_{ii}^2}, \tag{I.5}$$

$$\frac{\partial \ln p_i}{\partial t} = -\frac{\partial \ln \sigma_{ii}}{\partial t} - \frac{u_i^2}{2}\frac{\partial \sigma_{ii}^{-2}}{\partial t}, \tag{I.6}$$

$$\frac{\partial \ln p_i}{\partial x_i} = -\frac{\partial \ln \sigma_{ii}}{\partial x_i} - \frac{u_i^2}{2}\frac{\partial \sigma_{ii}^{-2}}{\partial x_i}. \tag{I.7}$$

The stochastic random forcing amplitude is defined it be:

$$b_i^2 = \frac{2\sigma_{ii}^2}{T_L}, \tag{I.8}$$

where T_L is the first order fading memory tensor. See Rodean (1996) for details on the derivation.

By integrating eq. (I.2) with respect to the velocity u_i we get:

$$a_i p_i = \frac{\partial}{\partial u_i}\left(\frac{1}{2}b_i^2 p_i\right) + \Phi_i, \tag{I.9}$$

where

$$\frac{\partial \Phi_i}{\partial u_i} = -\frac{\partial \rho}{\partial t} - \frac{\partial u_i p_i}{\partial x_i} \tag{I.10}$$

In order the satisfy the well mixedness condition (see Thomson (1987) for further details), as $|\mathbf{u}_i| \to \infty, \Phi_i \to 0$. From eq. (I.9), we get:

$$a_i = \frac{1}{p_i}\frac{\partial}{\partial u_i}\left(\frac{b_i^2}{2}p_i\right) + \frac{\Phi_i}{p_i}. \tag{I.11}$$

From eq. (I.8), we know that b_i is independent of the Lagrangian velocity u_i, and using eq. (I.5):

$$\frac{1}{p_i}\frac{\partial p_i}{\partial u_i} = \frac{\partial \ln p_i}{\partial u_i} = -\frac{u_i}{\sigma_{ii}^2}. \tag{I.12}$$

Hence

$$a_i = -\frac{u_i b_i^2}{2\sigma_{ii}^2} + \frac{\phi_i}{p_i} = -\frac{u_i}{T_L} + \frac{\phi_i}{p_i}. \tag{I.13}$$

Re-writing eq. (I.10) and applying eq. (I.6) and eq. (I.7) we get:

$$\frac{1}{p_i}\frac{\partial \phi_i}{\partial u_i} = -\frac{\partial \ln p_i}{\partial t} - u_i\frac{\partial \ln p_i}{\partial x_i}, \tag{I.14}$$

$$= \frac{\partial \ln \sigma_{ii}}{\partial t} + u_i\frac{\partial \ln \sigma_{ii}}{\partial x_i} + \frac{u_i^2}{2}\frac{\partial \sigma_{ii}^{-2}}{\partial t} + \frac{u_i^3}{2}\frac{\partial \sigma_{ii}^{-2}}{\partial x_i}. \tag{I.15}$$

Therefore, we can express ϕ_i/p_i as a quadratic equation:

$$\frac{\phi_i}{p_i} = \alpha + \beta u_i + \gamma u_i^2. \tag{I.16}$$

Differentiating with respect to u_i:

$$\frac{\partial}{\partial u_i}\left(\frac{\phi_i}{p_i}\right) = \frac{1}{p_i}\frac{\partial \phi_i}{\partial u_i} + \phi_i\frac{\partial}{\partial u_i}\left(\frac{1}{p_i}\right), \tag{I.17}$$

$$= \frac{1}{p_i}\frac{\partial \phi_i}{\partial u_i} - \phi_i\frac{1}{p_i^2}\frac{\partial p_i}{\partial u_i}, \tag{I.18}$$

$$= \frac{1}{p_i}\frac{\partial \phi_i}{\partial u_i} + \phi_i\frac{1}{p_i}\frac{\partial \ln p_i}{\partial u_i}, \tag{I.19}$$

$$= \frac{1}{p_i}\frac{\partial \phi_i}{\partial u_i} + \frac{\phi_i}{p_i}\frac{u_i}{\sigma_{ii}^2}. \tag{I.20}$$

Differentiating eq. (I.16):

$$\frac{\partial}{\partial u_i}\left(\frac{\phi_i}{p_i}\right) = \beta + 2\gamma u_i, \tag{I.21}$$

hence, combing the above expressions

$$\begin{aligned}
\frac{1}{p_i}\frac{\partial \phi_i}{\partial u_i} &= \beta + 2\gamma u_i - \frac{\phi_i}{p_i}\frac{u_i}{\sigma_{ii}^2}, && \text{(I.22)}\\
&= \beta + 2\gamma u_i - (\alpha + \beta u_i + \gamma u_i^2)\frac{u_i}{\sigma_{ii}^2}, && \text{(I.23)}\\
&= \beta + u_i\left(2\gamma - \frac{\alpha}{\sigma_{ii}^2}\right) - u_i^2\left(\frac{\beta}{\sigma_{ii}^2}\right) - \gamma\frac{u_i^3}{\sigma_{ii}^2}. && \text{(I.24)}
\end{aligned}$$

Therefore, matching up coefficients:

$$\begin{aligned}
\beta &= \frac{\partial \ln \sigma_{ii}}{\partial t}, && \text{(I.25)}\\
2\gamma - \frac{\alpha}{\sigma_{ii}^2} &= \frac{\partial \ln \sigma_{ii}}{\partial x_i}, && \text{(I.26)}\\
-\frac{\beta}{\sigma_{ii}^2} &= \frac{1}{2}\frac{\partial \sigma_{ii}^{-2}}{\partial t}, && \text{(I.27)}\\
-\frac{\gamma}{\sigma_{ii}^2} &= \frac{1}{2}\frac{\partial \sigma_{ii}^{-2}}{\partial x_i}. && \text{(I.28)}
\end{aligned}$$

Focusing on γ:

$$\frac{\partial \sigma_{ii}^{-2}}{\partial x_i} = -\frac{2}{\sigma_{ii}^3}\frac{\partial \sigma_{ii}}{\partial x_i} = -\frac{2}{\sigma_{ii}^2}\frac{\partial \ln \sigma_{ii}}{\partial x_i}. \tag{I.29}$$

Hence

$$\gamma = \frac{\partial \ln \sigma_{ii}}{\partial x_i}, \tag{I.30}$$

and

$$\alpha = \sigma_{ii}^2\frac{\partial \ln \sigma_{ii}}{\partial x_i}. \tag{I.31}$$

Combining all the above results, we get:

$$\frac{\phi_i}{p_i} = \sigma_{ii}^2 \frac{\partial \ln \sigma_{ii}}{\partial x_i} + u_i \frac{\partial \ln \sigma_{ii}}{\partial t} + u_i^2 \frac{\partial \ln \sigma_{ii}}{\partial x_i}. \tag{I.32}$$

Expressing the above in terms of partial derivatives of σ_{ii}^2 instead of $\ln \sigma_{ii}$:

$$\frac{\phi_i}{p_i} = \frac{1}{2} \frac{\partial \sigma_{ii}^2}{\partial x_i} + \frac{1}{2\sigma_{ii}^2} \left(\frac{\partial \sigma_{ii}^2}{\partial t} \right) u_i + \frac{1}{2\sigma_{ii}^2} \left(\frac{\partial \sigma_{ii}^2}{\partial x_i} \right) u_i^2. \tag{I.33}$$

Substituting the above into eq. (I.13), we obtain the following 1-D SDE governing the random flight velocity:

$$u_i'(t+dt) = u_i'(t) - \frac{u_i'}{T_L} dt + \frac{1}{2} \left(1 + \left(\frac{u_i'}{\sigma_{ii}} \right)^2 \right) \frac{\partial \sigma_{ii}^2}{\partial x_i} dt + \left(\frac{2\sigma_{ii}^2}{T_L} \right)^{1/2} dW(t). \tag{I.34}$$

Appendix J

Markov Model Figures

J.1 Single Particle Dispersion for a Markov Models comparing Diffusivity Estimates

J.1.1 Markov-0 Model

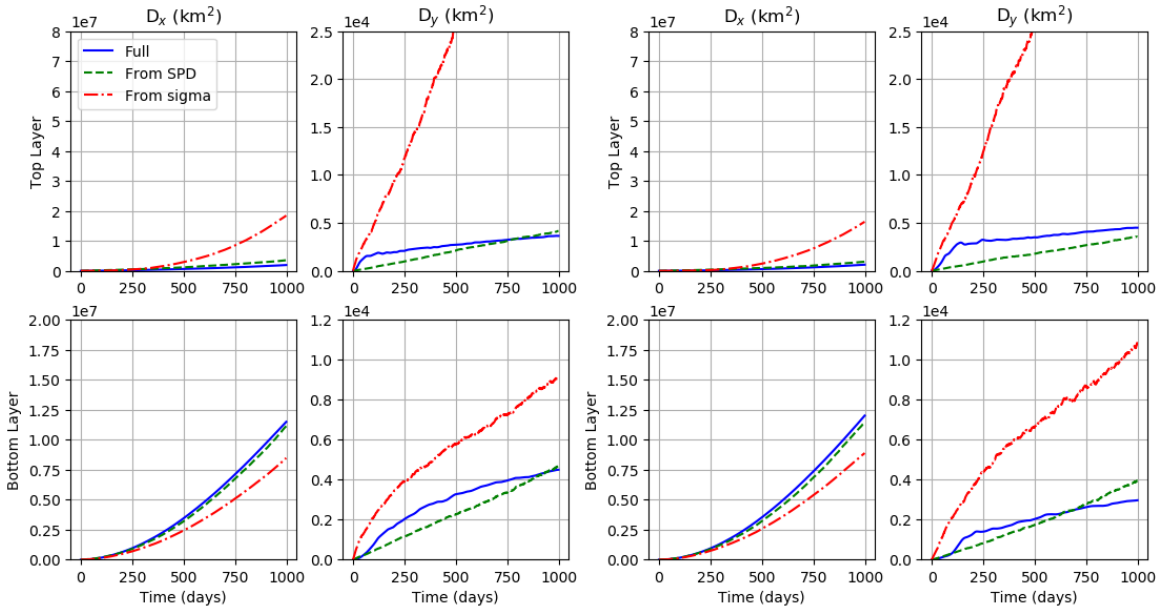

(a) Bin 1

(b) Bin 2

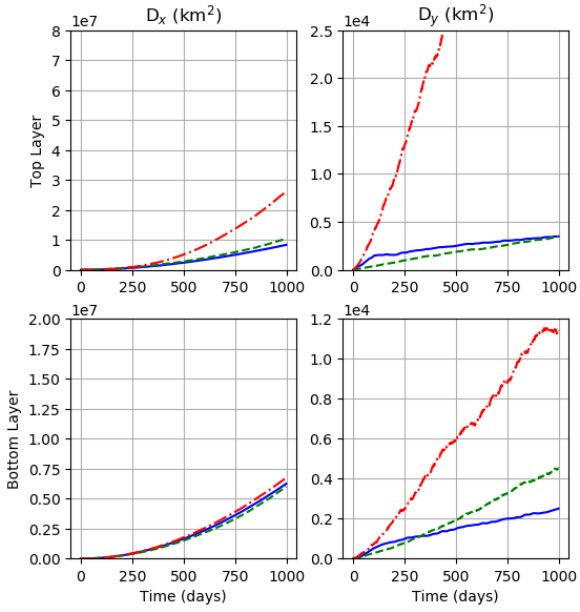

(c) Bin 3

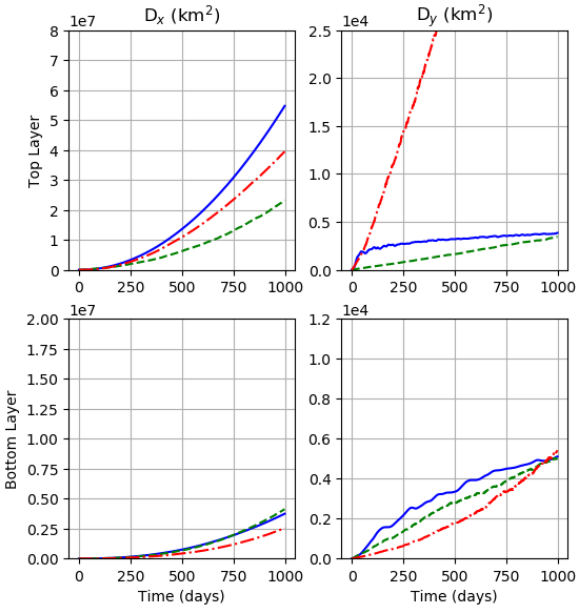

(d) Bin 4

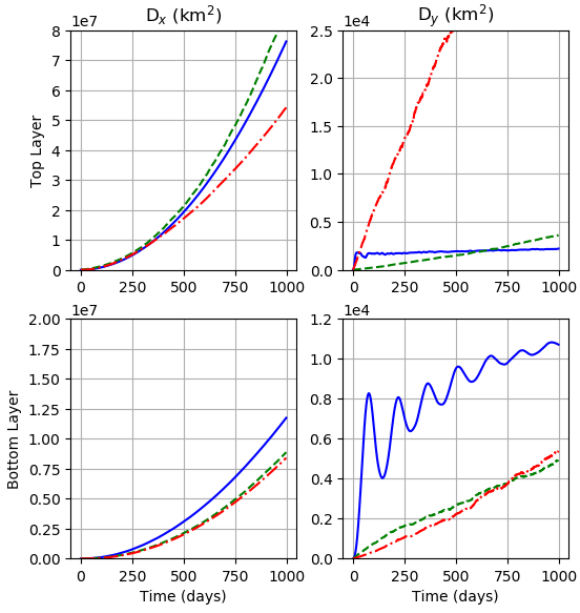

(e) Bin 5

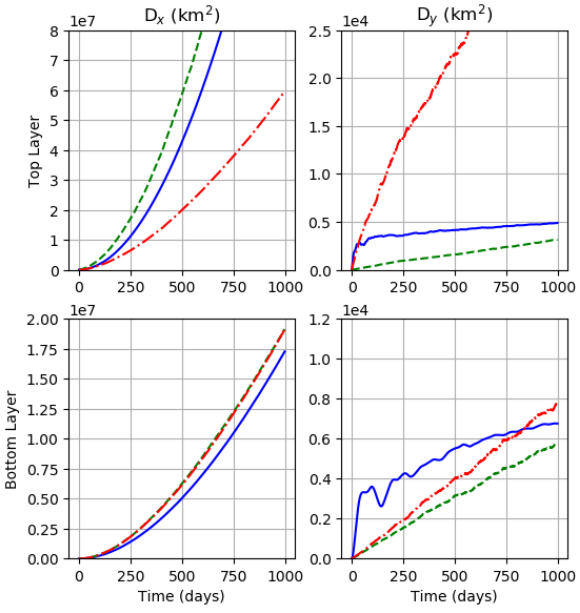

(f) Bin 6

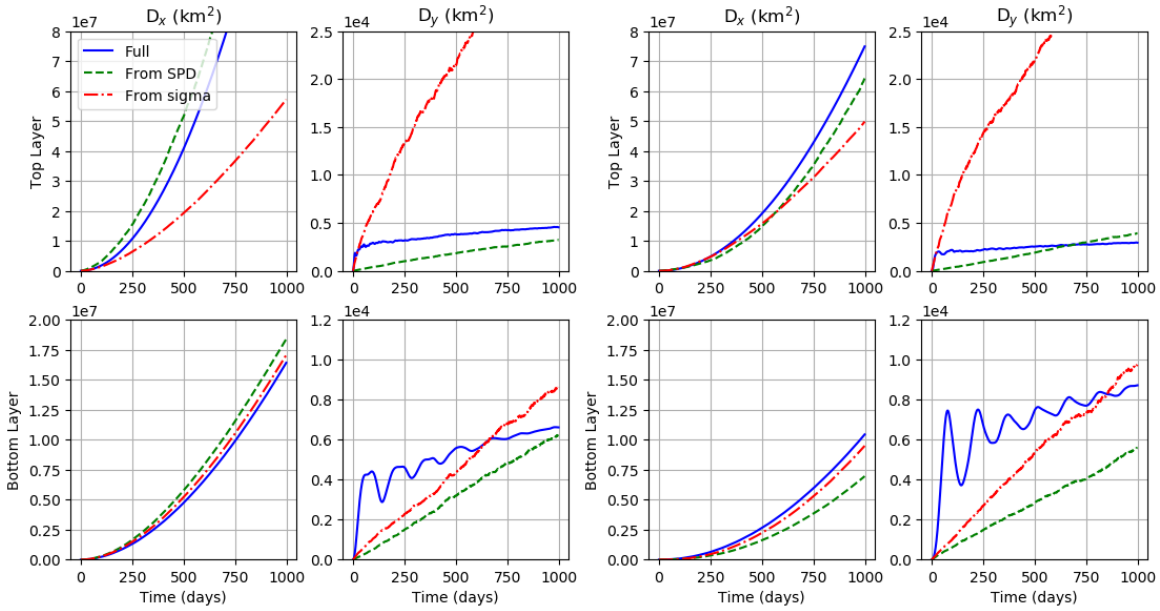

(g) Bin 7

(h) Bin 8

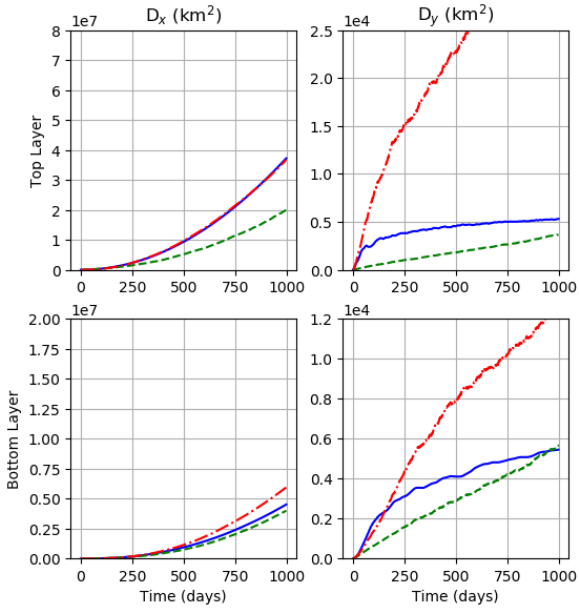

(i) Bin 9

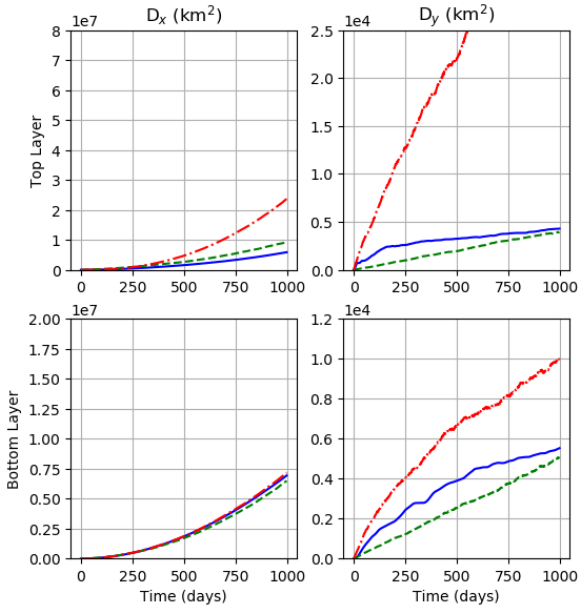

(j) Bin 10

Figure J.1: Single-Particle Dispersion (km^2) against time (days) for the Diffusion Model for the coherent jet comparing use of diffusivity calculated from the SPD or from the as $\sigma_{ii}^2 T_L^{(i)}$. Demonstrates SPD gives a more accurate asymptotic diffusivity estimate.

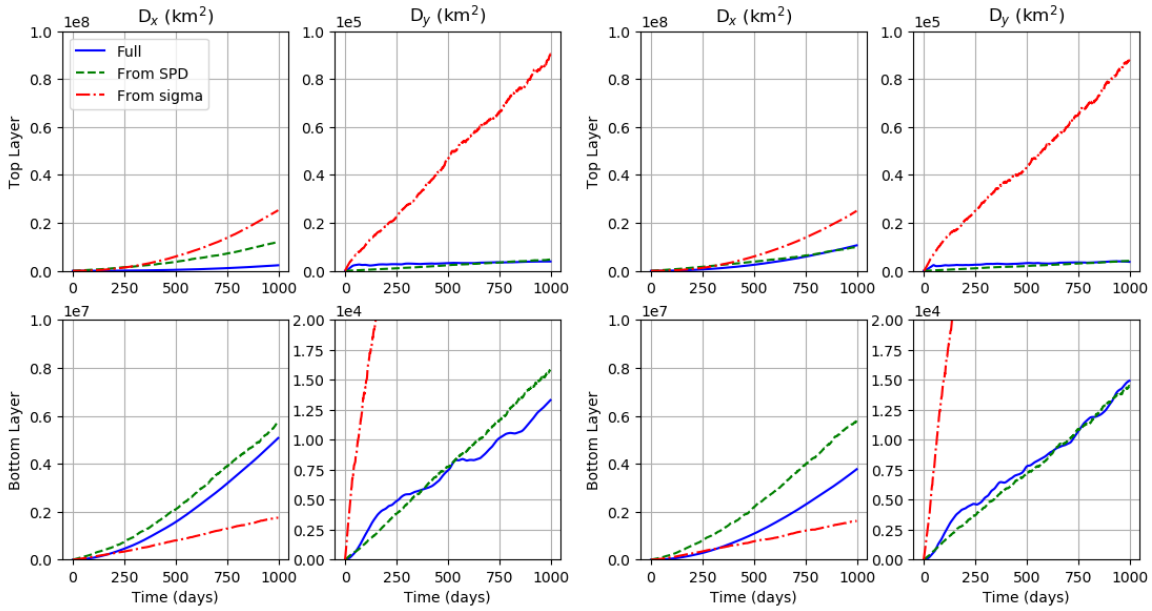

(a) Bin 1

(b) Bin 2

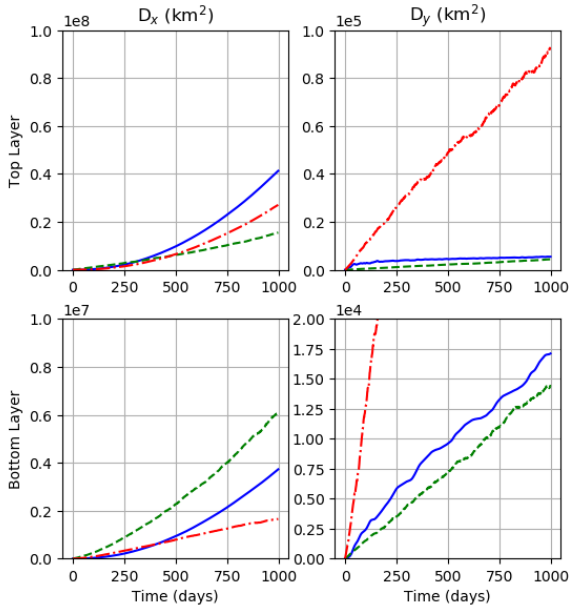

(c) Bin 3

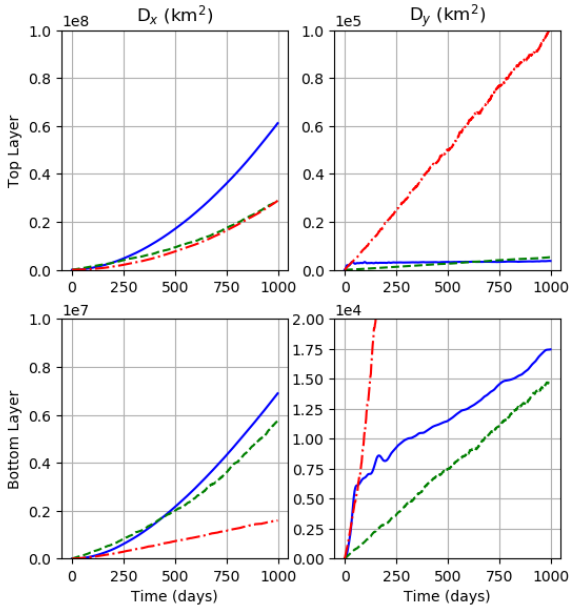

(d) Bin 4

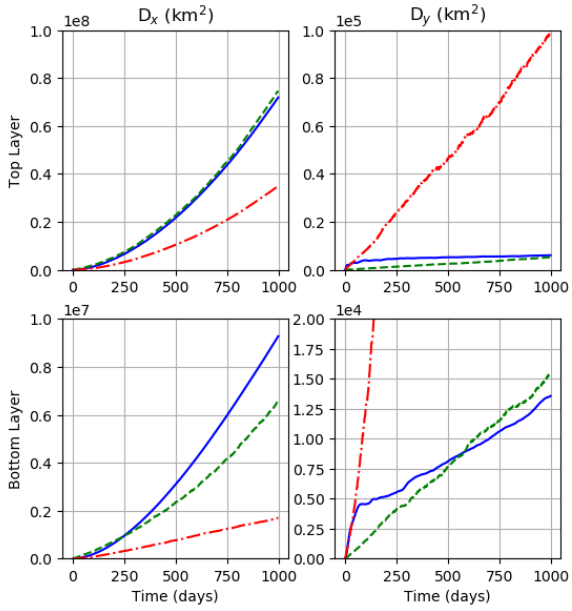

(e) Bin 5

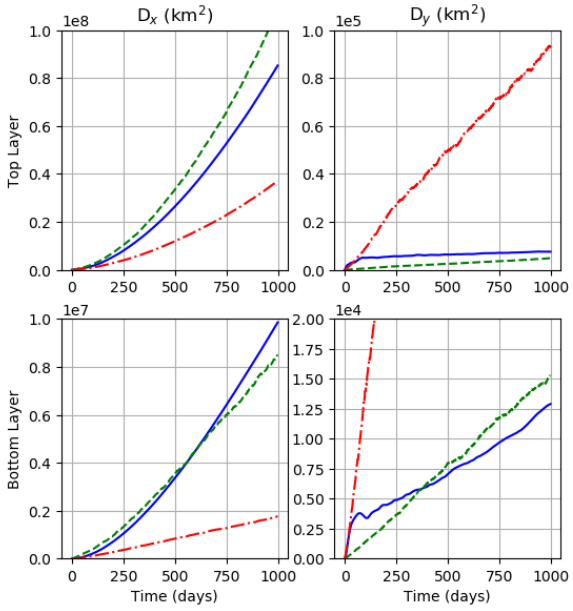

(f) Bin 6

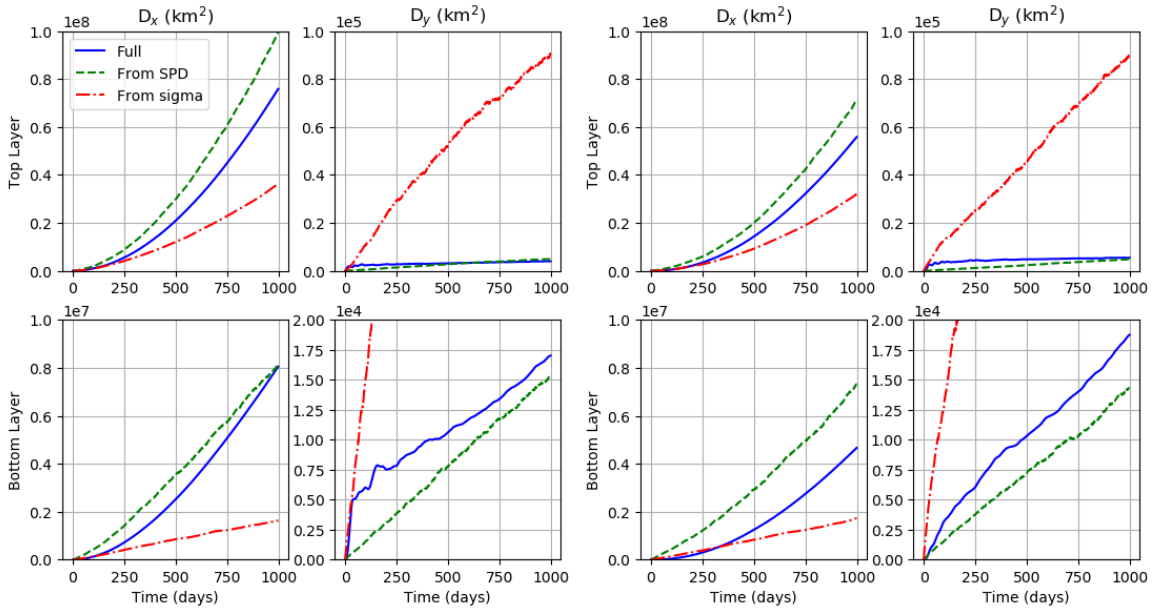

(g) Bin 7 (h) Bin 8

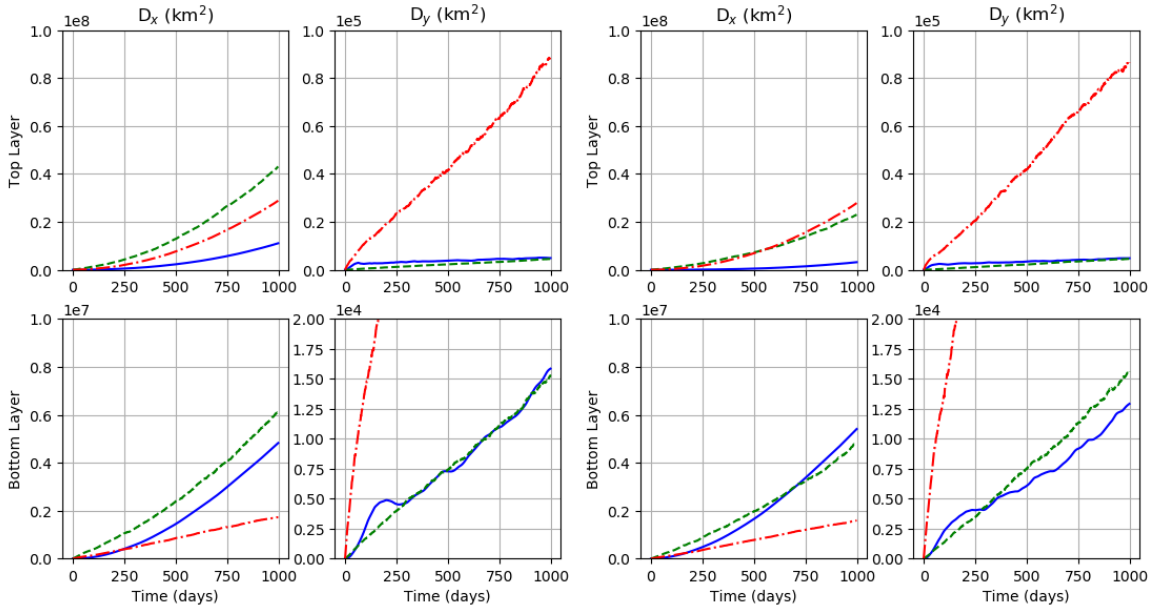

(i) Bin 9 (j) Bin 10

Figure J.2: Single-Particle Dispersion (km^2) against time (days) for the Diffusion Model for the latent jet comparing use of diffusivity calculated from the SPD or from $\sigma_{ii}^2 T_L^{(i)}$. Demonstrates SPD gives a more accurate asymptotic diffusivity estimate.

J.1.2 Markov-1 Model

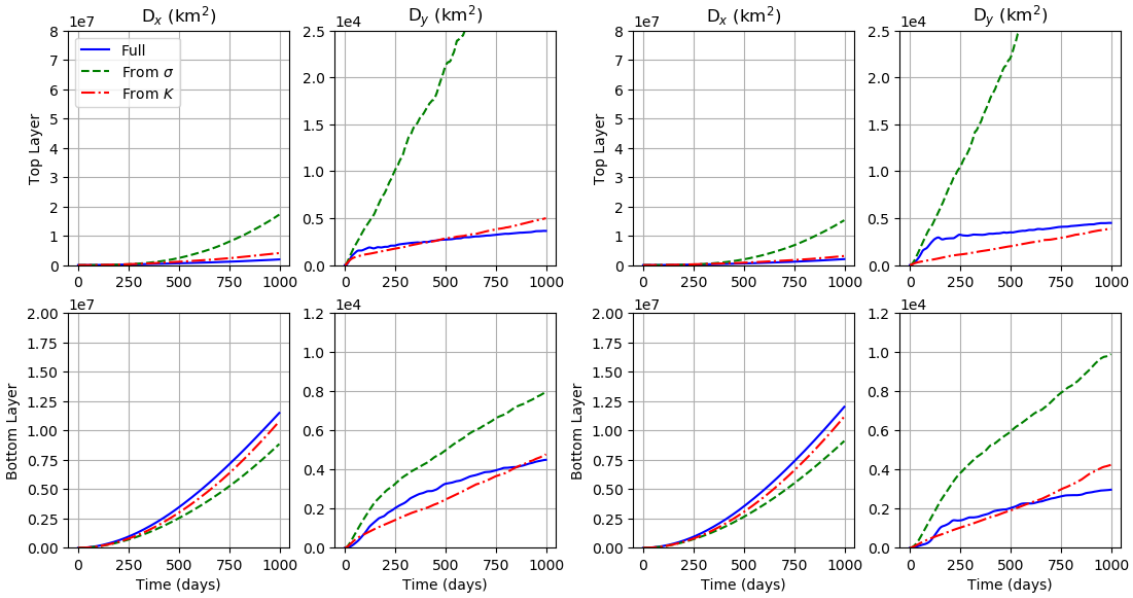

(a) Bin 1

(b) Bin 2

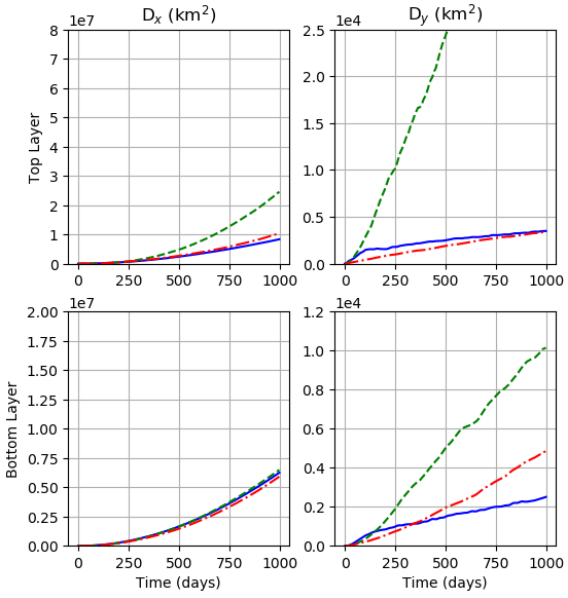

(c) Bin 3

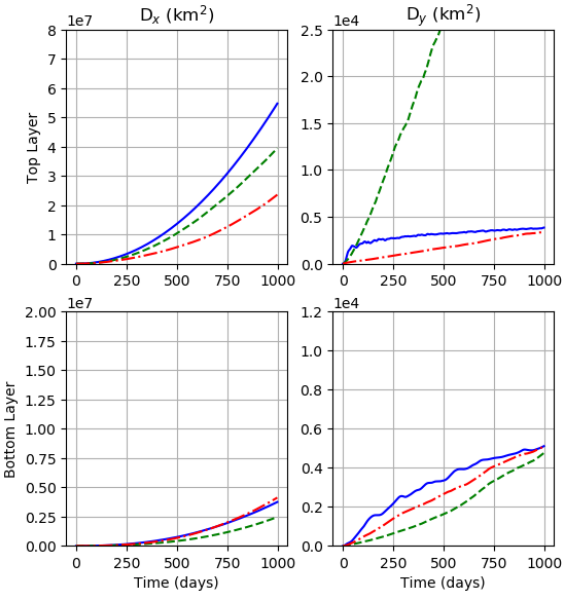

(d) Bin 4

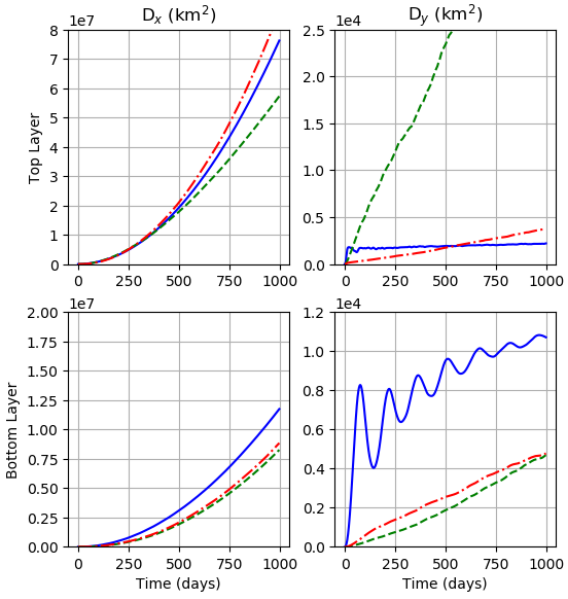

(e) Bin 5

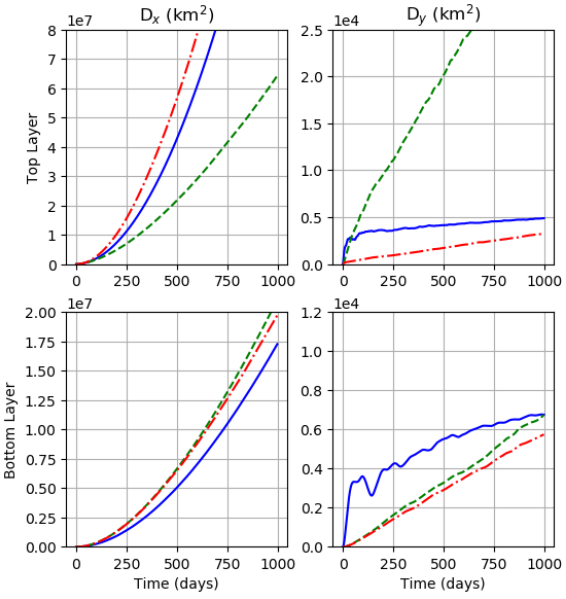

(f) Bin 6

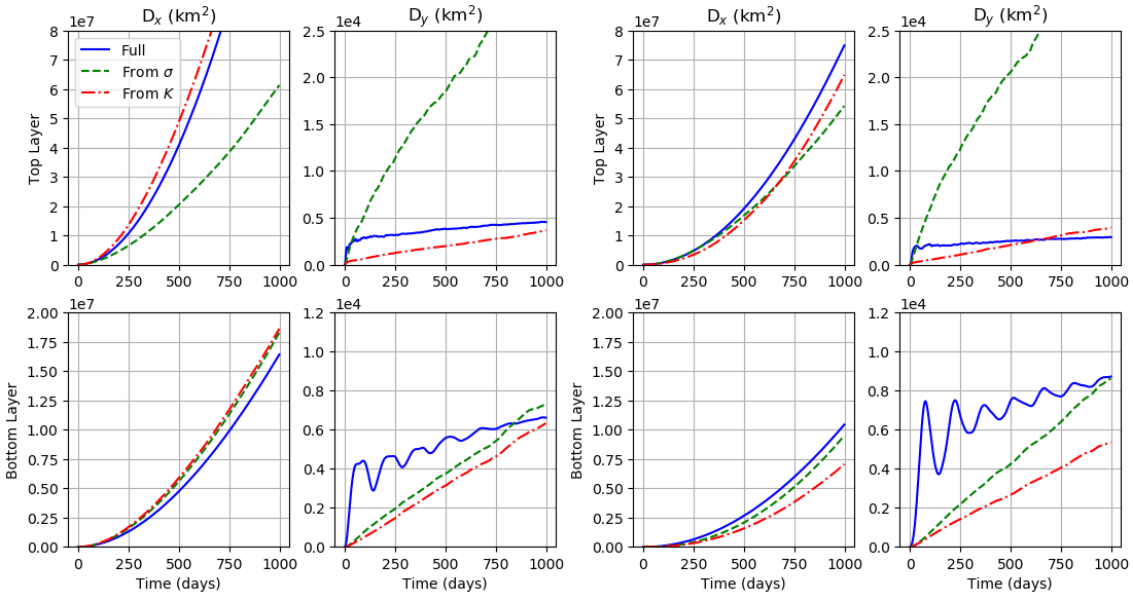

(g) Bin 7

(h) Bin 8

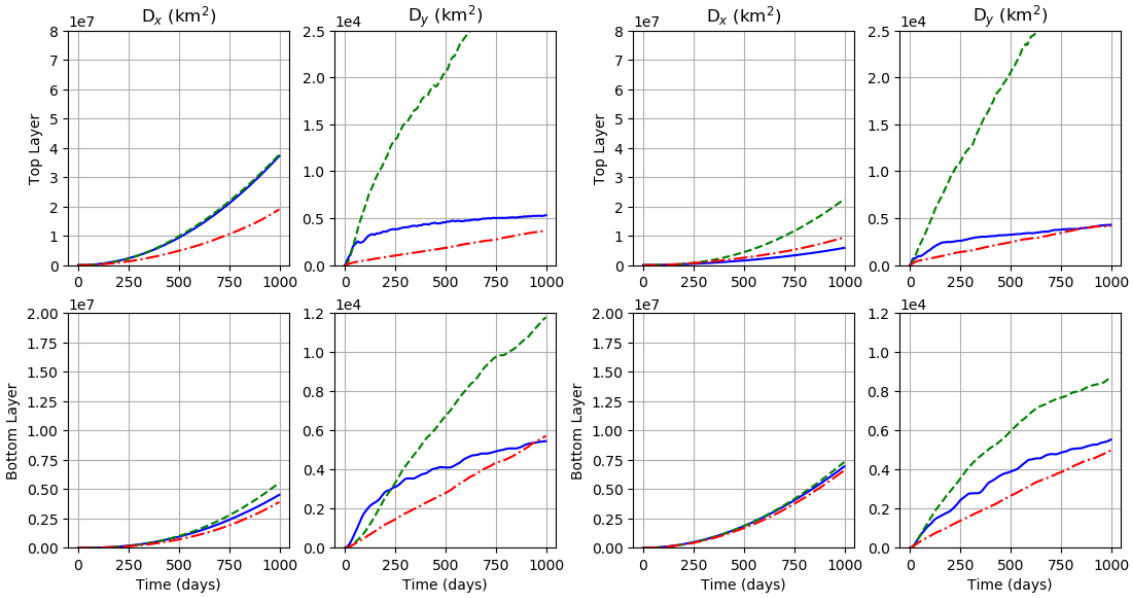

(i) Bin 9

(j) Bin 10

Figure J.3: Single-Particle Dispersion (km^2) against time (days) for the Markov-1 Model for the coherent jet comparing use of σ calculated directly from the Lagrangian trajectories or from K and T_L^i. SPD method is more accurate.

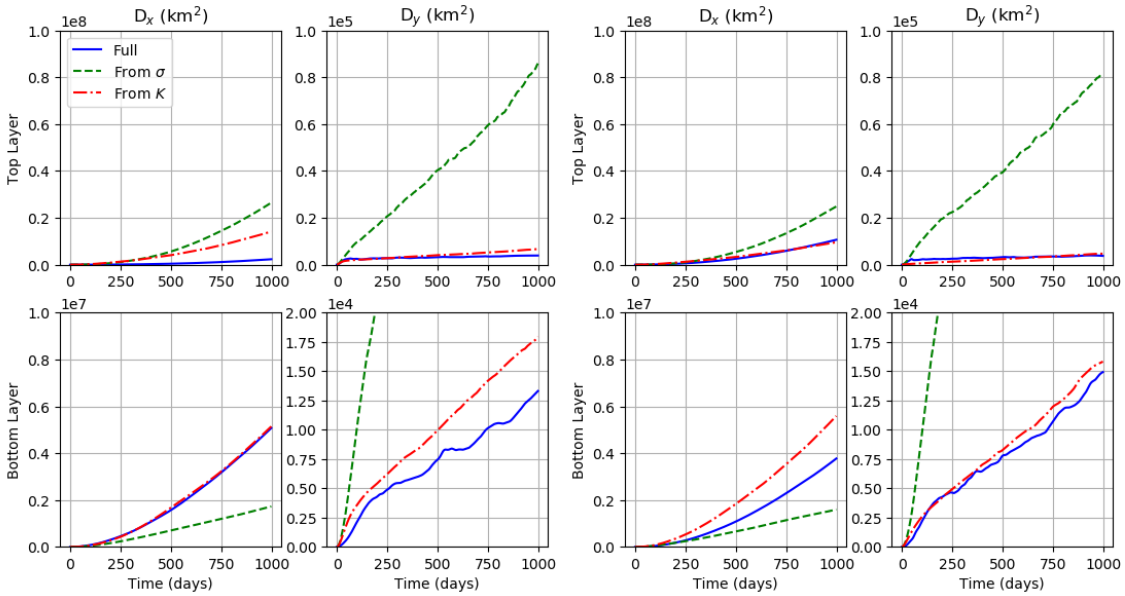

(a) Bin 1

(b) Bin 2

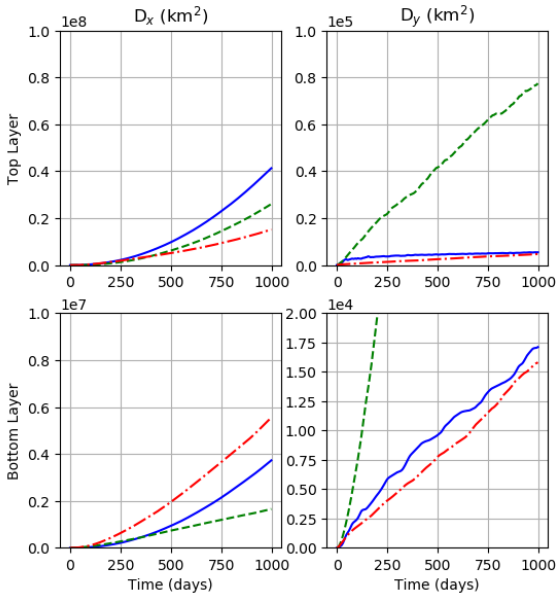

(c) Bin 3

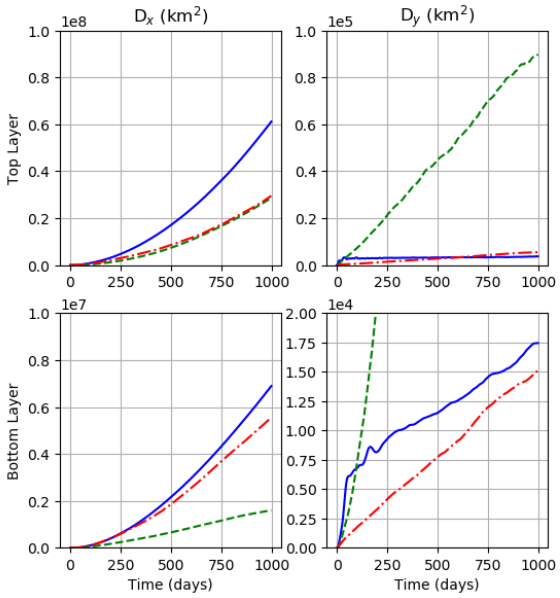

(d) Bin 4

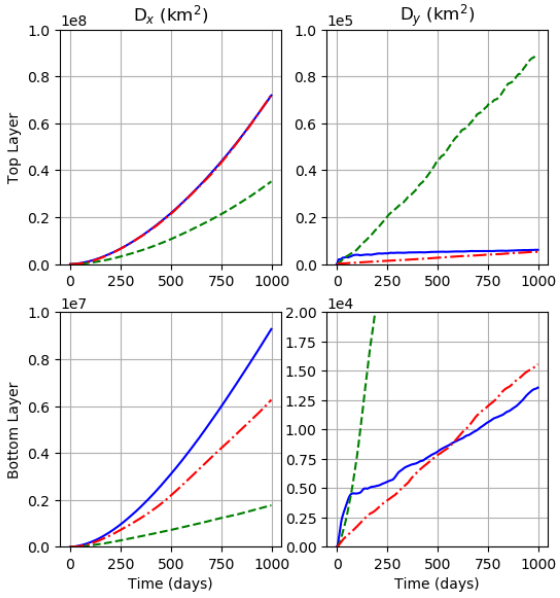

(e) Bin 5

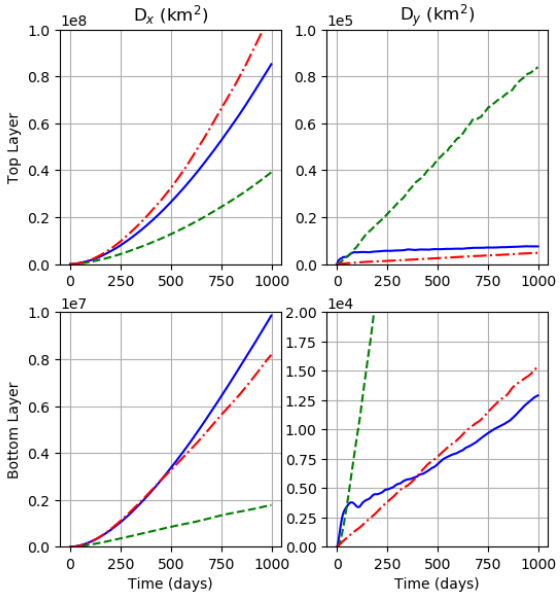

(f) Bin 6

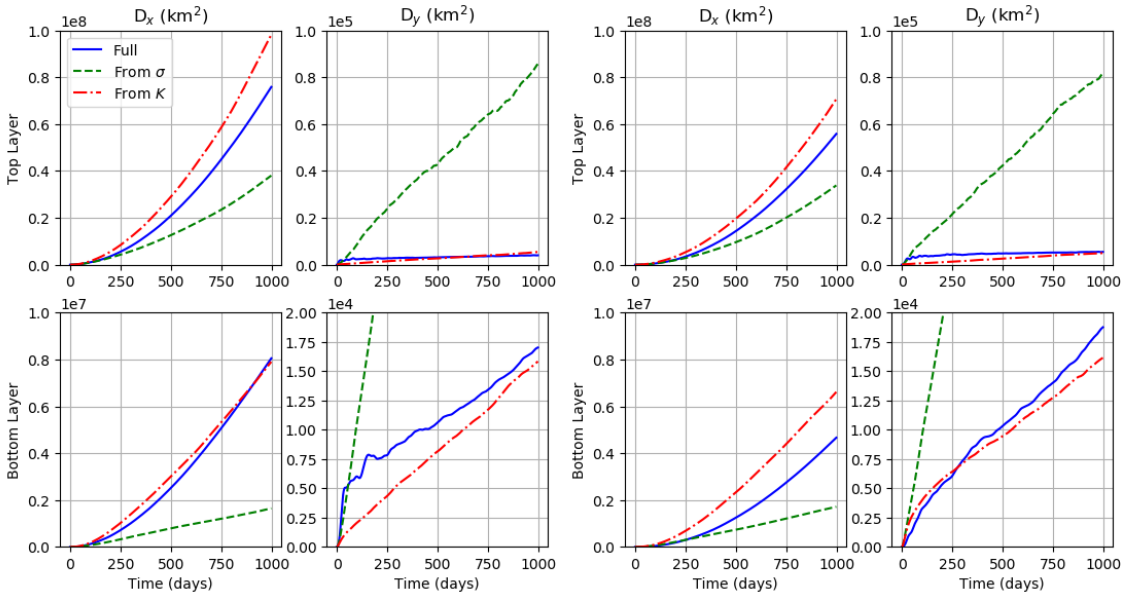

(g) Bin 7 (h) Bin 8

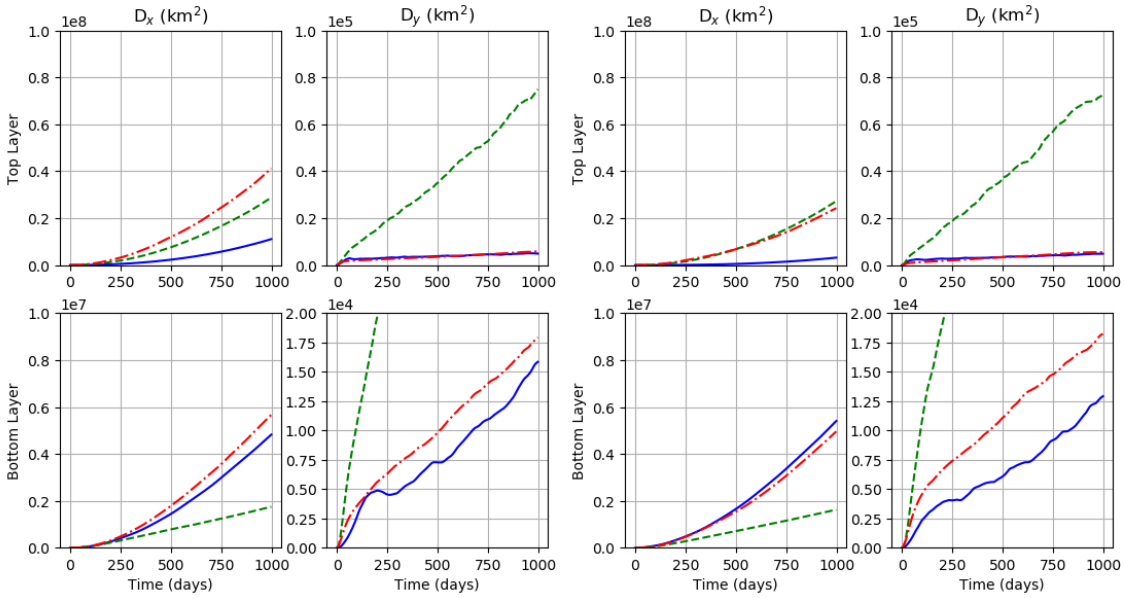

(i) Bin 9 (j) Bin 10

Figure J.4: Single-Particle Dispersion (km^2) against time (days) for the Markov-1 Model for the latent jet comparing use of σ calculated directly from the Lagrangian trajectories or from K and T_L^i. SPD method is more accurate.